

JOURNAL OF  
RESEARCH

OF THE U.S. GEOLOGICAL SURVEY

---

MARCH-APRIL 1978  
VOLUME 6, NUMBER 2

*Scientific notes and summaries  
of investigations in geology,  
hydrology, and related fields*



U.S. DEPARTMENT OF THE INTERIOR



UNITED STATES DEPARTMENT OF THE INTERIOR

CECIL D. ANDRUS, Secretary

GEOLOGICAL SURVEY

W. A. Radlinski, Acting Director

For sale by Superintendent of Documents, U.S. Government Printing Office, Washington, DC 20402. Annual subscription rate, \$18.90 (plus \$4.75 for foreign mailing). Make check or money order payable to Superintendent of Documents. Send all subscription inquiries and address changes to Superintendent of Documents at above address.

Purchase single copy (\$3.15) from Branch of Distribution, U.S. Geological Survey, 1200 South Eads Street, Arlington, VA 22202. Make check or money order payable to U.S. Geological Survey.

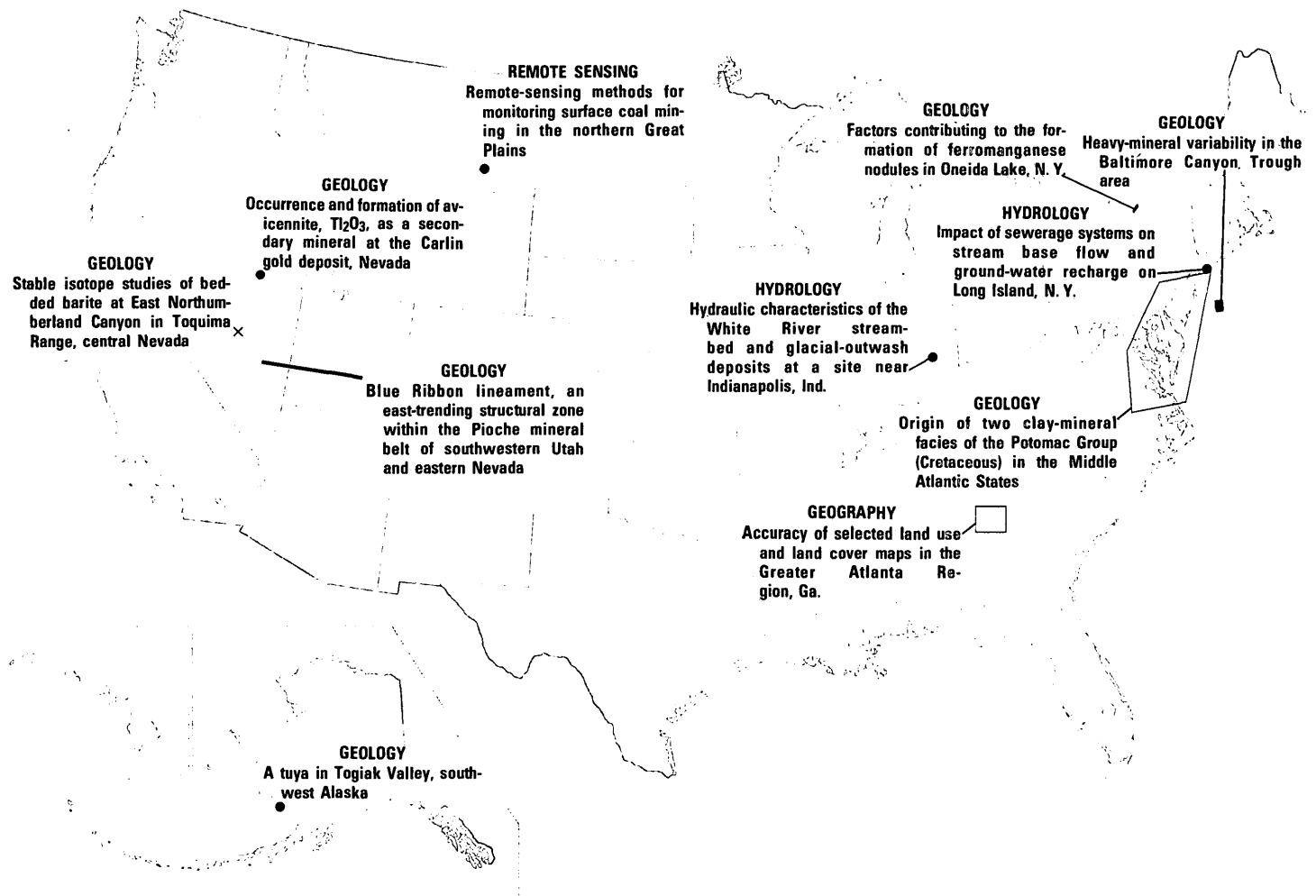
Library of Congress Catalog-card No. 72-600241.

The Journal of Research is published every 2 months by the U.S. Geological Survey. It contains papers by members of the Geological Survey and their professional colleagues on geologic, hydrologic, topographic, and other scientific and technical subjects.

Correspondence and inquiries concerning the Journal (other than subscription inquiries and address changes) should be directed to Anna M. Orellana, Managing Editor, Journal of Research, Publications Division, U.S. Geological Survey, 321 National Center, Reston, VA 22092.

Papers for the Journal should be submitted through regular Division publication channels.

The Secretary of the Interior has determined that the publication of this periodical is necessary in the transaction of the public business required by law of this Department. Use of funds for printing this periodical has been approved by the Director of the Office of Management and Budget through June 30, 1980.



GEOGRAPHIC INDEX TO ARTICLES

See "Contents" for articles concerning areas outside the United States and articles without geographic orientation.

# JOURNAL OF RESEARCH

of the

U.S. Geological Survey

---

Vol. 6 No. 2

Mar.-Apr. 1978

---

## CONTENTS

SI units and U.S. customary equivalents..... II

### APPLICATIONS OF REMOTELY SENSED DATA

Remote-sensing methods for monitoring surface coal mining in the northern Great Plains.....*Ned Mamula, Jr.* 149

### GEOGRAPHIC STUDIES

An "optimal" filter for maps showing nominal data.....*S. C. Gupta* 161  
Accuracy of selected land use and land cover maps in the Greater Atlanta Region, Ga.....*Katherine Fitzpatrick-Lins* 169

### GEOLOGIC STUDIES

Blue Ribbon lineament, an east-trending structural zone within the Pioche mineral belt of southwestern Utah and eastern Nevada.....*P. D. Rowley, P. W. Lipman, H. H. Mehnert, D. A. Lindsey, and J. J. Anderson* 175  
A tuya in Togiak Valley, southwest Alaska.....*J. M. Hoare and W. L. Coonrad* 193  
Origin of two clay-mineral facies of the Potomac Group (Cretaceous) in the Middle Atlantic States.....*L. M. Force and G. K. Moncure* 203  
Heavy-mineral variability in the Baltimore Canyon Trough area.....*H. J. Knebel and D. C. Twichell* 215  
Stable isotope studies of bedded barite at East Northumberland Canyon in Toquima Range, central Nevada.....*R. O. Rye, D. R. Shawe, and F. G. Poole* 221  
Factors contributing to the formation of ferromanganese nodules in Oneida Lake, N.Y.....*W. E. Dean and S. K. Ghosh* 231  
Occurrence and formation of avicennite,  $Tl_2O_3$ , as a secondary mineral at the Carlin gold deposit, Nevada.....*A. S. Radtke, F. W. Dickinson, and J. F. Slack* 241  
Models for calculating density and vapor pressure of geothermal brines.....*R. W. Potter II and J. L. Haas, Jr.* 247  
Spectrochemical determination of submicrogram amounts of tungsten in geologic materials.....*R. W. Leinz and D. J. Grimes* 259

### HYDROLOGIC STUDIES

Impact of sewerage systems on stream base flow and ground-water recharge on Long Island, N.Y.....*E. J. Pluhowski and A. G. Spinello* 263  
Hydraulic characteristics of the White River streambed and glacial-outwash deposits at a site near Indianapolis, Ind.....*William Meyer* 273  
Recent publications of the U.S. Geological Survey.....Inside of back cover

## SI UNITS AND U.S. CUSTOMARY EQUIVALENTS

[SI, International System of Units, a modernized metric system of measurement. All values have been rounded to four significant digits except 0.01 bar, which is the exact equivalent of 1 kPa. Use of hectare (ha) as an alternative name for square hectometer (hm<sup>2</sup>) is restricted to measurement of land or water areas. Use of liter (L) as a special name for cubic decimeter (dm<sup>3</sup>) is restricted to the measurement of liquids and gases; no prefix other than milli should be used with liter. Metric ton (t) as a name for megagram (Mg) should be restricted to commercial usage, and no prefixes should be used with it. Note that the style of meter<sup>2</sup> rather than square meter has been used for convenience in finding units in this table. Where the units are spelled out in text, Survey style is to use square meter]

SI unit	U.S. customary equivalent	
<b>Length</b>		
millimeter (mm)	= 0.039 37	inch (in)
meter (m)	= 3.281	feet (ft)
	= 1.094	yards (yd)
kilometer (km)	= 0.621 4	mile (mi)
	= 0.540 0	mile, nautical (nmi)
<b>Area</b>		
centimeter <sup>2</sup> (cm <sup>2</sup> )	= 0.155 0	inch <sup>2</sup> (in <sup>2</sup> )
meter <sup>2</sup> (m <sup>2</sup> )	= 10.76	feet <sup>2</sup> (ft <sup>2</sup> )
	= 1.196	yards <sup>2</sup> (yd <sup>2</sup> )
	= 0.000 247 1	acre
hectometer <sup>2</sup> (hm <sup>2</sup> )	= 2.471	acres
	= 0.003 861	section (640 acres or 1 mi <sup>2</sup> )
kilometer <sup>2</sup> (km <sup>2</sup> )	= 0.386 1	mile <sup>2</sup> (mi <sup>2</sup> )
<b>Volume</b>		
centimeter <sup>3</sup> (cm <sup>3</sup> )	= 0.061 02	inch <sup>3</sup> (in <sup>3</sup> )
decimeter <sup>3</sup> (dm <sup>3</sup> )	= 61.02	inches <sup>3</sup> (in <sup>3</sup> )
	= 2.113	pints (pt)
	= 1.057	quarts (qt)
	= 0.264 2	gallon (gal)
	= 0.035 31	foot <sup>3</sup> (ft <sup>3</sup> )
meter <sup>3</sup> (m <sup>3</sup> )	= 35.31	feet <sup>3</sup> (ft <sup>3</sup> )
	= 1.308	yards <sup>3</sup> (yd <sup>3</sup> )
	= 264.2	gallons (gal)
	= 6.290	barrels (bbl) (petroleum, 1 bbl=42 gal)
	= 0.000 810 7	acre-foot (acre-ft)
hectometer <sup>3</sup> (hm <sup>3</sup> )	= 810.7	acre-feet (acre-ft)
kilometer <sup>3</sup> (km <sup>3</sup> )	= 0.239 9	mile <sup>3</sup> (mi <sup>3</sup> )
<b>Volume per unit time (includes flow)</b>		
decimeter <sup>3</sup> per second (dm <sup>3</sup> /s)	= 0.035 31	foot <sup>3</sup> per second (ft <sup>3</sup> /s)
	= 2.119	feet <sup>3</sup> per minute (ft <sup>3</sup> /min)

SI unit	U.S. customary equivalent	
<b>Volume per unit time (includes flow)—Continued</b>		
decimeter <sup>3</sup> per second (dm <sup>3</sup> /s)	= 15.85	gallons per minute (gal/min)
	= 543.4	barrels per day (bbl/d) (petroleum, 1 bbl=42 gal)
meter <sup>3</sup> per second (m <sup>3</sup> /s)	= 35.31	feet <sup>3</sup> per second (ft <sup>3</sup> /s)
	= 15 850	gallons per minute (gal/min)
<b>Mass</b>		
gram (g)	= 0.035 27	ounce avoirdupois (oz avdp)
kilogram (kg)	= 2.205	pounds avoirdupois (lb avdp)
megagram (Mg)	= 1.102	tons, short (2 000 lb)
	= 0.984 2	ton, long (2 240 lb)
<b>Mass per unit volume (includes density)</b>		
kilogram per meter <sup>3</sup> (kg/m <sup>3</sup> )	= 0.062 43	pound per foot <sup>3</sup> (lb/ft <sup>3</sup> )
<b>Pressure</b>		
kilopascal (kPa)	= 0.145 0	pound-force per inch <sup>2</sup> (lbf/in <sup>2</sup> )
	= 0.009 869	atmosphere, standard (atm)
	= 0.01	bar
	= 0.296 1	inch of mercury at 60°F (in Hg)
<b>Temperature</b>		
temp kelvin (K)	= [temp deg Fahrenheit (°F) + 459.67]/1.8	
temp deg Celsius (°C)	= [temp deg Fahrenheit (°F) - 32]/1.8	

The policy of the "Journal of Research of the U.S. Geological Survey" is to use SI metric units of measurement except for the following circumstance:

When a paper describes either field equipment or laboratory apparatus dimensioned or calibrated in U.S. customary units and provides information on the physical features of the components and operational characteristics of the equipment or apparatus, then dual units may be used. For example, if a pressure gage is calibrated and available only in U.S. customary units of measure, then the gage may be described using SI units in the dominant position with the equivalent U.S. customary unit immediately following in parentheses. This also applies to the description of tubing, piping, vessels, and other items of field and laboratory equipment that normally are described in catalogs in U.S. customary dimensions.

S. M. LANG, *Metrics Coordinator,*  
*U.S. Geological Survey*

Any use of trade names and trademarks in this publication is for descriptive purposes only and does not constitute endorsement by the U.S. Geological Survey.

## REMOTE-SENSING METHODS FOR MONITORING SURFACE COAL MINING IN THE NORTHERN GREAT PLAINS

By NED MAMULA, Jr.,<sup>1</sup> Reston, Va.

*Abstract.*—Recent studies at a large surface coal mine in southern Montana confirm that remote sensing is both feasible and effective for gathering land-use and environmental data (spatial, dynamic, and seasonal) for large-scale surface mines in the northern Great Plains. The Western Energy Co.'s Rosebud mine near Colstrip, Mont., was selected as a test site because it typifies surface operations in the Powder River Basin of Montana and Wyoming and elsewhere in the northern Great Plains. Several basic interpretive and analytical remote-sensing techniques were used to identify and delineate various categories of surface-mining operations and concurrent stages of reclamation that characterize most, if not all, such mining operations. Color infrared and black-and-white aerial photographs and a black-and-white band 5 Landsat image were used to identify (1) highwall and bench areas, (2) ungraded spoils, (3) graded and recontoured areas, (4) revegetated recontoured areas, (5) natural and impounded surface water, and (6) miscellaneous areas. Over the lifespan of an extensive surface mine, cultural and natural processes and cumulative environmental effects can be monitored by capitalizing on the close correlation between enhanced satellite imagery, infrared and (or) black-and-white aerial photography, standard large-scale topographic maps (such as U.S. Geological Survey 7½-minute quadrangle maps), and results of onsite inspection of mining and reclamation by Federal or State agencies.

An investigation, using small-scale remotely sensed data, was made to determine land-use and environmental conditions within large areas of the public domain in the northern Great Plains which have been leased by the Federal Government for surface mining of coal. The investigation evaluated the feasibility of monitoring changes in surface-mining areas by using multispectral scanner (MSS) imagery from the Landsat-1 and -2 spacecraft and similar data. Coupled with aerial photography, MSS imagery allows changes of surface features caused by strip mining to be identified, interpreted, and mapped and, thereby, can assist certain Federal and State agencies to supervise producing mineral leases. Characteristics of special environmental interest are (1) spatial—the size of the area that is

affected directly or indirectly by surface mining and related activities, (2) dynamic—the rate of change in surface morphology as a result of mining and reclamation, and (3) seasonal—time-dependent aspects, such as the density, distribution, and health of native local vegetation, thus providing a measure of the rate and success of future reclamation efforts. The value of such assessments depends on the quality and availability of remotely sensed data, field observations, and the extent of development of the surface mine(s) at the time. Recent aerial photographs (low-, medium-, and high-altitude), topographic maps, and field observations are necessary to confirm the accuracy and precision of interpretation of repetitive satellite data. Numerous studies of remotely sensed data of surface mining operations confirm, however, that once the diagnostic criteria are established from repeated analysis of the Landsat imagery, subsequent analysis can be made solely on the basis of such imagery (Russell and others, 1973; Pettyjohn and others, 1974; Rehder, 1976).

### PREVIOUS RESEARCH AND RELATED STUDIES

Most of the strip-mine areas which have been studied with Landsat imagery are in the Eastern Interior Coal Basin and the Appalachian Coal Basin. Pettyjohn, Rogers, and Reed (1974) used computer-processed Landsat imagery to investigate the five counties (7500 square kilometers) in eastern Ohio that have been disrupted by surface coal mining. Strip-mine maps generated in that study have a classification accuracy ranging from 95.5 to 100 percent. The technique is rapid and inexpensive and demonstrates definite feasibility and precision. Anderson, Schultz, and Buchman (1975) investigated and mapped strip-mine areas in Garrett and Allegheny Counties in western Maryland, with an average accuracy of 93 percent; the accuracy was even higher for mines covering more than 100 acres (40 hectares). The U.S. Geological Survey, in cooperation with other Federal and State agencies, is

<sup>1</sup> Present address: Department of Geosciences, Pennsylvania State University, University Park, Pa.

assessing the effect of coal mining on water quality, sedimentation, and streamflow in eastern Tennessee. Aerial thermal infrared imagery (aerial thermography) is used to delineate ground-water outflow, ponding on strip-mining benches, storm runoff, surface-water flow, and acid drainage from mines. Digitally processed Landsat imagery is used to delineate land-cover categories, including forested areas, agricultural land, and bare earth caused by strip mining (U.S. Geological Survey, 1975).

The Landsat analyses are especially useful for updating maps to show current surface-mining activity and for direct comparison with the status of mining in the late 1960's, when the geologic field mapping was done. An analysis was made for the dates of February 19, 1973, March 23, 1974, October 10, 1974, and March 26, 1975, for the Duncan Flats quadrangle in Anderson and Campbell Counties, Tenn., at a scale of 1:24 000 (Coker and others, 1975). The resulting maps show both active and inactive strip mines, the extensions of bare-earth areas, regrowth of vegetation, and the effects of strip mining on sedimentation in streams. Using Landsat band 5 negative prints, Rehder (1976) produced a map of strip-mining landscape changes in the Cumberland Plateau region of eastern Tennessee. To facilitate the determination of landscape changes, his map was prepared at a scale of 1:120 000, the same as the aerial photography used for comparison of accuracy. Russell and others (1973), using band 7 Landsat imagery, prepared a mined-land inventory map which shows the status of surface mining in Pike, Warrick, and Gibson Counties in southwestern Indiana. Band 1 black-and-white Landsat imagery enlargements were by Wobber and Martin (1974) to assess strip-mine operations in northwestern Belmont County, Ohio. An enlarged part of a Landsat image was used in conjunction with a NASA high-altitude-aircraft color-infrared photograph. The image and photography, reproduced at a scale of 1:100 000, illustrated the utility of the Landsat image for identifying and classifying recent disturbance caused by area and contour mining, status of reclamation, surface water conditions, and vegetation density.

Landsat imagery has been used in several studies of large surface mines in the West and the northern Great Plains. Computer-enhanced Landsat imagery has previously been used to determine the land-use status and environmental effects of surface mining at more than 30 large and small coal mines scattered throughout the northern Great Plains (National Field Investigations Center, 1975). The computer classification subdivided mine areas into active-mining areas, ungraded spoils, and revegetated land and also identi-

fied certain other features such as ponds, roads, railroads, and cropland.

A U.S. Geological Survey study during 1973-75 of phosphate-mining areas in southeastern Idaho demonstrated the usefulness of aircraft and spacecraft remotely sensed data for assessing environmental effects of existing and proposed strip mining on range resources and wildlife habitat and established both the specific remote-sensing methods and the analysis procedures appropriate for monitoring environmental effects. Digital analysis of Landsat data produced maps accurately delineating broad land-cover categories and detected changes in the environment during the 2-year period (Carnegie, 1977).

Some studies utilized standard Landsat film products, whereas others relied on computer-compatible tapes (CCT's) to present Landsat imagery digitally. Each technique has advantages and disadvantages. Both formats can be produced at various scales for use with standard topographic maps. Landsat film products are available in a variety of image formats and are significantly cheaper than the computer tapes, although their preparation takes much longer. Landsat film products which cover the same area at different times (seasonal or longer time intervals) can be accurately compared by an analyst, with or without the use of computer processing. Landsat film products are very versatile and satisfy most needs if orders for Landsat imagery are tailored to the uses planned. Computer processing of Landsat imagery is more accurate in the mined-land-use classification and can provide exact acreage data for each land-use category. If so desired, cadastral boundaries can be programmed for display on computer images (Torbert and Hemphill, 1976).

#### CURRENT STUDY OF THE ROSEBUD MINE AREA

In the current study, standard Landsat film products, together with recent high-altitude aerial photographs and other data, were used to identify and delineate the following six major land-use categories related to mining and reclamation in large surface-mining areas: (1) highwall and bench areas, (2) ungraded spoils, (3) graded and recontoured areas, (4) revegetated recontoured areas, (5) natural and impounded surface water, and (6) miscellaneous areas.

#### DESCRIPTION OF THE TEST SITE

Western Energy Co.'s Rosebud mine, near Colstrip, Mont., was chosen for this study because it is the largest surface-coal-mining operation in the northern Great

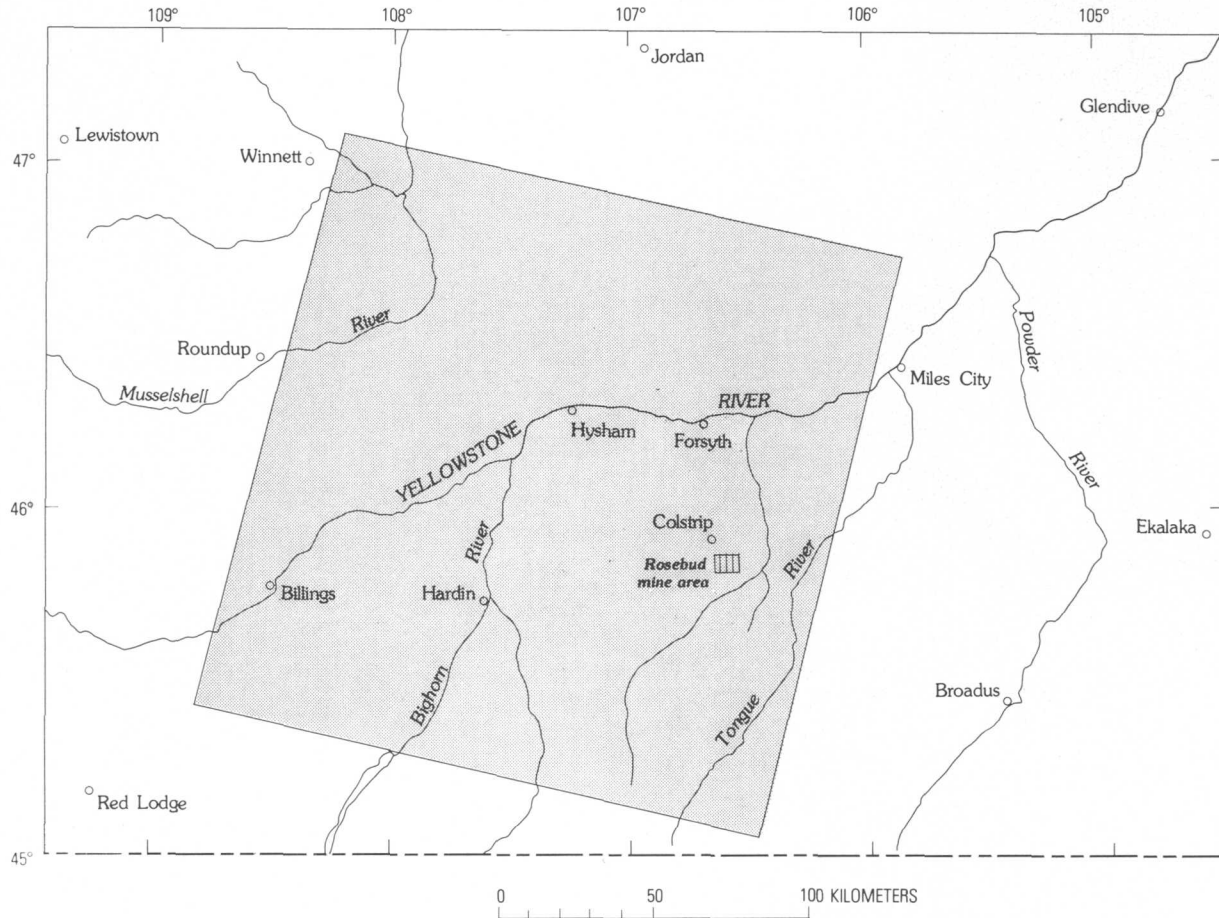


FIGURE 1.—Index map of southeastern Montana, show (shaded) 33 670 km<sup>2</sup> area of Landsat scene 2171-17174 (fig. 3) that was acquired by the satellite on July 12, 1975. This same area is imaged by one of the Landsat satellites every 18 days.

Plains, mining and reclamation activities proceed concurrently, and corroborating data are available—medium- and high-altitude aerial photographs, topographic maps, and a June 1976 field check of the area by the author. The Rosebud mine (fig. 1) is approximately 145 kilometers east-northeast of Billings, Mont., at an elevation of 3200 feet (969 meters) above sea level. The stream-dissected terrain of the area (fig. 2) is characterized by valleys, rolling hills, and numerous sandstone buttes and scattered low outcrops. The local relief is approximately 350 ft (106 m).

The Colstrip area has been a major site of surface-mined-land reclamation research because the Rosebud mine and Peabody Coal Co.'s Big Sky mine nearby disturb approximately 200 acres (80 ha) of rangeland annually. Their combined current annual production of subbituminous coal is 7.2 million to 8.5 million metric tons (National Field Investigations Center, 1975).

In an earlier study for the Environmental Protection Agency, the land-use classification of more than 2300

acres (920 ha) of the Rosebud mine area was experimentally determined using computer-enhanced July 1973 Landsat imagery (National Field Investigations Center, 1975). Graded spoils, ungraded spoils, revegetated areas, and surface water were individually distinguished. Railroad and highway corridors were also identified and included in the total acreage classification scheme. Some highwall and bench areas, not sufficiently extensive to be detected by Landsat sensors, could not be classified separately. The accuracy of the Landsat-based land-use classification was confirmed by conversations with Western Energy Co. personnel and comparison with mine plan maps and aerial photographs taken in the summer of 1973.

The principal Landsat scene used for the present study was made on July 12, 1975 (fig. 3). Aerial photographs used for verification and comparison were taken on September 30, 1975, and October 7, 1975. Comparison with 7½-minute quadrangle maps based on U.S. Geological Survey 1970 aerial photography (fig. 2) shows that prime reference points—road inter-

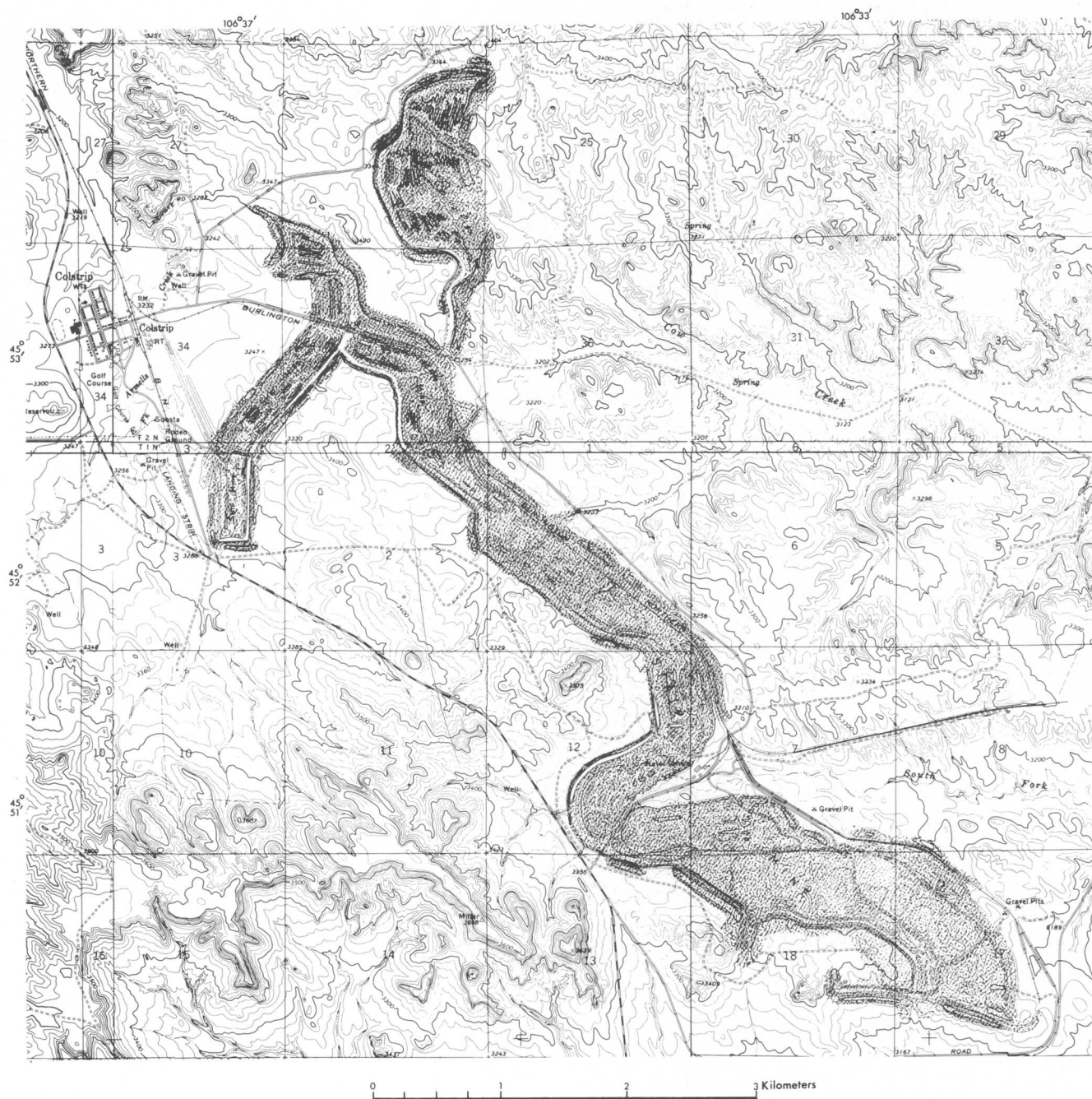


FIGURE 2.—Topographic map of the Rosebud mine area. Base from U.S. Geological Survey Colstrip West, Colstrip East, Colstrip SW, and Colstrip SE 7½-minute quadrangles, 1971 (based on 1970 aerial photography). Stipple indicates general extent of Rosebud mine.

sections, railroad lines, and drainage patterns, as well as some features of the Rosebud mine have scarcely changed since 1970. The topographic maps, together with later aerial photographs of the area, verify identifications made from enlarged Landsat images.

#### INTERPRETIVE AND ANALYTICAL METHODS

This study involved mainly visual techniques, as opposed to computer-processing of data. The imagery

received from the EROS Data Center comprises bands 4–7 positive and negative transparencies at a scale of 1:1 000 000 and 1:3 369 000. The 1:1 000 000 band 5 and band 7 transparencies were used for preparation of direct black-and-white contact prints and positive enlargements. Band 5 and band 7 black-and-white transparencies and the enlargements, coupled with available aerial photography, are useful in the study of environmental conditions. Repetitive remote-sensing

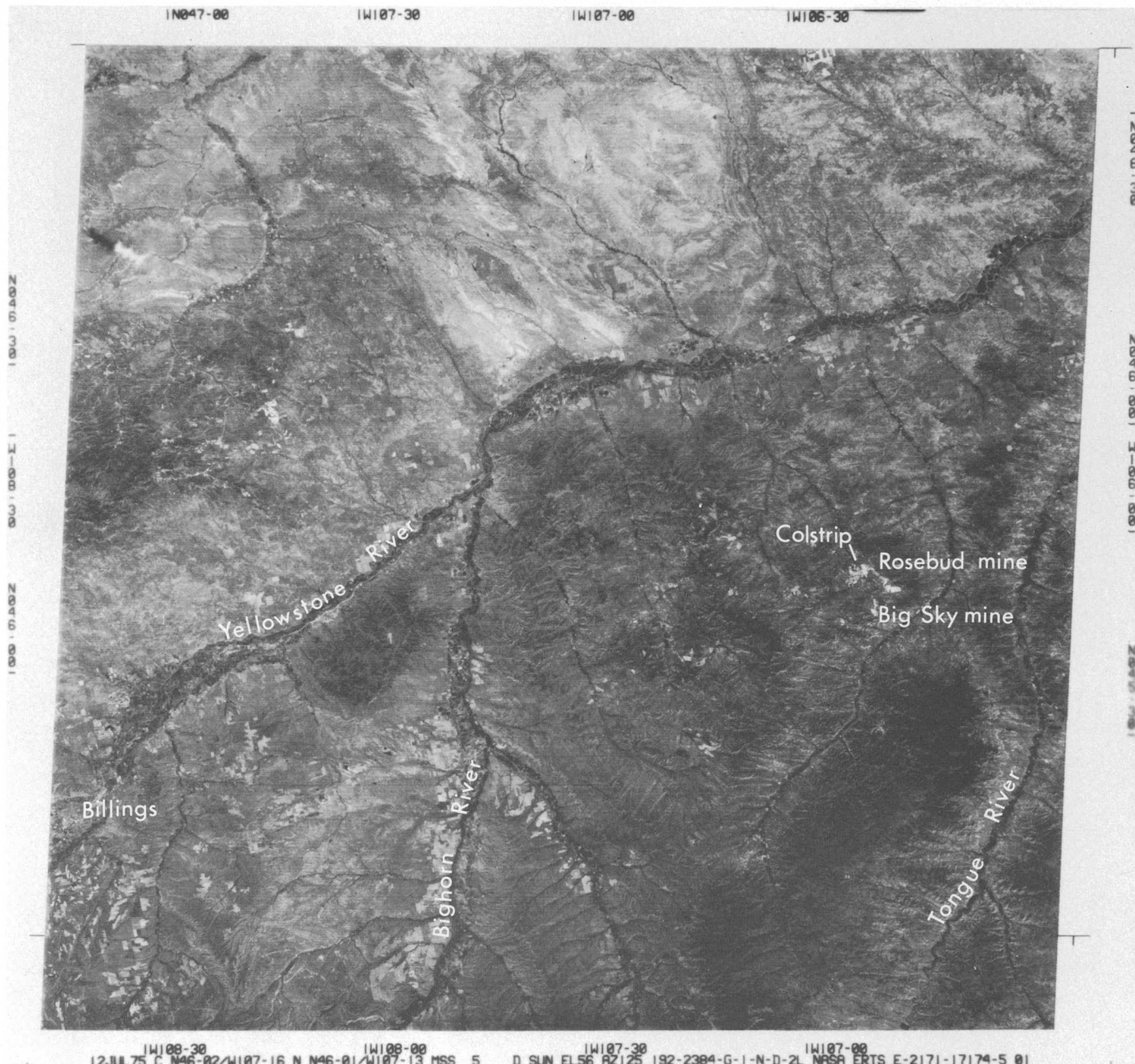


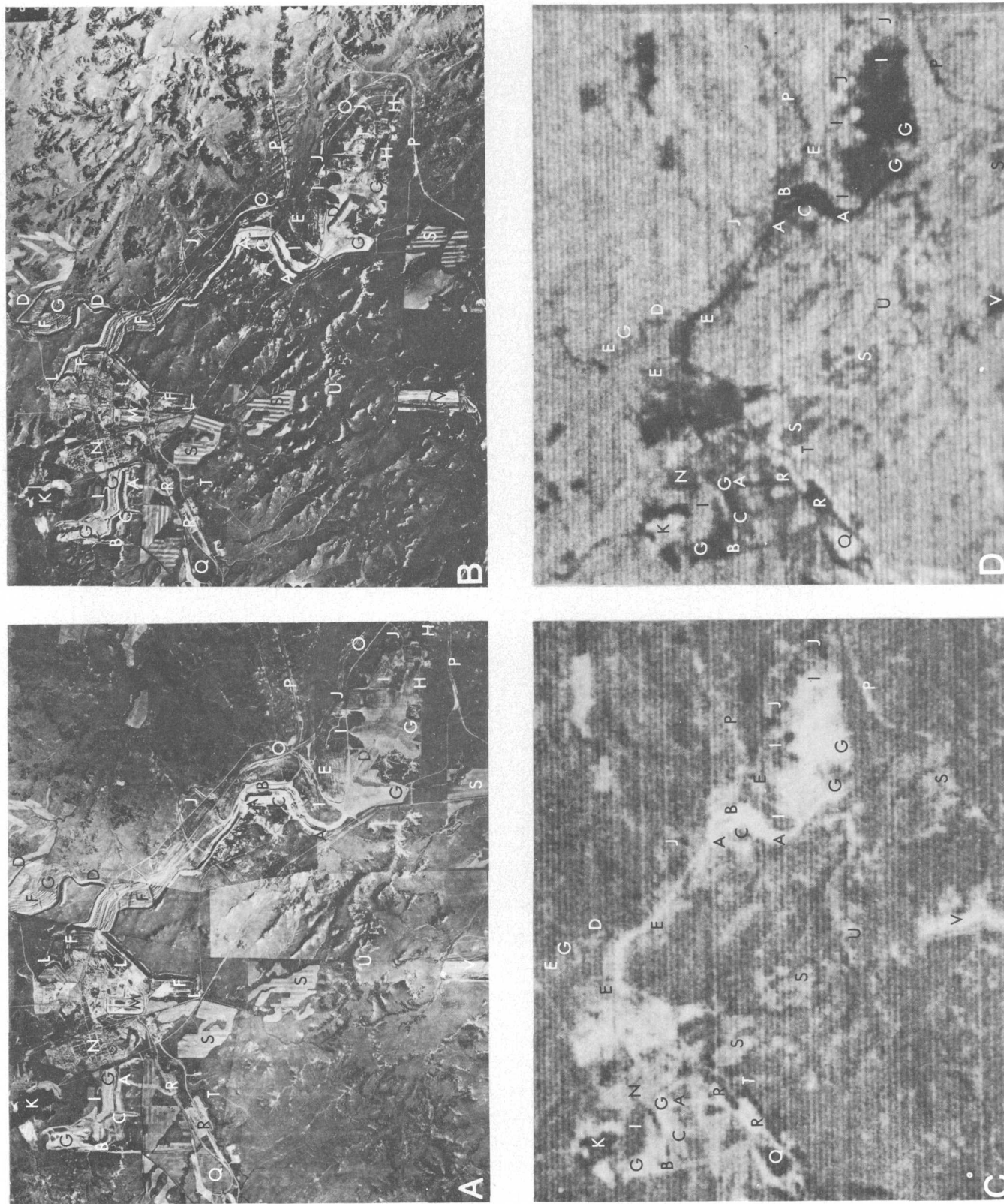
FIGURE 3.—Annotated Landsat image 271-17174 (band 5), showing (light-gray areas) of Western Energy Co.'s Rosebud mine and Peabody Coal Co.'s Big Sky mine. Area shown is outlined in figure 1.

coverage and data analysis enable environmental monitoring of changing features.

#### Visual techniques of interpretation

Photointerpretation of remotely sensed data of surface-mine areas is based mainly on obvious differences in the geometry, color, tone, and texture of linear and areal physical features (including vegetation) as they appear on a Landsat image or on high-, medium-, or low-altitude aerial photographs. Usually, the geometric

configuration and the contrast of strip-mine areas are the key to locating and identifying them against the surrounding background of a Landsat image. The size and shape of the disturbed area are apparent on both Landsat images and aerial photographs. Highwall and bench areas and surface waters (both natural and impounded) can usually be identified with the unaided eye on a good-quality band 5 or band 7 black-and-white print or transparency. Vegetation density and distribution are most apparent on a false-color com-



Surface features in Rosebud mine area	Identification from aerial photography		Identification from band 5 Landsat film
	Black-and-white	Color-infrared	
5. Natural and impounded surface water			
Large surge pond	K	K	K
Ponds along highwalls	L	L	( <sup>2</sup> )
Powerplant cooling ponds	M	M	( <sup>2</sup> )
6. Miscellaneous areas			
Town of Colstrip	N	N	N
Haul roads	O	O	---
Railroad spur	P	P	P
Railroad loop	Q	Q	Q
Equipment maintenance areas	R	R	R
Wheat fields	S	S	S
Stream channels	T	T	T
Sandstone ridges and buttes	U	U	U
Peabody's Big Sky mine	V	V	V

Surface features in Rosebud mine area	Identification from aerial photography		Identification from band 5 Landsat film
	Black-and-white	Color-infrared	
1. Highwall and bench areas			
Active highwall areas	A	A	A
Bench areas	B	B	B
Exposed overburden	C	C	C
Abandoned highwalls	D	D	D
2. Ungraded spoils			
Ungraded spoil piles	E	E	E
Abandoned spoil piles	F	F	( <sup>1</sup> )
3. Graded and recontoured areas			
Recontoured spoil piles	G	G	G
Highwall reduction	H	H	---
4. Revegetated recontoured areas			
First- and second-year revegetated areas	I	I	I
Third- and fourth-year revegetated areas	J	J	J

<sup>1</sup>Classified as ungraded spoils.

<sup>2</sup>Identifiable on band 7 Landsat imagery.

FIGURE 4.—Medium-altitude (A) and high-altitude (B) aerial photographs and Landsat images (C, D) of the Rosebud mine area, reproduced here at approximately same scale to facilitate comparison. Key to letters is shown in accompanying table. A, Medium-altitude aerial photograph, taken August 2,

1975; photograph courtesy of Western Energy Co. B, High-altitude (18900 m) aerial photograph taken October 7, 1975, from a NASA U2 aircraft. C, Band 5 positive enlargement of a Landsat image (fig. 3), taken July 12, 1975. D, Band 5 negative enlargement of the same Landsat image.

posite image. Such false-color composites are created by exposing three of the four black-and-white bands (bands 4-7) through different color filters onto color film. On false-color images, healthy vegetation appears bright red; diseased, dead, or dormant vegetation is green; clear water appears black; sediment-laden water is powder blue; and surface-coal-mine areas are medium and dark blue.

By means of a Bausch and Lomb stereomicroscope (zoom binocular) the image transparencies were studied closely. Optical enlargement, though facilitating the identification of features not discernible at 1:1 000 000 scale, sacrifices some resolution. The amount of resolution loss caused by increasing magnification depends on the initial quality and the type of transparency furnished by the EROS Data Center. Once the optimum magnification-resolution balance was established, the small area of interest was optically enlarged for black-and-white positives; and negatives from the enlargement were set aside for density-slicing study.

A comparison of the identifiable surface features on the medium- and high-altitude aerial photographs and the Landsat imagery is presented in figure 4. Despite variation in tone, texture, and clarity of print, a general land-use identification and classification is possible. Enlarging the 1:1 000 000-scale Landsat image (fig. 3) enables much greater precision in identification of surface mine features. Furthermore, an experienced analyst who is familiar with the mining area as represented on Landsat images can derive far more information than the inexperienced user can. Nevertheless, owing to resolution limitations, visual methods alone cannot be relied upon in the identification of certain features on Landsat films. Landsat CCT data, displayed at a scale of 1:24 000, can complement or replace visual analysis. For detailed investigations of complex surface-mining situations, an analyst now may have to rely solely on any available recent medium- or high-altitude aerial photography. Forthcoming Landsat missions are expected to provide improved resolution.

More precise areal comparisons of aerial photographs and Landsat enlargements is possible after both are gridded (Chapman, 1974) and identical fixed reference points located.

Enlargement to high magnification may necessitate mosaicking of individual images (McEwen and Schoonmaker, 1975).

Good-quality aerial photographs or mosaics of enlarged Landsat images can be periodically restudied and compared with later data. Features that pertain to mining and reclamation can be transferred from imagery or photographs to topographic or mine maps,

yielding a usable, current, and valuable land-use map of the surface mine site.

### Densitometric analysis

Films can also be analyzed by density slicing, or densitometry—a quantitative measurement of the magnitude and frequency of change in tonal values, from either film transparencies or prints. Using tone in the interpretation of remotely sensed data requires the interpreter to make a qualitative judgment. The interpreter must avoid basing his determination solely on results of density slicing because tonal variations on different images of an area may be caused by a change of the sun angle, different reflectance properties of the same surface features (caused, for example, by rain, snow, shadows from cloud cover), a change of vegetation appearance due to seasonal variations, or different film-processing techniques.

In this study, density slicing was done on black-and-white positives and negatives of the optically enlarged parts of Landsat images. Positive transparencies were deemed better suited for use in the DATACOLOR Model 703 density slicer. The density slicer employs a television camera that scans the surface of the transparency, which is illuminated by a light source. The various shades of gray detected by the television camera are electronically "read" by a color-analyzer that assigns ranges of color to particular levels of the gray scale. The interpreter, by means of a color keyboard, can assign as many as 32 various hues (4 hues for each of 8 distinct chromatic colors) so as to clearly discriminate the numerous shades of gray on the positive transparency. The analysis of the image transparency is then electronically displayed on a color television monitor. The electronic image displayed on the television monitor can be conveniently resolved at a scale of 1:24 000.

For densitometric analysis, the loss in resolution with increasing magnification was negligible; identification of the six land-use categories used generally depends not on spatial resolution but on each category's distinctive reflectance. In theory, each land-use category (fig. 4, table) has a particular level of spectral reflectance. In remote sensing of strip-mined areas from high altitude or from satellite orbit, the variations of spectral reflections from different surface features are represented on black-and-white transparencies by numerous shades of gray that then appear on the processed film. Through manipulation of the densitometer, the distribution of general and certain specific land-use areas is displayed in color on the television monitor. The monitor displays (fig. 5) of the July 12, 1975, Landsat

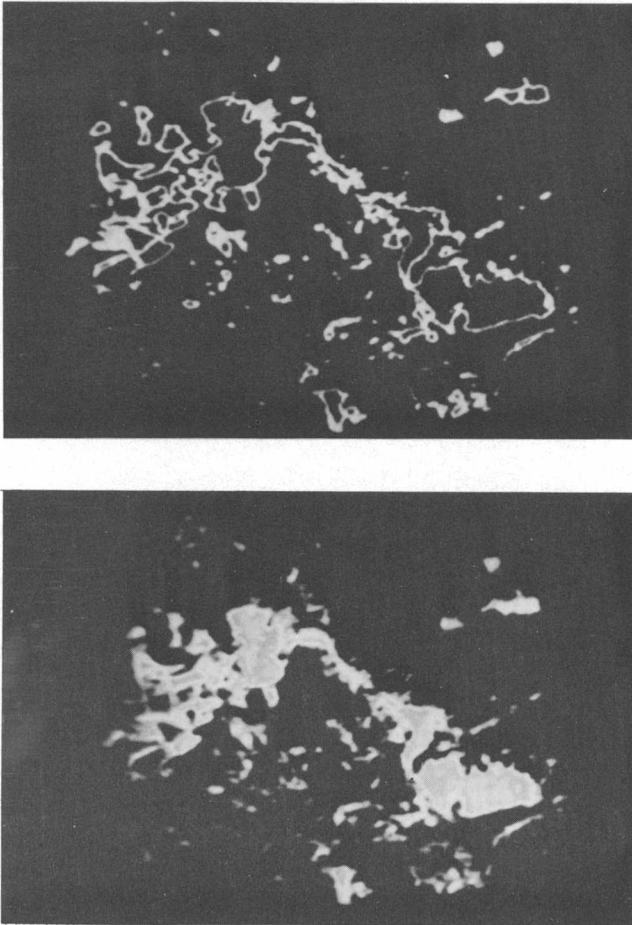


FIGURE 5.—Black-and-white rendition of specially processed color prints made from Landsat image (fig. 3) displayed on the television monitor of the DATACOLOR Model 703 density slicer. (The highlighted areas outside mining area are eroded tops of sandstone-capped buttes.)

scene (fig. 3) that highlight the pattern of the land-use areas and the areas most affected by surface disturbance correspond very well with the same areas identified in the aerial photographs (fig. 4 *A, B*), if one bears in mind that the value of densitometric analyses is, at best, directly proportional to the quality, resolution, and level of contrast of the remote-sensing image.

### Computer-assisted analysis

Computer processing of digital data is another method for analyzing remotely sensed data. This method is becoming increasingly popular with many investigators because of the speed with which digital data can be manipulated and analyzed. Computer analysis was not used in this particular study, but this approach was evaluated, using data collected by various

other investigators in the Rosebud mine area and in other surface-mining areas.

Landsat data in digital form are available on CCT's. The digital data corresponding to one Landsat image are contained on one (1600 bits per inch) or two (800 bpi) or four (800 bpi) CCT's. The data for all four MSS bands are interleaved on the tape(s) and can be easily manipulated into various formats by instruments such as the General Electric Image 100 image analyzer.

The Image 100, an independent digital display and analysis system, displays the digital multispectral line-scan data of Landsat CCT's. It operates on the general principle that objects possess a spectral characteristic and produce a spectral reflectance curve from the ultraviolet through the near-infrared part of the electromagnetic spectrum. These so-called signatures are used to identify similar features in an image by simultaneous comparison and classification of signatures, say in a small "known" land-use area, with the spectral characteristics in unknown land-use areas elsewhere. The reliability of any spectrally based classification of land use depends on the certainty with which each signature curve can be unambiguously discriminated. The spectral range of the MSS on Landsat is from 0.5 to 1.1 micrometers, encompassing the green band (visible) through the near-infrared range of the electromagnetic spectrum. Many objects have similar curves within this range, and this similarity may lead to erroneous classification. Varying spectral characteristics (such as seasonal variation in percentage of vegetative cover on reclaimed land) can also lead to misclassification. Water, for example, should be readily classified spectrally because of near-total absorption of incident solar energy above 0.2  $\mu\text{m}$ ; hence, water would appear black in MSS bands 6 and 7. But water's spectral character, as imaged with the MSS instrument on Landsat or by other remote sensors, is affected by factors such as water depth, amount of suspended sediment, character of the waves, and atmospheric moisture.

An EPA-sponsored study of surface-coal-mining areas employed computer-processed Landsat data to classify land-use (National Field Investigations Center, 1975). No numerical data are available on the classification accuracy of the resulting computer-derived map (fig. 6); however, a similar study of strip-mined land in Muskingum County, Ohio, achieved accuracy ranging from 95.5 to 100 percent (fig. 7), left very few areas unclassified, and was fairly reliable for determining acreage figures for each land-use category (Pettyjohn and others, 1974).

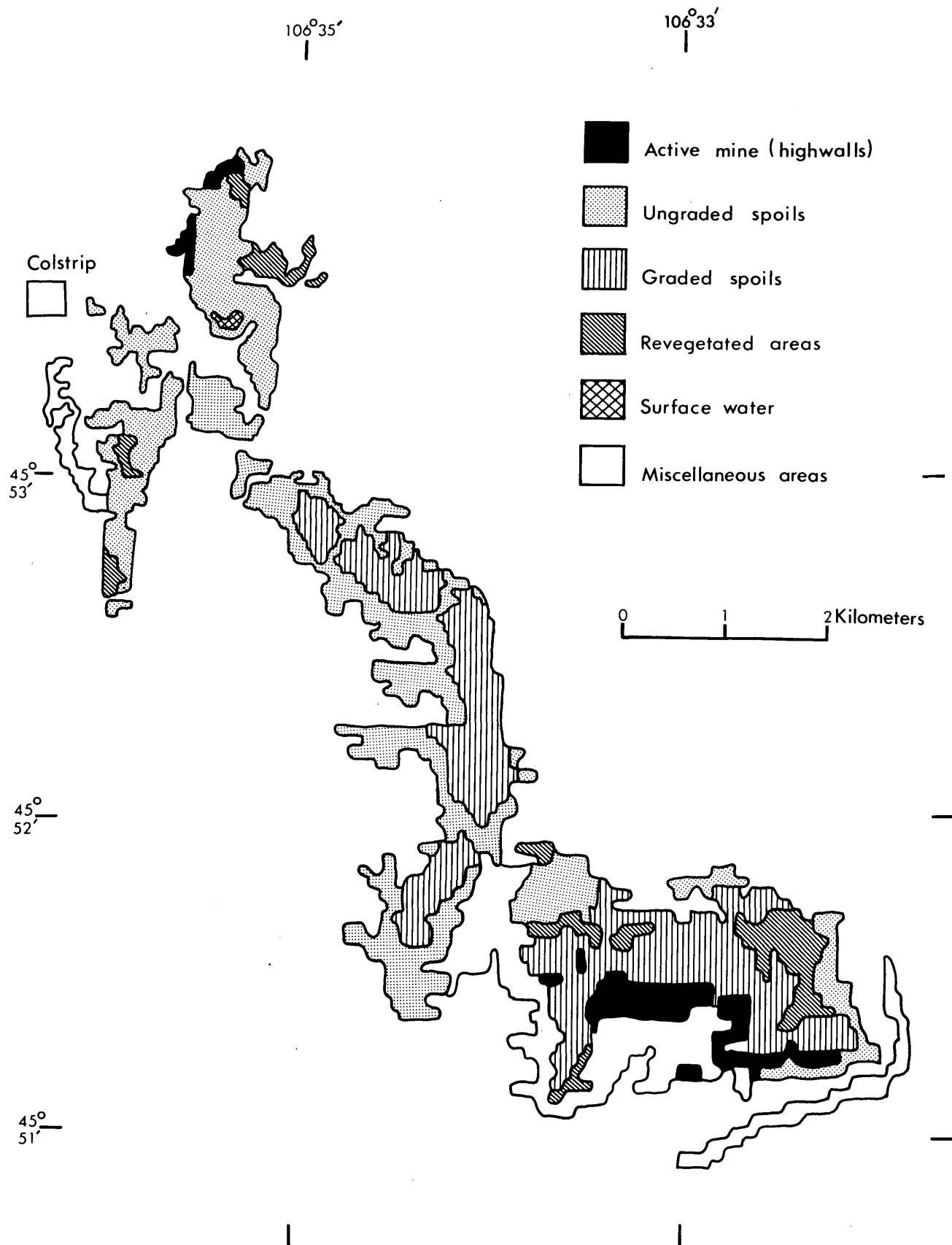


FIGURE 6.—Map of the Rosebud mine prepared from a digital data display of a Landsat image acquired July 15, 1973. Part of the data from this Landsat CCT was displayed on the monitor of an image analyzer and then photographed.

Each land-use area shown here was delineated according to the characteristic spectral reflectance properties of the features. (Modified from National Field Investigations Center, 1975.)

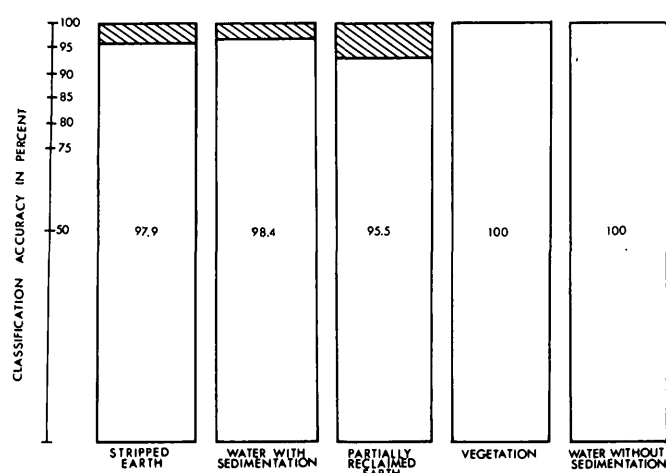


FIGURE 7.—Classification accuracy for five land-cover categories that were identified in a large surface coal mine in Muskingum County, Ohio, from an August 20, 1972, Landsat scene. Classification accuracy tests, necessary to evaluate the computer capability of making the desired land-use classification in an area, are made by comparing the computer-derived product to aerial photographs and standard maps of the area, along with data obtained from field observations. (From Pettyjohn and others, 1974).

### SUMMARY AND CONCLUSIONS

Remotely sensed data were used to detect, monitor, and map the environment of the Rosebud coal mine in southeastern Montana as a sample test site. Spatial, dynamic, and seasonal environmental characteristics were identified by employing various techniques to enhance band 5 and band 7 MSS Landsat data. Land-use information visually derived from enhanced remote-sensing data can be used in conjunction with aerial photography, standard U.S. Geological Survey 7½-minute quadrangle maps, and field observations to document dynamic cultural and natural processes associated with surface mining. Township, range, and sectional lines superimposed on aerial photographs and satellite imagery permit precise locating.

Techniques for detecting changes of surface coal mines have been successfully used to monitor surface mining of other resources if the disturbed area is sufficiently extensive. Computer processing of Landsat data, already widely used, will increase further as electronic systems improve. Computer-assisted digital analysis systems can rapidly and accurately detect even small environmental changes in a large area. The CCT's can produce planimetric maps of surface mines and measure acreage far more accurately than can the photographic elements now available.

Remote sensing, including Landsat imagery and high-altitude color and color-infrared aerial photography, is widely used in the petroleum and mining in-

dustries for planning, exploration, development, and other actions. Its use is expected to expand as more people become knowledgeable in its application and as even more sophisticated Earth-orbiting remote-sensing satellites are launched. Landsat-C, scheduled for launch in March 1978, will be equipped with a thermal-infrared channel and an improved return beam vidicon system that will provide high-resolution (40-m) panchromatic imagery not available from previous Landsat missions.

Satellites already in orbit can provide a wealth of information to investigators trained to fully utilize it. Future satellites now being planned can be made even more useful if prospective users make known their needs.

### ACKNOWLEDGMENTS

The author wishes to acknowledge Thomas O. Friz and Richard S. Williams, Jr., for their expert guidance and technical advice provided through personal communications and their critiques of the manuscript. Also, special acknowledgment is given to Dennis S. Kostick for his valuable help in the planning and development of the photography and illustrations contained in this article.

### REFERENCES CITED

- Anderson, A. T., Schultz, D. T., and Buchman, N. E., 1975, Monitoring surface mines from space—Landsat inventory of surface mined areas using extendible digital techniques: NASA Goddard Space Flight Center and the General Electric Co., June 30, 1975, 44 p.
- Carnegie, D. M., 1977, Remote sensing techniques for monitoring impacts of phosphate mining in southeastern Idaho, in Schoonmaker, J. W., Jr., ed., Proc. Second Ann. William T. Pecora Memorial Symposium: Am. Soc. Photogrammetry. [In press.]
- Chapman, W. H., 1974, Gridding of ERTS images: Talk presented at American Cong. on Surveying and Mapping, September 1974, Washington, D. C., 5 p. (mimeographed text).
- Coker, A. E., Higer, A. L., Sauer, S., and Rogers, R. H., 1975, Remote-sensed data used to delineate land-water cover in coal mining regions of eastern Tennessee: NASA. Johnson Space Center, Earth Resources Survey Symposium, Houston 1975, Abs. Paper E-8, p. 84.
- McEwen, R. B., and Schoonmaker, J. W., Jr., 1975, ERTS color image maps: Photogrammetric Eng. and Remote Sensing, v. 41, no. 4, p. 479-486.
- National Field Investigations Center, 1975, An application of ERTS technology to the evaluation of coal strip mining and reclamation in the northern Great Plains: Environmental Protection Agency Rep. 330/3-75001, 120 p.; available for purchase from Natl. Tech. Inf. Service, PB 255-590/2BE.
- Pettyjohn, W. A., Rogers, R. H., and Reed, L. E., 1974, Automated strip mine and reclamation mapping from ERTS: NASA Goddard Space Flight Center, Earth Resources Technology Satellite I Symposium, 3d, v. 2, p. 87-101.

- Rehder, J. B., 1976, Changes in landscape due to strip mining, *in* Williams, R. S., Jr., and Carter, W. D., eds., ERTS-1, A new window on our planet: U.S. Geol. Survey Prof. Paper 929, p. 254-257.
- Russell, O. R., Wobber, F. J., Weir, C. E., and Amato, Roger, 1973, Applications of ERTS-1 and aircraft imagery to mined land investigations: Tullahoma, Tennessee Univ. Space Inst., Remote Sensing of Earth Resources Symposium, p. 1095-1105.
- Torbert, Grover, and Hemphill, W. R., 1976, Cadastral boundaries on ERTS images, *in* Williams, R. S., Jr., and Carter, W. D., eds., ERTS-1, A new window on our planet: U.S. Geol. Survey Prof. Paper 929, p. 44-46.
- U.S. Geological Survey, 1975, Status and plans of the Department of the Interior EROS Program: U.S. Geol. Survey Open-File Rept. 75-376, 91 p.
- Wobber, F. J., and Martin, K. R., 1974, ERTS monitoring of surface mining operations: *World Mining*, v. 27, no. 3, p. 56-57.

## AN "OPTIMAL" FILTER FOR MAPS SHOWING NOMINAL DATA

By STEPHEN C. GUPTILL, Reston, Va.

*Abstract.*—An "optimal" filtering technique for use with nominal data, such as land use and land cover categories, has been developed. This method is based on the conditional probability joins of neighboring data elements. In addition to its use in performing filtering, the method can be used to calculate the likelihood of each data element being properly classified.

The technique was tested on a land use data set for an area in Walnut Valley, Calif. The computer program performing the filtering process proved to be computationally efficient and produced satisfactory results. Useful statistics of the error estimation process were also generated. Future applications of the method to spectrally classified Landsat data are being explored.

---

Filtering separates homogeneous components from a mixture of elements. In filtering, one may be concerned with the elements that pass through the filter, as in the case of filtering a bottle of wine to remove the sediment, or one may desire the components that is removed by the filter and not the effluent (for example, the insoluble precipitate of a reaction in an aqueous solution). Analogies to these physical filtering processes have been developed to treat analog impulse data and subsequently digitally coded data.

Many of the filtering procedures that can be applied to spatial data have evolved from one-dimensional techniques first used in electrical engineering and communications science. Researchers in these fields are concerned with the recovery of a pure signal from a transmission consisting of both signal and random noise. Although scientists in these fields have dealt primarily with electronic analog methods to perform the filtering, they were among the first to develop mathematical ways to describe signals and noise. Works such as Rowe's (1965) provide some useful insights into this field.

The digital equivalent of filtering an electronic signal is the filtering of a times series of scalar data. One purpose of filtering such data is to attenuate the amplitudes of the high-frequency components in the data without affecting the low-frequency parts. The high-frequency variations are assumed to be noise or are

oscillations not relevant to the type of analysis being applied to the data (for example, the separation of weekly temperature fluctuations from a time series of hourly temperature data). The filtered value is merely an estimate of what the value would be if the "noise" were not present. Holloway (1958) and Rayner (1971) discussed these topics in detail.

The extension of such techniques to two-dimensional data is relatively simple. Generally the filtering function applied to two-dimensional data can be considered a composite of two functions applied in orthogonal directions. The specific processes that perform filtering operations are many and varied. Common techniques include the use of weighted moving averages, Fourier transformations, and empirical functions. Tobler (1969) elaborated on these processes.

Although the discussion thus far has dealt with scalar data, some analogous techniques exist for working with nominal data, and others need to be developed. To create such techniques, one can substitute simple counting measures (that is, determining the presence or absence of a category) and decision functions for the arithmetic operations that are used on scalar data. Work with nominal data has largely concerned binary-valued functions such as those encountered in picture processing. Rosenfeld (1969) and Andrews (1970) dealt with these topics in great detail. Fewer attempts have been made to deal with the filtering of multi-category nominal data, although MacDougall (1972), Strong and Rosenfeld (1973) and Guptill (1975) conducted research in this field.

One of the problems associated with filtering transformations is the determination of the correct amount of filtering. Because filters can be applied in an iterative fashion, with various "strengths," how can one ascertain when a data set has been "sufficiently" filtered? One approach is to monitor the filtering process by qualitative and quantitative techniques. A second, more direct approach is to construct an "optimal" filter that yields results filtered in the proper amount and manner according to a set of predetermined standards. For example, Thompson (1956) de-

vised an "optimal linear smoothing process" for use on barometric pressure maps. His process is "optimum" in that the root-mean-squared difference between the true and smoothed fields is the least. Similarly, an optimal smoothing filter can be devised for use with nominal data.

### DEFINING AN OPTIMAL TRANSFORMATION

The first step in the construction of an optimal transformation process is to define "optimal." One formulation is as follows.

Consider a map represented by a geographical matrix with  $N$  rows and  $M$  columns and with  $K$  possible states. The object is to determine the conditional probability between the state (land use category) of a center cell ( $C$ ) and the state of each neighbor cell ( $N$ ). Each cell in the geographical matrix is taken in turn as a center cell that is surrounded by as many as eight neighbors. The first step is to count the number of transitions between the category of each center cell of the geographical matrix and the categories of the neighbor cells. Once the results are tallied in a matrix, the frequency of the transmissions between the categories may be computed by dividing each row entry by the sum of row values. If the number of transitions in a matrix cell is large enough, the frequency of occurrence satisfactorily approximates a conditional probability  $P(C/N)$ .

The conditional probability of the state of each cell on the map is represented by

$$P(C_k/N_j^i), \quad (1)$$

that is, the probability of the center cell being in state  $k$ , given that the  $i^{\text{th}}$  neighbor cell is in state  $j$ . This procedure permits one to determine the probability of occurrence of the center category,  $C_k$ , from the categories of the neighbors. If the center cell is not an edge cell and if the categories of the neighbors are denoted by  $\vec{N}$  (that is, each of the  $N^i$ ), then the total conditional probability of the  $C_k$  center category as determined by the neighbor is

$$P(C_k/\vec{N}) = \prod_{i=1}^8 P(C_k/N_j^i). \quad (2)$$

These conditional probabilities should be normalized to sum to 1; thus for  $n$  categories,

$$P'(C_k/\vec{N}) = \frac{\prod_{i=1}^8 P(C_k/N_j^i)}{\sum_{k=1}^n \prod_{i=1}^8 P(C_k/N_j^i)}, \quad (3)$$

where  $P'(C_k/\vec{N})$  is the normalized conditional probability. This equation provides an estimate of the like-

lihood of a center cell being in a certain state, given the states of its neighbors. When this procedure is applied to each cell and its associated neighborhood, a probability surface is produced that provides information as to where, in geographical space, the state of a cell is probably in error.

An approximation of the total error in the map, as well as the error within each category, is provided by a simple loss function. Define a symmetrical, zero-one loss function as follows:

$$\lambda(\alpha_k/\beta_p) = \begin{cases} 0 & \text{if } k=p \\ 1 & \text{if } k \neq p \end{cases} \quad k, p = 1, \dots, c, \quad (4)$$

where  $c$  is the number of categories,  $\alpha_k$  is the category observed at location  $x$ , and  $\beta_p$  is the "true" state of the cell at location  $x$ . If  $\alpha_k$  is not the same as the most likely occurrence  $\beta_p$ , then  $\lambda(\alpha_k/\beta_p) = 1$ . A total measure of error in the map can be compiled by applying the loss function over the entire map:

$$\text{Total error} = \sum_{n=1}^N \sum_{m=1}^M \lambda(\alpha_k/\beta_p) / N \cdot M \quad (5)$$

This specialized definition of error only slightly resembles error as defined by a field check, but it is a defensible definition. In this case, an "optimal" transformation is defined as the operation that minimizes the total map error.

This transformation, or filtering operation, is performed by selecting the category,  $k$ , which maximizes the a posteriori probability  $P(\beta_p/\vec{N})$ . That is, in determining the cell states in the transformed (filtered) map, decide

$$\beta_k \text{ if } P(\beta_k/\vec{N}) > P(\beta_p/\vec{N}) \text{ for all } k \neq p \quad (6)$$

where  $\beta_k$ ,  $\beta_p$  represent possible states of the central cell and  $\vec{N}$  represents the categories of the neighbors of the central cell.

This method is similar to the techniques used in determining nominal classifications in pattern recognition work. For example, Latham (1974), in classifying land use categories from remotely sensed data, used a method in which the category chosen for a site was the one in the most probable state, as determined by the characteristics of nearby sites.

### EXAMPLES

The calculations described in the previous section were made using a Fortran IV computer program written for experimentation with various data sets. The data set in these examples was taken from a 1971 land use map of the Walnut Valley area of California (10-

<	RESIDENTIAL	CATEGORY NO. 1
+	INDUSTRIAL	CATEGORY NO. 2
⊗	COMMERCIAL	CATEGORY NO. 3
⊕	INSTITUTIONAL	CATEGORY NO. 4
∩	RECREATIONAL	CATEGORY NO. 5
△	URBAN AGRICULTURAL	CATEGORY NO. 6
×	URBAN VACANT	CATEGORY NO. 7
⋈	FREEWAY UNDER CONSTRUCTION	CATEGORY NO. 8
△	COMPLETED FREEWAY	CATEGORY NO. 9
	FIELD CROPS	CATEGORY NO. 10
□	ROW CROPS	CATEGORY NO. 11
∖	ORCHARDS	CATEGORY NO. 12
∕	MOWN GRASSES	CATEGORY NO. 13
∕	GRAZING	CATEGORY NO. 14
—	VACANT	CATEGORY NO. 15

Land Use/Land Use Change Legend

FIGURE 1.—Symbols for different categories of land use.

cated east of Los Angeles). The original polygon map of this area, compiled by Goehring (1971), was digitized and converted to a grid-cell form, with each grid cell measuring 91.4 meters (300 feet) on a side. An explanation of the symbols used on these maps is shown in figure 1.

A 1600-cell portion (a 40 by 40 matrix of cells) of the map was tested first. This portion is shown in figure 2. The probability of occurrence of a given category in each cell,  $P'(C_k/\vec{N})$  of this data set was calculated as shown in equation 3. An error estimation parameter  $E_k$  was then computed by

$$E_k = 1 - P'(C_k/\vec{N}). \quad (7)$$

This calculation provides us with an "error surface" where high values indicate a possible uniqueness or misclassification of the area. A perspective-view contour map of this surface is shown in figure 3. The map, when transformed by the "optimal" filter, is shown in figure 4. Examination of the plot of the error surface of the transformed map (fig. 5) shows that the states of some cells have been reclassified to more probable

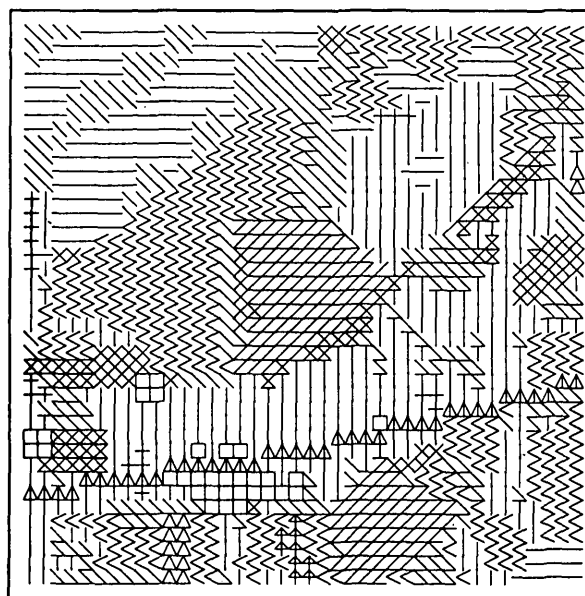


FIGURE 2.—Land use categories in central Walnut Valley, Calif., 1971. (See fig. 1 for explanation of symbols.)

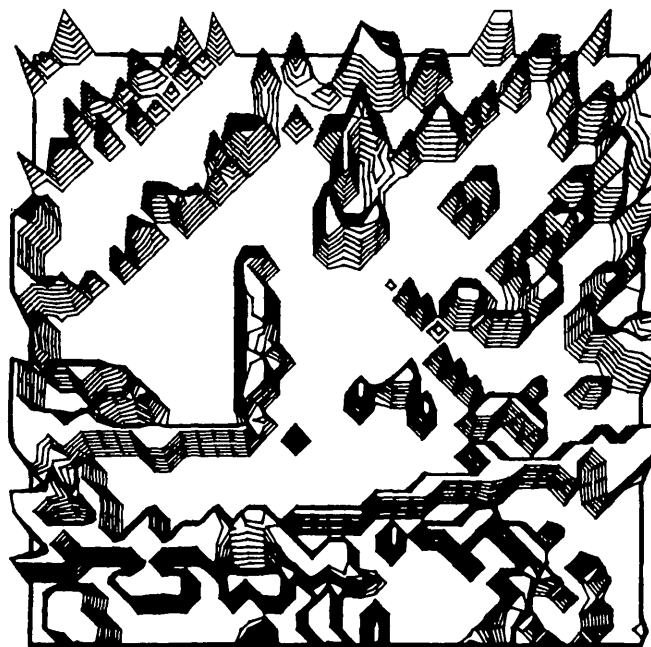


FIGURE 3.—Error surface on land use categories, central Walnut Valley, Calif., 1971. Contour interval = 0.1; minimum contour level = 0.1.

states. This transformation accounts for the smoother appearance of both the map and its error surface.

The next example shows the results of applying the filtering process to the entire Walnut Valley map (99 rows by 154 columns). The original map is shown in figure 6, and the filtered map, in figure 7. In this case, frequency counts were made to determine how often the original cell category was the same as the most

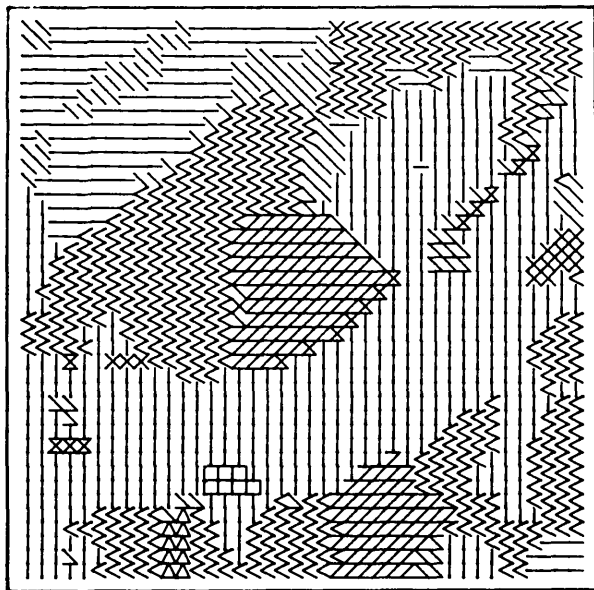


FIGURE 4.—Land use categories filtered by "optimal" transformation, central Walnut Valley, Calif., 1971. (See fig. 1 for explanation of symbols.)



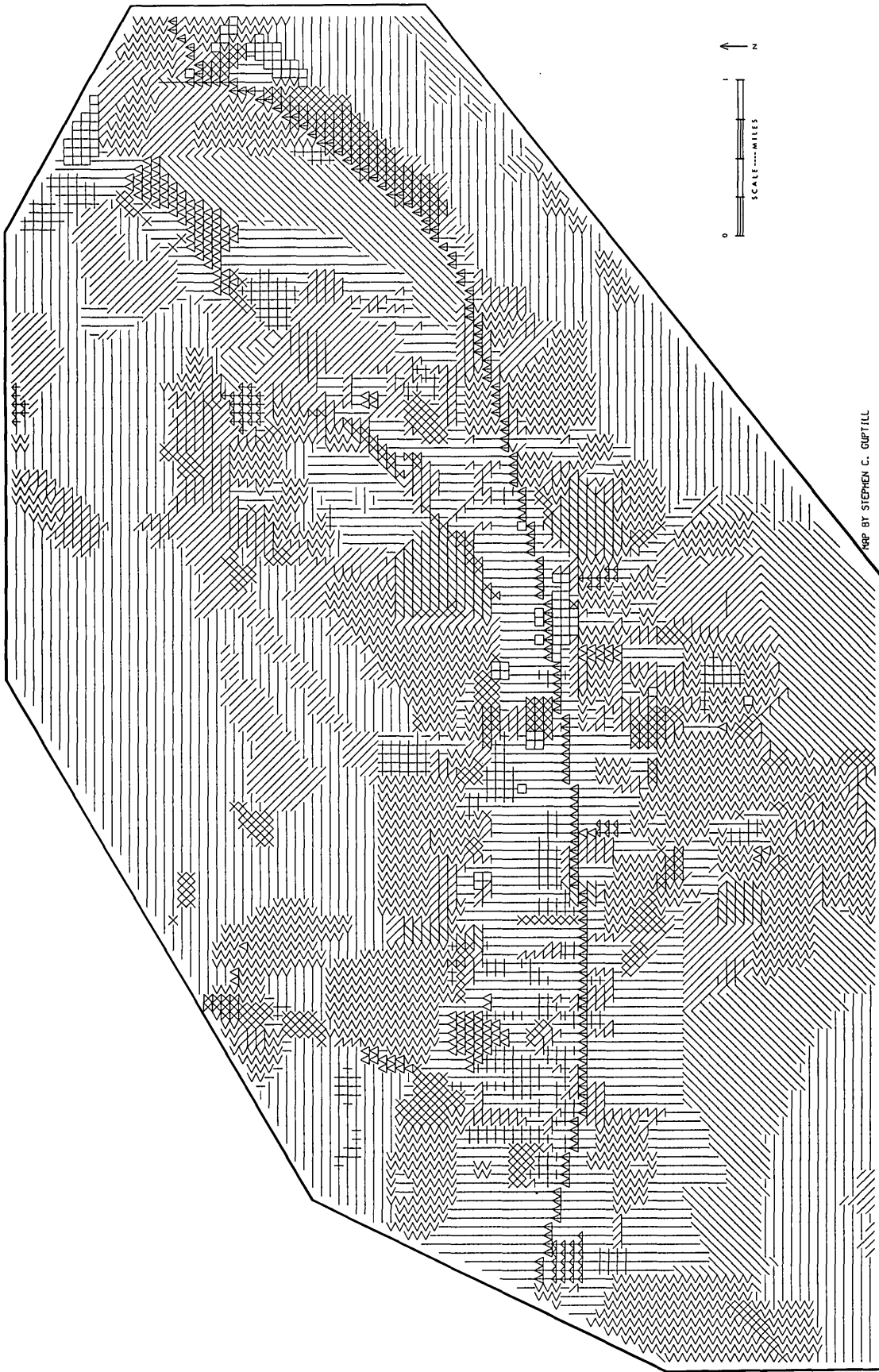
FIGURE 5.—Error surface on land use categories, after being filtered by "optimal" transformation, central Walnut Valley, Calif., 1971. Contour interval = 0.1; minimum contour level = 0.1.

TABLE 1.—Counts of the frequency of probable "correct" category classification, Walnut Valley, Calif., Map, 1971

"Correct" Category	Mapped Category															Total
	1	2	3	4	5	6	7	8	9	10	11	12	13	14	15	
1	1994	29	30	7	29	17	80	0	13	110	16	152	75	22	23	2597
2	0	127	0	0	29	0	1	0	0	6	0	1	0	0	1	165
3	0	0	90	0	0	0	0	0	8	0	1	0	1	0	0	100
4	0	0	0	20	0	0	0	0	0	0	0	0	0	0	0	20
5	0	0	1	0	127	0	1	0	1	0	0	0	0	0	0	130
6	0	0	0	0	0	65	0	0	0	0	0	0	0	1	0	66
7	0	1	0	0	1	0	97	0	0	1	0	0	1	0	1	102
8	0	0	0	0	0	0	0	1	0	0	0	0	0	0	0	1
9	0	0	0	0	0	0	0	0	1	5	0	0	0	0	0	6
10	48	176	50	29	14	49	73	0	110	1582	44	223	41	25	6	2470
11	0	0	0	0	0	0	0	0	0	0	15	0	0	0	0	15
12	2	4	1	2	3	0	10	0	14	7	1	240	7	1	2	294
13	7	2	7	4	3	0	14	1	4	7	1	27	676	2	5	760
14	8	3	0	1	0	3	2	0	3	5	0	5	10	1008	17	1065
15	50	26	1	0	0	2	47	0	0	28	4	38	125	36	3142	3499

TABLE 2.—Percent of probable "correct" category classification, Walnut Valley, Calif., Map, 1971

"Correct" Category	Mapped Category														
	1	2	3	4	5	6	7	8	9	10	11	12	13	14	15
1	76.8	1.1	1.2	0.3	1.1	0.7	3.1	0.0	0.5	4.2	0.6	5.9	2.9	0.8	0.9
2	0.0	92.7	0.0	0.0	0.7	0.0	0.7	0.0	0.0	4.4	0.0	0.7	0.0	0.0	0.7
3	0.0	0.0	90.0	0.0	0.0	0.0	0.0	0.0	8.0	0.0	1.0	0.0	1.0	0.0	0.0
4	0.0	0.0	0.0	100.0	0.0	0.0	0.0	0.0	0.0	0.0	0.0	0.0	0.0	0.0	0.0
5	0.0	0.0	0.8	0.0	97.0	0.0	0.8	0.0	0.8	0.0	0.0	0.0	0.0	0.0	0.0
6	0.0	0.0	0.0	0.0	0.0	98.5	0.0	0.0	0.0	0.0	0.0	0.0	0.0	0.0	1.5
7	0.0	1.0	0.0	0.0	1.0	0.0	95.1	0.0	0.0	1.0	0.0	0.0	1.0	0.0	1.0
8	0.0	0.0	0.0	0.0	0.0	0.0	0.0	100.0	0.0	0.0	0.0	0.0	0.0	0.0	0.0
9	0.0	0.0	0.0	0.0	0.0	0.0	0.0	16.7	83.3	0.0	0.0	0.0	0.0	0.0	0.0
10	1.9	7.1	2.0	1.2	0.6	2.0	3.0	0.0	4.5	64.0	1.8	9.0	1.7	1.0	0.2
11	0.0	0.0	0.0	0.0	0.0	0.0	0.0	0.0	0.0	0.0	100.0	0.0	0.0	0.0	0.0
12	0.7	1.4	0.3	0.7	1.0	0.0	3.4	0.0	4.8	2.4	0.3	81.6	2.4	0.3	0.7
13	0.9	0.3	0.9	0.5	0.4	0.0	1.8	0.1	0.5	0.9	0.1	3.6	88.9	0.3	0.7
14	0.8	0.3	0.0	0.1	0.0	0.3	0.2	0.0	0.3	0.5	0.0	0.5	0.9	94.6	1.6
15	1.4	0.7	0.0	0.0	0.0	0.1	1.3	0.0	0.0	0.8	0.1	1.1	3.6	1.0	89.8



MAP BY STEPHEN C. GUPTILL

FIGURE 6.—Land use categories in Walnut Valley, Calif., 1971. (See fig. 1 for explanation of symbols.)

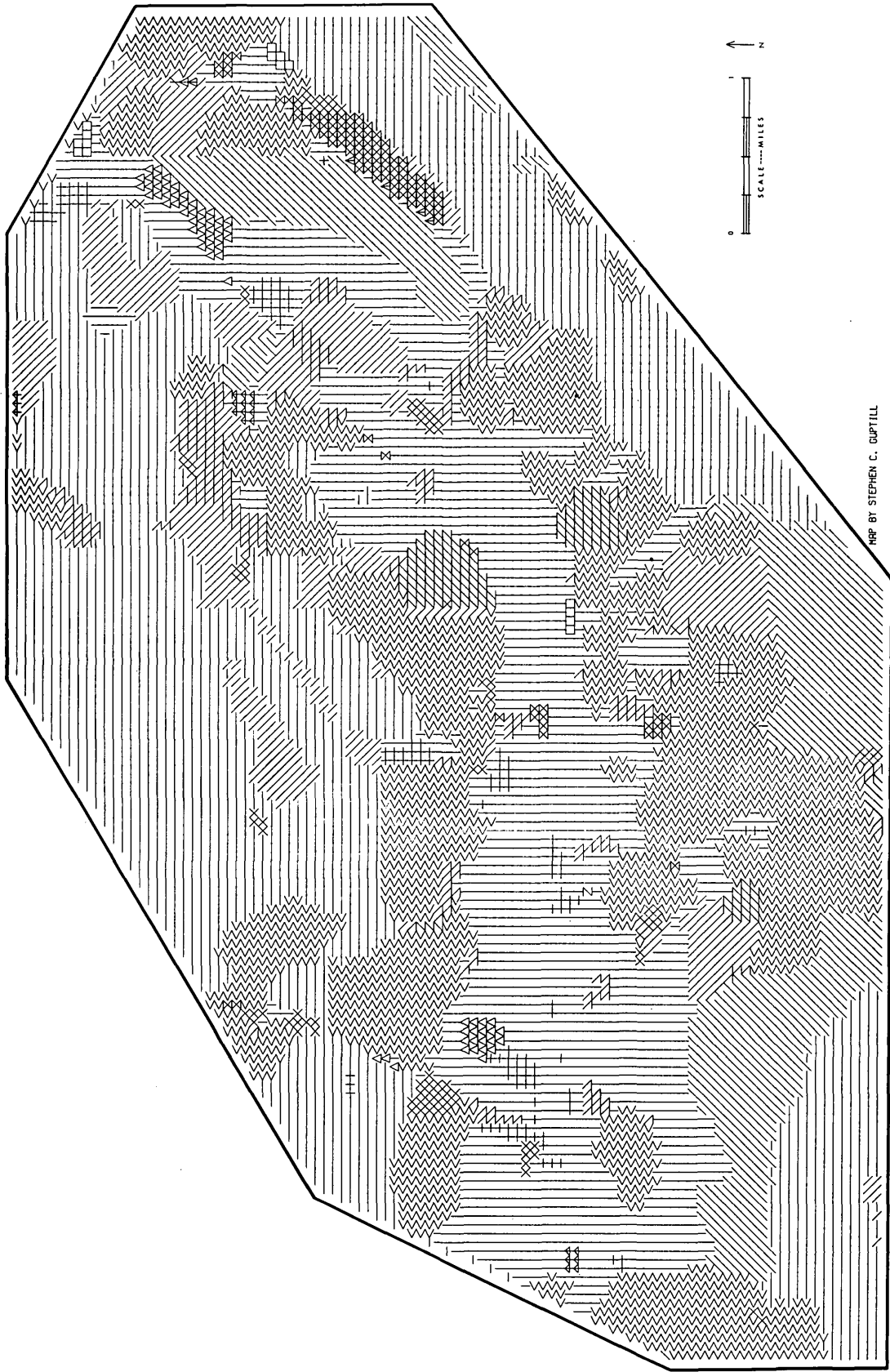


FIGURE 7.—Land use categories after "optimal" filtering. Walnut Valley, Calif., 1971. (See fig. 1 for explanation of symbols.)

probable (or "correct") cell state (see eq 4). The frequency counts are shown in table 1, and the same figures expressed as percentages are shown in table 2. Using these figures, one can estimate the total "error" in the map (eq 5). On the entire map, 86.4 percent of the categories were mapped "correctly." The filtering and error estimation process required 13.6 seconds of CPU time on an IBM 370/168.

The "optimal" filtering transformation is a useful technique for nominal data. It offers the advantages of high efficiency and satisfactory plots of the data coupled with the added benefits of producing statistics of the error estimation process.

Researchers are presently testing this technique for use in postprocessing Landsat images in which the pixels have been classified into land use and land cover categories. A statistical clustering technique is being used to classify pixel values derived from scalar radiometric data. Variations in spectral response cause imperfect separation of cover types, which, in turn, results in cluster overlap and the misclassification of some pixels. The use of the "optimal" filtering algorithm to change the pixel classifications from unlikely states to more probable states based on the states of their neighbors improves the appearance and accuracy of the map.

## REFERENCES CITED

- Andrews, H. C., 1970, *Computer techniques in image processing*: New York, Academic Press, 187 p.
- Goehring, Darryl R., 1971, *Monitoring the evolving land use patterns on the Los Angeles metropolitan fringe using remote sensing*: Riverside, California Univ. of, Dept. Geography, Technical Rept. T-71-5, 107 p.
- Guptill, S. C., 1975, *Spatial filtering of nominal data: an exploration*: Ann Arbor, Michigan Univ. of, unpublished Ph.D. dissert., 210 p.
- Holloway, J. L., Jr., 1958, *Smoothing and filtering of time series and space fields*: *Advances in Geophysics*, v. 4, New York, Academic Press, p. 351-89.
- Latham, J. P., 1974, *Urban pattern recognition and image color discrimination with TV waveforms and computerized matrix analysis and mapping*: Florida Atlantic Univ., Dept. Geography, Office of Naval Research Rept. NR 389-151, p. 3-1-3-14.
- MacDougall, E. B., 1972, *Optimal generalization of mosaic maps*: *Geog. Analysis*, v. 4, no. 4, p. 416-423.
- Rayner, J. N., 1971, *An introduction to spectral analysis*: London, Pion Limited, 174 p.
- Rosenfeld, Azriel, 1969, *Picture processing by computer*: New York, Academic Press, 196 p.
- Rowe, H. E., 1965, *Signals and noise in communication systems*: Princeton, N.J., D. Van Nostrand Co., Inc., 257 p.
- Strong III, J. P., and Rosenfeld, Azriel, 1973, *A region coloring technique for scene analysis*: *Commun. ACM*, v. 16, n. 4, p. 237-246.
- Thompson, P. D., 1956, *Optimum smoothing of two-dimensional fields*: *Tellus*, v. 8, no. 3, p. 384-393.
- Tobler, W. R., 1969, *Geographic filters and their inverses*: *Geog. Analysis*, v. 1, no. 3, p. 234-252.



## ACCURACY OF SELECTED LAND USE AND LAND COVER MAPS IN THE GREATER ATLANTA REGION, GEORGIA

by KATHERINE FITZPATRICK-LINS, Reston, Va.

*Abstract.*—The land use and land cover maps at 1:100 000 scale and at 1:24 000 scale in the Greater Atlanta Region were tested for accuracy. At 1:100 000 scale, 381 points were selected using a stratified systematic unaligned sampling technique. Of these 381 points, 343 points or 90 percent were found to be correct. At 1:24 000 scale, 71 points were tested for accuracy. Of these 71 points, 62 points or 87 percent were found to be accurate. Confidence intervals were determined based on the assumption that the data exhibited a binomial distribution. With 95-percent confidence the accuracy of the 1:100 000-scale maps was between 87 and 93 percent, and the accuracy of the 1:24 000-scale maps was between 79 and 96 percent. The accuracy of the interpretations was consistent from category to category.

Level II land use and land cover maps (Anderson and others, 1976) at a scale of 1:250 000 and 1:100 000 are prepared by the U.S. Geological Survey using high-altitude photographs and stable base copies of the black-and-blue line topographic map plates as a mapping base. The mapping criteria adhered to, specified by Anderson and others (1976), states that: (1) the land use and land cover maps must be at least 85 percent accurate; (2) the accuracy of the interpretation will be about equal for several categories; and, (3) the results must be repeatable from interpreter to interpreter and from one time to another. Once the maps are compiled, field verification is conducted to assure correct interpretation, and the maps are made available to local users for review. Additional corrections are then incorporated.

For this study, land use and land cover maps of the Greater Atlanta Region were chosen to test quantitatively the accuracy of the Level II land use and land cover maps and to ascertain objectively if the criterion of 85 percent classification accuracy is being met. The set of land use and land cover maps for the Atlanta area are the first in the nationwide land use and land cover program to be tested for accuracy. The procedures utilized for this study establish the methodology to be used for further research on the accuracy of the Geological Survey's land use and land cover maps.

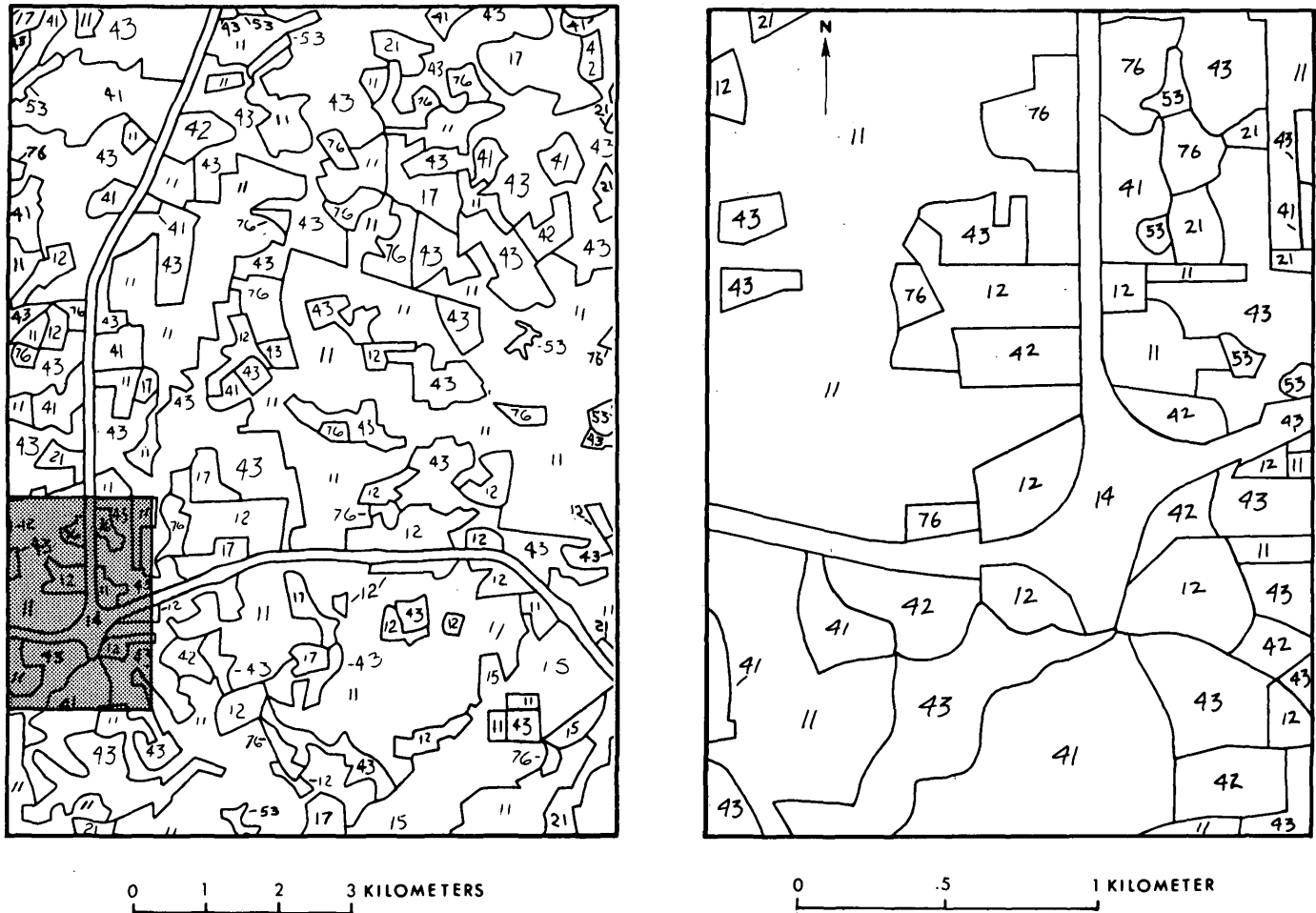
### COMPILATION OF LAND USE AND LAND COVER IN THE GREATER ATLANTA REGION

Land use and land cover maps were compiled at 1:100 000 for the entire Greater Atlanta Region and for twelve 7.5-minute quadrangles at 1:24 000 scale for parts of the same area in cooperation with the Georgia State Geological Survey. In addition, six 7.5-min quadrangles were selected for compilation at the scale of 1:24 000 for a river quality study by the U.S. Geological Survey. These eighteen 7.5-min quadrangles were compiled using the 1:24 000-scale orthophotoquads as a base and were mapped with a minimum mapping unit of 1 hectare.

The land use and land cover data were generalized from the 1:24 000-scale map to the 1:100 000 scale for that portion of the Greater Atlanta Region land use and land cover map originally compiled at 1:24 000 scale. The minimum mapping unit for the 1:100 000-scale land use and land cover maps was increased from 1 ha at 1:24 000 scale to 4 or 16 ha at 1:100 000 scale, according to the specifications (Anderson and others, 1976). The remaining 1:100 000-scale land use and land cover map was compiled to a stable base copy of the black-and-blue line print by using black-and-white high-altitude photographs at a contact scale of 1:76 000 and at a reduced scale of 1:100 000. An example of the land use and land cover maps of the Atlanta area is shown on figure 1.

The compilers experienced the greatest difficulties in interpretation of the forest land categories. The black-and-white aerial photographs were obtained in 3 different months, February, April, and May, and the degree of foliation varied with the time of photography. For this reason the shades of gray on the photographs varied for evergreen and deciduous trees from month to month, so that there was no consistent signature for forest types. The interpreters had the greatest difficulty separating evergreen and deciduous forests on the May photographs, as both forest types had similar gray tones. This problem was as difficult to resolve at 1:24 000 scale as it was at 1:100 000 scale.

These same difficulties were experienced in verify-



*Explanation*

- |  |                         |
|--|-------------------------|
| 11 Residential                                   | 21 Cropland and Pasture |
| 12 Commercial and Services                       | 41 Deciduous Forest     |
| 14 Transportation, Communications, and Utilities | 42 Evergreen Forest     |
| 15 Industrial and Commercial Complexes           | 43 Mixed Forest         |
| 16 Mixed Urban or Built-Up Land                  | 53 Reservoirs           |
| 17 Other Urban or Built-Up Land                  | 76 Transitional Areas   |

FIGURE 1.—Land use and land cover maps of a portion of the Greater Atlanta Region. On the left is a 1:100 000-scale land use map fitted to the U.S. Geological Survey 7.5-min Chamblee topographic quadrangle, Georgia. On the right is a 1:24 000-scale land use map which depicts in more detail the shaded portion of the map on the left.

ing the land use and land cover interpretation at the 381 sample points when the same photographs were used. As a result of these and other problems, 72 points were examined in the field. Most of these points were in areas of evergreen forest, deciduous forest, and mixed forest.

**RESEARCH METHOD**

A point sample designed to give equal chance of representation to all portions of the map (fig. 2) was

selected as the sampling method. According to Berry (1962):

The preferred areal sample is the stratified systematic unaligned sample. It is constructed as follows: First, point A is selected at random. The  $x$  coordinate of A is then used with a new random  $y$  coordinate to locate B, a second random  $y$  coordinate to locate E, and so on across the top row of strata. By a similar process the  $y$  coordinate of A is used in combination with random  $x$  coordinates to locate point C and all successive points in the first column of strata. The random  $x$

coordinate of C and  $y$  coordinate of B are then used to locate D, of E and F to locate G, and so on until all strata have sample elements. The resulting sample combines the advantages of randomization and stratification with the useful aspects of systematic sample, while avoiding possibilities of bias because periodicities are present.

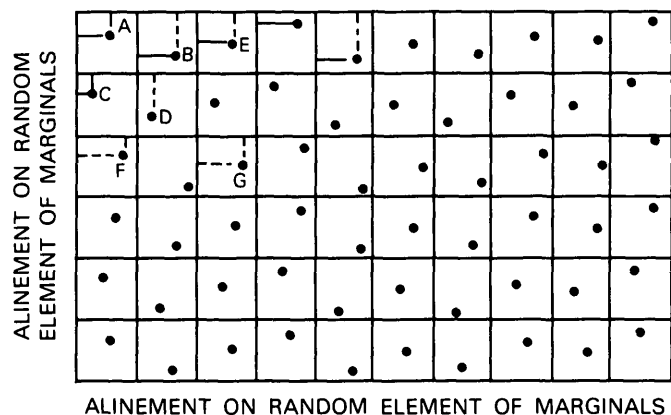


FIGURE 2.—A stratified systematic unaligned sample.

### Procedure

The Atlanta 1:100 000-scale land use and land cover map was stratified into ninety-six 7.5-min grid units. From each stratum, four samples with replacement were selected, giving a total of 381 unique points to verify. (Three points were duplicates of points already sampled.) This number of points is considered adequate to obtain results of 85-percent accuracy at a 95-percent confidence level, if we assume a binomial distribution (Gregory, 1963, p. 98-99). According to the formula  $n = (p \cdot q) / d^2$  (where  $p$  is the accuracy percentage desired,  $q$  is  $100 - p$ , and  $d$  is the standard error desired), the required number of the sample would be at least 318 points to obtain results of 85-percent average accuracy with a standard error of 2 percent. To assure reliable results for individual categories on the map and to obtain uniform coverage in the stratified sample, all 381 points were examined.

The interpretation of the land use and land cover at each of these points was verified with the original photographs where possible. When a question of interpretation remained for any point, it was field verified from a light aircraft. Where there were 1:24 000-scale land use and land cover maps available, the same points selected from the 1:100 000 scale were verified for accuracy at the 1:24 000 scale as well. A matrix comparing the interpretation at 1:100 000 scale and the correct land use was constructed, and the number of "correct" points as compared to the total number of points was then stated as the percentage of accuracy for the sample. From this matrix it was also possible

to compare the number of "correct" points for each category and compare this to the total number of points for each category.

## RESULTS

### Overall accuracy of the map at 1:100 000 and 1:24 000 scales

The method of determining the accuracy was primarily empirical, in that the percentage of accuracy is a simple ratio of correct interpretation to the total number of points sampled. The number of correct interpretations at the 1:100 000 scale was 343 (90 percent) of 381 points sampled. (See the matrix in fig. 3.)

Of the 71 points sampled on the eighteen 7.5-min. sheets at 1:24 000 scale (one point was a duplicate), 62 points or 87 percent were "correct." The 71 points sampled on the 1:24 000-scale maps were primarily in the urban areas. Of the same 71 points interpreted at 1:100 000, 63 points or 89 percent were "correct," indicating that the interpretation at both scales was the same.

These results, obtained by a stratified systematic unaligned selection of 381 points, were chosen to represent the complete map at a scale of 1:100 000. They do not, however, include more than 13 land use and land cover categories from a map containing as many as 20 land use and land cover categories. Of the 13 categories included, only 5 had more than 10 occurrences in the point selection.

### Accuracy of individual categories

Each of the points sampled is not within a unique polygon. Certain polygons, considered "background" polygons, encompass a major portion of the map and may contain several of these selected points. For this reason the categories of the most extensive land use or land cover receive the heaviest concentration in the analysis. One disadvantage, however, is that many of the small polygons of "intensive use" categories, often those affecting planning decisions, are overlooked.

This test of the accuracy of the maps has provided reliable data for only five categories, although we hope that all categories are interpreted at the same level of accuracy. The results for these five categories are as follows:

- Category 11, Residential Land—30 points verified of 32 points checked, or 94 percent accurate.
- Category 21, Cropland and Pasture—86 points verified of 92 points checked, or 93 percent accurate.
- Category 41, Deciduous Forest Land—21 points verified of 27 points checked, or 78 percent accurate.

		ORIGINAL CLASSIFICATION AT 1:100 000 SCALE												
		11	12	14	15	17	21	23	41	42	43	53	61	76
VERIFIED CLASSIFICATION AT 1:100 000 SCALE	11	30				1	1							
	12		1		2									
	14			3										
	15				1									
	17					3	1							
	21	1	1				86				4			
	23							3						
	41								21	2	3		1	
	42						1			44	3			1
	43	1					2		4	7	138			
	53											5		
	61								1				1	
76						1							7	
Correct .....		343 (90 percent)												
Errors .....		38 (10 percent)												
Total .....		381 (100 percent)												

FIGURE 3.—Matrix of land use and land cover classification at 1:100 000 scale as compared to the verified classification.

- Category 42, Evergreen Forest Land—44 points verified of 49 points checked, or 90 percent accurate.
- Category 43, Mixed Forest Land—138 points verified of 152 points checked, or 91 percent accurate.

To state a more statistically correct interpretation of these results, the 95-percent confidence limits for the percentage of accuracy must be obtained. One method is explained by Snedecor and Cochran (1967). The formula for the limits of  $p$  at 95-percent confidence levels is

$$\hat{p} \pm 1.96 \sqrt{\frac{\hat{p}(100 - \hat{p})}{n}} \quad (1)$$

plus a correction factor for a continuous curve, or

$$\hat{p} \pm \left[ 1.96 \sqrt{\frac{\hat{p}(100 - \hat{p})}{n}} + 50/n \right] \quad (2)$$

where  $\hat{p}$  is the approximate value of the true portion

“correct,” expressed as a percentage, and  $n$  is the number of points sampled. For the 381 points with an accuracy percentage of 90 percent the range of values with a 95-percent confidence would be:

$$\hat{p} \pm \left[ 1.96 \sqrt{\frac{90(100 - 90)}{381}} + \frac{50}{381} \right] \quad (3)$$

or  $90 \pm 3.0 = 87$  to  $93$  percent (well above the required accuracy of 85 percent).

Based on this formula, the range of percentage of accuracy for the 71 points checked on the 1:24 000 scale maps is 78 to 96 percent with a 95-percent level of confidence. These same points at 1:100 000 were accurate within the range of 81 to 97 percent with a 95-percent confidence.

The confidence limits of these results differ from category to category depending on the size of the sample. Table 1 is a synopsis of these results.

TABLE 1.—Accuracy percentages at the 95-percent confidence interval for five major categories

Land use and land cover categories	Points checked	Points verified	Accuracy percentage	95-percent confidence limits <sup>a</sup>
Residential (11) --	32	30	94	94-100
Cropland and Pasture (21) ---	92	86	93	87- 99
Deciduous Forest Land (41) -----	27	21	78	61- 95
Evergreen Forest Land (42) -----	49	44	90	81- 99
Mixed Forest Land (43) -----	152	138	91	86- 96

<sup>a</sup> Formula from Snedecor and Cochran (1967):

$$\hat{p} \pm [1.96 \sqrt{\hat{p}(100 - \hat{p}) / n + 50/n}]$$

<sup>b</sup> Calculates to 104 percent by the equation.

In the case of category 11, the 95-percent confidence limits based on formula 2 are 84 to 100 percent. The 95-percent confidence limits for the accuracy of category 21 is 87 to 99 percent. The accuracy of category 42 has 95-percent confidence limits of 81 to 99 percent. The accuracy of category 43 is between 86 and 96 percent with a 95-percent confidence.

From these results it appears that the accuracies of four of these categories are similar and approach or exceed the criterion of 85-percent accuracy. Category 41 is less accurate, yet the range in accuracy is so great that it would be necessary to test several more points for more precise results. For 78-percent accuracy with a standard error of 5 percent, and therefore an estimate of the true proportion at the 95-percent probability level to within  $\pm 10$  percent, at least 69 points should be checked. This required sample size is determined from the formula  $n = (p \cdot q) / d^2$  given in "Procedure" section (Gregory 1963, p. 98-99). For a smaller standard error, a much greater sample size would be required.

## CONCLUSION

The overall accuracy of the land use and land cover maps of the Greater Atlanta Region is between 87 and 93 percent with a 95-percent level of confidence, if we assume a binomial distribution. This level of accuracy is based primarily on categories of Residential Land, Cropland and Pasture, Evergreen Forest Land, Deciduous Forest Land, and Mixed Forest Land which constitute the major portion of the map.

Category 41, Deciduous Forest Land, was mapped with the least accuracy. The 27 points of Deciduous Forest Land checked are insufficient to give a reliable measure of the true accuracy of category 41 at the 95-percent probability level.

The accuracy of the 71 points sampled on the eighteen 1:24 000-scale Level II land use and land cover maps was between 78 and 96 percent with a 95-percent confidence, as compared to an accuracy of 81 to 97 percent at the 1:100 000 scale.

According to the results, the overall accuracy of the land use and land cover maps exceeds the criteria of 85-percent accuracy at the scale of 1:100 000, and the mapping results seem to be consistent from one scale to the next.

## REFERENCES CITED

- Anderson, J. R., Hardy, E. E., Roach, J. T., and Witmer, R. E., 1976, A land use and land cover classification system for use with remote sensor data: U.S. Geol. Survey Prof. Paper 964, 28 p.
- Berry, B. J. L., 1962, Sampling, coding, and storing flood plain data: U.S. Dept. Agriculture Handb. 237, 27 p.
- Gregory, S., 1963, Statistical methods and the geographer [2d ed.]: Atlantic Highlands, N.J., Humanities Press, p. 82-100.
- Snedecor, G. W., and Cochran, W. F., 1967, Statistical methods: Ames, Iowa State Univ. Press, p. 202-211.



## BLUE RIBBON LINEAMENT, AN EAST-TRENDING STRUCTURAL ZONE WITHIN THE PIOCHE MINERAL BELT OF SOUTHWESTERN UTAH AND EASTERN NEVADA

By PETER D. ROWLEY; PETER W. LIPMAN; HARALD H. MEHNERT,  
DAVID A. LINDSEY; and JOHN J. ANDERSON,<sup>1</sup> Denver, Colo.;  
Hawaii Volcano Observatory, Hawaii; Denver, Colo.; Kent, Ohio

*Abstract.*—The Blue Ribbon lineament is an east-west structural zone that is about 25 kilometers wide and passes through the Pioche mineral belt at about 38°10' N. It is best known in Utah, where it is at least 190 km long, and extends from the southern Sevier Plateau in the High Plateaus westward and across southern Mountain Home (Needle) Range in the Great Basin. It probably continues westward an additional 170 km into Nevada, where it connects with the eastern end of the 230-km Warm Springs lineament. The Blue Ribbon lineament is defined by range terminations and east-trending valleys, alignment of eruptive centers of middle Miocene (20 million years) to Pliocene(?) (5–1.8 m.y.) alkalic rhyolite, alignment of areas of middle Miocene to Pliocene mineralized rocks (mostly fluorine, uranium, tungsten) and hydrothermally altered rocks, east-trending magnetic highs and interruptions of magnetic anomalies, and east-striking basin-range faults of late Tertiary and Quaternary age. Mountains south of the lineament are topographically and structurally lower than those to the north. North-striking Quaternary basin-range faults, the Thermo hot springs area, several warm springs and former hot springs, and numerous dacitic to andesitic volcanic centers of early to middle Miocene age (26–20 m.y.) occur along the lineament. The Blue Ribbon lineament is believed to be a deep crustal fault zone dating from at least middle Miocene time and possibly much earlier. It thus developed generally coincident with northerly trending classical basin-range faults. Its fracture system was an important, long-lived conduit for mineralizing fluids, and it should be an attractive target for minerals exploration in the future. The lineament could be due to an east-trending warp in the subducting mantle plate, or it could be part of a past or present intracontinental transform fault that locally gets younger eastward and dies out eastward in the western Colorado Plateaus province.

This report is an outgrowth of various studies on the geology of southwestern Utah. One of these studies was a detailed geologic mapping of the southwestern part of the High Plateaus subprovince of the Colorado Plateaus and mapping of the nearby Black Mountains of the eastern Great Basin (Anderson and Rowley, 1975). Other studies were conducted farther west in

the Great Basin and consisted of an investigation of the Staats (Monarch) mine–Blawn Mountain area in the southern Wah Wah Mountains by D. A. Lindsey (unpub. data, 1976) and reconnaissance geochemical studies in the southern parts of the Wah Wah Mountains and Mountain Home Range (formerly called Needle Range) by D. R. Shawe and D. A. Lindsey (unpub. data, 1976). During these studies it became apparent that Tertiary volcanic centers, Tertiary mineralized and hydrothermally altered rock, geophysical anomalies, topographic features, and Tertiary and Quaternary basin-range faults defined an east-trending structural belt that passed through all the previously studied areas.

In 1975 an opportunity arose to investigate the hot springs and associated rhyolite centers along this east-trending structural feature, as well as those hot springs and rhyolites north of the feature, as part of a program of reconnaissance and detailed mapping of young rhyolite centers around the rim of the Colorado Plateaus province for their geothermal potential (for example, Lipman and others, 1975; 1978; Rowley and Lipman, 1975). A major phase of this program was the determination of K-Ar ages of alkalic rhyolite (Mehnert and others, 1977). These ages indicated that the rhyolite centers were 20 million years old and younger, generally coincident with the broad episode of basin-range faulting in this part of Utah. The youngest K-Ar age of four rhyolites was from a dome at Blue Ribbon Summit, which gives its name to the structural feature described here.

This report describes the nature of the Blue Ribbon lineament, a through-going structural feature at about 38°10' N., that crosses the Wasatch Front and the dominant trend of basin-range faults nearly at right angles. The Blue Ribbon lineament is about 25 kilometers wide

<sup>1</sup> Kent State University.

and extends about 190 km through the Great Basin and Colorado Plateaus of southwestern Utah and probably an additional 170 km westward through eastern Nevada. The lineament appears to be collinear at about  $116^{\circ}$  W., in Nevada, with the 230-km east-trending Warm Springs lineament (Ekren and others, 1976) of similar characteristics, which extends to the western edge of the Great Basin. In Utah, where detailed data are available and where we are most familiar with the geology, the lineament is traced from southwest of Indian Peak in the Mountain Home Range near the Nevada border east to the Antimony mining district, which is east of the southern Sevier Plateau (fig. 1A). The southern edge of the lineament is several kilometers south of the latitude of Antimony, and the northern edge is near the latitude of Beaver.

The Blue Ribbon lineament as here defined lies within the southern half of the broad Wah Wah-Tushar mineral belt (fig. 2) of Hilpert and Roberts (1964) and just north of the Pioche mineral belt of Roberts (1964). It crosses the axis of the "Pioche mineral belt" as redefined by Shawe and Stewart (1976) but, because of the overall coincidence with the Pioche mineral belt in Utah, the Blue Ribbon lineament is here considered to be a distinctive zone within the broader feature as defined by Shawe and Stewart (1976).

*Acknowledgments.*—Recognition and analysis of the Blue Ribbon lineament is due partly to discussions with T. A. Steven, G. P. Eaton, D. R. Shawe, and E. B. Ekren. We are grateful to E. B. Ekren, J. H. Stewart, and D. R. Shawe for making available much unpublished data on east-trending features in the Great Basin. R. K. Glanzman, G. L. Galyardt, and P. L. Williams provided information on some areas in the Great Basin with which they are familiar. J. S. Pallister assisted with collecting specimens for K-Ar study and made most mineral separations.

#### PREVIOUSLY DESCRIBED EAST-TRENDING BELTS IN GREAT BASIN

East-trending belts of mineral occurrences, geophysical anomalies, structural features, and patterns of Cenozoic igneous rocks in the Great Basin have been observed and described by many geologists, starting with Butler and others (1920). Various geologists and geophysicists have placed belt axes differently, as described in the following paragraphs and shown on figure 2; none of these axes are mutually exclusive because the authors used different scales and different criteria for plotting them. Most of the lineaments probably reflect in one way or another the effects of deep east-trending fault systems in the Great Basin,

apparently of an age coincident with classical basin-range structure but perhaps controlled by features that are partly older than basin-range structure.

Hilpert and Roberts (1964) summarized previous work and described three broad belts of intrusive rocks and metal mining districts in western Utah (fig. 2), from north to south the Oquirrh-Uinta, Deep Creek-Tintic, and Wah Wah-Tushar belts. The mining districts on the belts account for 95 percent of Utah's copper, lead, silver, gold, and zinc. Erickson (1974) discussed the northernmost belt, which he renamed the Uinta-Gold Hill trend and which he extended farther eastward. The southern two belts continue into Nevada as the Cherry Creek belt and the Pioche belt (Roberts, 1964); Roberts (1966) later described the broad curving Cortez-Uinta axis, which connects with the Oquirrh-Uinta belt, and the Hamilton-Ely belt at about  $39^{\circ}10'$  N. Callaghan (1973) also called attention to east-trending mineral belts. Zietz and others (1969) noted east-trending aeromagnetic patterns in the Oquirrh-Uinta, Deep Creek-Tintic, and Cortez-Uinta belts. Cook and his coworkers (for example, Cook and Montgomery, 1974) postulated three broad east-trending zones in Utah defined by gravity data. The axes of these zones are at  $40^{\circ}40'$  N.,  $40^{\circ}$  N., and  $38^{\circ}40'$  N., within the mineral belts of Hilpert and Roberts (1964).

Shawe and Stewart (1976) discussed the three major Utah mineral belts as well as Nevada mineral belts. Their Pioche mineral belt, which extends east-northeastward from Nevada into Utah, contains the Wah Wah-Tushar belt of Hilpert and Roberts (1964) and the Pioche belt of Roberts (1964). The axes of their belts generally are defined by aligned Cretaceous and Tertiary plutons, zones of faults that are transverse to the northerly basin-range faults, gross aeromagnetic patterns, and major mineral occurrences. To the three major belts they added another, smaller belt south of the Pioche belt, which they called the Delamar-Iron Springs mineral belt (fig. 2). Stewart, Moore, and Zeitz (1977) discussed the belts in terms of distribution of igneous rocks; they observed that broad east-trending zones of volcanic rocks in Nevada and western Utah decrease in age from north to south. The axes of their volcanic belts correspond to the axes of the belts of Shawe and Stewart (1976).

Eaton (1975, 1976; unpub. data, 1976) described a major east-trending crustal boundary that crosses Nevada at about  $37^{\circ}$  N. (fig. 2), thence gently swings northeasterly into southern Utah, coincident with the Intermountain Seismic Belt. This zone, which is defined largely by gravity and magnetic data, seismicity, and depth to the M-discontinuity, marks the southern

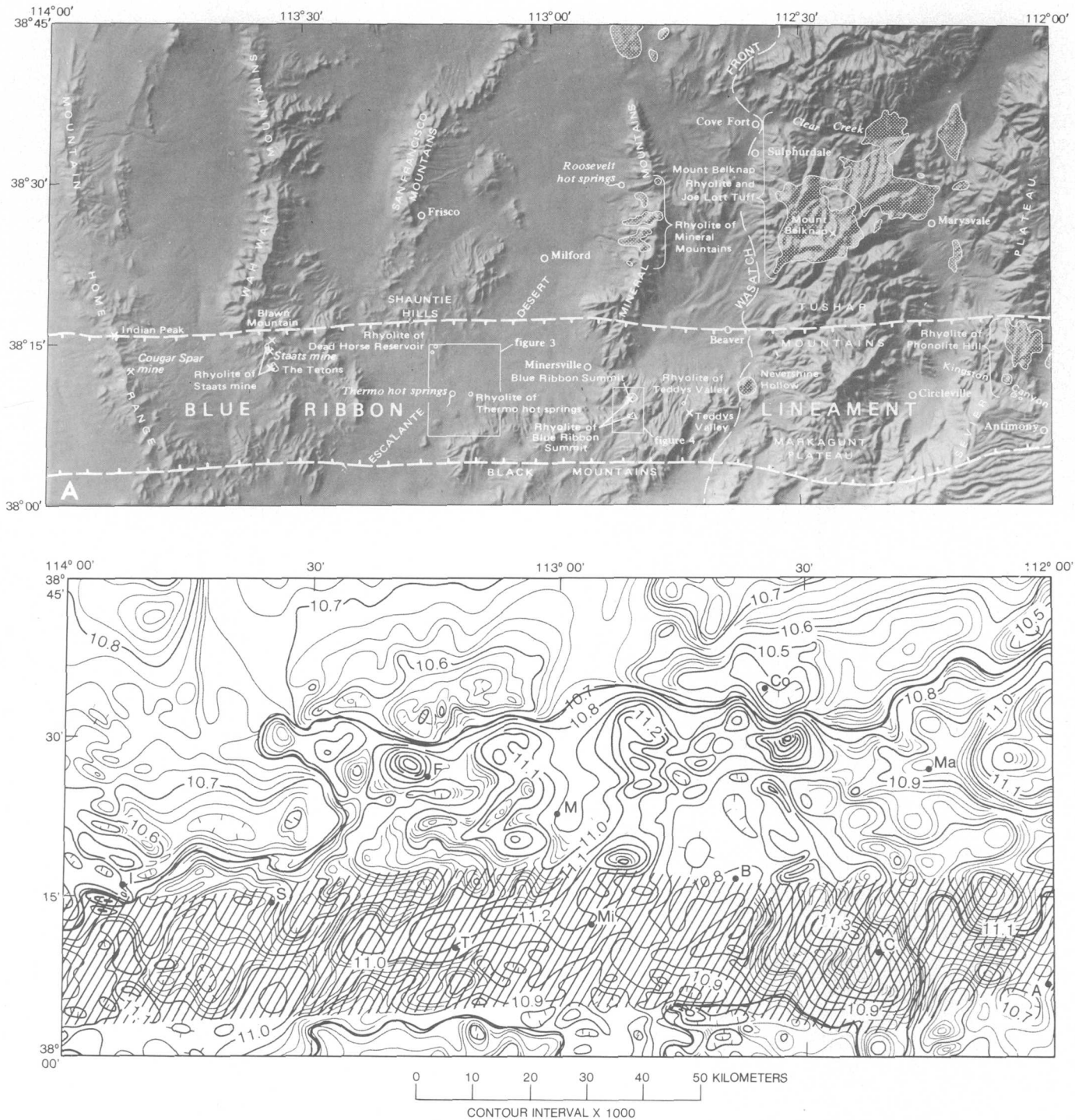


FIGURE 1.—Index maps showing topographic and aeromagnetic expression of most of the Utah part of the Blue Ribbon lineament. A, Raised relief map showing location of geographic and geologic features near the Blue Ribbon lineament as well as location of areas of figures 3 and 4. Approximate boundaries of Blue Ribbon lineament shown by dashed hachured lines. Wasatch Front shown by dashed line. Occurrence of alkalic rhyolite, stippled. B, Aeromagnetic

map, from Zeitz, Shuey, and Kirby (1976). Blue Ribbon lineament shown by lined ruling. Outlines of aeromagnetic ridge of Pioche mineral belt, modified from Stewart, Moore, and Zeitz (1977, fig. 5), is shown by heavy solid line. Contour intervals are 20 and 100 gammas. I, Indian Park; S, Staats (Monarch) mine; F, Frisco; T, Thermo hot springs; M, Milford; Mi, Minersville; B, Beaver; Co, Cove Fort; C, Circleville; Ma, Marysvale; and A, Antimony.

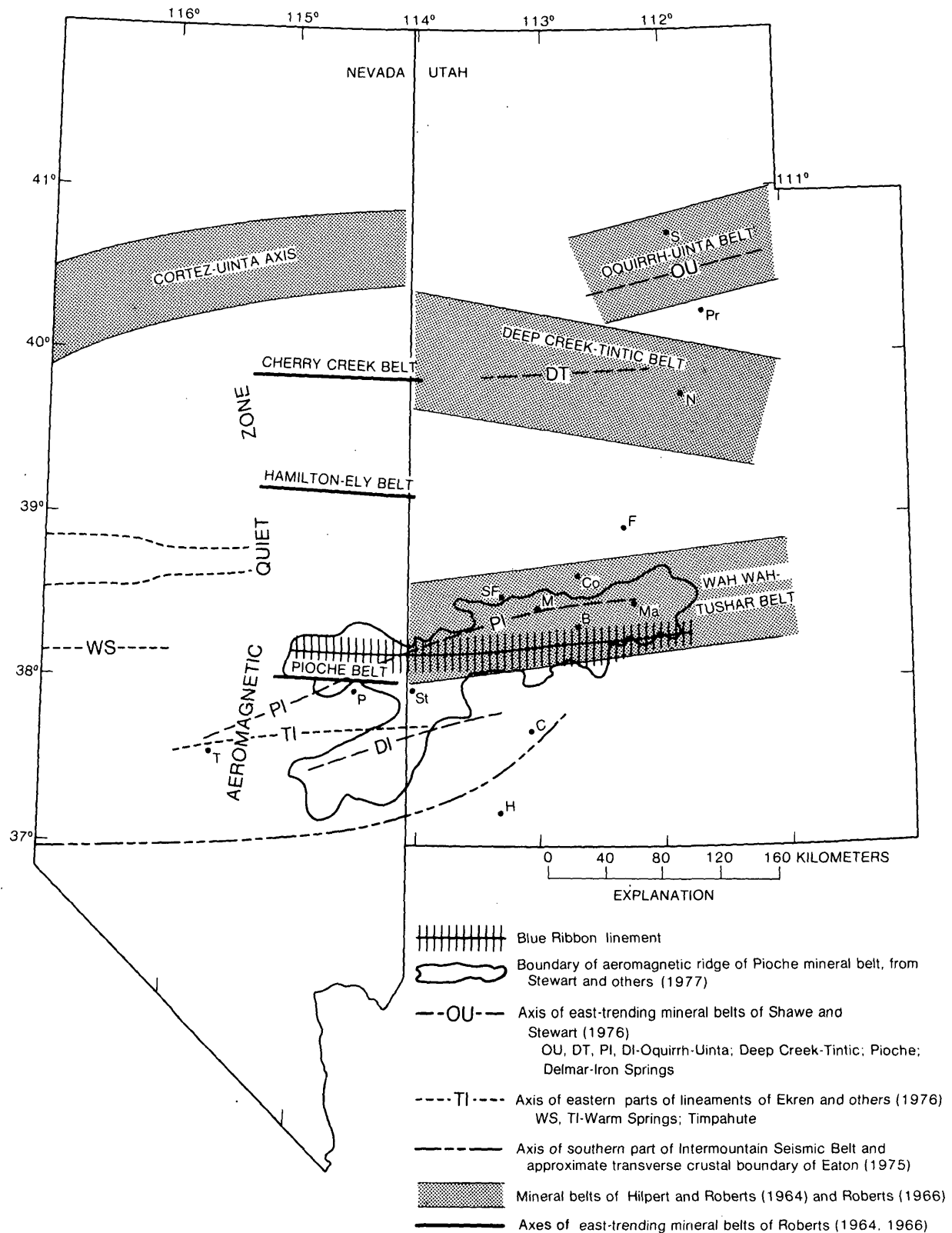


FIGURE 2.—Index map of eastern Nevada and western Utah showing location of the Blue Ribbon lineament and other east-trending structural, mineral, and geophysical belts described in the published literature. S (Salt Lake City), Pr (Provo), N (Nephi), F (Fillmore); Co (Cove Fort); B (Beaver), C (Cedar City), and H (Hurricane) mark the

extreme eastern edge (Wasatch Front) of the Great Basin. T (Temptiute); P (Pioche); St (Stateline mining district); SF, (San Francisco mining district), M (Milford), and Ma (Marysville) occur at sites of major mining activity in the east-trending Pioche mineral belt of Shawe and Stewart (1976).

edge of volcanic rocks and mining districts in the Great Basin. In Utah, this belt coincides with faults of the same strike and with strings of plutons and volcanic centers (Cook, 1960, maps 1-21; Blank and Mackin, 1967, pl. 1).

Ekren and others (1976) documented four lineaments between lat 37°40' and 39° N. in south-central Nevada, each of which ranges in length from 200 to 300 km (fig. 2). Their evidence consists mostly of topographic discontinuities and disruptions, terminations and alignments of aeromagnetic anomalies, alignments of plutons and volcanic centers, and other structural features. Their northern lineament may connect with a similar lineament in west-central Nevada described by Binger (1971). The southern two lineaments of Ekren and others (1976) were called the Warm Springs lineament and Timpahute lineament. The Warm Springs lineament probably connects with the Blue Ribbon lineament, and the Timpahute lineament extends into Utah as the northern edge of the Clover Mountains and Bull Valley Mountains and into the Iron Springs mining district, which occurs at the intersection between the Timpahute lineament and Eaton's crustal boundary (1975, 1976; unpub. data, 1976).

#### PIOCHE MINERAL BELT

The Pioche mineral belt, as defined by Shawe and Stewart (1976), is a broad zone more than 50 km wide that extends more than 300 km from the Tempiute mining district in Nevada east through the Marysville volcanic pile in Utah (fig. 2). As Shawe and Stewart noted, considerable commodities have been produced along the belt, such as gold, silver, lead, zinc, tungsten, uranium, fluorine, manganese, copper, and alunite. Some mining districts in the belt are shown on figure 2. Those along the Blue Ribbon lineament are described in the following discussion.

In addition to the features enumerated by Shawe and Stewart (1976), other characteristics of the mineral belt are noteworthy. The easterly to east-northeasterly trends of occurrences of fluorine, tungsten, gold, copper, molybdenum, lead-zinc-silver, manganese, uranium, and barium minerals are apparent from published compilations (for example, Walker and Osterwald, 1963; U.S. Geological Survey, Utah Geological and Mineralogical Survey, 1964; U.S. Geological Survey, Nevada Bureau of Mines, 1964); occurrences of iron, beryllium, alunite, sulfur, and other minerals have a less well defined but nonetheless general east-trending distribution. Many mineral occurrences, notably those of fluorine, beryllium, uranium, tungsten, and sulfur, are young and commonly occur near centers

of alkalic rhyolites that range in age from middle Miocene (20 m.y.) to Pleistocene. At Marysville, for example, uranium deposits (Kerr and others, 1957; Kerr, 1968) were dated at about 13 m.y. by Bassett and others (1963). Steven and others (1977) concluded that much alunite, uranium, fluorine, and molybdenite at Marysville are 16-9 m.y. old, but that other deposits of alunite and base and precious metals are early to middle Miocene in age. Most other mineral deposits of the Pioche mineral belt are of middle to late Tertiary age, and some, as at Tempiute and Pioche (Krueger and Schilling, 1971; Johnston, 1972), may be totally Cretaceous in age. In the Pioche mineral belt, many hot spring areas occur, including known geothermal resource areas (KGRA's) that may provide geothermal energy in future years such as the Roosevelt area just west of the Mineral Mountains and the Cove Fort-Sulfurdale area just northeast of the Mineral Mountains. Clearly the overall Pioche mineral belt has been in existence at least from middle Tertiary to Holocene time and perhaps even longer.

The Pioche mineral belt of Shawe and Stewart (1976) includes the topographically highest mountains in southern Utah and is also structurally high. East-striking faults occur in the mineral belt. Callaghan and Parker (1962), Kennedy (1963), and Callaghan (1973) noted that the Tushar Mountains probably occupy part of an east-trending arch that is bounded on its northern side (in the major east-trending valley of Clear Creek near the northern edge of the mineral belt) by a parallel downwarp. The arch occurs in the same area where an east-trending highland of probable Late Cretaceous or early Tertiary age extended both east and west of the Tushar Mountains (Butler and others, 1920; Callaghan, 1973; Anderson and Rowley, 1975). Because of the highland, lacustrine and fluvial rocks of early Tertiary age in the northern High Plateaus are different in lithology from lacustrine and fluvial rocks of the same age in the southern High Plateaus, and sedimentary rocks of early Tertiary age in the Tushar Mountains are absent or are thin and of different character from beds of the same age to the north and south.

As noted by Shawe and Stewart (1976, fig. 2), the Pioche mineral belt is characterized by plutons and volcanic rocks mostly of Cenozoic age. One of these is the granitic batholith of the Mineral Mountains (Liese, 1957; Earll, 1957), which is in the first range west of the Wasatch Front (fig. 1), and is the largest pluton in Utah; published K-Ar ages of 15-9 m.y. (Park, 1968; Armstrong, 1970) have received some confirmation from Rb-Sr dating (C. E. Hedge, unpub. data, 1976). Lava and tuff fields of alkalic rhyolite are

abundant in the Pioche mineral belt. The largest such field is the Mount Belknap Rhyolite, about 21–17 m.y. old (Bassett and others, 1963; Cunningham and Steven, 1977; Steven and others, 1977), and the related Joe Lott Tuff (Callaghan, 1939) in the Tushar Mountains. Alkalic rhyolite is exposed at several places south of the San Francisco Mountains (P.L. Williams, oral commun., 1976). Alkalic rhyolite of Pleistocene age overlies the Mineral Mountains batholith (Liese, 1957; Earll, 1957; Lipman and others, 1975, 1978). A large province of Quaternary basalt and minor rhyolite occurs north of the Mineral Mountains on the northern side of the Pioche mineral belt (Mehnert and others, 1977). Upper Cenozoic alkalic rhyolites are extensive in the southern parts of the Mountain Home Range and the Wah Wah Mountains (D. A. Lindsey and D. R. Shawe, oral commun., 1975).

The mineralized and hydrothermally altered rocks in the Pioche mineral belt are closely outlined by a broad aeromagnetic ridge (fig. 2; Stewart and others, 1977, fig. 5). The overall magnetic high (fig. 1B) contains numerous high-amplitude (that is, shallow crustal) hills and depressions (Zietz and others, 1976) that mostly reflect the presence of plutons (Hilpert and Roberts, 1964) and volcanic centers (Stewart and others, 1977). In contrast, the areas north and south of the ridge are magnetically low and contain few superimposed magnetic hills and depressions. The aeromagnetic ridge extends from about 115° W. east to about 111° 45' W.; the west end is terminated by a broad north-trending "quiet" aeromagnetic belt that bisects the Great Basin (Eaton, 1976; Stewart and others, 1977; G. P. Eaton, unpub. data, 1976). In detail (fig. 1B), the aeromagnetic ridge consists of both east- and east-northeast-trending components. One effect of the two trends within the magnetic ridge is that the western half of the ridge is forked, containing a branch that continues west and a branch extending from about 113°30' W. south-southwest to the western end of the Delamar-Iron Springs mineral belt.

The Pioche mineral belt has striking similarities to the Deep Creek-Tintic mineral belt. For example, the Deep Creek-Tintic mineral belt contains major occurrences of beryllium, fluorine, lead-zinc-silver, copper, manganese, gold, uranium, tungsten, and other minerals. Most of these mineral occurrences clearly show a general east-trending distribution (U.S. Geological Survey, Utah Geological and Mineral Survey, 1964; U.S. Geological Survey, Nevada Bureau of Mines, 1964; Cohenour, 1963; Park, 1968; Lindsey and others, 1973, 1975; Van Alstine, 1976) or a northeast-trending distribution (Shawe, 1966). The Deep Creek-Tintic belt contains numerous centers of young (10–3 m.y.)

alkalic rhyolite (Lindsey and others, 1975; Armstrong, 1970; Mehnert and others, 1977), numerous plutons (Hilpert and Roberts, 1964), and numerous east-striking faults (Stokes, 1963; Loring, 1972). It is axial to a broad zone of Cenozoic volcanic rocks and is the site of a broad east-trending magnetic ridge, with superimposed highs and lows, that extends into Nevada (Zietz and others, 1969; Zietz, Shuey, and Kirby, 1976; Stewart and others, 1977). The Crater Springs hot springs area occurs along its southern edge. Like the Pioche belt, the eastern end of the Deep Creek-Tintic belt contains a base metal and precious metal mining district (Tintic) near the Wasatch Front, while just west of this district the young, 17- to 16-m.y.-old (Armstrong, 1970; Cohenour, 1970; D. A. Lindsey, unpub. data, 1976) granite of Sheeprock Mountains is exposed in a configuration similar to that of the Marysvale mining district and Mineral Mountains batholith of the Pioche belt.

#### BLUE RIBBON LINEAMENT IN UTAH

The Blue Ribbon lineament in Utah occupies an east-trending zone, about 25 km wide and 190 km long (fig. 1A), that is defined by magnetic highs and interruptions of magnetic anomalies, alignment of Tertiary centers of alkalic rhyolite and dacitic to andesitic rocks, range terminations and valleys, Tertiary and Quaternary basin-range faults, and Tertiary mineralized (mostly fluorine, uranium, and tungsten) and hydrothermally altered rock. Several hot springs also occur along the lineament, and their presence suggests that hot water circulation along the lineament, which in Tertiary time produced altered rock and carried minerals, is remarkably long lived.

The lineament concentrates many diverse features, but not exclusively so with respect to those in other parts of the Pioche mineral belt; the lineament is only one of several controls of such features within the broad mineral belt. Another such feature is a second, less clearly defined east-west lineament that occurs along the northern edge of the Pioche belt, mostly between the latitudes of Cove Fort and Marysvale (centered on 38°30' N.) and extending from at least 30 km west of Frisco to at least Marysvale. Parts of this feature were recognized by G. L. Galyardt (oral commun., 1976), who observed east-trending geophysical patterns in the Cove Fort-Sulfurdale area, and T. A. Steven (oral commun., 1977) who observed east-trending alignments of published mineral occurrences (U.S. Geological Survey, Utah Geological and Mineralogical Survey, 1964). The lineament also is defined by folds and faults (especially in the Clear Creek area west of Cove Fort),

topography, aeromagnetic anomalies, coincidence with hot springs, and alinement of plutons and volcanic centers.

Of the types of evidence for the presence of the Blue Ribbon lineament, the magnetic patterns are especially instructive. As the aeromagnetic map (fig. 1B) shows, the Blue Ribbon lineament contains a series of east-aligned highs and lows. These are superimposed on the larger Pioche magnetic ridge. Thus the lineament forms one of several east-trending details in the Pioche magnetic high. In Utah the Blue Ribbon lineament occupies the southern edge of the Pioche magnetic ridge, but in Nevada the Blue Ribbon lineament is near the central part of the Pioche aeromagnetic ridge (fig. 2; Zietz, Shuey, and Kirby, 1976). We believe that the magnetic pattern shown by the lineament results from a combination of geologic features. These features will be described from west to east.

### Volcanic centers and hot springs

Volcanic centers and plutons mark the lineament throughout its length but are rare or nonexistent south of the lineament. Several hot springs occur near the volcanic centers. At the western end of the lineament in Utah, south of Indian Peak in the southern Mountain Home (Needle) Range (fig. 1A), two Tertiary porphyritic plutons, each underlying an area of 1 square kilometer, have been mapped (Hintze, 1963). These are intrusive into lower Tertiary ash-flow tuff of intermediate composition. The southern of these plutons is 1.5 km west of the Cougar Spar mine, the main producer of fluorspar in the Indian Peak mining district. Thurston and others (1954, p. 6, pl. 1) reported that rhyolite lava flows, including perlite and rhyolite dikes, occur in the vicinity of the Cougar Spar and other mines.

Farther east along the Blue Ribbon lineament, in the Staats (Monarch) mine—Blawn Mountain area of the southern Wah Wah Mountains, two alkalic rhyolite plugs or sills occupy an area of more than 1 km<sup>2</sup> near the Staats (Monarch) mine (Miller, 1966; Whelan,

1965). One of these, called by Whelan the "main intrusion," yielded a new K-Ar age of 20.2 m.y. (table 1); it is here called the rhyolite of Staats mine. Petrography of the rhyolite is summarized in table 2. Mineral separations demonstrate that considerable accessory topaz occurs in the rock, and semiquantitative spectrographic analyses show anomalously high amounts of fluorine, beryllium, niobium, lead, tin, europium, and lithium in fresh rock of the main intrusion (D. A. Lindsey, unpub. data, 1976). New mapping revealed that lava flows of similar composition underlie The Tetons, about 2 km south of the Staats (Monarch) mine. Taylor and Powers (1953) and Whelan (1965) mapped numerous other areas of rhyolite in the Staats (Monarch) mine—Blawn Mountain area, but at least some of these are of Oligocene age (Bushman, 1973).

Erickson and Dasch (1963) mapped two plugs of alkalic rhyolite in the southern Shauntie Hills. These are intrusive into volcanic rocks that they correlated with the Isom Formation, but recent mapping (fig. 3) shows that these rocks belong to a local sequence of Tertiary lava flows and volcanic mudflow breccia of intermediate composition. The southern of the two rhyolite plugs, near Dead Horse Reservoir, yielded a new K-Ar age of 11.6 m.y. (table 1). The plugs are here called the rhyolite of Dead Horse Reservoir.

A deeply eroded dome and possible lava flows of alkalic rhyolite yielded a new K-Ar age of 10.3 m.y. (table 1). It is here called the rhyolite of Thermo hot springs area. It forms two small hills about 3 km east of the hot springs, in the Escalante Desert between the Shauntie Hills and the Black Mountains (fig. 3). Most rhyolite is devitrified, the exception being a vitrophyre zone on the southwestern part of the rhyolite exposures (table 2). The Thermo hot springs area is the site of a KGRA. The hot springs occur in two en echelon north-trending silica mounds controlled by Quaternary north-striking fractures, probably faults (Petersen, 1973). East-striking faults east of the hot springs cut Quaternary surficial deposits, including Pleistocene shorelines of the Escalante arm of Lake Bonneville. Thus an

TABLE 1.—Analytical data for K-Ar ages for alkalic rhyolites along the Blue Ribbon lineament

[Decay constants for K<sup>40</sup>:  $\lambda = 0.581 \times 10^{-10} \text{ yr}^{-1}$ ,  $\lambda_{\beta} = 4.963 \times 10^{-10} \text{ yr}^{-1}$ ; atomic abundance:  $K^{40}/K = 1.167 \times 10^{-4}$ ; \*Ar<sup>40</sup>=radiogenic argon; mineral analyzed for all samples: sanidine; potassium determinations made with Instrumentation Laboratories flame photometer with a Li internal standard]

Location of rhyolite	Sample No.	Locality		K <sub>2</sub> O		*Ar <sup>40</sup>	*Ar <sup>40</sup>	Age
		Lat N.	Long W.	(percent)		x10 <sup>-10</sup>	(percent)	(m.y. ±2σ)
Staats mine-----	ST-R	38°14'45"	113°34'45"	8.86,	8.84	2.582	74.0	20.2±0.86
Dead Horse Reservoir--	75L-14A	38°14'25"	113°14'25"	10.44,	10.37	1.755	87.2	11.6±0.46
Thermo hot springs----	75L-13A	38°10'30"	113°9'50"	9.11,	9.04	1.347	82.0	10.3±0.40
Blue Ribbon Summit----	75L-12	38°10'10"	112°50'25"	8.96,	8.94	.950	50.2	7.4±0.40

TABLE 2.—Modal data and petrographic descriptions of rhyolites along the Blue Ribbon lineament

[1,000 points or more counted on thin sections; --- = not present]

Mineral	Modes (volume percent)						
	Staats mine <sup>1</sup>	Dead Horse Reservoir <sup>2</sup>	Thermo hot springs <sup>3</sup>	Muddy Hill <sup>4</sup>	Blue Ribbon Summit <sup>5</sup>	Teddys Valley <sup>6</sup>	Phonolite Hill <sup>7</sup>
Plagioclase-----	2.9	5.9	0.3	---	1.1	0.1	2.9
Quartz-----	1.3	7.6	.9	Trace	1.7	---	Trace
K-feldspar-----	7.8	5.7	.5	6.7	1.9	---	.4
Biotite-----	.1	1.0	Trace	.4	.1	---	---
Hornblende-----	---	---	.3	Trace	Trace	---	---
Pyroxene-----	---	---	---	---	---	.3	---
Sphene-----	---	.1	---	---	---	---	---
Opaque minerals--	.1	.5	Trace	.4	.1	---	Trace
Groundmass-----	87.8	79.2	97.9	89.5	95.1	99.6	96.5
Xenoliths-----	---	---	---	2.9	---	---	.1

<sup>1</sup>Devitrified flow-foliated rhyolite containing vapor-phase minerals and some feldspar microlites.

<sup>2</sup>Devitrified resistant, locally vesicular pink rhyolite from a plug with a diameter of about 1/2 km.

<sup>3</sup>Average of 2 thin sections. Obsidian and mostly devitrified flow-foliated rhyolite containing feldspar microlites and vapor-phase minerals.

<sup>4</sup>Average of 5 thin sections. Devitrified poorly welded tuff structure. Some specimens contain vapor-phase minerals. Scattered ash-flow tuff, dikes, plugs, and volcanic mudflow breccia at and near Muddy Hill (2 km southeast of Minersville).

<sup>5</sup>Average of 5 thin sections. Mostly devitrified flow-foliated rhyolite. Some specimens contain bands of slightly devitrified rhyolite alternating with bands of lighter colored devitrified rhyolite. Some specimens contain feldspar microlites, and some contain vesicles and spherulites. One specimen is of slightly devitrified perlitic glass. Two specimens from dikes 3 km south of Blue Ribbon Summit, other two from dome at Blue Ribbon Summit.

<sup>6</sup>Mostly devitrified flow-foliated rhyolite that is somewhat vesicular and contains feldspar microlites.

<sup>7</sup>Average of 5 thin sections, given in Rowley (1968, p. 319-321); chemical analyses of two specimens also in Rowley (1968, p. 44-49). Mostly flow-foliated rhyolite containing bands of slightly devitrified rhyolite alternating with bands of lighter colored devitrified vesicular and amygdular spherulitic rhyolite. One sample essentially nondevitrified perlitic glass; another an intrusive breccia. Four specimens from Phonolite Hill, and one from basal glass of a lava flow on the eastern flank of the southern Sevier Plateau north of Kingston Canyon.

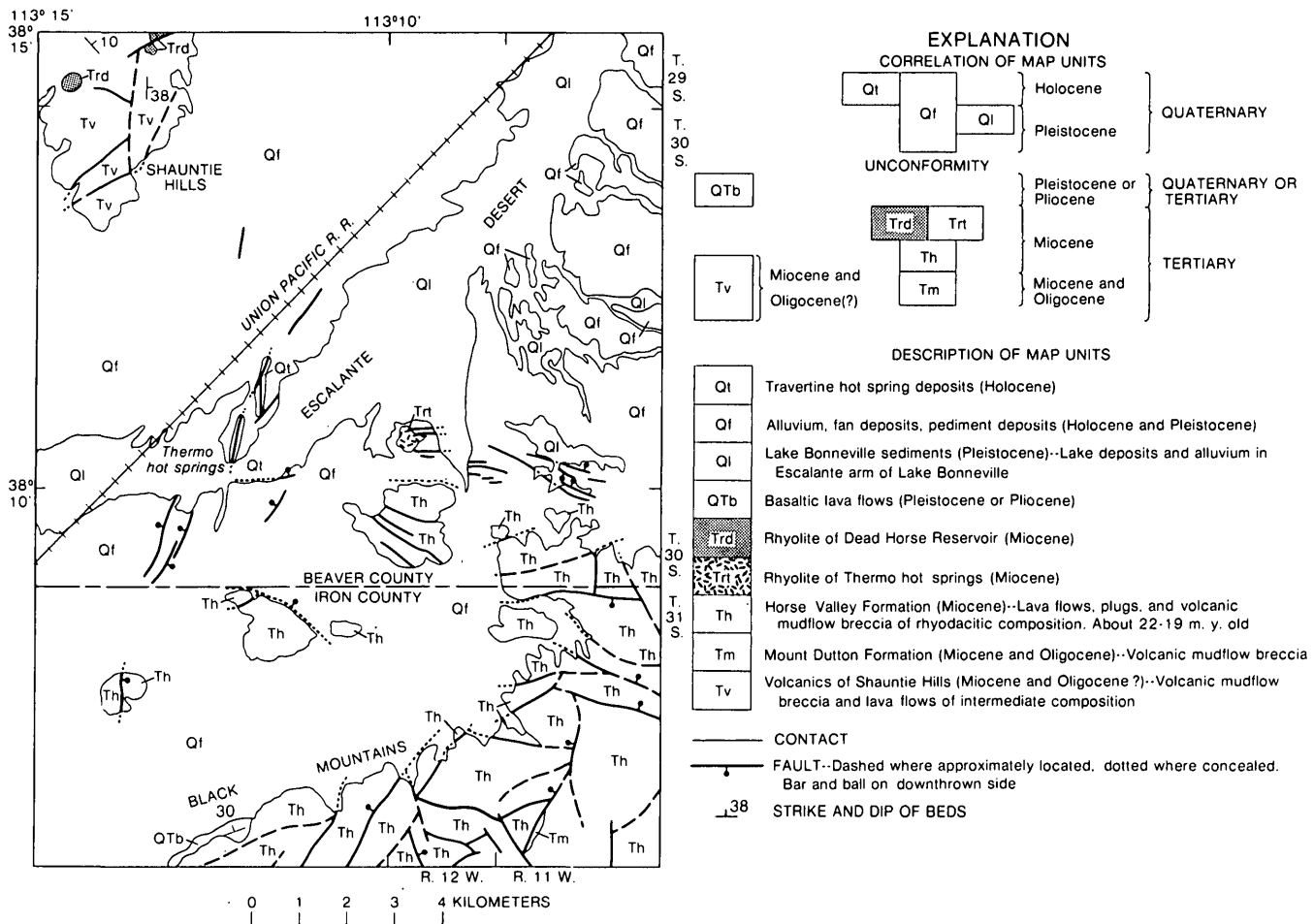


FIGURE 3.—Preliminary geologic map of Thermo hot springs area and southern Shauntie Hills (P. D. Rowley, unpub. data, 1975) showing distribution of alkalic rhyolite (Trd, Trt). Note east-trending faults at the latitude of the hot

springs and of the rhyolite of Thermo hot springs. See Anderson and Rowley (1975) and Fleck, Anderson, and Rowley (1975) for additional details.

orthogonal system of faults appears to control the hot springs (Rowley and Lipman, 1975); this interpretation is supported by geophysical studies by the University of Utah (Robert Sawyer, oral commun., 1977).

About 10-15 km south and southeast of the Thermo hot springs area, in the northwestern Black Mountains (Anderson and Rowley, 1975), stratovolcano sources for rhyodacitic volcanic mudflow breccia, plugs, and lava flows of the Horse Valley Formation (22-19 m.y. old) are exposed.

Most volcanic rocks (volcanic mudflow breccia and lava flows) lying north of the canyon east of Minersville and extending south through the Black Mountains belong to the Mount Dutton Formation (26-20 m.y. old). One source for these volcanic rocks of intermediate composition is a dacitic(?) plug, the apparent core of a stratovolcano, at Black Mountain, about 4 km southeast of Minersville. A major N. 10° W.-striking fault that passes through Minersville and

partly coincides with several centers of silicic tuff south and southeast of Minersville postdates the Miocene dacitic to andesitic rocks; this silicic tuff here is called the rhyolite(?) of Muddy Hill (table 2). Dotson's warm spring (Mundorff, 1970, p. 43) on the eastern outskirts of Minersville lies along a major north-trending fault zone. Lee (1908) noted silica mounds, indicative of former hot springs, near North Spring about 5.5 km north of Minersville, and Earl (1957) recorded sulfurous fumes and warm water at Oak Spring nearly 1 km northeast of North Spring.

Blue Ribbon Summit, in the northern Black Mountains about 9 km southeast of Minersville, is underlain by a dome and lava flows of alkalic rhyolite (fig. 4) that are partly covered by basalt lava flows (Anderson and Rowley, 1975, p. 37). The rhyolite yielded a new K-Ar age of 7.4 m.y. (table 1). Alkalic rhyolite also is exposed less than 3 km south-southeast of Blue Ribbon Summit. These rocks, here called the rhyolite of Blue

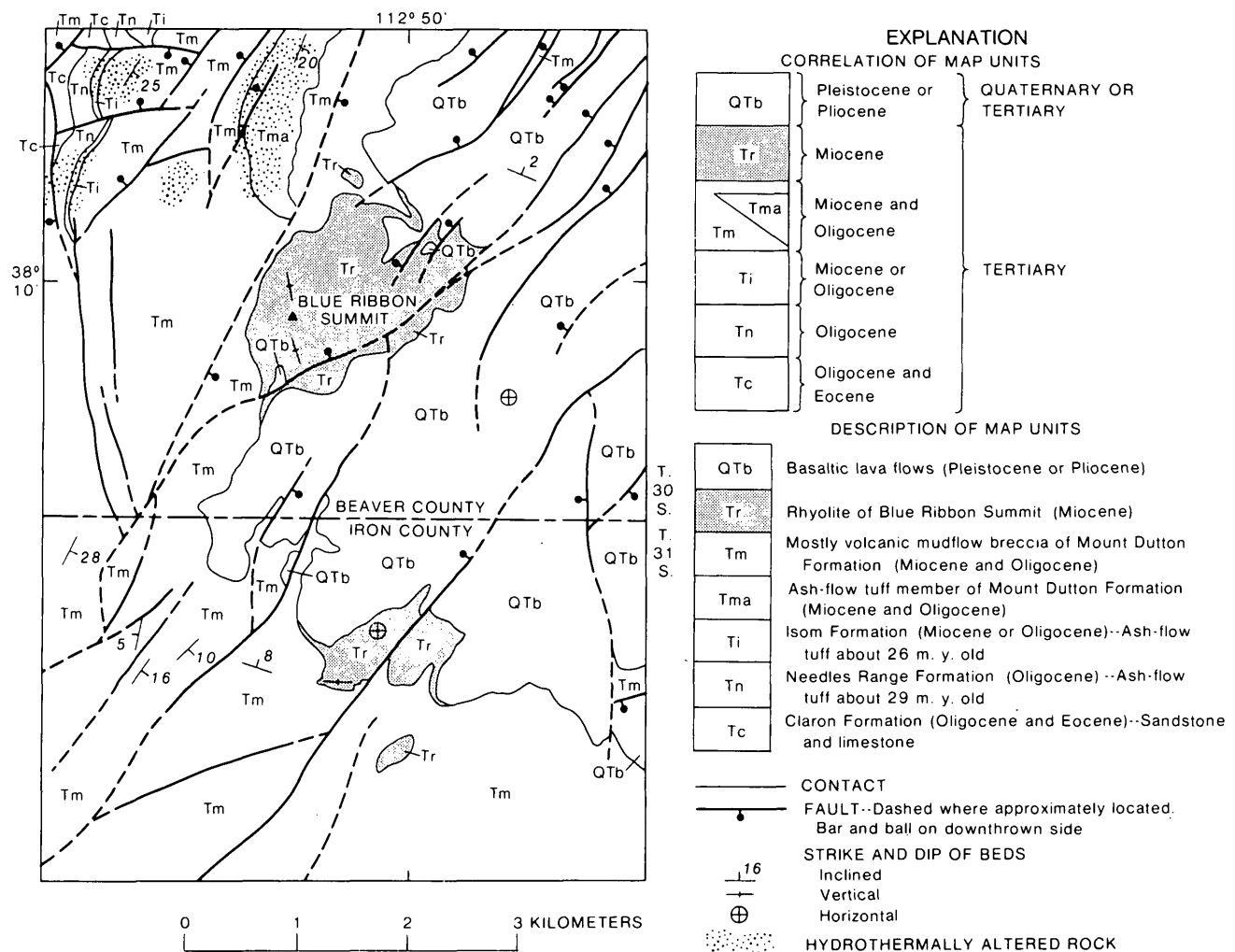


FIGURE 4.—Preliminary geologic map of the Blue Ribbon Summit area, northern Black Mountains (P. D. Rowley, unpub. data, 1975), showing distribution of alkalic rhyolite (Tr). See Anderson and Rowley (1975) and Fleck, Anderson, and Rowley (1975) for additional details.

Ribbon Summit, are mostly perlite and devitrified rhyolite; obsidian is rare (table 2). Vents of alkalic basalt lie 1–2 km east of Blue Ribbon Summit. The rhyolite and basalt are cut by north-northeast-striking faults, most with displacements of less than 50 m.

A dissected rhyolite dome, the rhyolite of Teddys Valley, occurs in a similar geologic setting, and of an assumed similar age, 10 km east of Blue Ribbon Summit (table 2). It covers an area of about 0.2 km<sup>2</sup> just north of Teddys Valley and is partly covered by basalt that is transected by north-northeast-striking faults.

Nevershine Hollow, draining north, and Fremont Wash, draining south, separate the Black Mountains on the west from the Tushar Mountains and Markagunt Plateau on the east. Dacitic, coarsely porphyritic lava flows of the Beaver Member (25 m.y. old) of the Mount Dutton Formation and their probable plutonic source were mapped by Anderson and Rowley (1975)

east and west, respectively, of Nevershine Hollow. East of Nevershine Hollow, J. J. Anderson (unpub. data, 1976) mapped a small caldera less than 3 km in longest diameter that erupted a green poorly welded to non-welded silicic ash-flow tuff (Rowley and Anderson, 1975, p. 12). This rock is crystal poor except for abundant tiny hornblende crystals. The tuff, as well as caldera breccia and landslide breccia, occupies the inner sides of the caldera and the low grassy valley in the interior of the caldera. Some tuff also occurs in Nevershine Hollow. The caldera is cut by numerous youthful basin-range faults of relatively small displacement. The topographic expression of the caldera and the presence of the tuff exhumed from Nevershine Hollow argue that the caldera and tuff are young, probably Pliocene or late Miocene, and thus the tuff is roughly correlative in age with other rhyolites along the lineament.

A very large positive magnetic anomaly (Eppich, 1973; Zietz, Shuey, and Kirby, 1976) underlies the southern Tushar Mountains, on line with the Blue Ribbon lineament. Major vents of the Mount Dutton Formation, the Dry Hollow Formation (22 m.y. old), older basalt flows (22 m.y. old.), and perhaps younger (upper Cenozoic) basalt flows (Anderson and Rowley, 1975) occur on the lineament in the southern Tushar Mountains. The largest of these vent structures is identified by the presence of a large arcuate fault, convex southward, that was mapped by J. J. Anderson (unpub. data, 1974) on the southern side of Birch Creek Mountain near the southwestern side of the large positive magnetic anomaly. The fault is of major displacement that is down on the northern side and is considered to reflect collapse due to eruption of magma of the Mount Dutton Formation. The fault probably is the partial surface trace of a deeply eroded caldera, about 6 km in diameter, that is concealed on the western, northern, and eastern sides by basin-range faults and younger rocks. Locations of other nearby major vent complexes (J. J. Anderson, unpub. data, 1976) of the Mount Dutton Formation—marked by dike swarms and autoclastic flows and locally by hydrothermally altered rocks—include the following areas: Circleville Canyon (Rowley and Anderson, 1975, p. 25), two places about 4 km west and west-southwest of Circleville, two places about 12 km east of Nevershine Hollow, and several places on the southeastern flank of the Tushar Mountains (Circleville Mountain and north) between the latitudes of Junction and Circleville (Douglas Kohout, unpub. data, 1972). A dike swarm vent area for older basalt flows occurs in Little Dog Valley about 14 km south-southwest of Circleville. A large laccolith of Oligocene age, the Spry pluton, and several inferred laccoliths of Miocene age occur in the northern Markagunt Plateau along the southern side of the Blue Ribbon lineament (Anderson and Rowley, 1975, p. 16–17, 38–39); the Spry pluton, in particular, forms a large positive aeromagnetic anomaly (Eppich, 1973, p. 38–39).

At the extreme eastern end of the lineament, extensive alkalic rhyolite occurs in the eastern Kingston Canyon area of the southern Sevier Plateau. Here three plugs of alkalic rhyolite underlie an area of 1 km<sup>2</sup> near the bottom of the canyon, and lava flows of alkalic rhyolite about 300 m thick underlie an area of 36 km<sup>2</sup> on the Sevier Plateau north of the canyon and in Grass Valley east of the plateau (Rowley, 1968, pl. 1; Rowley and Anderson, 1975, p. 27). A pronounced positive anomaly, shown on the aeromagnetic map (fig. 1A), under the rhyolite suggests the presence of a shallow intrusive body beneath the anomaly. The

possibility of a shallow intrusive body is suggested because rhyolite lavas, in general, are magnetically benign and rarely give rise to pronounced magnetic anomalies (G. D. Bath, oral commun., 1976). The largest rhyolite plug in Kingston Canyon, probably a main vent for the lava flows, was pictured by Dutton (1880) in his classic report and the rock was named phonolite, although Dutton noted that the samples he collected were too altered for microscopic examination. Chemistry and petrography clearly show that the plugs and flows are mostly devitrified rhyolite (table 2); minor obsidian at the intrusive contacts of the plug and at the base of the flows, as well as perlite, composes some of the rock. On the basis of petrographic similarity, the rhyolite in Kingston Canyon was correlated (Rowley, 1968; Anderson and Rowley, 1975) with the Mount Belknap Rhyolite, which has a K-Ar age of about 21–17 m.y. (Bassett and others, 1963; Cunningham and Steven, 1977; Steven and others, 1977). The rhyolite in Kingston Canyon may be considerably younger than the Mount Belknap Rhyolite, however. The rhyolite of the plugs and lava flows is here called informally the rhyolite of Phonolite Hill.

Most dacitic to andesitic volcanic centers along the Blue Ribbon lineament probably are late Oligocene to middle Miocene (27–20 m.y.) in age, in keeping with the middle Tertiary volcanic sequence that characterizes this part of Utah (Anderson and Rowley, 1975). The four dated centers of alkalic rhyolite along the Blue Ribbon lineament, however, are revealed to be middle to late Miocene (20–7 m.y.) in age, generally correlative in age with the upper Tertiary and Quaternary sequence that roughly coincides with basin-range faulting (Anderson and Rowley, 1975; Rowley and others, 1977). The four rhyolite centers get progressively younger toward the east. Hamblin and Best (1975) and Best and Brimhall (1974), among other workers, observed a similar eastward progression of ages in upper Cenozoic basalt centers in extreme southwestern Utah and northwestern Arizona. They attributed the progression to an eastward migration of basin-range block faulting.

### Topographic and structural features

The Blue Ribbon lineament is marked by gross east-trending topographic and structural patterns. The mountains are both topographically and structurally higher on the northern side of the lineament than on the southern side. In fact, the south-facing step in topography is similar in trend, amplitude, and facing direction to that of the lineament at 37° N. (G. P.

Eaton, written commun., 1976). East-striking faults, rare in this part of the Great Basin where most faults strike north-northwest to north-northeast, also characterize the lineament. South of the lineament, east-striking faults are rare or nonexistent. Topographic and structural features are discussed from west to east.

The long linear north-trending Mountain Home Range and Wah Wah Mountains and intervening Pine Valley are broken up within and south of the lineament into a series of scattered hills with no clear trend and with no major valley separating them (fig. 1A). However, these hills form a block of east-trending high ground that is nearly continuous with the Black Mountains and High Plateaus to the east (fig. 1A). Paleozoic rocks are exposed widely in the Mountain Home Range and Wah Wah Mountains north of the lineament, but are exposed only sparsely south of it; this suggests that the northern area is structurally higher than the southern area. Taylor and Powers (1953) and Hintze (1963) mapped east-striking faults in the mountains north of Indian Peak and north of the Staats (Monarch) mine-Blawn Mountain area. Landsat images clearly show large east-trending linear features, presumably faults, just south of Indian Peak and the Staats (Monarch) mine-Blawn Mountain area.

The Shauntie Hills and other hills forming the southern end of the San Francisco Mountains terminate abruptly on the northern side of the lineament (fig. 1A). Paleozoic rocks are widely exposed in these areas. Many east-striking faults are mapped (Hintze, 1963) through these hills, and are considered by Baer (1962) to be younger than the faults with northerly trends, even though younger(?) uplift of these hills seems to be more strongly influenced by north-striking faults.

A deep east-trending canyon along the lineament east of Minersville separates the low Black Mountains to the south from the high Mineral Mountains to the north. The northern edge of the Black Mountains has an easterly trend for over 50 km. A major north-trending fault zone, which terminates the western side of the Mineral Mountains, offsets the easterly trend of the northern Black Mountains at Minersville; the northern flank of the eastern Black Mountains is 6 km north of the northern flank of the western Black Mountains. The southern part of the Mineral Mountains has a general plunge to the south, and Paleozoic and Mesozoic rocks, abundant to the north, are exposed in only a few small areas in the northernmost Black Mountains. The southern Mineral Mountains and northern Black Mountains are broken into scores of small blocks by the intersection of northerly and easterly faults. Numerous east-striking faults occur in the southern

Mineral Mountains and northern Black Mountains (Hintze, 1963; P. D. Rowley, unpub. data, 1976). They are confined to an east-trending zone that extends from about 10 km north to about 6 km south of Minersville. A major east-striking fault zone (Earll, 1957; Hintze, 1963) passes through the Mineral Mountains about 10 km north of Minersville, at the northern side of the lineament. The area north of the fault zone has been uplifted more than 350 m (Earll, 1957, p. 67) relative to the southern side. The huge, young Mineral Mountains batholith is on the northern side of the fault zone. At least some east-striking faults, as in the Escalante Desert north of the western Black Mountains, are clearly Quaternary (fig. 3). A swarm of north-striking faults, extending eastward in the valley between Minersville Reservoir and Beaver, are also Quaternary (J. J. Anderson and P. D. Rowley, unpub. data, 1976).

The lineament crosses the Wasatch Front near Beaver and passes along the southern edge of the Tushar Mountains, which range in altitude from 3000 to more than 3400 meters, and along the northern edge of the lower Markagunt Plateau, which ranges in altitude from 2100 to 2600 m. The Tushar Mountains are much higher structurally than the Markagunt Plateau; Mesozoic rocks are exposed in the former but not the latter area. The abrupt south-facing scarp between the southern Tushar Mountains and northern Markagunt Plateau (at the southern side of the lineament) probably was not caused by east-striking faults. For the Tushar Mountains, however, vertical offset along northerly striking faults certainly was much greater and the type of faulting was different; horsts and grabens characterize the northern Markagunt Plateau, but a single giant horst forms the Tushar Mountains. Intersecting north-northeast- and north-northwest-striking faults produce rhombic blocks along the south-facing mountain front; these are believed to reflect twisting due to different senses of tilting between the Markagunt Plateau and Tushar Mountains (P. D. Rowley and J. J. Anderson, unpub. data, 1976), along the Blue Ribbon lineament. On the southern side of the lineament, Anderson (1965, 1971) mapped major east-striking faults, about 24 m.y. old, that controlled part of the distribution of rocks of the lower Miocene Buckskin Breccia and Bear Valley Formation.

Near its eastern end, the lineament underlies the 1200-m-deep Kingston Canyon, where an east-flowing antecedent stream crosses the Sevier Plateau. The Sevier Plateau is slightly higher north of Kingston Canyon than it is south of the canyon. The western end of the canyon is incised in fault blocks of the Sevier fault zone. The Sevier fault zone, along which the western side of the Sevier Plateau is uplifted, consists

of en echelon faults that strike north-northeast south of the Blue Ribbon lineament and north-northwest north of the lineament (Rowley, 1968). These two sets of faults intersect and produce a rhombic pattern of fault blocks in the eastern Kingston Canyon region. A similar, but mirror image, zone of intersecting faults occurs 40 km to the north (P. D. Rowley and J. J. Anderson, unpub. data, 1976) at the eastern end of the canyon of Clear Creek and the northern edge of the Pioche mineral belt and on the east-trending lineament at lat 38°30' N. Just west of Clear Creek, Crosby (1973) and Cook and Montgomery (1974) postulated right-lateral offset of the Wasatch Front along a hypothetical east-trending transverse fault.

### Mineralized and hydrothermally altered areas

Mineralized and hydrothermally altered rocks are the major features in several areas along the Blue Ribbon lineament in Utah. Fluorine, uranium, and tungsten minerals are the most important additions. Many mineral occurrences along the lineament are in the youngest rocks and commonly occur near centers of relatively young alkalic rhyolite. In contrast, mineralized and hydrothermally altered rocks are essentially unknown south of the lineament in the Black Mountains, Markagunt Plateau, and Sevier Plateau. There is a good possibility that additional deposits of these or other minerals may be present at shallow depth along the lineament. For this reason the deposits and altered rock will be described in detail.

*Indian Peak mining district and vicinity.*—The Indian Peak mining district (also called Washington District) in the southern Mountain Home Range (fig. 1A) was a leading producer of fluor spar in southwestern Utah (Thurston and others, 1954) but now is largely inactive; uranium has also been reported in the district. The Cougar Spar mine is the main producer (Whelan, 1973). The rocks in the district consist largely of faulted and hydrothermally altered ash-flow tuff of the Oligocene Needles Range Formation (Bullock, 1976). Most fluor spar occurs as veins in and near breccia zones (Thurston and others, 1954). The deposits may accompany or postdate rhyolite or one or more Tertiary porphyritic plutons that have been mapped in the area (Thurston and others, 1954; Hintze, 1963; Bullock, 1976).

*Staats (Monarch) mine—Blawn Mountain area.*—The Staats (Monarch) mine and Blawn Mountain area, also known as the Pine Grove mining district, in the southern Wah Wah Mountains (fig. 1A), has been an intermittent minor producer of fluor spar and lesser uranium and base metals for many years. Fluor spar at the Staats (Monarch) mine occurs as lenticular shoots

in the faulted, brecciated, and hydrothermally altered contact between alkalic rhyolite and lower Paleozoic carbonates (Thurston and others, 1954; Whelan, 1965, 1973; Bullock, 1976). Uranium (uraninite, autunite, uranophane, and metatorbernite) occurs as impregnations and coatings on fluorite (Whelan, 1965). At Blawn Mountain, Whelan (1965) mapped intensely hydrothermally altered rock (kaolinite, alunite, silica) and minor mineralized rock (iron, uranium, fluorine) at the contact between Tertiary rhyolite and lower Paleozoic carbonates and quartzites. Alunite resources, perhaps related to ancient hot springs, recently have been discovered in and north of the Blawn Mountain area (William Walker, Earth Sciences, Inc., oral commun., 1976). Intensely hydrothermally altered rocks occur about 15 km east-southeast of the Staats (Monarch) mine (R. K. Glanzman, oral commun., 1976).

*Shauntie Hills.*—All rocks in the southern Shauntie Hills (fig. 3) are hydrothermally altered and silicified to some degree, and the most intensely altered rocks are adjacent to plugs of the rhyolite of Dead Horse Reservoir, prompting Erickson and Dasch (1963) to suggest that at least some alteration is due to emplacement of the plugs. No detailed work has been done on the types and amounts of mineralized and altered rocks.

Significant mineralized and altered rocks are exposed elsewhere in the Shauntie Hills and areas to the north (Hintze and Whelan, 1973). For example, 7 km north of the rhyolite of Dead Horse Reservoir, Stringham (1963) mapped an 11- by 2-km east-trending belt of mineralized rocks (sulfur related to former hot-spring activity, uranium minerals, and hematite) and hydrothermally altered rocks (mostly alunite, kaolinite, and silica). Undated rhyolite plugs occur north of the belt (Stringham, 1963, pl. 4; Erickson, 1973; P. L. Williams, oral commun., 1976) and may have produced some of the mineralized and altered rocks; mineralization postdates rock of the 24- to 21-m.y.-old Quichapa Group.

*Northern Black Mountains and southern Mineral Mountains.*—Local areas of intense hydrothermally altered rocks occur along the northern edge of the Black Mountains (Erickson and Dasch, 1963, 1968) but few introduced metals other than minor iron have been recorded. The Jarloose mining district (Erickson and Dasch, 1968), several kilometers southeast of Minersville, has several mines, but the type of mineral deposit is not known and apparently no ore was produced. The area is broadly hydrothermally altered at and outward from Black Mountain, which is underlain by a Tertiary dacitic plug. Probably this plug was a main vent for lava flows and volcanic mudflow breccia of the Mount Dutton Formation in this area, and the vent

area likely was the source of altered and sparsely mineralized rocks.

Most rocks near Minersville are mineralized and hydrothermally altered to some degree, and, as its name suggests, the town was a mining center during its early days. Copper staining is visible in rocks exposed below a dissected pediment about 1 km northeast of Minersville. Lincoln mining district, in the southern Mineral Mountains about 5 km north of Minersville, produced mostly lead, silver, and zinc. Bradshaw district, 8 km north of Minersville, produced tungsten, gold, silver, and lead. Granite district, about 13 km northeast of Minersville and continuing farther north along the eastern side of the Mineral Mountains, produced mostly tungsten (Hobbs, 1945; Earll, 1957); the beryllium mineral helvite was discovered in this district by Sainsbury (1962). Minor fluor spar also occurs in the Bradshaw and Granite districts (Bullock, 1976). Most minerals north of Minersville are contact-metamorphic and fissure-vein deposits that formed during intrusion of the young Mineral Mountains batholith.

*Southern Tushar Mountains and vicinity.*—Mineralized and hydrothermally altered rocks occur in most of the Tushar Mountains, including the southern end. One of these, in the southern Birch Creek Mountain area, was mentioned by Anderson and Rowley (1975, p. 28); it consists of intense hydrothermally altered rock, including silicified sandstone, in a north-northwest-trending zone at least 4 km long, and it postdates rocks of the Mount Dutton Formation. On the southern side of the Blue Ribbon lineament, cinnabar deposits, silicified rock, argillic altered rock, fluor spar, and other minerals have been reported (Doelling, 1975, p. 139-143) on the northwestern side of the Spry pluton.

*Eastern Kingston Canyon and vicinity.*—Kingston Canyon, cut in the southern Sevier Plateau, contains scattered patches of intense hydrothermally altered rocks, at least some of which are associated with rhyolite plugs (Rowley, 1968). Antimony and arsenic have been mined east of the town of Antimony (Doelling, 1975).

#### BLUE RIBBON LINEAMENT IN NEVADA

Because of our lack of firsthand knowledge of the geology of eastern Nevada and because of the absence of a detailed aeromagnetic map of this region, the extension of the Blue Ribbon lineament into Nevada is more speculative, and the discussion brief. At 113°30' W., in Utah, the southern branch of the Pioche magnetic ridge crosses the Blue Ribbon lineament and extends west-southwesterly into Nevada, where it terminates at the north-trending "quiet" magnetic zone

(Eaton, 1976; Stewart and others, 1977; Eaton, unpub. data, 1976) and at the western end of the Delamar-Iron Springs mineral belt of Shawe and Stewart (1976).

The northern branch of the aeromagnetic expression of the Pioche mineral belt (fig. 1), as shown on the generalized aeromagnetic map of Stewart, Moore, and Zietz (1977, fig. 5), extends westward into Nevada as far as 115° W., where it terminates at the quiet zone. The Blue Ribbon lineament coincides with the crest of this northern branch and is centered at about 38°10' N. A large east-trending magnetic high at 38°10' N. underlies the White Rock Mountains and Wilson Creek Mountains. The crest of this high, in the Wilson Creek Mountains, is overlain by a large area of rhyolite (Stewart and Carlson, 1975); the area has not been mapped in detail, but Tschanz and Pampeyan (1970) noted that glassy flows and significant reserves of perlite occur there, near the Hollinger mine. The magnetic high may reflect a pluton at depth.

The lineament passes through the southern edge of the next two ranges to the west, the Fairview and the Schell Creek; the area is underlain by a circular magnetic high, and rhyolites and east-striking faults are known at the surface (Tschanz and Pampeyan, 1970; Stewart and Carlson, 1974). The largest exposures of rhyolite are in the southern Fairview Range; here the rhyolite is described as perlitic pitchstone (Westgate and Knopf, 1932, p. 32) and is the site of one of Nevada's largest perlite mines (Tschanz and Pampeyan, 1970). A Tertiary granodiorite pluton is mapped in the southern Schell Creek Range (Tschanz and Pampeyan, 1970).

The north-trending magnetic quiet zone is just west of these ranges, from about 115° to 116° W. and no expression of the lineament can be seen on the gross aeromagnetic maps available. Even though aeromagnetic expression is not evident, the geology at the surface suggests that the lineament passes through the quiet zone. Thus large rhyolitic intrusive and extrusive masses underlie the Quinn Canyon Range at about 38° N. (Stewart and Carlson, 1974), and, from 38° to 38°25' N., the range is dotted by numerous mines which have produced fluorine, uranium, and tungsten, and which contain occurrences of beryllium (U.S. Geological Survey, Nevada Bureau of Mines, 1964; Shawe, 1966; Sainsbury and Kleinhampl, 1969; Tschanz and Pampeyan, 1970). Just west of the Quinn Canyon Range, at 38°10' N., is the eastern end of the Warm Springs lineament of Ekmen and others (1976); here the Warm Springs lineament exhibits interruptions of aeromagnetic anomalies (U.S. Geological Survey, 1968).

## CONCLUSIONS

Although the genesis of east-trending mineralized structural belts in the eastern Great Basin is poorly known, it is possible to draw a modest set of conclusions from the observations on the Blue Ribbon lineament. The lineament is a fault zone, as indicated by alinement of topographic features, alinement with aeromagnetic contours, and coincidence with major high-angle faults. Although at least some major faults of the Warm Springs lineament have strike-slip movement (Ekren and others, 1976), only dip-slip movement is known for major faults along the Utah portion of the Blue Ribbon lineament. The lower topography and structure south of the lineament indicates that cumulative throw is down to the south. Major post basin-range transcurrent movement is not indicated along the lineament in Utah because the basins and ranges and related structures are not known to be offset laterally. Strike-slip movement along the lineament might have occurred prior to about 20 m.y. ago, however. Alternately, the Blue Ribbon lineament in Utah may be an incipient strike-slip fault. This is suggested by a general similarity between the fault patterns along the Blue Ribbon lineament and those Riedel shear patterns of "peak structure" illustrated by Tchalenko (1970, fig. 9). East-striking faults of the Blue Ribbon lineament are rare east of the Wasatch Front, indicating that the fault system dies out eastward.

The age of the lineament is unknown, but igneous and (or) hydrothermal activity along the lineament started 20 m.y. ago or earlier and continued to at least as late as 7 m.y. ago, as indicated by new K-Ar ages of rhyolites, and probably to as young as Holocene, as suggested by the presence of past and present hot springs. Thus it has been a persistent geologic feature. Furthermore, it is generally coincident with extensional rifting of the eastern Great Basin. Rhyolite and basalt along the lineament, for example, are correlated with Anderson and Rowley's (1975) upper Tertiary and Quaternary sequence (20 m.y. to present), which is generally synchronous with basin-range development in this part of Utah (Rowley and others, 1977) and with young extensional tectonics in the western United States (Christiansen and Lipman, 1972). Some features on the lineament, however, belong to the middle Tertiary sequence (Anderson and Rowley, 1975), and still others may date to early Tertiary or older.

The lineament fracture system extends to a depth where partial melting and fractionation of the rhyolite magma occurred. As the magma rose along the

fracture system and the pressure decreased, metal-laden hydrothermal fluids were released. Thus the lineament should serve as a guide to mineral exploration because it marks the locus of a fracture system that controlled the migration of mineralizing solutions.

The larger mechanism of control of such faults is open to question, but Stewart, Moore, and Zietz (1977) hypothesized that east-trending features may be due to east-trending warps in the subducting mantle plate, and credited one of us (Lipman) with preliminary suggestion of the idea. Another possible explanation is that the Blue lineament was or is part of an intracontinental transform fault, which extends from a zone of clear strike-slip faulting (Warm Springs lineament) eastward along strike to the forerunning fracture zone and from there to die out in the Colorado Plateaus province. The K-Ar ages of rhyolites suggest that at least some parts of the fault system are younger eastward, in keeping with recent ideas on the eastward expansion of the eastern Great Basin (Best and Hamblin, 1977). The Blue Ribbon lineament is parallel with the general worldwide pattern of transform faults (Moore, 1973). At right angles to the lineament, classical northerly trending basin-range faults of the same age as the lineament occur in the extension direction, analogous to the trend in the extension direction of spreading lines in an ocean basin and rifts on a continent where they are parallel to and above the typical (Moore, 1973) north-trending spreading ocean ridge. Both hypotheses need considerable further testing, however, and resolution of the genesis of east-trending features in the Great Basin must await new studies.

## REFERENCES CITED

- Anderson, J. J., 1965, Geology of northern Markagunt Plateau, Utah: Austin, Texas Univ., Ph. D. dissert., 194 p.
- , 1971, Geology of the southwestern High Plateaus of Utah; Bear Valley Formation, an Oligocene-Miocene volcanic arenite: *Geol. Soc. America Bull.*, v. 82, no. 5, p. 1179-1205.
- Anderson, J. J., and Rowley, P. D., 1975, Cenozoic stratigraphy of southwestern High Plateaus of Utah, in Anderson, J. J., Rowley, P. D., Fleck, R. J., and Nairn, A. E. M., *Cenozoic geology of southwestern High Plateaus of Utah: Geol. Soc. America Spec. Paper 160*, p. 1-52.
- Armstrong, R. L., 1970, Geochronology of Tertiary igneous rocks, eastern Basin and Range Province, western Utah, eastern Nevada, and vicinity, U.S.A.: *Geochim. et Cosmochim. Acta*, v. 34, no. 2, p. 203-232.
- Baer, J. L., 1962, Geology of the Star Range, Beaver County, Utah: Brigham Young Univ. Geology Studies, v. 9, pt. 2, p. 29-52.
- Bassett, W. A., Kerr, P. F., Schaeffer, O. A., and Stoenner, R. W., 1963, Potassium-argon dating of the late Tertiary

- volcanic rocks and mineralization of Marysvale, Utah: *Geol. Soc. America Bull.*, v. 74, p. 213-220.
- Best, M. G., and Brimhall, W. H., 1974, Late Cenozoic alkalic basaltic magmas in the western Colorado Plateaus and the Basin and Range transition zone, U.S.A., and their bearing on mantle dynamics: *Geol. Soc. America Bull.*, v. 85, no. 11, p. 1677-1690.
- Best, M. G., and Hamblin, W. K., 1977, Origin of the Basin Range-implications from the geology of its eastern boundary, in Smith, R. B., and Eaton, G. P., eds., *Cenozoic tectonics and regional geophysics of the western United States*: *Geol. Soc. America Mem.* (In press.)
- Bingler, E. C., 1971, Major east-west lineament in west-central Nevada: *Geol. Soc. America Abs. with Programs*, v. 3, no. 2, p. 83.
- Blank, H. R., Jr., and Mackin, J. H., 1967, Geologic interpretation of an aeromagnetic survey of the Iron Springs district, Utah: *U.S. Geol. Survey Prof. Paper* 516-B, 14 p.
- Bullock, K. C., 1976, Fluorite occurrences in Utah: *Utah Geol. and Mineral Survey Bull.* 110, 89 p.
- Bushman, A. V., 1973, Pre-Needles Range silicic volcanism, Tunnel Spring Tuff (Oligocene), west-central Utah: *Brigham Young Univ. Geol. Studies*, v. 20, pt. 4, p. 159-190.
- Butler, B. S., Loughlin, G. F., Heikes, V. C., and others, 1920, The ore deposits of Utah: *U.S. Geol. Survey Prof. Paper* 111, 672 p.
- Callaghan, Eugene, 1939, Volcanic sequence in the Marysvale region in southwest-central Utah: *Am. Geophys. Union Trans.*, 20th Ann. Mtg., Washington 1939, pt. 3, p. 438-452.
- 1973, Mineral resources potential of Piute County, Utah and adjoining area: *Utah Geol. and Mineralog. Survey Bull.* 102, 135 p.
- Callaghan, Eugene, and Parker, R. L., 1962, Geology of the Sevier quadrangle Utah: *U.S. Geol. Survey Geol. Quad. Map* GQ-156.
- Christiansen, R. L., and Lipman, P. W., 1972, Cenozoic volcanism and paleo-tectonic evolution of the Western United States—pt. 2, Late Cenozoic: *Royal Soc. London Philos. Trans. A*, v. 271, p. 249-284.
- Cohenour, R. E., 1963, The beryllium of western Utah, in *Beryllium and uranium mineralization in western Jaub County, Utah*: *Utah Geol. Soc. Guidebook to the Geology of Utah*, no. 17, p. 4-7.
- 1970, Sheeprock granite, in Whelan, J. A., compiler, *Radioactive and isotopic age determinations of Utah rocks*: *Utah Geol. and Mineralog. Survey Bull.* 81, p. 31.
- Cook, E. F., 1960, Geologic atlas of Utah—Washington County: *Utah Geol. and Mineralog. Survey Bull.* 70, 119 p.
- Cook, K. L., and Montgomery, J. R., 1974, Crustal structure and east-west transverse structural trends in eastern Basin and Range province as indicated by gravity data: *Geol. Soc. America Abs. with Programs*, v. 6, no. 3, p. 158.
- Crosby, G. W., 1973, Regional structure in southwestern Utah, in Hintze, L. F., and Whelan, J. A., eds., *Geology of the Milford area, 1973*: *Utah Geol. Assoc. Pub.* 3, 27-32.
- Cunningham, C. G., and Steven, T. A., 1977, Mount Belknap and Red Hills calderas and associated rocks, Marysvale volcanic field, west-central Utah: *U.S. Geol. Survey Open-File Rept.* 77-568, 40 p.
- Doelling, H. H., 1975, Geology and mineral resources of Garfield County, Utah: *Utah Geol. Mineral Survey Bull.*, 107 p.
- Dutton, C. E., 1880, Report on the geology of the high plateaus of Utah: *U.S. Geol. Geol. Survey, Rocky Mtn. Region* (Powell), 307 p.
- Earll, F. N., 1957, Geology of the central Mineral Range, Beaver County, Utah: *Salt Lake City, Utah Univ.*, Ph. D. thesis, 112 p.
- Eaton, G. P., 1975, Characteristics of a transverse crustal boundary in the Basin and Range Province of southern Nevada: *Geol. Soc. America Abs. with Programs*, v. 7, no. 7, p. 1062.
- 1976, Fundamental bilateral symmetry of the western Basin and Range Province: *Geol. Soc. America Abs. with Programs*, v. 8, no. 5, p. 583.
- Ekren, E. B., Bucknam, R. C., Carr, W. J., Dixon, G. L., and Quinlivan, W. D., 1976 East-trending structural lineaments in central Nevada: *U.S. Geol. Survey Prof. Paper* 986, 16 p.
- Eppich, G. K., 1973, Aeromagnetic survey of south-central Utah: *Salt Lake City, Utah Univ.*, M.S. thesis, 78 p.
- Erickson, A. J., 1974, The Uinta-Gold Hill trend—an economically important lineament, in Hodgson, R. A., Gay, S. P., Jr., and Benjamins, J. Y., eds., *Proceedings of the First International Conference on the New Basement Tectonics*: *Utah Geol. Assoc. Pub.* 5, p. 126-138.
- Erickson, M. P., 1973, Volcanic rocks of the Milford area, Beaver County, Utah, in *Geology of the Milford area*: *Utah Geol. Assoc. Pub.* 3, p. 13-21.
- Erickson, M. P., and Dasch, E. J., 1963, Geology and hydrothermal alteration in northwestern Black Mountains and southern Shauntie Hills, Beaver and Iron Counties, Utah: *Utah Geol. and Mineralog. Survey Spec. Studies*, no. 6, 32 p.
- 1968, Volcanic stratigraphy, magnetic data and alteration, geologic map, and sections of the Jarloose mining district southeast of Minersville, Beaver County, Utah: *Utah Geol. Mineralog. Survey, Map* 26.
- Fleck, R. J., Anderson, J. J., and Rowley, P. D., 1975, Chronology of mid-Tertiary volcanism in High Plateaus region of Utah, in Anderson, J. J., Rowley, P. D., Fleck, R. J., and Nairn, A. E. M., *Cenozoic geology of southwestern High Plateaus of Utah*: *Geol. Soc. America Spec. Paper* 160, p. 53-62.
- Hamblin, W. K., and Best, M. G., 1975, The geologic boundary between the Colorado Plateau and the Basin Range Province: *Geol. Soc. America Abs. with Programs*, v. 7, no. 7, p. 1097.
- Hilpert, L. S., and Roberts, R. J., 1964, Geology—Economic geology, in *U.S. Geological Survey, Mineral and water resources of Utah*: *U.S. 88th Cong.*, 2d sess., p. 28-38.
- Hintze, L. F., 1963, Geologic map of southwestern Utah: *Salt Lake City, Utah Geol. and Mineralog. Survey.*
- Hintze, L. F., and Whelan, J. A., eds., 1973, *Geology of the Milford area, 1973*: *Utah Geol. Assoc. Pub.* 3, 94 p.
- Hobbs, S. W., 1945, Tungsten deposits in Beaver County, Utah: *U.S. Geol. Survey Bull.* 945-D, p. 81-111.
- Johnston, W. P., 1972, K-Ar ages of the Blind Mountain stock and Yuba dike, Lincoln County, Nevada: *Isochron/West*, no. 3, p. 30.
- Kennedy, R. R., 1963, Geology of Piute County, Utah: *Tucson, Arizona Univ.*, Ph.D. thesis, 282 p.
- Kerr, P. F., 1968, The Marysvale, Utah, uranium deposits, in *Ore deposits of the United States, 1933-1967* (Graton-

- Sales Volume): Am. Inst. Mining, Metall. and Petroleum Engineers, v. 2, p. 1020-1042.
- Kerr, P. F., Brophy, G. P., Dahl, H. M., Green, Jack, and Woolard, L. E., 1957, Marysvale, Utah, uranium area—Geology, volcanic relations, and hydrothermal alteration: Geol. Soc. America Spec. Paper 64, 212 p.
- Krueger, H. W., and Schilling, J. H., 1971, Geochron/Nevada Bureau of Mines K/Ar age determinations—list 1: Isochron/West, no 71-1, p. 9-14.
- Lee, W. T., 1908, Water resources of Beaver Valley, Utah: U.S. Geol. Survey Water Supply Paper 217, 57 p.
- Liese, H. C., 1957, Geology of the northern Mineral Range, Millard and Beaver Counties, Utah: Salt Lake City, Utah Univ. M.S. thesis, 88 p.
- Lindsey, D. A., Ganow, Harold, and Mountjoy, Wayne, 1973, Hydrothermal alteration associated with beryllium deposits at Spor Mountain, Utah: U.S. Geol. Survey Prof. Paper 818-A, 20 p.
- Lindsey, D. A., Naeser, C. W., and Shawe, D. R., 1975, Age of volcanism, intrusion, and mineralization in the Thomas Range, Keg Mountain, and Desert Mountain, western Utah: U.S. Geol. Survey Jour. Research, v. 3, no. 5, p. 597-604.
- Lipman, P. W., Rowley, P. D., and Pallister, J. S., 1975, Pleistocene rhyolite of the Mineral Range, Utah—geothermal and archeological significance: Geol. Soc. America Abs. with Programs, v. 7, no. 7, p. 1173.
- Lipman, P. W., Rowley, P. D., Mehnert, H. H., Evans, S. H., Jr. Nash, W. P., and Brown, F. H., 1978, Pleistocene rhyolite of the Mineral Mountains, Utah—Geothermal and archeological significance: U.S. Geol. Survey Jour. Research, v. 6, no. 1, p. 133-147.
- Loring, A. K., 1972, Temporal and spatial distribution of basin-range faulting in Nevada and Utah: Los Angeles, Southern California Univ., M.S. thesis, 163 p.
- Mehnert, H. H., Rowley, P. D., and Lipman, P. W., 1977, K-Ar ages and geothermal implications of young rhyolites in west-central Utah: Isochron/West. (In press.)
- Miller, G. M., 1966, Structure and stratigraphy of southern part of Wah Wah Mountains, southwest Utah: Am. Assoc. Petroleum Geol. Bull., v. 50, p. 858-900.
- Moore, G. W., 1973, Westward tidal lag as the driving force of plate tectonics: Geology, v. 1, no. 3, p. 99-100.
- Mundorff, J. C., 1970, Major thermal springs of Utah: Utah Geol. and Mineralog. Survey Water-Resources Bull. 13, 60 p.
- Park, G. H., 1968, Some geochemical and geochronologic studies of the beryllium deposits in western Utah: Salt Lake City, Utah Univ., M. S. thesis, 91 p.
- Petersen, C. A., 1973, Roosevelt and Thermo hot springs, Beaver County, Utah, in Hintze, L. F., and Whelan, J. A., eds., Geology of the Milford area, 1973: Utah Geol. Assoc. Pub. 3, p. 73-74.
- Roberts, R. J., 1964, Economic geology, in Mineral and water resources of Nevada: U.S. 88th Cong., 2d sess., Senate Doc. 87, p. 39-48.
- 1966, Metallogenic provinces and mineral belts in Nevada, in AIME Pacific Southwest Mineral Industry Conf., Sparks, Nev., 1965, Papers, pt. A: Nevada Bur Mines Rept. 13, pt. A, p. 47-72.
- Rowley, P. D., 1968, Geology of the southern Sevier Plateau, Utah: Austin, Texas Univ. Ph.D. thesis, 385 p.
- Rowley, P. D., and Anderson, J. J., 1975, Guidebook to the Cenozoic structural and volcanic evolution of the southern Marysvale volcanic center, Iron Springs mining district, and adjacent areas, southwestern Utah—Geol. Soc. America Ann. Mtg., Salt Lake City, Utah, 1975, Field Trip 2: Gamma Zeta Chapter, Sigma Gamma Epsilon, Kent State Univ., Kent, Ohio, 37 p.
- Rowley, P. D., and Lipman, P. W., 1975, Geologic setting of the Thermo KGRA (known geothermal resource area), Beaver County, Utah: Geol. Soc. America Abs. with Programs, v. 7, no. 7, p. 1254.
- Rowley, P. D., Anderson, J. J., Williams, P. L., and Fleck, R. J., 1977, Age of structural differentiation between the Colorado Plateaus and Basin and Range provinces in southwestern Utah: Geology (In press).
- Sainsbury, C. L., 1962, Helvite near Beaver, Utah: Am. Mineralogist, v. 47, nos. 3-4, p. 395-398.
- Sainsbury, C. L., and Kleinhampl, F. J., 1969, Fluorite deposits of the Quinn Canyon Range, Nevada: U.S. Geol. Survey Bull. 1272-C, 22 p.
- Shawe, D. R., 1966, Arizona-New Mexico and Nevada-Utah beryllium belts, in Geological Survey research 1966: U.S. Geol. Survey Prof. Paper 550-C, p. C206-C213.
- Shawe, D. R., and Stewart, J. H., 1976, Ore deposits as related to tectonics and magmatism, Nevada and Utah: Am. Inst. Mining, Metall., and Petroleum Engineers Trans., v. 260, p. 225-232.
- Steven, T. A., Cunningham, C. G., Naeser, C. W., and Mehnert, H. H., 1977, Revised stratigraphy and radiometric ages of volcanic rocks and mineral deposits in the Marysvale area, west-central Utah: U. S. Geol. Survey Open-File Rept. 77-569, 45 p.
- Stewart, J. H., and Carlson, J. E., 1974, Preliminary geologic map of Nevada: U.S. Geol. Survey Misc. Field Studies Map MF-609.
- Stewart, J. H., Moore, W. J., and Zietz, Isidore, 1977, East-west patterns of Cenozoic igneous rocks, aeromagnetic anomalies, and mineral deposits, Nevada and Utah: Geol. Soc. America Bull., v. 88, no. 1, p. 67-77.
- Stokes, W. L., 1963, Geologic map of northwestern Utah: Salt Lake City, Utah Geol. and Mineralog. Survey.
- Stringham, Bronson, 1963, Hydrothermal alteration in the southeast part of the Frisco quadrangle, Beaver County, Utah: Utah Geol. and Mineralog. Survey Spec. Studies, no. 4, 21 p.
- Taylor, A. O., and Powers, J. F., 1953, Reconnaissance geologic map of the Wah Wah Range, Beaver County, Utah: U.S. Geological Survey, open-file map.
- Tchalenko, J. S., 1970, Similarities between shear zones of different magnitudes: Geol. Soc. America Bull., v. 81, no. 6, p. 1625-1640.
- Thurston, W. R., Staatz, M. H., Cox, D. C., and others, 1954, Fluorspar deposits of Utah: U.S. Geol. Survey Bull. 1005, 53 p.
- Tschanz, C. M., and Pampeyan, E. H., 1970, Geology and mineral deposits of Lincoln County, Nevada: Nevada Bur. Mines Bull. 73, 188 p.
- U.S. Geological Survey, 1968, Aeromagnetic map of the Hot Creek Range region, south-central Nevada: U.S. Geol. Surveys Geophys. Inv. Map GP-637.

- U.S. Geological Survey, Utah Geological and Mineralogical Survey, 1964, Mineral and water resources of Utah: U.S. 88th Cong., 2d sess., Comm. rept., (Utah Geol. and Mineralog. Survey Bull. 73) 275 p.
- U.S. Geological Survey, Nevada Bureau of Mines, 1964, Mineral and water resources of Nevada: U.S. 88th Cong., 2d sess., Senate Doc. 87 (Nevada Bur. Mines Bull. 65), 314 p.
- Van Alstine, R. E., 1976, Continental rifts and lineaments associated with major fluorspar districts: *Econ. Geology*, v. 71, no. 6, p. 977-987.
- Walker, G. W., and Osterwald, F. W., 1963, Introduction to the geology of uranium-bearing veins in the conterminous United States, including sections on geographic distribution and classification of veins: U. S. Geol. Survey Prof. Paper 455-A, p. A1-A28.
- Westgate, L. G., and Knopf, Adolph, 1932, Geology and ore deposits of the Pioche district, Nevada: U.S. Geol. Survey Prof. Paper 171, 79 p.
- Whelan, J. A., 1965, Hydrothermal alteration and mineralization, Staats mine and Blawn Mountain areas, central Wah Wah Range, Beaver County, Utah: Utah Geol. and Mineralog. Survey Spec. Studies 12, 31 p.
- 1973, Mineral resources of the Milford area, Beaver County, Utah, in Hintze, L. F., and Whelan, J. A., eds., *Geology of the Milford area, 1973*: Utah Geol. Assoc. Pub. 3, p. 1-3.
- Zietz, Isidore, Bateman, P. C., Case, J. E., Crittenden, M. D., Jr. Grissom, Andrew, King, E. R., Roberts R. J., and Lorentzen, G. R., 1969, Aeromagnetic investigation of crustal structure for a strip across the western United States: *Geol. Soc. America Bull.*, v. 80, no. 9, p. 1703-1714.
- Zietz, Isidore, Shuey, R. T., and Kirby, J. R., 1976, Aeromagnetic map of Utah: U.S. Geol. Surveys Geophys. Inv. Map GP-907.

## A TUYA IN TOGIAC VALLEY, SOUTHWEST ALASKA

By J. M. HOARE and W. L. COONRAD, Menlo Park, Calif.

*Abstract.*—The shape, composition, structure, and location of a conspicuous flat-topped mountain in the lower Togiak Valley, southwest Alaska, all indicate that it formed by a subglacial volcanic eruption of olivine basalt. Volcanoes of this type are known as “tuyas.” The Togiak tuya erupted into an intraglacial lake in a hole thawed through a glacier that occupied Togiak Valley in Pleistocene time. The eruption was localized along the Togiak fault, which defines the east side of a shallow graben that is floored by older olivine basalt flows. The tuya, which has an area of 15 square kilometers, is a parallelogram. The flat summit, about 300 meters above the valley floor, is capped by glassy, fine-grained subaerial flows of alkali olivine basalt. To the north, the capping flows overlie palagonitized glassy tuffs; to the south, they overlie pillow basalts and breccia. The elevation of the pillow basalts indicates that surface of the melt-water lake was at least 250 m above present-day sea level. Basalt xenoliths in the tuffs and comparison with other better exposed tuyas suggest that the tuffs probably overlie an older pile of subaqueous pillow basalts that erupted beneath the intraglacial lake. The tuya overlies and is much younger than the preglacial flows on valley floor that yielded a potassium-argon age of  $0.758 \pm 0.2$  million years.

In the course of reconnaissance mapping of the Goodnews and Hagemester Island 1:250 000-scale quadrangles in southwest Alaska (Hoare and Coonrad, 1961a, b), we found that much of the lower Togiak Valley was underlain by basalt flows of late Cenozoic age. The widespread flows are obviously preglacial because they are overlain by glacial deposits. We assumed that a prominent volcanic table-mountain near the east side of the valley was a glacially truncated volcano and that it was the same age as the flows and a major source of the flows on the valley floor.

A recent investigation of the mineral resource potential of the same area afforded an opportunity to reexamine the volcanic rocks in greater detail. We found that the volcano is younger than and petrologically unlike the flows on the valley floor. The occurrence, shape, gross structure, and composition of the volcano show that it was formed by a subglacial volcanic eruption. Similar volcanoes have been described in Iceland (Sigvaldason, 1968; Jones, 1969, 1970, and in British

Columbia, where Mathews (1947) suggested that such volcanic features be called “tuyas.” A short preliminary description of the Togiak tuya has already been published (Coonrad and Hoare, 1976, p. 44-45). The present report, which is based upon additional fieldwork, laboratory data, and search of the literature, describes the composition, structure, and history of the tuya in greater detail and corrects or supplements the previously published report. However, additional field study of the brush-covered lower slopes and sides of the tuya might yield more information on this unusual type of volcano.

### LOCATION AND PHYSICAL DESCRIPTION

The Togiak tuya (fig. 1) is located near the lower end of Togiak Valley about 3 kilometers from the east side of the valley on the boundary between the Goodnews A-3 and A-4 1:63 360-scale quadrangles. It is a parallelogram 6 km long and 2.5 km wide and elongate northwestward parallel to the regional strike and to the flow of ice in Togiak Valley.

The tuya rises abruptly above the valley floor to a maximum elevation of 353 meters. The summit is nearly planar, sloping a little more than  $1^\circ$  southwestward. The sides of the tuya are steep and locally precipitous except at the south end, which is overlain and flanked by low ridges of glacial drift.

The sides of the tuya are almost everywhere covered by dense alder growth, and there are few visible bedrock exposures on the northwest and southeast sides. On the northeast end, a few ledges of north-dipping tuff are visible among the alders at least 130 m below the summit. Fortunately, the rim of the tuya is cut by small valleys and steep gullies in which bedrock exposures reveal the composition and structure of the upper part of the tuya. The truncated edges of numerous flows crop out on the flat top of the tuya, but most of the summit is covered by tundra and fields of frost-riven boulders.

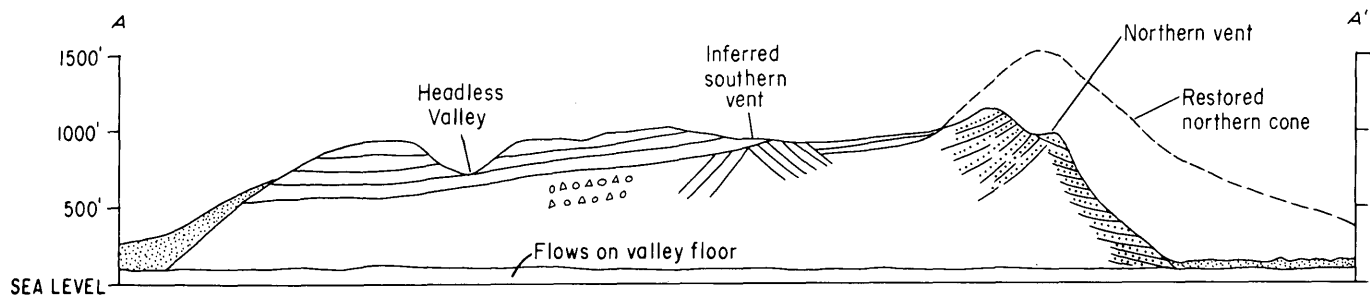
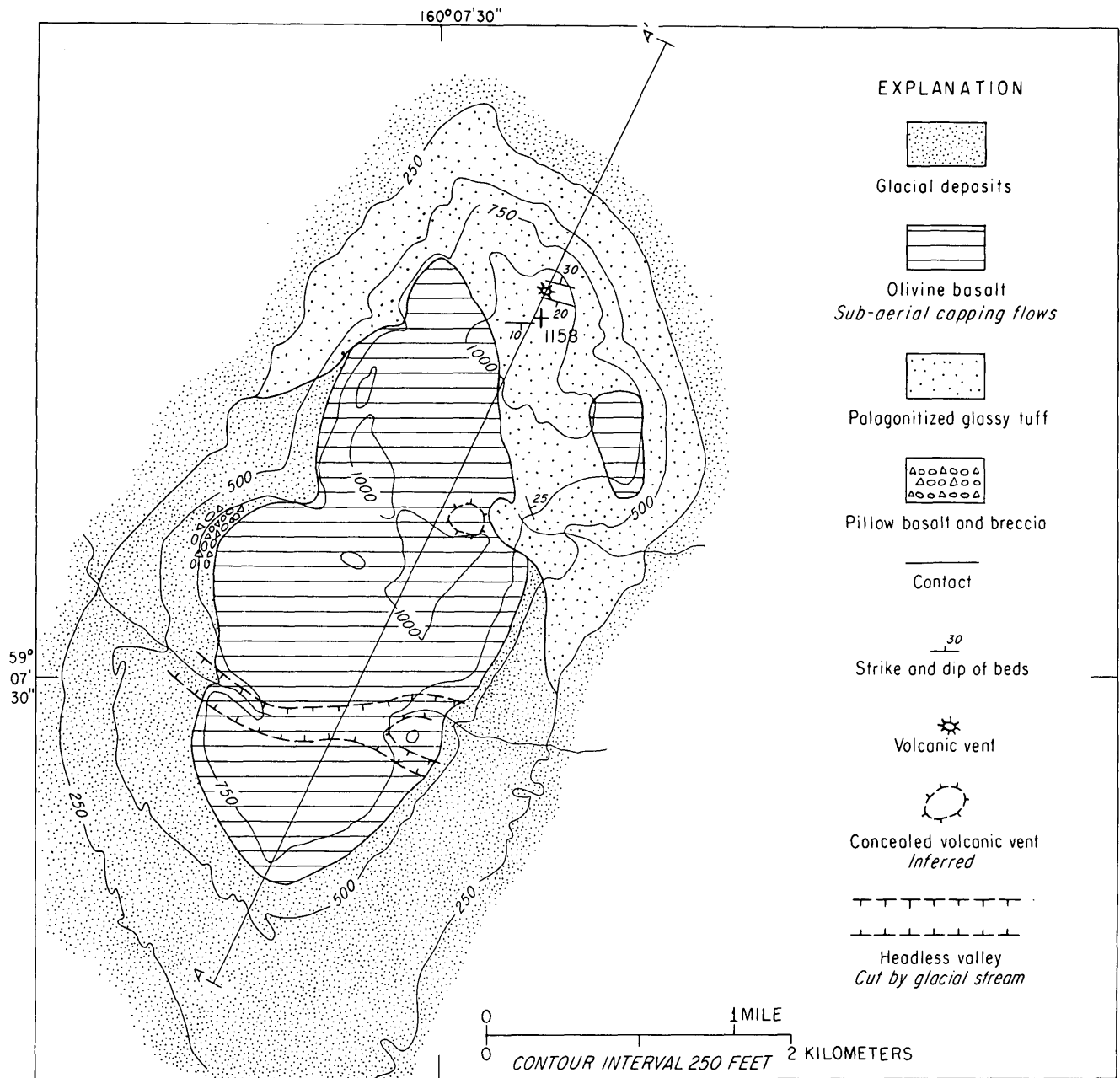


FIGURE 1.—Geologic map and section of the Togiak tuya.

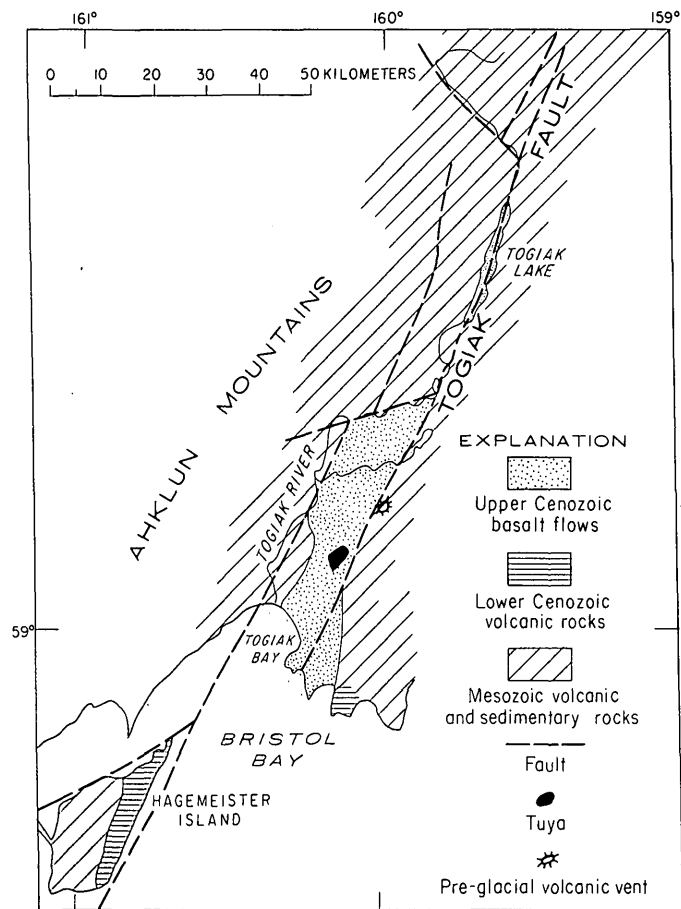


FIGURE 2.—Generalized geologic map of Togiak Valley and vicinity showing the geologic setting of the Togiak tuya. (Plutonic rocks and unconsolidated deposits omitted.)

### GEOLOGIC SETTING

The Togiak Valley is eroded in highly deformed strata of Mesozoic age that form the mountains on either side and are overlain by glacial deposits and lava flows on the valley floor (fig. 2). The trend and shape of the valley are, to a large degree, controlled by two or more northeast-trending faults that are part of the Denali fault system (Hoare, 1961, p. 608, fig. 3). The valley has been highly modified by glacial ice because it was a major channel down which a number of glaciers advanced in Pleistocene time. The upper valley, a deep glacial trough that was excavated along the Togiak fault, widens abruptly westward where it joins the lower valley, which is rectangular in plan. The lower Togiak Valley is 25 km wide from east to west and 40 km long. A fault trending about N. 70° E. probably separates the upper and lower valleys.

The lower valley east of the Togiak River is mostly underlain by horizontal basalt flows of late Cenozoic age. We believe this part of the lower valley to be a graben. The course of the Togiak River in the lower

valley is apparently fault controlled. We infer the existence of this concealed fault from the alignment of the river with the southeast coast of Hagemeister Island, which is clearly a fault scarp (Hoare and Coonrad, 1961b; Hoare, 1961). Also, contours on the magnetic map of the Goodnews quadrangle (Alaska Division of Geological and Geophysical Surveys, 1973) are offset along a line that coincides with the river course. The fault is apparently upthrown on the west side because rocks of Mesozoic age underlie the valley west of the river but are overlain by horizontal lava flows east of the river. The high east wall of the lower valley is aligned with the upper valley and is considered to be a fault scarp developed along the Togiak fault.

The widespread flows on the valley floor are preglacial in age. They apparently erupted from vents that were localized along the faults. Most of the older volcanic vents were probably destroyed by glacial ice, and only one of them has been identified. It is located about 11 km northeast of the tuya on a small shelf that projects out from the valley wall about 170 m above the valley floor (fig. 2). The shelf is underlain by highly oxidized vesicular breccia, the probable remnant of an old preglacial cone. The location and elevation of the cone remnant suggest vertical uplift on the Togiak fault. A second, larger shelf at about the same elevation projects out from the valley wall east of the tuya. This shelf is underlain by horizontal flows. The flows and shelf can be traced up a tributary valley where the flows overlie highly deformed rocks of Mesozoic (Jurassic?) age. We conclude that there has been about 170 m of vertical movement on the Togiak fault since the flows erupted on the valley floor.

The radiometric age of a flow on the valley floor 20 km north of the tuya was determined by the potassium-argon method to be  $0.76 \pm 0.2$  million years (J. G. Smith, written commun., 1976).

We determined the magnetic polarity of the flows on the valley floor and on the tuya at several places and found that all of the flows are normally magnetized. The polarity of the flows and the radiometric age determination indicate that the flows on the valley floor erupted near the beginning of the present (Brunhes) polarity epoch, which began approximately 700 000 years ago (Cox and others, 1963).

The tuya is clearly younger than the flows on the valley floor because it overlies them. Because the structure and composition of the tuya indicate that it resulted from a subglacial eruption, it must have erupted when the valley was filled with ice. The last two major ice advances occurred about 15 000 years ago and somewhat over 35 000 years ago (Hopkins, 1959, p. 1525). The tuya probably erupted before the last major

ice advance because the northeast end and the sides of the tuya have been strongly eroded by glacial ice. The location of the tuya near the east side of the valley suggests that it erupted on or near the Togiak fault. This was the last volcanic eruption in Togiak Valley.

### COMPOSITION AND STRUCTURE

The tuya consists of olivine basalt in the form of glassy tuffs, fine-grained flows, pillow lava, and pillow breccia. The northeast end of the tuya is chiefly palagonitized black glassy tuffs (fig. 3A, B). The altered tuffs are yellow-brown and contain as much as 25 percent unaltered black glass. Most of the tuff, particularly on the northeast rim of the tuya, consists of fragments of vesicular glass less than 20 millimeters in size. Layers of sand-sized accretionary lapilli and volcanic dust are locally interbedded with the coarser material. In thin section, tiny olivine, augite, and plagioclase crystals are visible in the altered and unaltered glass. The small areas of clear unaltered glass are generally less than 5 mm in diameter and are embayed by the yellow-brown palagonite.

The palagonitization of glassy tuffs has been explained in two different ways. In Iceland, the development of palagonite is attributed to short-term hydrothermal reaction. Sigvaldason (1968, p. 12-15) suggested that the necessary heat comes from pillow basalts that characteristically underlie the altered tuffs. On the island of Surtsey, hydrothermal palagonite developed in 1-2 years in tuffs that erupted in 1963 and 1964 (Friedman and others, 1976, p. 652-653). The altered tuffs are restricted to a relatively small area of high heat flow. They were altered by hydrothermal vapor made from marine and meteoric water at temperatures ranging from 60°-100°C.

However, in Hawaii, the development of palagonite is attributed to weathering (Macdonald, 1972, p. 194) or to long-term, low-temperature hydrochemical reactions that take place above the water table (Hay and Iijima, 1968, p. 374). It is now evident that palagonite develops by both rapid hydrothermal reaction and by slow weathering reactions. The warm climate and high rate of precipitation in Hawaii provide a favorable environment for palagonite formed by weathering, and most of the palagonite probably formed in this manner. In Iceland, however, the cool climate and low rate of precipitation do not favor weathering, and most of the palagonite probably formed by short-term hydrothermal reaction. The climate in southwest Alaska is similar to that of Iceland, and it seems likely that the palagonitization of the tuffs on the Togiak tuya is due to short-term hydrothermal reaction rather than to weathering.

No pillow basalts have been found beneath the palagonitized tuffs on the Togiak tuya, but the base of the tuya is concealed by vegetation and glacial drift. The tuffs, however, contain abundant xenolithic fragments of dense black basalt that presumably come from pre-existing flows. Comparison with better exposed tuyas in Iceland (Jones, 1969, p. 201-205; Sigvaldason, 1968, p. 6-7) suggests that the xenoliths are probably fragments derived from underlying pillow basalts.

The dip of the tuff at various places suggests that it erupted from two separate vents and formed two cones. The known location of one vent and the inferred location of the other (fig. 1) suggest that the cones are aligned northeastward approximately parallel the long dimension of the tuya. The northern cone is probably larger and younger than the southern cone. The structural apex of the northern cone is near the northeast rim of the tuya. On the tuya rim, about 400 m northeast of the highest point on the tuya (elevation, 353 m), the dip of the tuff changes from 30° N. to 20° S. The dip angle diminishes to the south and southwest, and, on the high point, the tuffs dip 10° S.

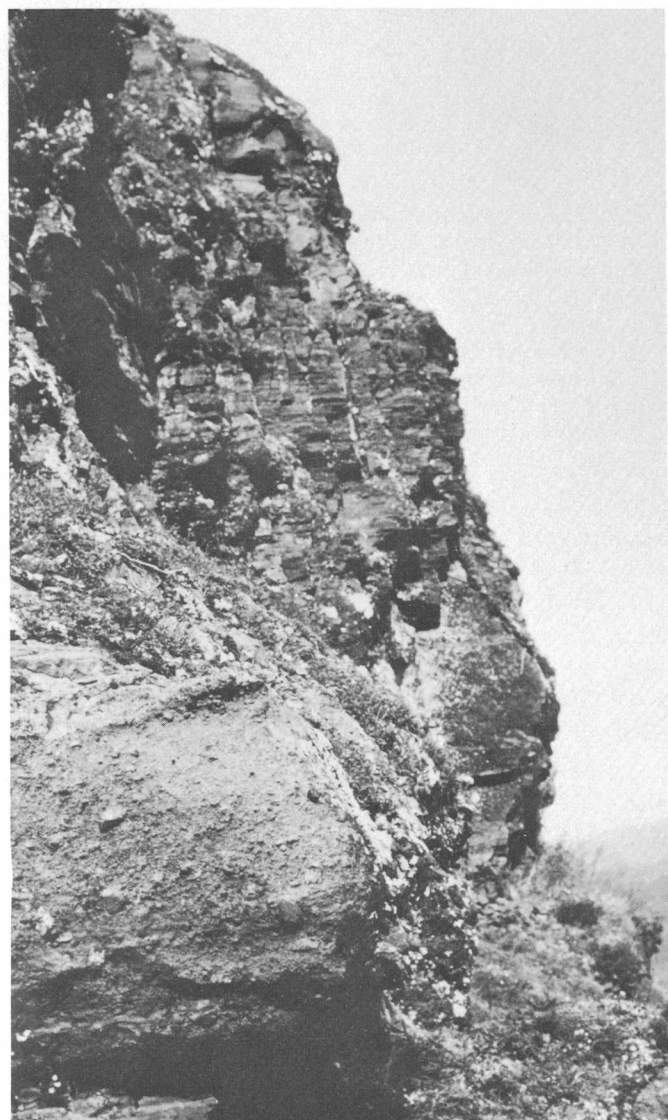
Between the high point and the northeast rim is a shallow saucer-shaped depression that we previously interpreted (Coonrad and Hoare, 1976, p. 44) as a crater remnant in the top of the northern cone. However, additional study suggests that a large amount of tuff has been eroded off the top and northeast side of the cone. It now seems likely that the depression is probably an erosional feature whose shape was controlled by the dip of the tuffs rather than a remnant crater.

The character of the tuffs changes southwestward between the vent area on the northeast rim and a gully on the northwest rim. The tuffs on the northeast rim are relatively coarse grained and poorly sorted; the beds are thick to massive and poorly defined (fig. 3A). The truncated west side of the northern cone is exposed in a steep gully 900 m west of the high point. The tuffs dip very gently westward and are overlain by about 50 m of fine-grained basalt flows (fig. 3C). Most of the tuffs in the gully are finer grained, better sorted, and thinner bedded. Many of the well-defined beds grade upward from coarse to fine. No examples of reversely graded beds were noted, but the rocks were not examined in detail. In general, the tuffs in the gully are less vesicular than those on the northeast rim. They include earthy-looking beds of silt-sized material as well as beds of sand-sized accretionary lapilli.

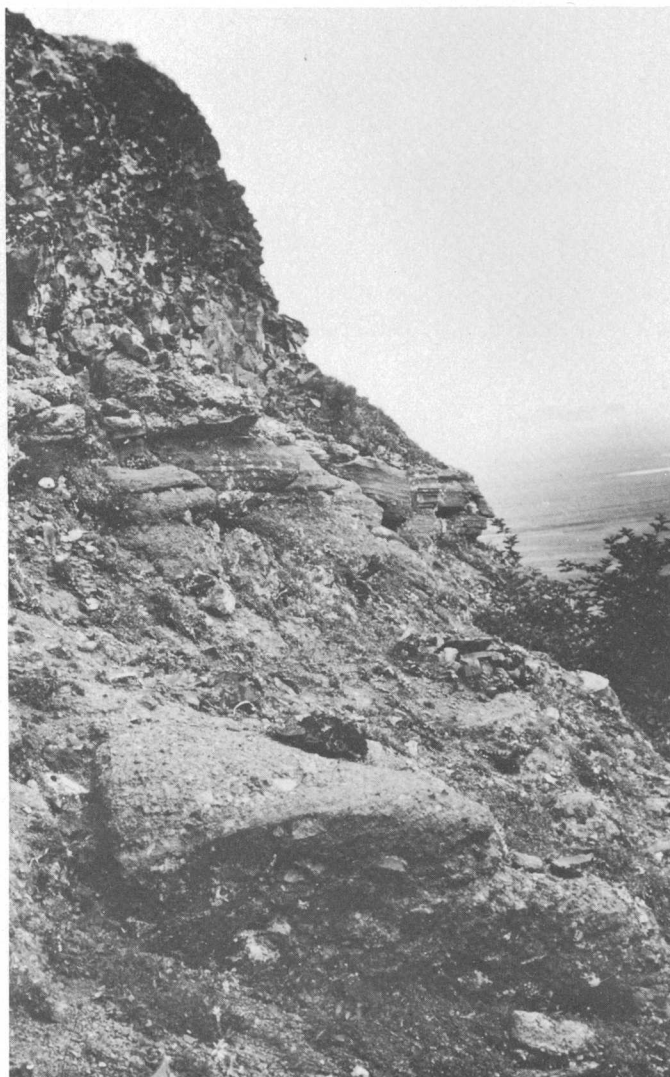
The tuffs in the gully are apparently water-deposited air-fall material, whereas the tuffs on the northeast rim were probably deposited subaerially around the erupting vent.



A



B



C

FIGURE 3.—Palagonitized tuffs. *A*, Thick-bedded, poorly sorted palagonitized tuff near center of the northern cone on the northeast rim of the tuya. Outcrop is about 4 m high. *B*, Thin-bedded, well-sorted, mostly fine- to medium-grained palagonitized tuff overlying poorly sorted coarser grained tuff in gully, northeast rim of the tuya. Height of exposure is about 15 m. *C*, Contact between well-sorted palagonitized tuffs and subaerial capping flows, in gully northwest rim of tuya. The valley-floor flows are exposed on the floor of Togiak Valley in the background. View is west.

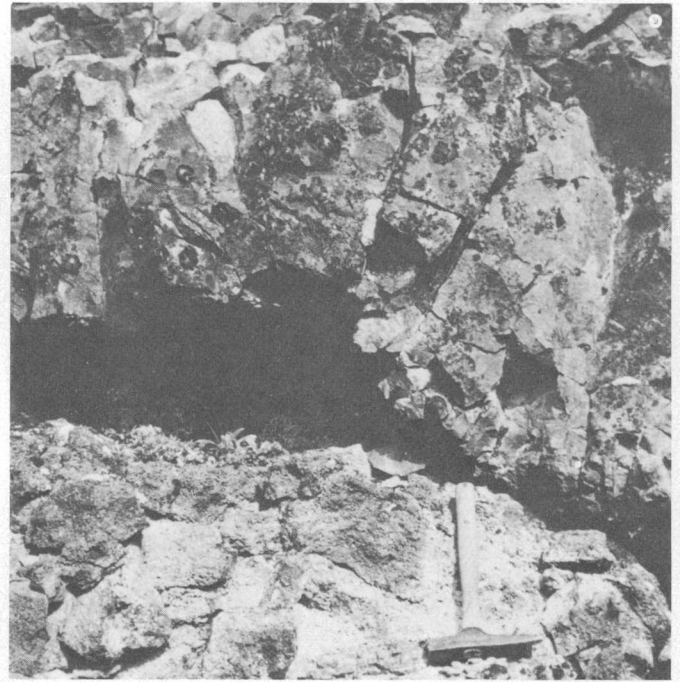
Tuffs exposed in a small valley on the southeast side of the tuya about 1200 m south of the high point dip  $25^{\circ}$  NE. The attitude of the tuffs at this point suggests that they were probably deposited northeastward from a second volcanic vent that is now concealed by overlying flows some distance to the southwest (fig. 1).



A



B



C

FIGURE 4.—Subaerial capping flows. *A*, View southward across frost-jumbled top of capping flows on the tuya summit. The lake-pocked coastal plain in the background is underlain by tholeiite and alkaline-olivine flows that form the low sea cliffs farther south. *B*, Truncated edge of a subaerial capping flow showing the irregular fracture pattern. *C*, Contact between two subaerial capping flows. Note the vesicular top of the lower flow and the curved conchoidal fracture in the massive base of the upper flow.

The flat top of the tuya is capped by a number of flows that dip gently southward (fig. 4A). The inferred southern tuff cone is largely concealed by these flows, and most of the capping flows probably came from the northern cone, which was larger and younger. The individual flows are fine grained and generally less than 10 m thick. They contain scattered vesicles throughout and are capped by a relatively thin layer of vesicular rock. Truncated flow margins have a very rough, hackly surface because the rock is broken by many closely spaced irregular fractures (fig. 4B, C). Some flows have poorly developed columnar structure. The small ill-formed columns are generally less than 0.3 m in diameter and are broken by many irregular cross fractures. The crude columnar structure is generally more easily recognized from a distance.

The structure and general character of the capping flows indicate that they erupted subaerially. In the northeastern part of the tuya, they overlie palagoni-

tized tuffs; farther south, they overlie pillow basalts and breccia.

The base of the capping flows is exposed in a steep gully in the northwest rim of the tuya where about 40–50 m of subaerial flows overlie a thick section of well-bedded tuffs. The tuffs in the gully dip very gently westward and are on the southwest side of the northern cone.

Basalts with pillow structure (fig. 5) crop out below the northwest rim of the tuya approximately 1.6 km southwest of the gully. The small exposure is on a steep slope about 25 m below the rim and 200 m above the valley floor. The pillows are rimmed by partly palagonitized glass and are surrounded by fragmental basalt that we interpret as pillow breccia.

The stratigraphic relation of the pillow basalts is uncertain because their contact with the overlying subaerial flows is concealed, and the nearest tuff exposures are 1.6 km to the north. In Iceland, the elevated occurrence of pillow basalts and pillow breccia high on the

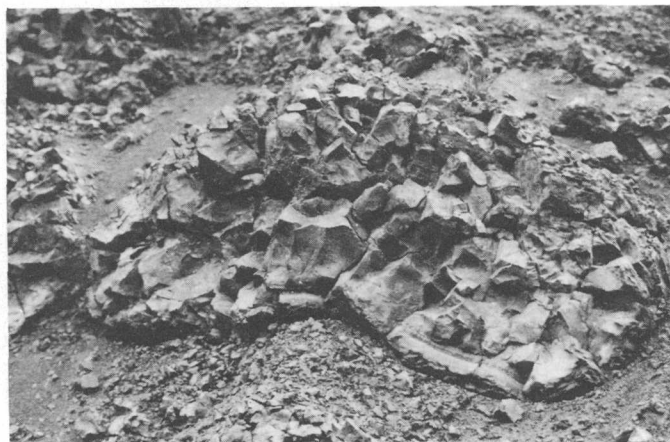


FIGURE 5.—Pillow structure in basalt, approximately 25 m below the tuya rim on the northwest side a short distance south of the valley that opens northwestward near the middle of the tuya. The structure is about 1 m across. The partly palagonitized glassy rim is visible bottom right. The individual pillows are separated by fragmental basalt that is probably pillow breccia.

sides of tuyas has been interpreted in two different ways. Sigvaldason (1968, p. 2-6) pictured them as being part of the initial subaqueous eruption which began with the eruption of pillow basalts and culminated with the eruption of glassy tuffs. The mixture of pillows and breccia was interpreted as being transitional between underlying pillows and overlying tuffs. However, Jones (1969, p. 201-204) found that the pillow-breccia mixture overlies the glassy tuffs. He interpreted it as having formed where subaerial flows entered the intraglacial lake that surrounded the growing tuya. On the Togiak tuya, the relative location of the tuffs, subaerial capping flows, and pillow basalts seem to accord best with Jones' interpretation. In other words, if the pillow basalt could be traced updip (northward), it would presumably grade into one of the subaerial capping flows.

It is interesting to compare the subaerial flows on the tuya with the older subaerial flows on the valley floor that underlie the tuya. From a chemical standpoint, the tuya and valley floor basalts are similar (table 1), but, from a physical standpoint, they are very different (compare fig. 4B, C and fig. 6A, B). The tuya flows are highly fractured, black, fine-grained rock with scattered olivine phenocrysts and 10-20 percent interstitial glass, whereas the flows on the valley floor are gray, medium-grained, nonporphyritic rock with a loose diktytaxitic texture and little or no glass. They contain large, well-shaped columns and many vesicle cylinders (Goff, 1976) consisting of fine-grained glassy vesicular rock. The general character of the valley flows shows that they were a fluid holocrys-

TABLE 1.—Chemical analysis of basalts in Togiak Valley

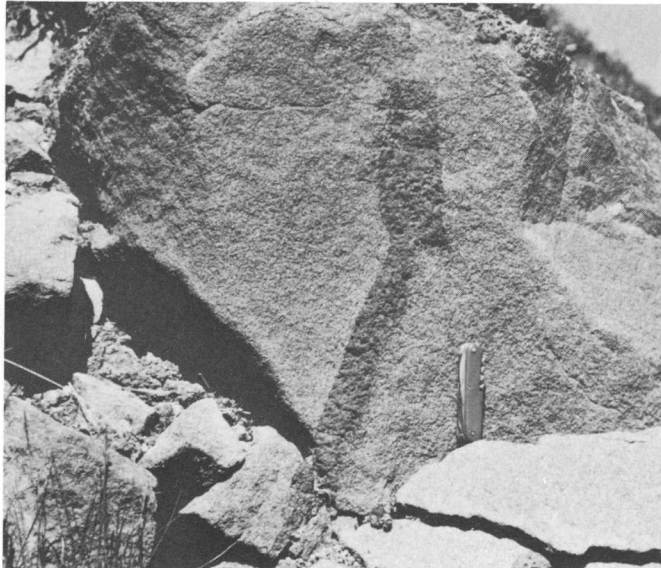
[Rapid-rock analysis by method of Shapiro (1975, p. 43-54). Analyst: Hezekiah Smith]

Sample -----	1	2	3
SiO <sub>2</sub> -----	51.7	48.6	49.5
Al <sub>2</sub> O <sub>3</sub> -----	15.4	14.9	14.7
Fe <sub>2</sub> O <sub>3</sub> -----	1.3	1.7	1.0
FeO -----	8.7	8.7	9.6
MgO -----	8.5	9.2	10.0
CaO -----	8.6	9.0	8.0
Na <sub>2</sub> O -----	3.7	3.5	3.8
K <sub>2</sub> O -----	0.67	1.4	1.0
H <sub>2</sub> O+ -----	0.24	0.93	0.27
H <sub>2</sub> O- -----	0.06	0.42	0.13
TiO <sub>2</sub> -----	2.0	2.4	2.2
P <sub>2</sub> O <sub>5</sub> -----	0.36	0.48	0.42
MnO -----	0.12	0.14	0.13
CO <sub>2</sub> -----	0.03	0.03	0.02
Total ---	101	101	101

1. Tholeiite from valley-floor flow forming sea cliffs on east side of Togiak Bay (M124635W).
2. Alkali-olivine basalt from capping flow on southeast rim of Togiak tuya (M124638W).
3. Alkali-olivine basalt from valley floor 20 km north of tuya (M124639W).

talline mush when they froze, but the tuya flows were a glassy melt that froze before it became completely crystalline.

A major factor that helps to explain the physical difference in the two groups of flows is their respective environments of eruption. The valley flows erupted on the wide, gently sloping floor of Togiak Valley in preglacial time, but the tuya flows erupted in a deep hole that had melted through the Togiak glacier. In this cold wet environment, they cooled quickly, froze while incompletely crystalline, and fractured in a highly irregular fashion.



A



B

FIGURE 6.—Valley floor basalt. *A*, Vertical cross section of vesicle cylinders in massive columnar-jointed tholeiite (sample 1, table 1), 25 km south of the tuya in the sea cliffs. Knife is 90 mm long. *B*, Truncated ends of several vesicle cylinders, same rock and location as above. Note the diktytaxitic texture.

### HISTORY OF CONSTRUCTION

The construction of the tuya began with the subaqueous eruption of basalt beneath a lake that had melted out of an overlying glacier. The heat of the eruption eventually melted a hole through the glacier.

The size of the tuya and the height of glacial erratics on the walls of Togiak Valley suggest that the hole was at least 8 km in diameter and 330–500 m deep. The elevation of the pillow basalts on the northwest side of the tuya (fig. 1) indicates that the surface altitude of the melt-water lake was at least 250 m above present sea level.

The Icelandic tuyas reflect a three-part eruptive succession—a quiet subaqueous effusive phase, an emergent explosive phase, and a final quiet subaerial effusive phase (Jones, 1969, p. 201–205). The first phase is represented by pillow lavas, and the second, by basaltic glass tuff. The third phase is represented by “sheet” flows that became brecciated and developed pillow structure where they entered the intraglacial lake. Because the base of the Togiak tuya is concealed by glacial deposits and vegetation, there is no direct evidence that the glassy tuffs rest upon pillow lavas. However, the tuffs contain abundant angular xenoliths of dense black basalt that probably came from preexisting flows. There is no proof that the xenoliths are fragments of pillow lavas, but it seems likely.

The second eruptive phase saw the growth of two pyroclastic cones consisting largely of fragmental basaltic glass, most of which is now altered to yellow-brown palagonite. The glassy tuffs indicate an explosive eruptive phase primarily caused by steam made from water introduced into the volcanic vent from the melt-water lake. The change from quiet pillow basalt to violent tuff eruption probably began when the growing pile of pillows approached lake level and the pressure of overlying water was no longer enough to prevent the rapid exsolution of dissolved magmatic gases. The tuff eruption presumably continued until the thickness of the porous tuff walls around the vent no longer permitted lake water to enter the vent. A number of subaerial flows erupted from the northern cone some time after it emerged above lake level. At the time they erupted, the flows were probably symmetrically distributed around the cone summit, but they have been eroded off the north and northeast sides and for some distance south of the summit on the south side.

Flows that advanced south and southwestward apparently buried the southern cone. Somewhat farther south, the earlier flows entered the melt-water lake where they developed pillow structure. Many of the pillows broke up, and the advancing flow fronts became mixtures of pillows and pillow breccias. This material came to rest in the melt-water lake in the form of deltas that were subsequently overridden by the subaerial flows that cap the tuya.

Glacial ice overrode the tuya some time after volcanic activity ceased. The ice truncated the northeast end of the tuya as well as the northwest and southeast sides. It also removed the capping flows from the northeast end of this tuya and deposited erratic boulders on the summit. Conspicuous among the glacial erratics are basalt boulders derived from the older valley flows. They are easily recognized by their texture and coarser grain size, and some of them also contain vesicle cylinders (fig. 6) which do not occur in the tuya basalts.

The shape of the Togiak tuya suggests that it was originally much larger before it was reshaped by glacial ice. In British Columbia and Iceland, the tuyas are characterized as being "roughly circular to elliptical in outline" (Mathews, 1947, p. 562) and "roughly circular" (Jones, 1970, p. 132). However, the Togiak tuya is a parallelogram, twice as long as it is wide (6×2.5 km). The truncated north-dipping tuff beds on the northeast end of the tuya suggest that it was originally several hundred meters longer than it is now. The straight northwest and southeast sides of the tuya (fig. 1) also indicate a large amount of glacial erosion. If the tuya was originally elliptical in outline, it was approximately twice as wide as it is now and perhaps 8 km long.

The rounded and elliptical shapes of the tuyas in British Columbia and Iceland suggest that they erupted beneath ice that was nearly static. In British Columbia, the tuyas erupted beneath the large Cordilleran ice sheet, but "none of the tuyas \* \* \* is deeply eroded by ice" (Mathews, 1947, p. 565). The shape and location of the Togiak tuya in a large glacial valley suggest that it erupted beneath an active glacier.

Toward the southwest end, the flat summit is incised by an unusual headless valley that transects the tuya from the northwest to southeast sides (fig. 1). At its shallowest point in the middle of the tuya, the valley is 35–50 m deep. It is drained by two streams that flow in opposite directions and appear to be too small to have excavated the valley. It seems likely that the valley was initially cut by a melt-water stream that flowed across the top of the tuya. The present streams have presumably deepened the northwest and southeast ends of the valley.

The probability of finding other tuyas in interior Alaska is small because there are few areas of late Cenozoic basaltic volcanism and most of interior Alaska was never glaciated. A possible exception is the Seward Peninsula where the mountains supported numerous alpine-type glaciers, and there are several

basalt lava fields of late Cenozoic age. The southern part of the Alaska Range and the Aleutian Peninsula were the scene of considerable volcanic activity in Pleistocene time when most of this area was probably covered by ice. But there probably are few, if any, tuyas in the area because the volcanism was mostly andesitic rather than basaltic.

#### REFERENCES CITED

- Alaska Division of Geological and Geophysical Surveys, 1973, Aeromagnetic map, Goodnews quadrangle, Alaska: Alaska Div. Geol. Geophys. Surveys open-file rept. 15, 1 sheet, scale 1:250 000.
- Coonrad, W. L., and Hoare, J. M., 1976, The Togiak tuya, in Cobb, E. H., ed., *The United States Geological Survey in Alaska: Accomplishments during 1975*: U.S. Geol. Survey Circ. 733, p. 44–45.
- Cox, Allan, Doell, R. R., and Dalrymple, G. B., 1963, Geomagnetic polarity epochs and Pleistocene geochronometry: *Nature*, v. 198, no. 4885, p. 1049–1051.
- Friedman, J. D., Preble, D. M., and Jakobsson, S., 1976, Geothermal flux through palagonitized tephra, Surtsey, Iceland—The Surtsey temperature-data-relay experiment via Landsat-1: *U.S. Geol. Survey Jour. Research*, v. 4, no. 6, p. 645–659.
- Goff, E. F., 1976, Vesicle cylinders formed in vapor-differentiated basalt flows [abs.]: *Geol. Soc. America Bull.*, v. 8, no. 6, p. 887–888.
- Hay, R. L., and Iijima, A., 1968, Nature and origin of palagonite tuffs of the Honolulu Group on Oahu, Hawaii: *Geol. Soc. America Mem.* 116, p. 331–376.
- Hoare, J. M., and Coonrad, W. L., 1961a, Geologic map of the Goodnews quadrangle, Alaska: *U.S. Geol. Survey Misc. Geol. Inv. Map I-339*.
- 1961b, Geologic map of the Hagemeister Island quadrangle, Alaska: *U.S. Geol. Survey Misc. Geol. Inv. Map I-321*.
- Hoare, J. M., 1961, Geology and tectonic setting of lower Kuskokwim-Bristol Bay region, Alaska: *Am. Assoc. Petroleum Geologists Bull.*, v. 45, no. 5, p. 594–611.
- Hopkins, D. M., 1959, Cenozoic history of the Bering land bridge: *Science*, v. 129, no. 3362, p. 1519–1528.
- Jones, J. G., 1969, Intraglacial volcanoes of the Laugarvatn region, southwest Iceland—1: *Geol. Soc. London Quart. Jour.*, v. 124, p. 197–211.
- 1970, Intraglacial volcanoes of the Laugarvatn region, southwest Iceland: *Jour. Geology*, v. 78, no. 2, p. 127–140.
- Macdonald, G. A., 1972, *Volcanoes*: Englewood Cliffs, N. J., Prentice-Hall, 492 p.
- Mathews, W. H., 1947, "Tuyas," flat-topped volcanoes in northern British Columbia: *Am. Jour. Sci.*, v. 245, no. 9, p. 560–570.
- Shapiro, Leonard, 1975, *Rapid analysis of silicate, carbonate, and phosphate rocks—revised edition*: U.S. Geol. Survey Bull. 1401, 76 p.
- Sigvaldason, G. E., 1968, Structure and products of subaquatic volcanoes in Iceland: *Contr. Mineralogy and Petrology*, v. 18, p. 1–16.



## ORIGIN OF TWO CLAY-MINERAL FACIES OF THE POTOMAC GROUP (CRETACEOUS) IN THE MIDDLE ATLANTIC STATES

By LUCY M. FORCE and GEORGE K. MONCURE,<sup>1</sup>

Reston, Va., and Laramie, Wyo.

**Abstract.**—Sedimentary clay that crops out in the coastal plains of New Jersey, Delaware, the part of Maryland north and east of Washington, D.C., and the northeast half of Washington, D.C., in the nonmarine Cretaceous Potomac Group is predominantly kaolinite and illite. In contrast, in part of southeastern Maryland, the southwest half of Washington, D.C., and most of eastern Virginia, Potomac Group clay is predominantly montmorillonite.

Kaolinite and illite were probably derived by intense acid weathering of metamorphic and granitic rocks to the west during the Cretaceous and were deposited in a well-drained basin. Montmorillonite was most likely produced by deep weathering of a mainly granitic source. Poor drainage and alkaline surface- and ground-water conditions probably accompanied the production, transportation, deposition, and burial of the montmorillonite. Kaolinization of the montmorillonite is taking place now at the surface in northern Virginia.

Previous petrologic studies of the Potomac Group (Glaser, 1969; Owens, 1969) resulted in the discovery of two regional sedimentary facies: orthoquartzitic sand interbedded with kaolinite and illite clay beds north of Washington, D.C. (northern facies of this paper), and arkosic sand with montmorillonite<sup>2</sup> and mixed layer clay to the south (southern facies of this paper; fig. 1). We find that the abrupt change in clay mineralogy is accompanied by differences in coarse sediment characteristics, ground-water chemistry, and stratigraphy.

The purpose of the present study is to determine the origin of the two sedimentary facies and to investigate the relationship between the sedimentary facies and the ground-water ion-concentration pattern. We present new stratigraphic details as well as a brief summary of previously published information to provide a depositional framework. Our discussions of provenance, primary weathering reactions, and postde-

positional changes are based on published data on source rocks, Potomac Group mineralogy and ground-water chemistry, and new mineralogic analyses of the Potomac Group sediments.

**Acknowledgments.**—For samples outside northern Virginia and for unpublished data, we thank J. P. Owens, L. C. Conant, James Rankin, R. B. Mixon, D. J. Fanning, A. J. Froelich, and Deleuw, Cather and Co.

### REGIONAL GEOLOGY

The middle Atlantic Coastal Plain extends from the Fall Line to the edge of the Continental Shelf. The Coastal Plain consists of a wedge of continental and marine sediments, deposited in Jurassic(?) through Quaternary time, which thins landward from a thickness of roughly 9000 m (Minard and others, 1974) at the continental break. Exposed Cretaceous sediments range in age from Early Cretaceous (Barremian) through earliest Late Cretaceous (earliest Cenomanian; Doyle and others, 1975).

The basal beds, which constitute the lower two-thirds of the sedimentary wedge beneath the emerged Coastal Plain, were assigned to the Potomac Group by McGee (1888). They consist of interbedded continental clay, silt, sand, and gravel deposited on a slightly irregular surface of Precambrian to lower Paleozoic rocks. The Potomac Group is as much as 1,500 m thick along the Atlantic shoreline (Weed and others, 1974) and is apparently considerably thicker farther east. Its beds crop out in an arc 550 km long along the edge of the Salisbury Embayment from central New Jersey to southern Virginia (fig. 1).

The Potomac Group sediments were subsequently subdivided by Brenner (1963) on the basis of pollen age zones. From southern Virginia to the head of the Chesapeake Bay, beds of pollen Zone I (mostly Aptian) occupy the western and northern part of the Potomac Group outcrop belt and beds of Zone II (Albian, 100–108 million years), the seaweed part

<sup>1</sup> Department of Geology, University of Wyoming.

<sup>2</sup> In this paper, montmorillonite is the term used for a clay with a 14- to 15-angstrom *d*-spacing in air-dried samples, which typically expands to 17 Å with ethylene glycolation, and which collapses to 10 Å after heating to 300°C for an hour. It is found both as a discrete phase and, more commonly, as layers in mixed-layer clay.

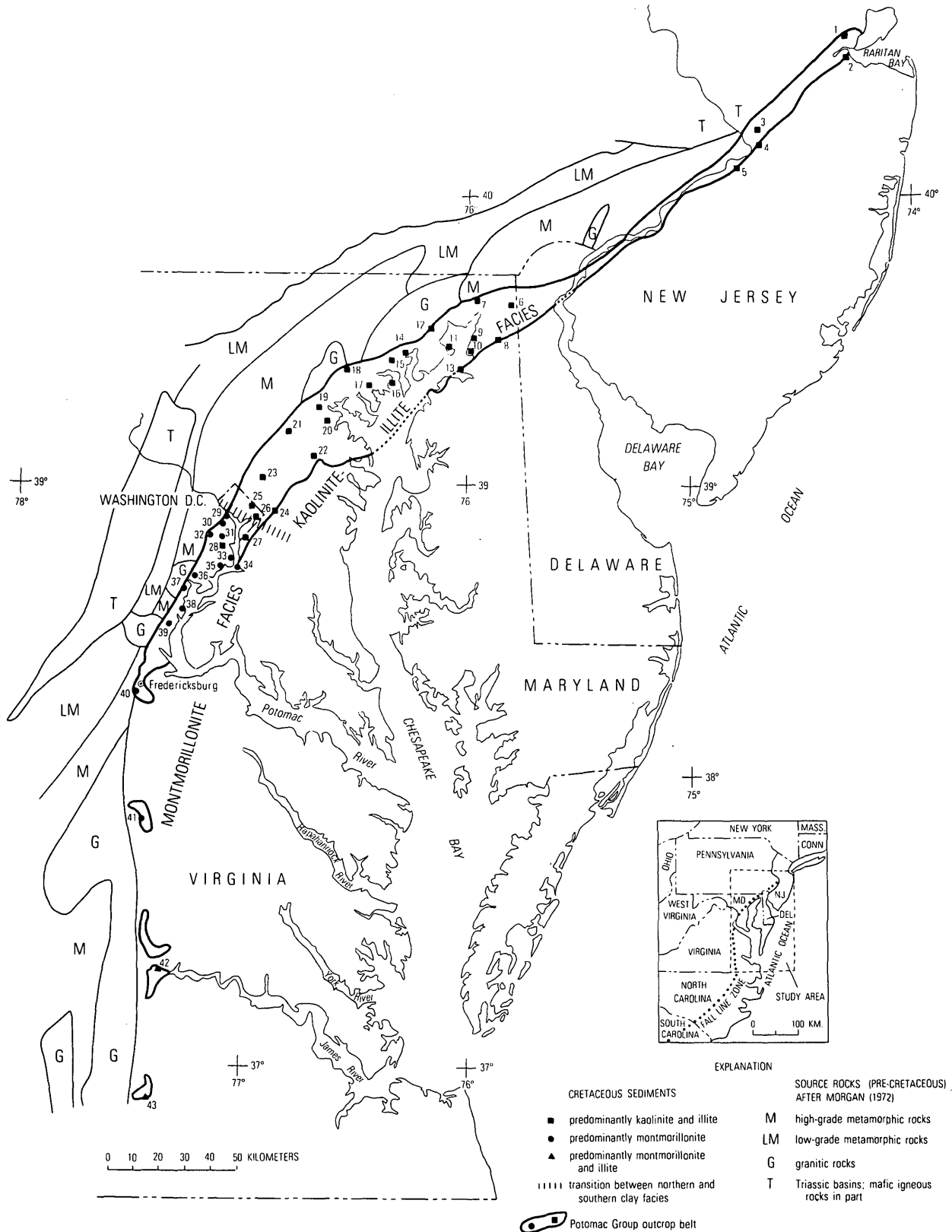


FIGURE 1.—Potomac Group outcrop belt (partly after Darton, 1947; Calver, 1963; U.S. Geological Survey, 1967; and references—below). Source rocks after Morgan (1972). Numbers refer to clay sample localities: J. P. Owens (unpub. data, 1978), 1–5, 10–14, 16, 24, 37, 38; L. C. Conant (unpub. data, 1978), 6–9; Knechtel and others (1961), 15, 17, 18, 21–23; A. J. Froelich (unpub. data, 1978), 25; Hack (1975), 27, 34; Deleuw, Cather and Co. (unpub. data, 1978), 26, 28, 29; R. B. Mixon and D. J. Fanning (unpub. data, 1978), 40; James Rankin (unpub. data, 1978), 41–43; remainder of samples were collected by the writers.

(Doyle and Hickey, 1976). Zone III (early Cenomanian, 93 m.y.) crops out in the Delaware Valley as far northwest as the Trenton, N.J. area, and Zone IV (late Cenomanian, 91 m.y.) is found farther northeast. Thus, there is a regional but very gradual trend of progressively younger beds to the northeast in the Potomac Group.

**OBSERVATIONS**  
**Stratigraphy**

Division of the Potomac Group into three formations in the northern facies (Clark, 1897) is determined mainly by the presence of the distinctive, dark clayey Arundel Formation stratigraphically between the rather similar Patapsco (above) and Patuxent (below) Formations. The Patuxent Formation is characterized by gravels and mature quartzose sand and minor clay; the Arundel is a distinctive, dark-gray to black, silty clay containing abundant carbonaceous plant fossils; the Patapsco is lithologically similar to the Patuxent but has a higher proportion of clay beds. Trough crossbeds are common in northern facies sand bodies in both the Patapsco and Patuxent Formations. Irregular bedding, probably due to differential compaction (Glaser, 1969) and rapid tectonism, is also common.

A marker unit such as the Arundel Formation is absent in the southern facies, and formational partition of the interbedded sand and clay bodies into formations is not yet possible (U.S. Geological Survey, 1967; Owens, 1969; Mixon and others, 1972). Sand and clay units have been delineated in part of northern Virginia (Force, 1975), however, and certain sedimentary features were noted. Individual 5- to 20-cm-thick sand or clay beds may change thickness and grain size in a short distance, but clay or sand units as much as 40 m thick commonly persist for kilometers. Crossbeds and channel cut-and-fill structures are part of sand-filled channels which range in size from a few meters to hundreds of meters across and extend for kilometers. The sedimentary structures, locally abundant plant accumulations, rare dinosaur remains, and the complete absence of marine fossils also suggest a fluvial, continental environment of deposition (Weir, 1976).

Basal beds of the Potomac Group in both facies dip seaward at 8 to 18 m/km, and uppermost beds dip less than 2 m/km.

**Description of sediments**

The Potomac Group is texturally diverse but is predominantly sand with lesser amounts of gravel



**FIGURE 2.—Sample collection and preparation.**

and clay. The sediments were analyzed mainly by microscope and X-ray diffractometry (fig. 2). Clay compositions and other characteristics of the sedimentary facies are summarized in figure 3 and table 1.

**TABLE 1.—Characteristics of northern and southern facies sediments**

		NORTHERN FACIES	SOUTHERN FACIES
S	CLAY	KAOLINITE & ILLITE	MONTMORILLONITE
	LIGHT	ORTHOQUARTZITE: QUARTZ	ARKOSE: QUARTZ & FELDSPAR (MICROLINE, PERTHITE, NA-PLAG)
N	HEAVY	ZIRCON, TOURMALINE, KYANITE, RUTILE, GOETHITE, LEUCOXENE, ILMENITE	ZIRCON, TOURMALINE, GOETHITE LEUCOXENE, ILMENITE; TRACE KYANITE, STAUROLITE
	GRAVEL	VEIN QUARTZ (MOSTLY), METAQUARTZITE, QUARTZ SANDSTONE	VEIN QUARTZ (MOSTLY), GRANITE OR GNEISS CLASTS
	GROUND-WATER pH	4.5 - 6.5	7.0 - 8.5

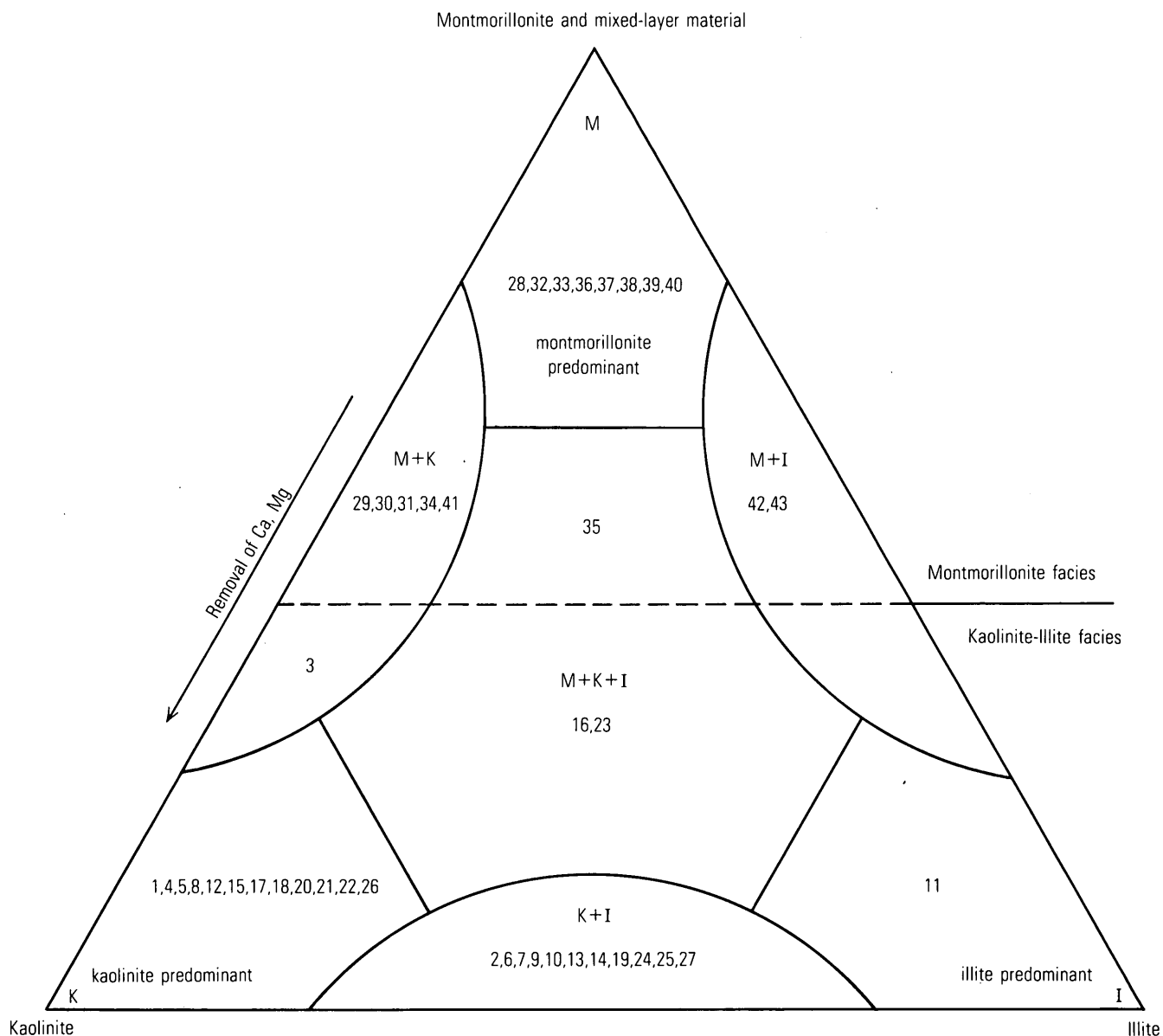


FIGURE 3.—Composition of Potomac Group clays and two samples (Nos. 1 and 2) from the Raritan Formation. Sample numbers from figure 1 are plotted to show the predominant clay mineral species in each sample; the display is qualitative, the exact position of locality numbers having only

rough quantitative significance. There is a relatively good mineralogic separation of clays in 30 of the 41 Potomac Group samples; 11 other samples fall along the facies boundary. Arrow indicates most likely postdepositional alteration trend.

### Clay

Clay in the northern facies is typically dull white, yellow, or red except where carbonaceous material is abundant, and it is primarily kaolinite and illite, commonly containing a small amount of vermiculite in the top few meters, and rarely, montmorillonite. Large blocks result from near-surface weathering of illite and kaolinite. The small amount of silt- and sand-sized material in most clay samples is mainly quartz.

Sample 20 (figs. 1 and 4) from northern Maryland

is representative of the northern facies. Samples 1 and 2 (fig. 1), from the marine Raritan Formation (Upper Cretaceous) in New Jersey are primarily kaolinite and illite. These samples are included to illustrate the character of the first Cenomanian clays and the similarity to the northern facies of the Potomac Group.

The southern facies clays are dominated by relatively pure montmorillonite and montmorillonite-illite mixed layer material. They are usually a waxy gray or greenish brown and contain a notable proportion of

silt. Sample 36 (fig. 5) is representative of the southern facies clays. Weathering of montmorillonitic clay produces "soft ground" (swelling when wet) or a layer of small chips (shrinking during drying) near the surface and abundant closely spaced, curved, intersecting cracks at depth; the deep cracks may be partly due to unloading.

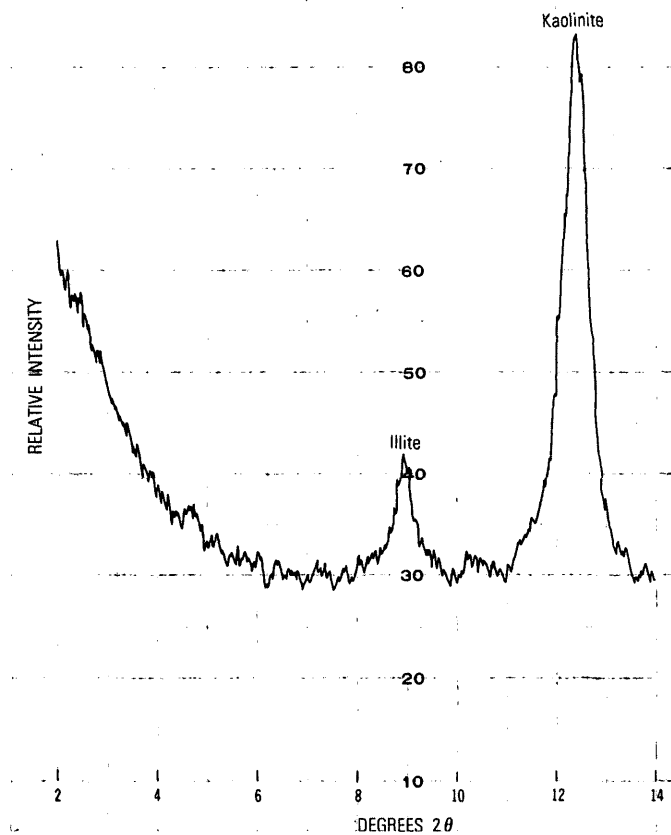


FIGURE 4.—X-ray diffractogram of sample 20, northern facies.

Silt-sized epidote and biotite, which are relatively unstable minerals, are found in montmorillonite clay beds but not in the associated arkosic sands.

In addition to X-ray analysis of the finer than 2- $\mu$ m and finer than 1- $\mu$ m fractions of sample 36 (fig. 5), a simple swelling test was made with a dried portion of the 2- $\mu$ m cut in deionized water. Both the position of the low-angle montmorillonite peak (14–15 Å) and its low bulk-swelling property suggest that the sample is calcium-rich montmorillonite rather than sodium-rich montmorillonite.

Potomac Group clay in the southern third of Virginia contains an unusually high proportion of mixed-layer material and illite (fig. 6). It may belong to a separate domain within the southern facies.

#### Sand and gravel

Quartz is the predominant sand-sized mineral of the northern facies and constitutes as much as 95 percent

of the total sample. The quartz grains of the white to yellow orthoquartzitic sand are generally clear to slightly cloudy, angular to subangular, and commonly pitted and embayed. Feldspars are a minor constituent. Moderately rounded nonopaque heavy minerals are zircon, tourmaline, staurolite, kyanite, and rutile. Goethite, leucosene, and ilmenite are the dominant opaque minerals throughout the Potomac Group. The mineralogy and texture indicate postdepositional solution and (or) intense weathering of the source rock with only moderate transport. The scarcity of feldspars and other less stable minerals implies maturity. A high-grade metamorphic source is suggested by the heavy-mineral suite (Glaser, 1969).

Most of the coarse clasts in the northern facies are vein quartz (as much as 79 percent), metaquartzite, and quartz sandstone (as much as 17 percent). Whereas the metaquartzite and quartz sandstone come from a more distant source, most of the pebbles (vein quartz) probably come from nearby metamorphic rocks.

Clayey gray to yellow sand is characteristic of the southern facies. Alkali feldspar (microcline, perthite, sodic plagioclase) and its clay weathering products comprise as much as 65 percent of a sample; quartz, the other major mineral, is generally fine to medium sand size, clear, and subrounded to subangular. Accessory minerals are zircon, tourmaline, ilmenite, and rarely, high-grade metamorphic minerals.

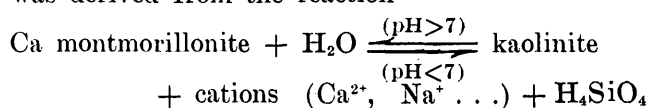
Southern facies gravels consist mostly of vein quartz and metaquartzite, but fragments of highly weathered igneous and metamorphic rocks such as quartzo-feldspathic gneiss or granite are present in small quantities (Glaser, 1969).

#### Ground-water Geochemistry

Differences in concentrations of major ions in the ground water of the lower part of the Potomac Group (Otton, 1955; Johnston, 1962; table 2, this paper) coincide with differences in sediment mineralogy (figs. 1 and 7). In order to investigate the relationship between the two volumetrically important clay minerals, montmorillonite and kaolinite, and ground-water ion concentrations, the ratio

$$\frac{\text{Log } a(\text{Ca}^{2+}) / a^2(\text{H}^+)}{\text{Log } a(\text{H}_4\text{SiO}_4)}$$

was derived from the reaction



where pH < 7 is due to rainwater and organic acids in the soil zone. Because Potomac Group ground water is

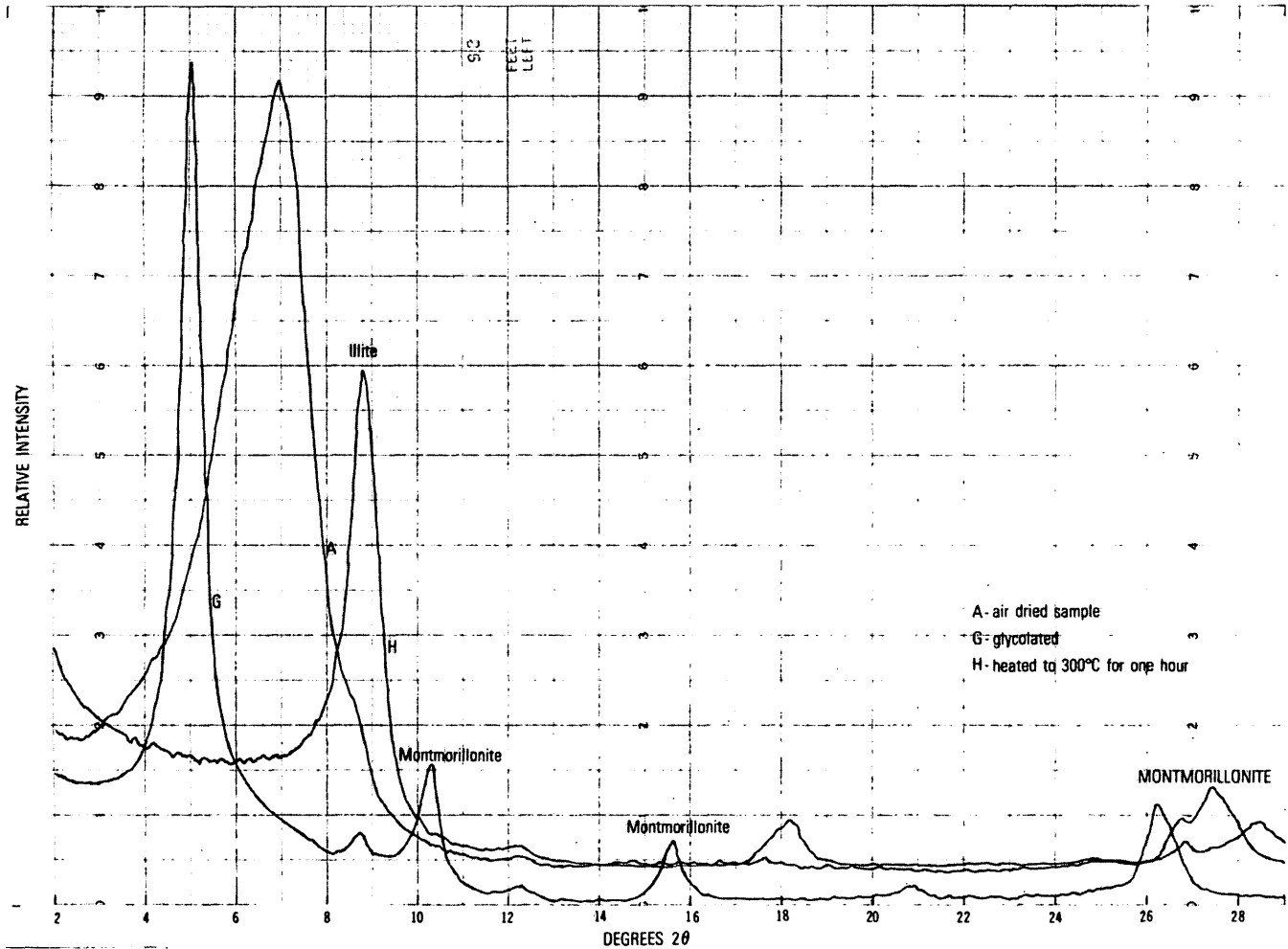


FIGURE 5.—X-ray diffractogram of sample 36, southern facies.

very dilute, ionic activity values are approximately equal to the molar concentration values. Values of the ratio were plotted over well locations and contoured. The map (fig. 7) defines two general fields: one of lower values corresponding to the kaolinite-illite zone, separated by a marked change in slope from another field of high values corresponding to the predominantly montmorillonite zone.

Ratio value symbols (fig. 7) were plotted on the  $\text{Ca}^{2+}$ ,  $\text{Na}^+$ , and  $\text{K}^+$  activity diagrams of Helgeson and others (1969) (figs. 8, 9, 10). Ground water is in apparent equilibrium with kaolinite in the northern facies; in the southern facies, ground-water composition is either in equilibrium with calcium montmorillonite or is slightly deficient in silica with respect to calcium montmorillonite (fig. 8). A rough separation of higher and lower ratio values is shown on the

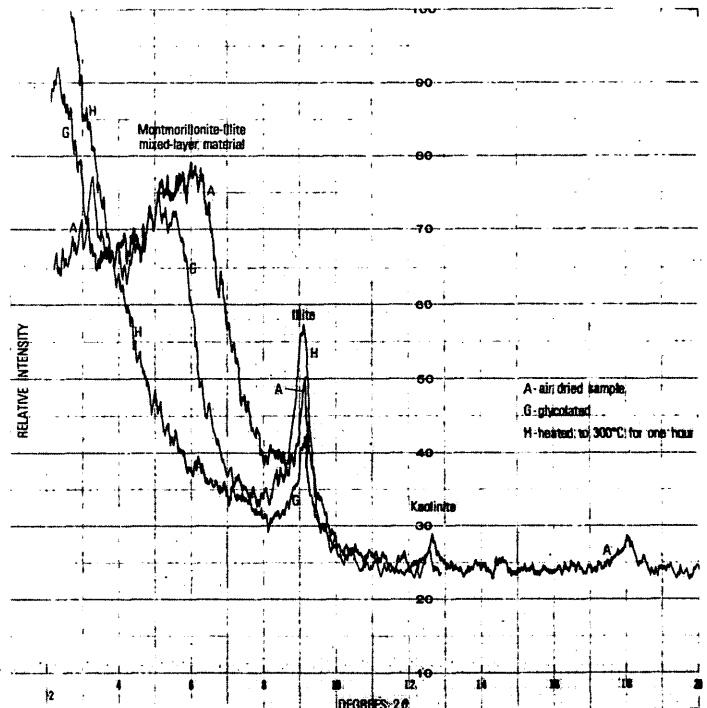


FIGURE 6.—X-ray diffractogram of sample 42, southern facies; note the unusually high proportion of illite and mixed-layer material typical of southern Virginia.

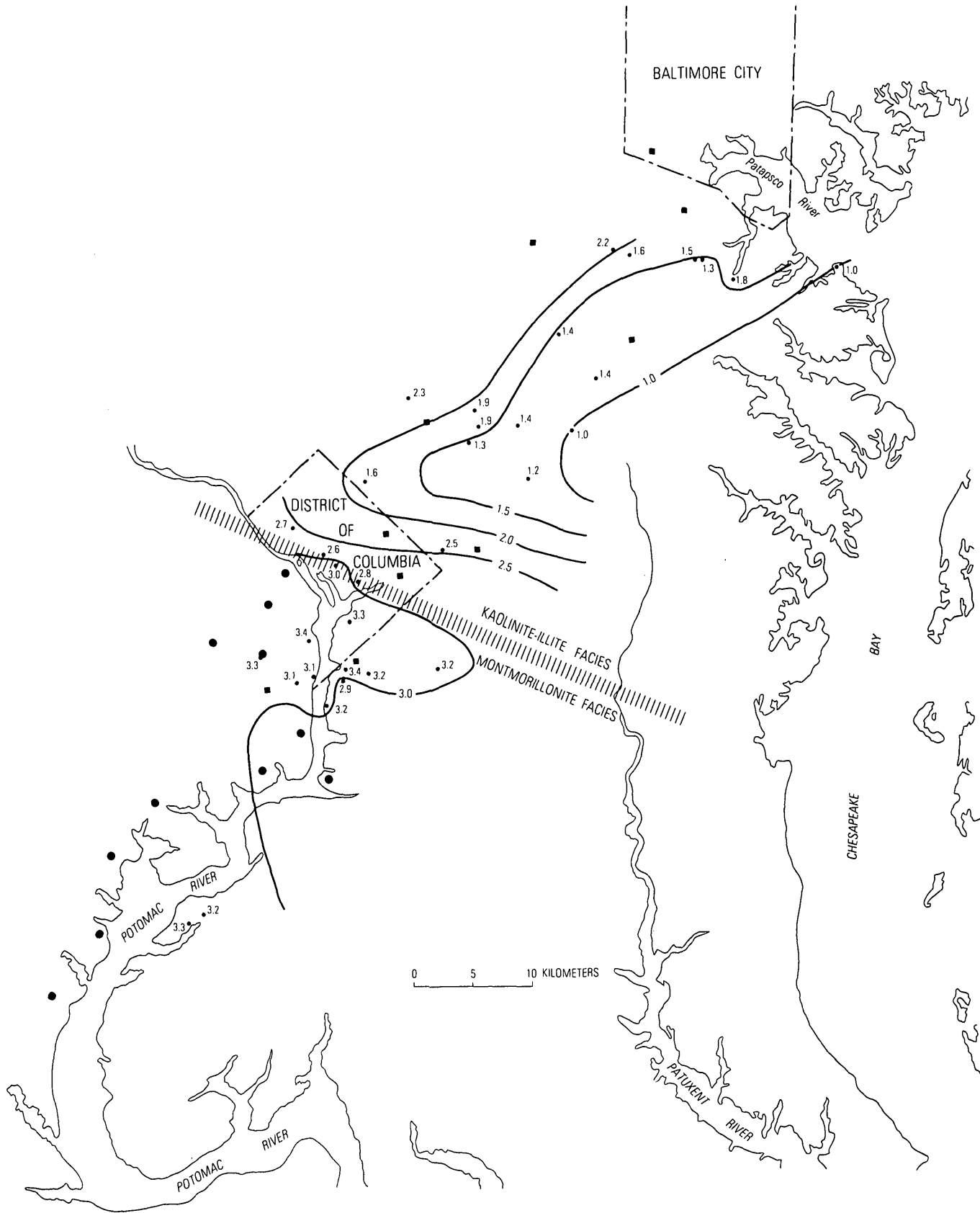


FIGURE 7.—Map showing ratios of  $\text{H}^+$  and  $\text{Ca}^{2+}$  to  $\text{H}_4\text{SiO}_4$  in ground water from the Potomac Group (Johnston, 1962; Otton, 1955). Solid circles indicate locality where montmorillonite is predominant clay mineral; solid squares indicate locality where kaolinite and illite are predominant.

Numbers over well locations represent the ratio  $\frac{\text{Log } a_{\text{Ca}^{2+}}/a_{\text{H}^{+}}}{\text{Log } [\text{H}_4\text{SiO}_4]}$ ; contour interval is 0.5.

Na<sup>+</sup> (fig. 9) and K<sup>+</sup> (fig. 10) diagrams. Some of the water samples appear to be in equilibrium with gibbsite and microcline, but most of them are in equilibrium with kaolinite. These equilibria suggest a strong tendency for alteration of potassium feldspar to kaolinite and a slight tendency for alteration of kaolinite to gibbsite (leaching).

### INTERPRETATION

An explanation of the present distribution of Potomac Group mineral assemblages must take into account (1) probable source rocks and production of clay in the source area, (2) depositional environment, and (3) postdepositional environment.

### Provenance

The likely source rocks north and west of the Potomac Group outcrop belt are metamorphic rocks (pelitic schist and granitic gneiss) for the northern facies and mafic (Mesozoic diabase) and felsic igneous rocks (Ocoquan Adamellite; Seiders and others, 1975) for the southern facies. The clay facies distribu-

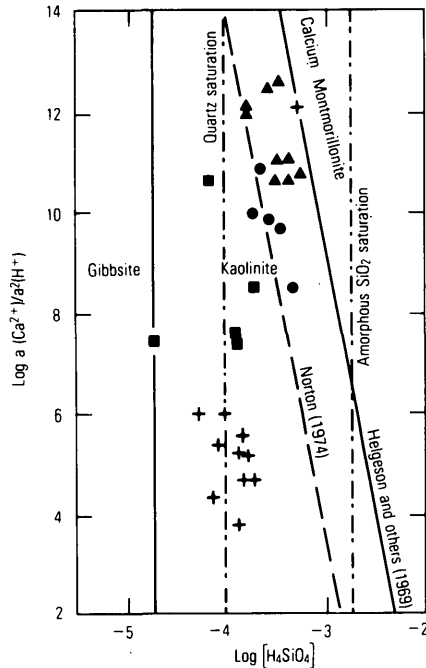


FIGURE 8.—Ground-water values from this report shown on activity diagram for part of the system  $H_2O-Al_2O_3-CaO-SiO_2$  at 25°C. (Format for this diagram from Helgeson and others, 1969, based on thermodynamic data.) Symbols for ground-water values are plus, 1.0–1.5; solid square, 1.5–2.0; no samples, 2.0–2.5; solid circle, 2.5–3.0; solid triangle, over 3.0. Dashed line determined by Norton (1974).

TABLE 2.—Concentrations of certain ions in ground water from Potomac Group wells

[Except pH, units are parts per million. Ratio values plotted on figure 7. Starred entries are from Johnston (1962); remainder are from Otton (1955)]

pH	SiO <sub>2</sub>	Ca	Na	K	$\frac{\text{Log } a \text{ Ca}^{2+}/a^{2}\text{H}^{+}}{\text{Log } [H_4SiO_4]}$
6.0	1.0	1.1	---	---	1.56
6.4	10.0	1.8	2.6	1.0	1.98
5.2	6.3	0.9	2.1	0.5	1.50
4.7	11.0	0.9	1.5	1.0	1.25
5.0	8.0	1.1	1.2	0.3	1.40
4.1	9.0	1.8	1.3	1.6	1.14
5.1	7.2	0.5	1.4	0.3	1.35
5.2	8.5	0.3	5.9	0.3	1.36
5.3	5.4	0.3	---	---	1.35
7.3	3.7	5.6	6.0	3.8	2.55
6.0	7.4	1.0	2.0	0.4	1.89
4.7	4.7	0.3	---	---	1.04
5.3	3.1	1.0	14.0	2.3	1.39
4.7	8.8	0.9	4.0	---	1.23
7.5	19.0	0.8	30.0	---	1.37
7.8	13.0	3.4	50.0	4.8	1.11
8.1	32.0	2.8	6.0	0.6	1.27
7.7	13.0	29.0	4.2	9.2	3.31
*7.8	13.0	3.4	50.0	4.8	3.15
*7.7	10.0	17.0	5.9	1.6	3.25
*7.8	21.0	1.3	53.0	2.4	3.21
*5.9	7.1	2.5	2.4	1.1	1.94
*5.2	9.9	1.7	18.0	---	1.58
7.7	34.0	1.1	60.0	2.1	3.34
7.8	27.0	0.5	77.0	2.8	3.19
7.9	19.0	5.9	88.0	7.6	3.57
*7.3	23.0	16.0	7.1	6.5	3.27
*6.7	19.0	10.0	2.8	4.7	2.80
*6.6	14.0	22.0	7.3	2.6	2.73
*6.4	33.0	32.0	13.0	5.6	2.97
*5.8	30.0	30.0	11.0	9.5	2.57
*7.3	21.0	18.0	9.4	5.5	3.06
*8.3	12.0	0.4	80.0	2.6	3.13
*8.0	24.0	1.2	60.0	0.8	3.38

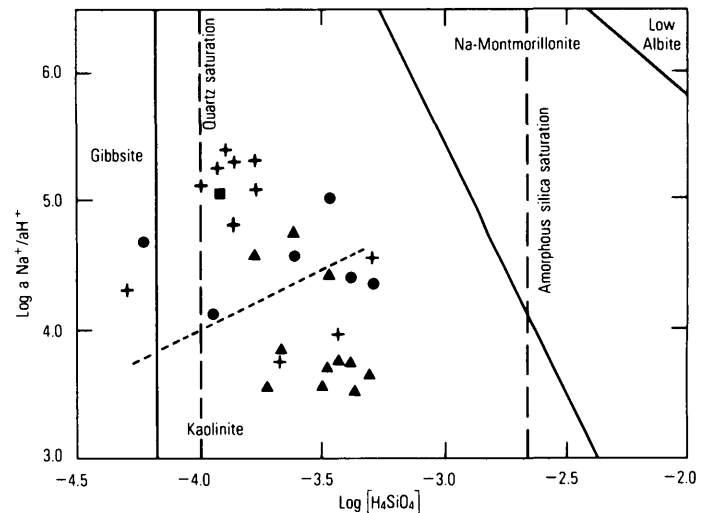


FIGURE 9.—Activity diagram for part of the system  $H_2O-Al_2O_3-Na_2O-SiO_2$  at 25°C (from Helgeson and others, 1969). Symbols as for fig. 8. Short dashed line emphasizes rough separation of higher and lower concentration ratio values (fig. 8).

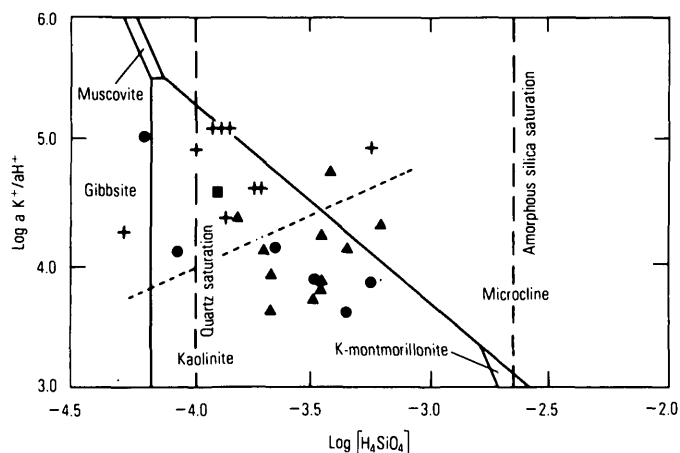


FIGURE 10.—Activity diagram for part of the system  $H_2O-Al_2O_3-K_2O-SiO_2$  at  $25^\circ C$  (from Helgeson and others, 1969). Symbols as for fig. 8. Short dashed line emphasizes rough separation of higher and lower concentration ratio values (fig. 8).

tion is probably partly related to the variation in source-rock composition: judging from the predominant minerals in source rocks and Potomac Group sediments, alumina is more abundant in the northern facies, silica and calcium in the southern facies. Quartz as such is more abundant in the north, but it is less soluble than silica in feldspars, for example, and therefore less available for recombination in weathering products (Garrels and Christ, 1965; Curtis, 1970). Available silica is more abundant in southern facies source rocks, more recombined silica is found in montmorillonite than in kaolinite or illite, and dissolved silica is more abundant in the southern facies ground water.

Different conditions can produce different weathering products from one source-rock type (figs. 11 and 12). Weathering may control the chemical and mineralogic composition of the derived sediment as much or

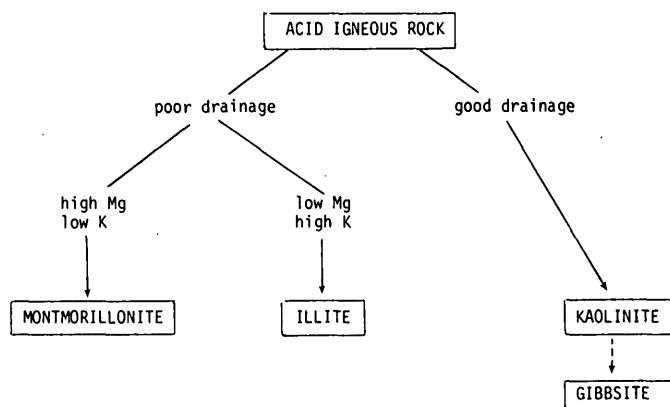


FIGURE 11.—Weathering of acid igneous rock (La Iglesia and others, 1976; Leopold and others, 1964; Garrels and Mackenzie, 1971; Millot, 1970).

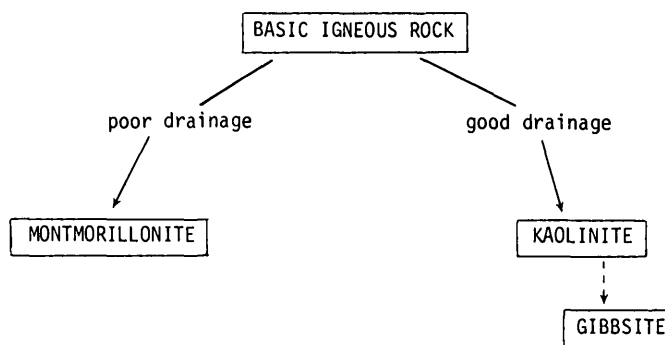
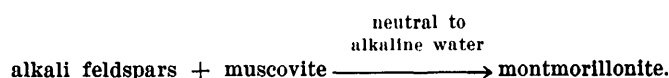


FIGURE 12.—Weathering of basic igneous rock (Wilson, 1967; Leopold and others, 1964; Garrels and Mackenzie, 1971; Mavrot and Singer, 1976; Millot, 1970).

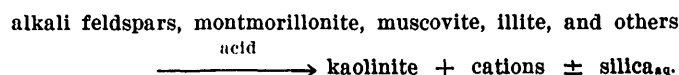
more than the composition of the source rocks. When we consider the mineralogic composition of the two Potomac Group sedimentary facies, two of the many weathering reactions appear to be particularly important. Predominant reactants were inferred from source rock composition; the solute during weathering was inferred from Leopold and others (1964); and the predominant clay products were determined from samples analyzed in this study. Reaction 1 takes place commonly in the southern facies, as follows:



Reaction 2 is predominant in the northern facies, as follows:



Kaolinite may be derived from several minerals under acid, leaching (well-drained) conditions (Garrels and Mackenzie, 1971; La Iglesia and others, 1976):



Volumetrically minor reactions such as  $\text{biotite} \rightarrow \text{kaolinite}$ , intermediate steps such as  $\text{biotite} \rightarrow \text{vermiculite-chlorite} \rightarrow \text{montmorillonite} \rightarrow \text{kaolinite}$ , and the kinetics of the reactions shown are discussed elsewhere (references cited for figs. 11 and 12).

### Depositional Environment

Orthoquartzitic sand, kaolinite and illite, and vein quartz pebbles of the northern facies were probably deposited in a well-drained basin (La Iglesia, and others, 1976).

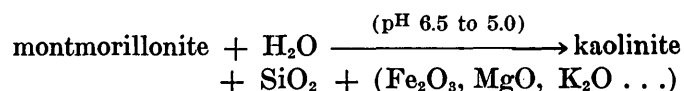
The arkose in the southern facies, with its high proportion of feldspar and interbedded montmorillonite, probably reflects an intensely weathered source,

short transport distance, and rapid deposition and burial in a poorly drained basin (Millot, 1970; Andersson and Wiklander, 1975).

### Postdepositional Alteration

#### Present ground-water equilibria

Whereas ground-water is in equilibrium with kaolinite northeast of the Potomac River, some dissolution of montmorillonite and alteration to kaolinite may be inferred from the composition of ground water (silica deficient) in the southern facies, if we assume that Helgeson's (1969) kaolinite-montmorillonite boundary is correct (fig. 8). The silica from dissolving feldspars is also in the ground water. If this contribution is removed, ground-water ion concentration values in the southern facies may fall farther into the kaolinite stability field than is shown. We have found incipient kaolinization of near-surface alkali feldspar and montmorillonite (montmorillonite increases with depth in at least two localities) in northern Virginia. Altschuler and others (1963) also documented kaolinization of montmorillonite in Florida as follows:



Norton (1974) found that his kaolinite samples fell to the left of the dashed line (fig. 8), samples containing both kaolinite and montmorillonite fell between his and Helgeson's (1969) lines, and montmorillonite samples fell to the right of Helgeson's line. In figure 8, ground-water values from Potomac Group wells show a pattern similar to Norton's values (not shown); high values ( $\blacktriangle$ ) are from the southern facies of the Potomac Group where montmorillonite in contact with flowing ground water is altering to kaolinite.

#### Persistence of montmorillonite

Both clay facies have lenses of sand within the clay units, and clay lenses surrounded by sand. Water continually moves through the sand and through the clay where it is fractured (near the surface) or contains a high proportion of silt and sand. The persistence of unstable epidote and biotite grains within the montmorillonite beds and their absence from interbedded sand show that montmorillonite units are preferentially preserved.

#### Stability of montmorillonite

Studies show that little alteration occurs with burial and compaction of mud at depths less than 1000 m (Hower and others, 1976; Burst, 1959) at least during and since the Cretaceous (Grim, 1968). In contrast, alteration of clays closely associated with sand or porous rock is notable (Milne and Earley, 1958). Apparently, montmorillonite is effectively impermeable to moving ground water, except near sand or silt interfaces and cracks.

#### Preservation of montmorillonite

Montmorillonite may owe its preservation since the Cretaceous to several factors: (1) rapid deposition and burial in a low relief or swampy environment, (2) the low permeability of montmorillonite, (3) possibly a marine overlap, and (4) a hardpan umbrella in the uppermost gravels.

Rapid deposition and burial would tend to remove the montmorillonite from contact with dilute ground water which could initiate alteration to kaolinite.

Lessening of seaward dip upward through the Cretaceous sedimentary wedge suggests gradual offshore downwarping during the Cretaceous, but well-preserved sedimentary structures in the southern facies indicate relative local stability. Tectonic stability would have tended to increase the residence time of ground water, thus permitting more calcium, magnesium, and silica to remain to equilibrate with montmorillonite.

#### Inferred development of the two clay facies

Kaolinite and illite in the northern facies can be accounted for by intense to moderate weathering of the source rocks and deposition of the weathered products in a well-drained basin. Slumped bedding suggests tectonism during deposition.

The basin in which the southern facies was deposited likely remained a topographic low after Cretaceous deposition and prior (?) to marine overlap. Low relief would have caused a lower hydrostatic head and slower movement of ground water, thus producing more alkaline conditions suitable for montmorillonite preservation.

During and since the Paleocene and Eocene, calcium and magnesium from two sources inhibited the alteration of montmorillonite to kaolinite, at least south and possibly north of Fredericksburg, Va. One source was seawater associated with marine overlap (Calver, 1963); the other was shells in the overlying marine sediments.

Later, lowering of sea level was accompanied by a major influx of fluvial gravel across the inner Coastal

Plain. Impermeable clay hardpans formed in the upper part of the gravel sheets and protected the underlying clays from intense degradation. Major dissection of the gravel sheets began in the Pleistocene.

Today, some montmorillonite in northern Virginia is altering to kaolinite because of reaction with acidic ground water; the alteration front is within a few feet of the surface.

### Summary

The kaolinite-illite clay accompanied by orthoquartzitic sand and a varied but mature heavy-mineral suite of the northern facies suggests deep weathering in the Piedmont and Appalachian metamorphic source areas to the west during the Cretaceous (Glaser, 1969). Montmorillonite clay with arkosic sand and a restricted, mature heavy-mineral suite of the southern facies reflects a nearby youthful granite source with few heavy minerals.

The clays in each facies represent primary sediments which survived change through time. Kaolinite and illite in the northern facies appear to have been stable since the Cretaceous. Persistence of montmorillonite in the southern facies is probably due to deposition under alkaline, nonleaching conditions with relatively abundant calcium and silica, and subsequent exclusion of acidic ground water because of the impermeability of montmorillonitic clay bodies.

### References Cited

- Altschuler, Z. S., Dwornik, E. J., and Kramer, H., 1963, Transformation of montmorillonite to kaolinite during weathering: *Science*, v. 141, p. 148-152.
- Andersson, A., and Wiklander, L., 1975, Release of crystal constituents by chemical weathering of some minerals: *Soil Science*, v. 120, p. 13-19.
- Brenner, G. J., 1963, The spores and pollen of the Potomac Group of Maryland: Maryland Dept. Geology, Mines and Water Resources Bull. 27, 215 p.
- Burst, J. F., Jr., 1959, Postdiagenetic clay mineral environmental relationships in the Gulf Coast Eocene: *Clays and Clay Minerals*, v. 6, p. 327-341.
- Calver, J. L., 1963, Geologic map of Virginia, 1:500,000: Virginia Dept. of Conserv. and Econ. Devel.
- Clark, W. B., 1897, Outline of present knowledge of the physical features of Maryland, embracing an account of the physiography, geology, and natural resources: Maryland Geol. Survey Repts., v. 1, p. 139-228.
- Curtis, C. D., 1970, Differences between lateritic and podzolic weathering: *Geochim. et Cosmochim. Acta*, v. 34, p. 1351-1353.
- Darton, N. H., 1947, Sedimentary formations of Washington, D.C., and vicinity: U.S. Geol. Survey Map, scale 1:31,680.
- Doyle, J. A., and Hickey, L. J., 1976, Pollen and leaves from the mid-Cretaceous Potomac Group and their bearing on early angiosperm evolution, in Beck, C. B., ed., Origin and early evolution of angiosperms: Columbia Univ. Press, p. 139-206.
- Doyle, J. A., Van Campo, M., and Lugarden, B., 1975, Observations on exine structures in *Eucommiidites* and Lower Cretaceous angiosperm pollen: *Pollen et Spores*, v. 17, p. 429-486.
- Force, L. M., 1975, Preliminary geologic map of the Coastal Plain of Fairfax County, Va.: U.S. Geol. Survey Open-File Rep. 76-415.
- Garrels, R. M., and Christ, C. L., 1965, Solutions, minerals, and equilibria: New York, Harper and Row, 450 p.
- Garrels, R. M., and Mackenzie, F. T., 1971, Evolution of sedimentary rocks: New York, Norton, 397 p.
- Glaser, J. D., 1969, Petrology and origin of Potomac and Magothy (Cretaceous) sediments, Middle Atlantic Coastal Plain: Maryland Geol. Survey Rept. Inv., no. 11, 101 p.
- Grim, R. E., 1968, Clay mineralogy [2d ed.]: New York, McGraw-Hill, 596 p.
- Hack, J. T., 1975, Prince Georges County geologic map for land use planning: U.S. Geol. Survey Open-File Map 75-208.
- Helgeson, H. C., Brown, T. H., and Leeper, R. H., 1969, Handbook of theoretical activity diagrams depicting chemical equilibria in geologic systems involving an aqueous phase at one atm. and 0° to 300°C: New York, Freeman, Cooper & Co., 253 p.
- Hower, J., Eslinger, E. V., Hower, M. E., and Perry, E. A., 1976, Mechanism of burial metamorphism of argillaceous sediments: 1. Mineralogical and chemical evidence: *Geol. Soc. Amer. Bull.*, v. 87, p. 725-737.
- Johnston, P. M., 1962, Geology and groundwater resources of Washington, D.C. and vicinity: U.S. Geol. Survey Water-Supply Paper 1776, 97 p.
- Knechtel, M. M., Hamlin, H. P., Hosterman, J. W., and Carroll, Dorothy, 1961, Physical properties of nonmarine Cretaceous clays in the Maryland Coastal Plain: Maryland Dept. Geology, Mines and Water Resources Bull. 23, 11 p.
- La Iglesia, A., Martin-Vivaldi, J. L., Jr., and Aguayo, F. L., 1976, Kaolinite crystallization at room temperature by homogeneous precipitation—III: Hydrolysis of feldspars: *Clays and Clay Minerals*, v. 24, p. 36-42.
- Leopold, L. B., Wolman, M. G., and Miller, J. P., 1964, Fluvial processes in geomorphology: San Francisco, Freeman and Co., 522 p.
- McGee, W. J., 1888, Three formations of the middle Atlantic slope: *Am. Jour. Sci.*, 3d ser., v. 35, p. 120-143, 328-388, 448-466.
- Millot, G., 1970, Geology of clays; translated by Farrand, W. R., and Paquet, H.: New York, Springer-Verlag, 429 p.
- Milne, I. H., and Earley, J. W., 1958, Effect of source and environment on clay minerals: *Am. Assoc. Petroleum Geologists Bull.*, v. 42, p. 328-338.
- Minard, J. P., Perry, W. J., Weed, E. G. A., Rhodehamel, E. C., Robbins, E. I., and Mixon, R. B., 1974, Preliminary report on geology along the Atlantic continental margin of the northeastern United States: *Am. Assoc. Petroleum Geologists Bull.* v. 58, p. 1169-1178.
- Mixon, R. B., Southwick, D. L., and Reed, J. C., Jr., 1972, Geologic map of the Quantico quadrangle, Prince William and Stafford Counties, Va., and Charles County, Md., U.S. Geol. Survey Geol. Quad. Map GQ-1044 [1973].

- Morgan, B. A., 1972, Metamorphic map of the Appalachians: U.S. Geol. Survey Misc. Geol. Inv. Map I-724.
- Navrot, J. and Singer, A., 1976, Geochemical changes accompanying basic igneous rocks—clay transition in a humid Mediterranean climate: *Soil Sci.*, v. 121, p. 337-345.
- Norton, D., 1974, Chemical mass transfer in the Rio Tanama system, west-central Puerto Rico; *Geochim. et Cosmochim. Acta*, v. 38, p. 267-277.
- Otton, E. G., 1955, Groundwater resources of southern Maryland Coastal Plain: Maryland Dept. Geology Mines and Water Resources Bull. 15, 347 p.
- Owens, J. P., 1969, Coastal Plain rocks of Harford County, in Southwick, D. L., Owens, J. P., and Edwards, Jonathan, Jr., *The geology of Harford County, Maryland*: Baltimore, Maryland Geol. Survey, p. 77-103.
- Seiders, V. M., Mixon, R. B., Stern, T. W., Newell, M. F., and Thomas, C. B., Jr., 1975, Age of plutonism and tectonism and a new minimum age limit on the Glenarm series in the northeast Virginia Piedmont near Occoquan: *Am. Jour. Sci.*, v. 275, p.481-511.
- U.S. Geological Survey, 1967, Engineering geology of the Northeast Corridor, Washington, D.C., to Boston, Massachusetts—Coastal Plain and surficial deposits: U.S. Geol. Survey Misc. Geol. Inv. Map I-514-B, 8 sheets, scale 1:500,000.
- Weed, E. G. A., Minard, J. P., Perry, W. J., Jr., Rhodehamel, E. C., and Robbins, E. I., 1974, Generalized pre-Pleistocene geologic map of the northern United States Atlantic continental margin: U.S. Geol. Survey Misc. Inv. Map I-861, 2 sheets, scale 1:1,000,000.
- Weir, G. W., 1976, Crossbedding of the Potomac Formation in Fairfax County, Virginia: U.S. Geol. Survey Open-File Rept. 76-193.
- Wilson, M. J., 1967, The clay mineralogy of some soils derived from a biotite-rich quartz-gabbro in the Strathdon area, Aberdeenshire: *Clay Minerals*, v. 7, p. 91-100.

## HEAVY-MINERAL VARIABILITY IN THE BALTIMORE CANYON TROUGH AREA

By HARLEY J. KNEBEL and DAVID C. TWICHELL, Woods Hole, Mass.

*Abstract.*—Petrographic analyses of bottom sediments from 87 stations within a relatively large subarea (1700 square kilometers) define the local variability and the distributional processes of heavy minerals in the Baltimore Canyon Trough area (13 500 km<sup>2</sup>). Of the 29 mineral groups that were identified, those most diagnostic of differences between stations were opaque minerals, garnet, hornblende, orthopyroxene, other amphiboles, and staurolite. Some of the common components cannot be used to define areal trends. The association of minerals by their specific gravities reflects the modern reworking and sorting of sediments in this area. The poor correlation between mineral abundance and the ridge-and-trough topography suggests either that our analyses and samples did not resolve bathymetrically induced changes or that smaller bed forms (such as ripples) largely control the heavy-mineral distribution. Data from this study provide a baseline for evaluating manmade disturbances of the bottom sediments and show that relatively large changes in the heavy-mineral composition can take place over small distances on this part of the Continental Shelf.

The heavy-mineral assemblages in grab samples were examined as part of a comprehensive study of the surficial sand sheet in the Baltimore Canyon Trough area (fig. 1). Previous studies of the heavy-mineral distribution in this area either have been of a regional nature (Hubert and Neal, 1967; Ross, 1970; Milliman and others, 1972) or, if localized, have discussed data qualitatively (Frank and Friedman, 1973; Stubblefield and others, 1975). Until now, quantitative estimates of the local heavy-mineral variability were lacking.

In this paper, we evaluate the changes in the heavy minerals within one subarea (1700 square kilometers) that may be leased for oil exploration (fig. 1). By studying this subarea in detail, we sought to determine the kinds and amounts of heavy minerals in the sediments as well as to make some inferences about the processes that have affected the heavy-mineral variability in the Baltimore Canyon Trough area (13 500 km<sup>2</sup>).

The topography within the subarea is typical of this section of the Outer Continental Shelf as shown in figure 1 (Swift and others, 1972; Knebel and Spiker, 1977). The northwestern part is a plateau that ranges in depth from 34 to 48 meters and includes several

small ridges and troughs (3-4 m relief). The southeastern part, on the other hand, is 50-74 m deep and contains several prominent ridges (8-10 m relief) in addition to many smaller undulations. The zone that separates the two parts of the subarea has a declivity of 0.5° to 2.0° and is 0.4-2.4 kilometers wide; it is known as the Tiger Scarp (U.S. Coast and Geodetic Survey and U.S. Bureau of Commercial Fisheries, 1967).

*Acknowledgments.*—We thank D. A. Ross of the Woods Hole Oceanographic Institution and O. H. Pilkey of Duke University for their critical reviews of the manuscript. The samples were collected aboard the R/V *Mt. Mitchell* in cooperation with the National Oceanic and Atmospheric Administration.

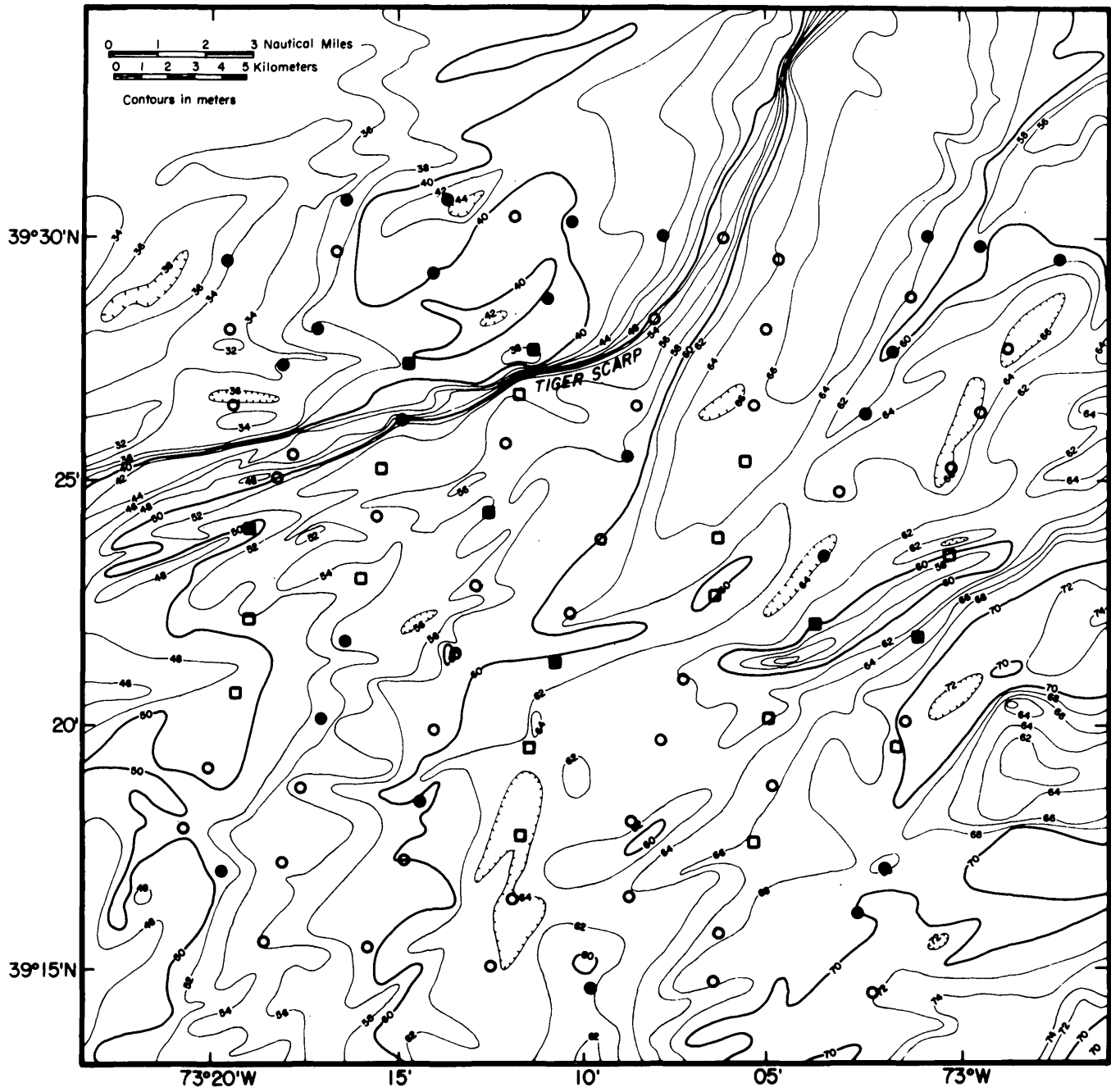
### METHODS

Bottom-sediment samples were collected at 87 stations during May 23-24, 1974, by means of a Smith-McIntyre sampler (Smith and McIntyre, 1954). The choice of station locations was based on both the bathymetry and the attainment of areal coverage (fig. 1). Stations were located by using automatic-tracking loran-C receivers.

At least one sample of the upper 30 millimeters of the sediments was obtained at each station. Replicate samples were collected at 21 stations (fig. 1) by twice lowering the sampler and then taking two subsamples from each grab.

In the laboratory, the heavy minerals were separated from the 125- to 250-micrometer (2 to 3- $\phi$ <sup>1</sup>)-size fraction by using a solution of tetrabromoethane and dimethyl formamide (specific gravity = 2.82-2.86). After the separation, the heavy- and light-mineral fractions were weighed; then, the heavy fractions were mounted on slides in Cadex (refractive index = 1.65) for identification and counting under a petrographic microscope. The ribbon counting method (Galehouse, 1971) was used to estimate the mineral frequency. At least 400 heavy-mineral grains were identified and counted in each slide.

<sup>1</sup>A  $\phi$  unit ( $\phi$ ) is the negative logarithm to the base 2 of the particle diameter in millimeters.



STATION	}	● Opaque or Garnet Dominant	} One Sample
		○ Hornblende Dominant	
LOCATIONS	}	■ Opaque or Garnet Dominant	} Replicate Samples
		□ Hornblende Dominant	

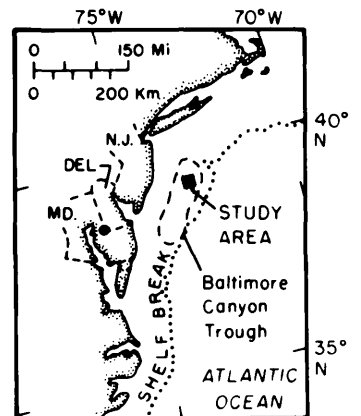


FIGURE 1.—Bathymetric map of the study area, showing locations and kinds of sample stations and the dominant heavy-mineral component at each station. Index map locates the study area within the Baltimore Canyon Trough area. Bathymetry from Knebel and Spiker (1977).

DISCUSSION OF RESULTS

Twenty-nine minerals or mineral groups were identified in the slides. The common constituents, which account for at least 90 percent of the total assemblage, are opaque minerals, garnet, hornblende, rock fragments, clinopyroxene, orthopyroxene, altered grains, other amphiboles (exclusive of hornblende), staurolite, and tourmaline (table 1). Of these, opaque minerals, garnet, and hornblende are dominant. Minerals that are present in trace amounts (< 2 percent) include anatase, andalusite, apatite, brookite, cassiterite, chlorite, corundum, dumortierite, epidote, glauconite, kyanite, monazite, olivine, rutile, siderite, sillimanite, sphene, spinel, and zircon.

To assess the sources of variation for the common heavy-mineral components, we first had to determine whether the observed variability reflected real differences between stations or only local differences at a station. We made this determination by subjecting the data from the replicate samples to a three-level hierarchical analysis of variance (table 2). In each analysis, two *F*-ratios were calculated. The first ratio compares the variability between stations with that within stations, whereas the second *F*-value compares the variation between grabs (at a station) with that between subsamples (within grabs).

TABLE 1.—Range, mean, and standard deviation of the common heavy-mineral components within the 125- to 250- $\mu$ m (2-3- $\phi$ )-size fraction of surface sediments from 87 stations [Mineral components are in percent as determined by grain counts]

Component	Minimum	Maximum	Mean	Standard deviation
Opaque minerals	4.8	57.7	18.8	10.7
Garnet	11.3	33.9	22.0	5.1
Hornblende	13.1	49.3	29.5	7.3
Rock fragments	.5	10.9	5.4	2.3
Clinopyroxene	0	13.9	4.5	2.6
Orthopyroxene	1.5	7.8	4.8	1.4
Altered grains	.5	8.4	3.6	1.6
Other amphiboles	.2	7.0	2.6	1.5
Staurolite	0	6.2	2.1	1.4
Tourmaline	0	3.0	0.7	0.6
Heavy fraction (weight percent)	5.2	48.1	19.5	10.5

The results of the analyses of variance show that, of the 10 common constituents, only the percentages of opaque minerals, garnet, hornblende, orthopyroxene, other amphiboles, and staurolite may be used to distinguish between stations. For these variables, the first *F*-ratios are highly significant. On the other hand, the percentages of rock fragments, clinopyroxene, altered grains, and tourmaline are highly ineffective variables. The decreased effectiveness of these groups in differentiating between stations is due to

TABLE 2.—Analysis of variance for 10 common heavy mineral components in replicate samples from 21 stations

SV	SS	df	MS	F	SV	SS	df	MS	F
<b>Opaque minerals</b>					<b>Orthopyroxene</b>				
Stations	8972.39	20	448.62	5.07***	Stations	68.03	20	3.40	3.00***
Grabs	1859.34	21	88.54	2.01**	Grabs	23.82	21	1.13	0.94
Subsamples	1850.46	42	44.06		Subsamples	50.76	42	1.21	
Total	12682.19	83			Total	142.61	83		
<b>Garnet</b>					<b>Altered grains</b>				
Stations	1434.89	20	71.74	4.48***	Stations	47.97	20	2.40	0.91
Grabs	336.09	21	16.00	2.04**	Grabs	55.56	21	2.65	2.32**
Subsamples	329.70	42	7.85		Subsamples	47.97	42	1.14	
Total	2100.68	83			Total	151.50	83		
<b>Hornblende</b>					<b>Other amphiboles</b>				
Stations	5592.13	20	279.61	9.14***	Stations	87.40	20	2.87	2.34***
Grabs	642.43	21	30.59	1.70*	Grabs	25.75	21	1.23	0.59
Subsamples	754.36	42	17.96		Subsamples	86.87	42	2.07	
Total	6988.92	83			Total	170.02	83		
<b>Rock fragments</b>					<b>Staurolite</b>				
Stations	86.95	20	4.35	0.53	Stations	75.94	20	3.80	9.74***
Grabs	171.75	21	8.18	1.70*	Grabs	8.19	21	0.39	0.96
Subsamples	201.76	42	4.80		Subsamples	17.06	42	0.41	
Total	460.46	83			Total	101.19	83		
<b>Clinopyroxene</b>					<b>Tourmaline</b>				
Stations	70.80	20	3.54	0.72	Stations	3.76	20	0.19	1.76
Grabs	102.67	21	4.89	1.63*	Grabs	2.25	21	0.11	0.51
Subsamples	126.35	42	3.01		Subsamples	8.87	42	0.21	
Total	299.82	83			Total	14.88	83		

SV = Source of variation; SS = Sums of squares; MS = Mean square; F = Snedecor's F Value; df = Degrees of freedom

df (Stations) = n-1 = 20  
df (Grabs) = n(g-1) = 21  
df (Subsamples) = ng(s-1)

\* Significant with 90 percent confidence  
\*\* Significant with 95 percent confidence  
\*\*\* Significant with 99 percent confidence

n = number of stations = 21  
g = number of grabs per station = 2  
s = number of subsamples per grab = 2

relatively large variations either between grabs at a station or between subsamples from a grab.

Previous textural studies by Frank and Friedman (1973), Hollister (1973), McClennen (1973), Knebel (1975), and Stubblefield and others (1975) have shown that the surface sediments in the Baltimore Canyon Trough area have been, or are still being, reworked and sorted. To discern the effect of this reworking and sorting on the heavy-mineral variability, we calculated the correlation coefficients for those heavy minerals that effectively distinguish differences among stations (table 3). The correlation coefficient commonly is used in statistics as a measure of the degree to which variables are associated. In our analysis, we also included the amount (by weight) of

TABLE 3.—Matrix of correlation coefficients for selected heavy-mineral variables

[Values computed from 87 samples, one from each station. Absolute values greater than 0.28 are significant with at least 99-percent confidence. Absolute values greater than 0.50 indicate the highest degree of similarity or dissimilarity between variables and have been enclosed in boxes]

Variable	Opaque	Garnet	Hornblende	Orthopyroxene	Other amphiboles	Staurolite
Heavy fraction (weight percent)	<b>0.60</b>	0.25	<b>-0.53</b>	-.20	-.27	-.24
Staurolite	-.43	.40	-.13	-.30	-.35	
Other amphiboles	-.20	-.45	<b>0.52</b>	.27		
Orthopyroxene	-.36	-.43	<b>0.56</b>			
Hornblende	<b>-0.68</b>	<b>-0.60</b>				
Garnet		.18				

the heavy minerals in the 125- to 250- $\mu\text{m}$ -size fraction. For reworked sediments, this variable should be an indicator of winnowing.

The matrix of correlation coefficients (table 3) clearly reflects the sorting of heavy minerals by specific gravity. Accordingly, opaque minerals (sp gr  $> 4.0$ ) and garnet (sp gr = 3.8) are negatively correlated with hornblende (sp gr = 3.2), suggesting the tendency for hornblende to occur apart from these heavier mineral groups. Hornblende, on the other hand, is positively correlated with other amphiboles and with orthopyroxene, which have similar specific gravities. This relationship suggests that these minerals tend to be together. Staurolite (sp gr = 3.7) is most closely associated with garnet, which has a similar specific gravity; it is negatively correlated with all other variables. Finally, opaque minerals and the weight of the heavy fraction have a strong positive correlation. This correspondence probably reflects the concentration of opaque minerals in the sediments at locations where lighter grains have been winnowed.

One might argue that the association of mineral groups by specific gravity is only symptomatic of grain-size differences within the 125- to 250- $\mu\text{m}$  (2-3- $\phi$ )-size fraction. To assess the effect of size on mineral abundance, the percentages of the composite weight for the 210- $\mu\text{m}$  (2.25- $\phi$ ), the 176- $\mu\text{m}$  (2.50- $\phi$ ), and the 148 plus 125- $\mu\text{m}$  (2.75 plus 3.00- $\phi$ )-size fractions were determined for those samples that had the 10 highest percentages of opaque minerals, garnet, and hornblende. The results were then plotted on a ternary diagram (fig. 2). Nearly all samples plot as a group,

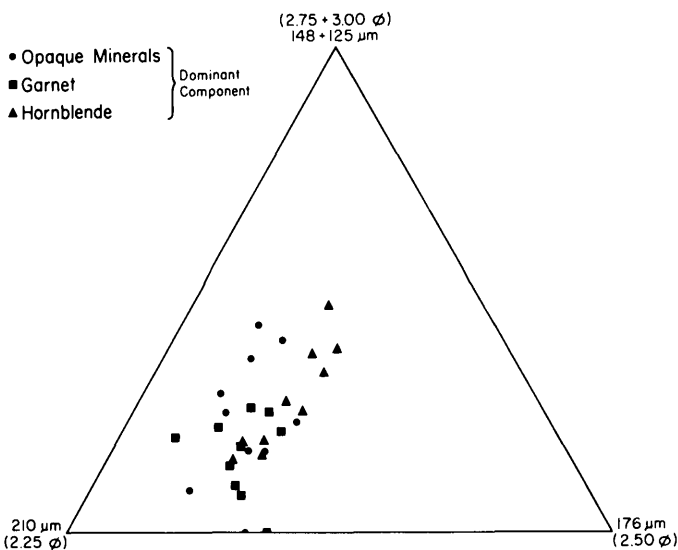


FIGURE 2.—Relationship of groups of samples (with the 10 highest percentages of opaque minerals, garnet, and hornblende) to the percentages of the composite weight of the 210- $\mu\text{m}$  (2.25- $\phi$ ), 176- $\mu\text{m}$  (2.50- $\phi$ ), and 148 plus 125- $\mu\text{m}$  (2.75 plus 3.00- $\phi$ )-size fractions in analyzed surface samples.

most being enriched in sediments of the 210- $\mu\text{m}$ -size fraction. Because no set of samples has marked textural differences, grain size probably has an insignificant effect on the mineral content.

The areal distribution of the heavy-mineral components is not closely associated with the ridge-and-trough topography of the study area. Distributional maps of individual constituents as well as data derived from factor analysis failed to elucidate a more geologically meaningful pattern than that outlined by a simple plot of the dominant component in each sample (fig. 1). This plot shows that opaque minerals or garnet are dominant in most samples from atop the Tiger Scarp and a large linear ridge in the northeastern part of the study area. Otherwise, hornblende dominates the suite except at scattered locations.

The dominance of opaque minerals and garnet atop ridges can readily be explained by winnowing. However, the poor correlation between the mineralogy and the more subdued topography may reflect several factors. First, mineralogic changes, if any, may have been too subtle to be discerned by our analyses. Second, the spacing of sample locations may have been too great to detect bathymetrically induced changes. Finally, the ridges and troughs may not completely control the mineral distribution. Knebel and others (1976), for example, have shown that ripples are rapidly formed and modified within the study area by wave-induced oscillatory flow. Similarly, McKinney, Stubblefield, and Swift (1974) found low-relief ( $< 1.5$  m) textural lineations that have been superimposed on the ridge-and-trough topography of the central New Jersey Continental Shelf. Small bed forms such as these may produce pronounced changes in the heavy-mineral distribution over short distances.

## IMPLICATIONS

This study provides baseline data that might be used to evaluate manmade disturbances of the bottom sediments in the Baltimore Canyon Trough area. Here, we not only document the kinds of heavy minerals that are present in the 125- to 250- $\mu\text{m}$ -size fraction of the sediments but also provide estimates of the variability of these minerals. Without variability estimates, inferred changes based on later sampling would be only conditional because the magnitude of local mineralogic differences would be unknown. We consider the variability that we found in this study to be typical of the entire Baltimore Canyon Trough area. Indeed, we collected a set of samples in a traverse across the outer shelf about 75 km south of the study area and found that the kinds and abundances of the heavy minerals in these samples agree with the data

presented here. Disturbances of the bottom sediments in the Baltimore Canyon Trough area may arise from such activities as the emplacement of structures and pipelines, sand-mining operations, and waste disposal.

The kinds, amounts, and variability of the heavy minerals are also characteristic of the modern sedimentary environment in the Baltimore Canyon Trough area. In particular, the sorting of heavy minerals by specific gravity reflects the modern reworking of the sediments on this part of the shelf. By comparing the heavy minerals present at the surface with those present in subsurface samples (from drilling and coring), one might be able to distinguish between relict and modern deposits.

Estimates of the within-station variance indicate which heavy-mineral variables provide the best discrimination between stations. The present study shows that some variables are ineffective because the differences between samples at a station are large. However, those variables that are diagnostic of between-station differences can reliably be used as indicators of regional mineralogic changes. A determination of the effectiveness of variables is useful in any areal study of heavy minerals, but it is crucial for those components of interest that have small regional differences.

Finally, this study demonstrates that relatively large changes in the heavy-mineral composition can occur within a small area of the shelf (table 1). Often, in regional surveys, one or perhaps a few samples may represent an area the size of the study area, yet the range of values that we found for some components in this study is so large that no single sample could be considered typical of the entire area. Local variations, therefore, should be kept in mind when interpreting the results of regional surveys.

#### REFERENCES CITED

- Frank, W. M., and Friedman, G. M., 1973, Continental-shelf sediments off New Jersey: *Jour. Sed. Petrology*, v. 43, no. 1, p. 224-237.
- Galehouse, J. S., 1971, Point counting, in Carver, R. E., ed., *Procedures in sedimentary petrology*: New York, Wiley-Interscience, p. 385-407.
- Hollister, C. D., 1973, Atlantic Continental Shelf and Slope of the United States—Texture of surface sediments from New Jersey to southern Florida: U.S. Geol. Survey Prof. Paper 529-M, 23 p.
- Hubert, J. F., and Neal, W. F., 1967, Mineral composition and dispersal patterns of deep-sea sands in the western North Atlantic petrologic province: *Geol. Soc. America Bull.*, v. 78, no. 6, p. 749-771.
- Knebel, H. J., 1975, Significance of textural variations, Baltimore Canyon Trough area: *Jour. Sed. Petrology*, v. 45, no. 4, p. 845-851.
- Knebel, H. J., and Spiker, Elliott, 1977, Thickness and age of the surficial sand sheet, Baltimore Canyon Trough area: *Am. Assoc. Petroleum Geologists Bull.*, v. 61, no. 6, p. 861-871.
- Knebel, H. J., Butman, Bradford, Folger, D. W., Cousins, P. W., and McGirr, R. R., 1976, Maps and graphic data related to geologic hazards in the Baltimore Canyon Trough area: U.S. Geol. Survey Misc. Field Studies Map MF-828, 3 sheets.
- McClennen, C. E., 1973, Nature and origin of the New Jersey continental shelf topographic ridges and depressions: Rhode Island Univ., Kingston, Ph.D. thesis, 94 p.
- McKinney, T. F., Stubblefield, W. L., and Swift, D. J. P., 1974, Large-scale current lineations on the central New Jersey shelf—Investigations by side-scan sonar: *Marine Geology*, v. 17, no. 2, p. 79-102.
- Milliman, J. D., Pilkey, O. H., and Ross, D. A., 1972, Sediments of the continental margin off the Eastern United States: *Geol. Soc. America Bull.*, v. 83, no. 5, p. 1315-1334.
- Ross, D. A., 1970, Atlantic Continental Shelf and Slope of the United States—Heavy minerals of the continental margin from southern Nova Scotia to northern New Jersey: U.S. Geol. Survey Prof. Paper 529-G, 40 p.
- Smith, W., and McIntyre, A. D., 1954, A spring-loaded bottom sampler: *Jour. Marine Biol. Assoc.*, v. 33, p. 257-264.
- Stubblefield, W. L., Lavelle, J. W., and Swift, D. J. P., 1975, Sediment response to the present hydraulic regime on the central New Jersey shelf: *Jour. Sed. Petrology*, v. 45, no. 1, p. 337-358.
- Swift, D. J. P., Kofoed, J. W., Saulsbury, F. P., and Sears, Phillip, 1972, Holocene evolution of the shelf surface, central and southern Atlantic shelf of North America, in Swift, D. J. P., Duane, D. B., and Pilkey, O. H., eds., *Shelf sediment transport—Process and pattern*: Stroudsburg, Pa., Dowden, Hutchinson, and Ross, Inc., p. 499-574.
- U.S. Coast and Geodetic Survey and U.S. Bureau of Commercial Fisheries, 1967, Bathymetric map, Hudson Canyon (0807N-52): Washington, D.C., U.S. Coast and Geod. Survey, scale 1:125 000.



## STABLE ISOTOPE STUDIES OF BEDDED BARITE AT EAST NORTHUMBERLAND CANYON IN TOQUIMA RANGE, CENTRAL NEVADA

By R. O. RYE, D. R. SHAW, and F. G. POOLE, Denver, Colo.

**Abstract.**—Several beds of barite occur in the Slaven Chert at East Northumberland Canyon in the Toquima Range of central Nevada. Most of the barite is internally laminated but shows massive weathering. However, rosette, disseminated, conglomeratic, and concretionary varieties also occur. New fossil evidence from conodonts and brachiopods indicates a Late Devonian age for the Slaven Chert at East Northumberland Canyon. Preliminary  $\delta^{34}\text{S}$  values of most disseminated and massive-laminated barite within the Slaven Chert average about 25 permil; these are within the range of values that is typical of sulfate from Late Devonian seawater and are distinctly different from  $\delta^{34}\text{S}$  values of most crosscutting hydrothermal barite veins in the area. Primary  $\delta^{34}\text{S}$  values of the bedded barite appear to be retained during recrystallization and hydrothermal alteration, suggesting that  $\delta^{34}\text{S}$  data of bedded barites could be developed into a useful stratigraphic tool. The  $\delta^{34}\text{S}$  values of rosette and concretionary barites range from 29.1 to 56.3 permil and indicate that these varieties of barite formed in restricted microenvironments where extensive bacterial reduction of seawater sulfate occurred. The  $\delta^{18}\text{O}$  data on cherts associated with the barite beds and  $\delta^{13}\text{C}$  and  $\delta^{18}\text{O}$  data on carbonate beds within the Slaven Chert indicate that the depositional environment at times had restricted communication with normal seawater of the open ocean.

Bedded barite deposits at East Northumberland Canyon, Nye County, Nev., have produced about 500 000 tons of drilling-grade barite since their discovery by a U.S. Geological Survey field party in 1967. Preliminary geologic, geochemical, and mineralogic studies of the deposits were made by Shawe and others (1967, 1969), who concluded from field evidence that the bedded barite deposits were of syngenetic-diagenetic origin.

The purpose of this paper is to present preliminary stable isotope data and other data that pertain to the age and origin of the East Northumberland Canyon deposits. These deposits occur in a bedded barite province that forms a wide belt through central Nevada (fig. 1) and is associated with transitional and eugeosynclinal rocks of Cambrian, Ordovician, and Devonian age. This study is part of a larger project to investigate the origin of barite at East Northumberland

Canyon and elsewhere in Nevada and to evaluate the resource potential of the bedded barite province.

### GEOLOGIC SETTING

A geologic map of part of the Toquima Range is presented in figure 2. The bedded deposits at East Northumberland Canyon lie in the northern part of the Toquima Range and consist of a dark-gray barite

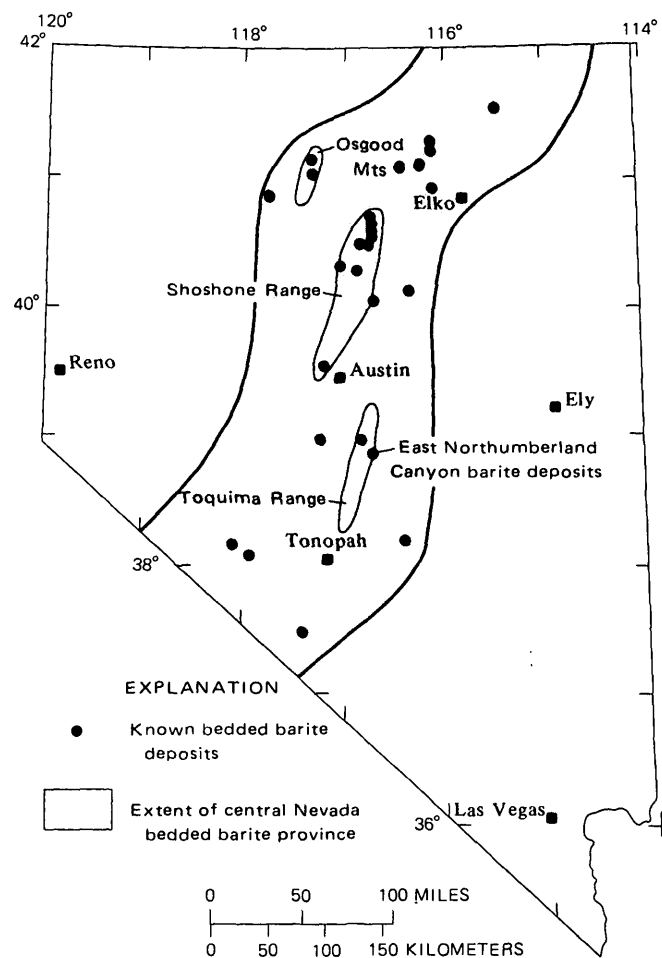


FIGURE 1.—Locality map of Nevada showing known bedded barite deposits and bedded barite province.



FIGURE 2.—Generalized geologic map of the East Northumberland Canyon area showing sample localities. Base from U.S. Geological Survey Northumberland Pass topographic quadrangle map, scale 1:24 000, 1971.

unit approximately 18 meters thick and thinner barite units, which contain some intercalated chert and shaly mudstone and which are part of an allochthonous eugeosynclinal sequence composed principally of dark-gray and black chert and siliceous mudstone of the Devonian Slaven Chert. Deposits which are believed to be equivalent occur on both the north and south sides of the canyon near its mouth. Other bedded barite deposits are found at the Lost Soldier property in the upper drainage area of West Northumberland Canyon on the west side of the Toquima Range. These deposits, which are probably equivalent to those near the mouth of East Northumberland Canyon, have been slightly recrystallized in places due to the thermal effect of a nearby Jurassic pluton. Between the East and West Northumberland bedded barite deposits, clear barite crystals occur as fracture fillings near the Northumberland gold deposit south of Northumberland Pass. All of these barite occurrences were analyzed in this study.

The marine beds that contain bedded barite in East Northumberland Canyon were assigned to Ordovician strata by Kay and Crawford (1964). Since then, these beds have been recognized as the Slaven Chert of Middle and Late(?) Devonian age. However, new fossil evidence now indicates the age of the Slaven spans much of the Devonian (J. T. Dutro, Jr., written commun., 1977). A conodont fauna of very late Devonian age has been obtained from a thin impure cherty limestone layer near the base of the allochthonous eugeosynclinal sequence in the canyon (Poole and Sandberg, 1975). In addition, a fragmentary brachiopod valve possibly belonging to the Famennian (late Late Devonian) rhychonelloid genus *Dzieduszyckia* has been found in a conglomeratic barite bed (Poole and Sandberg, 1975). Numerous attached pedicle and brachial valves of *Dzieduszyckia* were seen in a single horizon in bedded barite of the Slaven Chert in the Shoshone Range, north-central Nevada. Many of the brachiopod shells, which are well preserved and similarly oriented, appear to have been buried at or near their normal habitat. Cloud and Boucot (1971) reported *Dzieduszyckia* in the Slaven Chert at several localities in the Shoshone Range. The Slaven Chert in this area is in part a sedimentary facies and is the time equivalent of the barite-bearing section at East Northumberland Canyon.

Eugeosynclinal siliceous rocks several hundred meters thick were deposited in northern California and western Nevada during the late Devonian; then, in latest Devonian time (during the Antler orogeny), they were tectonically transported eastward into thrust contact with transitional and miogeosynclinal, dominantly carbonate rocks of comparable (locally greater)

thickness (Poole and others, 1967). The Antler orogeny may have resulted from a possible increased subduction rate beneath an offshore island arc along the western margin of the eugeosynclinal basin near the end of Devonian time. If this inferred plate-tectonic model is correct, the Late Devonian eugeosyncline would have occupied a marginal ocean basin between the continental edge and the island arc (Poole, 1974). The absence of recognizable Antler orogenic sediment in the Upper Devonian eugeosynclinal deposits indicates that initial downwarping of the marginal ocean basin was mild and that only a small volume, if any, of orogenic sediments was deposited in the Slaven Chert. The Upper Devonian carbonate shelf or miogeosyncline east of the eugeosyncline was characterized by a marked north-northeast-trending belt of thick carbonate deposits (Poole and others, 1967, figs. 9, 10). The eugeosynclinal facies are being further evaluated to provide a better understanding of the depositional setting and origin of the bedded barite and chert deposits.

#### EVIDENCE OF A SYNGENETIC-DIAGENETIC ORIGIN

A syngenetic-diagenetic origin of the bedded barite at East Northumberland Canyon is indicated by several lines of evidence. The bedded barite, consisting of several varieties including massive-laminated,<sup>1</sup> disseminated, rosette, conglomeratic, and concrectionary barite, displays features of primary sedimentation and early diagenesis. The barite rosettes were formed by growth of radiating barite blades and commonly nucleated on radiolarian tests, which suggests they were formed on the sea floor or in soft pelagic sediments. Graded bedding in barite beds is evident where bedding layers of rosettes decrease in size upward and grade into fine-grained massive-laminated barite. Conglomeratic barite that contains angular and rounded clasts of broken barite rock and chert, fragmental large barite rosettes, and phosphatic nodules is intercalated with beds of massive-laminated and rosette barite; this relationship attests to erosion and resedimentation during barite deposition. Barite concretions in mudstone may have been segregated during early diagenesis from mudstone containing disseminated barium and sulfate.

A <sup>87</sup>Sr/<sup>86</sup>Sr ratio of 0.7083 for a massive-laminated dark-gray barite sample from the south side of East Northumberland Canyon is consistent with a marine origin for the barite, although the ratio is also within the range of ratios for Cenozoic volcanic rocks in the region (C. E. Hedge, written commun., 1974).

<sup>1</sup> Internally laminated massive weathering.

Late Devonian conodonts recovered from the cherty limestone layer in the eugeosynclinal section at East Northumberland Canyon are dark yellowish brown in color and indicate a moderate postdepositional temperature history (Poole and Sandberg, 1975), judged from the method of Epstein, Epstein, and Harris (1975). The dark-yellowish-brown color of the conodonts indicates that they have not been subjected to prolonged temperatures above 200°C.

Madsen (1974) described "spongy-surface" chert from Devonian (reported by Madsen as Ordovician) chert layers interbedded with bedded barite rock at East Northumberland Canyon. The chert's texture was inherited from authigenic cristobalite forming bedded porcelanite. Bedded porcelanite was considered by Madsen to be of sedimentary origin. Metamorphosed chert consists of quartz that has an equigranular texture unlike that of the spongy-surface chert. Madsen pointed out that experiments by Ernst and Calvert (1969) on porcelanite from the upper Tertiary Monterey Formation of California showed that in relatively pure water the fine-grained cristobalite would recrystallize to quartz in about 180 million years at 20°C and in about 4–5 m.y. at 50°C. The occurrence of spongy-surface chert at East Northumberland Canyon, therefore, suggests that the beds have not been subjected to prolonged high temperatures since deposition, and this finding is compatible with the moderate temperature history inferred from the conodont alteration color.

### STABLE ISOTOPE STUDIES

Table 1 presents  $\delta^{34}\text{S}$  data on bedded and vein barites occurring in East and West Northumberland Canyons and on occurrences of barite crystals in veins near the Northumberland gold deposit. Table 2 presents  $\delta^{18}\text{O}$  data on cherts and  $\delta^{18}\text{O}$  and  $\delta^{13}\text{C}$  data on carbonates from the Slaven Chert at East Northumberland Canyon. The locations of most of the samples are shown in figure 2. Samples DRS-28-67A, B, C, and D were collected at the Northumberland gold deposit 5.5 kilometers N. 5° W. of the junction of Perkins and East Northumberland Canyons, and samples 67FP-46 and 67FP-45 were collected 1.6 km N. 21° W. and 7.5 km N. 26° W., respectively, of the junction of Perkins and East Northumberland Canyons.

The  $\delta^{34}\text{S}$  values were determined by the technique described by Thode, Monster, and Dunford (1961). This method was used because total sulfate can be extracted from the impure barites without special purification procedures. The  $\delta^{18}\text{O}$  values in cherts were determined by  $\text{BrF}_5$  extraction (Clayton and Mayeda,

1963) after boiling in aqua regia to remove organic material. Isotope data on carbonates were determined as described by McCrea (1950). All measurements were made on a modified Nuclide 6-60-RMS mass spectrometer. The isotope data are presented in the familiar  $\delta$  notation relative to international standards for each isotope: the oxygen isotope data are relative to SMOW (Craig, 1961), the carbon isotope data are relative to PDB (Craig, 1957), and the sulfur isotope data are relative to Cañon Diablo troilite (Ault and Jensen, 1962). Analytical precision for all measurements was  $\pm 0.1$  permil or better.

### Sulfur isotope data and barite

Most of the bedded barite at East Northumberland Canyon is massive-laminated. The  $\delta^{34}\text{S}$  values of 10 samples of the massive-laminated barite range from 20.9 to 28.6 permil, while 7 of the 10 samples have  $\delta^{34}\text{S}$  values near 25 permil. The  $\delta^{34}\text{S}$  values of oceanic sulfate have varied from about 10 to 33 permil throughout geologic time, as indicated by analyses of marine evaporites (Holser and Kaplan, 1966; Thode and Monster, 1965; Claypool and others, 1972). During the Devonian, the  $\delta^{34}\text{S}$  of seawater underwent large systematic variations and was between 24 and 30 permil during the Late Devonian. Values in this range are fairly rare for the  $\delta^{34}\text{S}$  of seawater sulfate throughout geologic time. Available data on recent marine barites have  $\delta^{34}\text{S}$  values similar to present-day seawater sulfate (Goldberg and others, 1969). The  $\delta^{34}\text{S}$  data on the massive-laminated barite at East Northumberland thus strongly suggest a Late Devonian marine origin for the sulfate in the bedded barite.

Even though most of the  $\delta^{34}\text{S}$  values of the massive-laminated barites cluster near 25 permil, a considerable range of values was obtained for individual beds. This is in contrast to published data on individual evaporites, which normally show very small ranges in  $\delta^{34}\text{S}$  values for an entire formation (Holser and Kaplan, 1966).

Samples from measured sections on both the north and south sides of East Northumberland Canyon were analyzed (table 1). There appear to be no general systematics to the distribution of  $\delta^{34}\text{S}$  values of the massive-laminated barites, although the values decrease toward the top of the section at locality 11. There is also no apparent correlation between  $\delta^{34}\text{S}$  values and the silica, carbon, iron, organic, or clay content of the barites when the data are compared with the chemical data reported by Shawe and others, (1967). Furthermore, the iron (pyrite) content of the barites is apparently very low. Barite deposition ob-

TABLE 1.— $\delta^{34}\text{S}$  data on barites near East Northumberland Canyon, Nye County, Nev.  
[n.d.—not determined. n.a.—not applicable.]

Field sample no.	Meters above base	Locality no. (fig. 2)	Description	$\delta^{34}\text{S}$ (permil)						
				Massive-laminated	Disseminated	Recrystallized	Rosettes	Concretion	Veins	
East Northumberland Canyon, south side										
DAB-6-----	2.5	13	Massive-----	24.9	-----	-----	-----	-----	-----	
DRS-24-A-67	0.5		4-7 mm rosettes in 20 percent chert matrix.	-----	-----	-----	38.4	-----	-----	
DRS-24-B-67	0.5		1-5 mm rosettes in 20 percent chert matrix.	-----	-----	-----	31.8	-----	-----	
DAB-5-----	1	12	Massive-----	25.1	-----	-----	-----	-----	-----	
DRS-25-67--	14		<1 mm rosettes in 5-10 percent silica matrix.	-----	-----	-----	29.1	-----	-----	
DAB-4-----	13	11	Sugary, massive-----	20.9	-----	-----	-----	-----	-----	
DAB-3-----	7		Massive-----	22.6	-----	-----	-----	-----	-----	
DAB-2-----	4		1-3 mm rosettes in 5 percent silica matrix.	-----	-----	-----	30.0	-----	-----	
DRS-27-67--	2		Massive-----	24.9	-----	-----	-----	-----	-----	
DAB-1-----	1	19	Laminated-----	25.3	-----	-----	-----	-----	-----	
67FP-142A--	n.d.		Massive-laminated-----	23.9	-----	-----	-----	-----	-----	
67FP-142B--	n.d.		8-9 mm rosettes in barite matrix--	-----	-----	-----	36.5	-----	-----	
67FP-142C--	n.d.		Concretion conglomeratic barite--	-----	-----	-----	-----	33.6	-----	
67FP-59-----	n.d.		do-----	-----	-----	-----	-----	40.2	-----	
67FP-65-----	n.d.		22	Concretion in mudstone-----	-----	-----	-----	56.3	-----	
67FP-162A--	n.d.		20	Massive-interlaminated with chert--	25.5	-----	-----	-----	-----	
67FP-162B--	n.d.		20	3-5 mm rosettes in black chert----	-----	-----	-----	45.3	-----	
East Northumberland Canyon, north side										
DRS-55-68--	7		3	7-8 mm rosettes in silica matrix---	-----	-----	-----	42.2	-----	-----
DRS-52-68--	4	Shaley barite-----		-----	22.8	-----	-----	-----	-----	
DRS-51-68--	1.5	Baritic mudstone-----		-----	27.1	-----	-----	-----	-----	
DRS-50-68--	1	2-3 mm rosettes in shale-----		-----	-----	-----	35.6	-----	-----	
DRS-49-68--	0.5	Massive-laminated-----		22.1	-----	-----	-----	-----	-----	
DRS-48-68--	0	9	3-4 mm rosettes in siltstone-----	-----	-----	-----	42.1	-----	-----	
DRS-10-68--	n.d.		3-4 mm irregular rosette layer-----	-----	-----	-----	42.4	-----	-----	
DRS-72-68--	n.d.	2	Detrital massive barite-----	28.6	-----	-----	-----	-----		
67FP-188A--	n.d.	11	"Bull's eye" phosphatic concretion--	-----	-----	-----	35.6	-----		
DRS-31-68A--	n.d.	6	Massive recrystallized-----	-----	-----	21.6	-----	-----		
DRS-31-68B--	n.a.	6	Vein cutting recrystallized barite--	-----	-----	-----	-----	40.9		
DRS-61-68--	n.a.	4	Hydrothermally silicified vein-----	-----	-----	-----	-----	39.0		
DRS-141-67--	n.a.	8	Vein in chert-----	-----	-----	-----	-----	36.4		
DRS-35-68--	n.d.	5	Recrystallized white massive-----	-----	-----	26.4	-----	-----		
DRS-38-68--	n.d.	7	Recrystallized light-gray massive--	-----	-----	25.0	-----	-----		
West Northumberland Canyon (Lost Soldier Mine)										
67FP-45----	n.d.	n.a.	White recrystallized-----	-----	-----	21.6	-----	-----	-----	
67FP-46----	n.d.	n.a.	Gray recrystallized-----	-----	-----	24.2	-----	-----	-----	
Northumberland gold deposit										
DRS-28-67A--	n.a.	n.a.	Coarse clear crystal-----	-----	-----	-----	-----	-----	39.3	
DRS-28-67B--	n.a.	n.a.	do-----	-----	-----	-----	-----	-----	29.8	
DRS-28-67C--	n.a.	n.a.	do-----	-----	-----	-----	-----	-----	24.5	
DRS-28-67D--	n.a.	n.a.	do-----	-----	-----	-----	-----	-----	31.7	

viously involved more than just supersaturation and precipitation of barium with seawater sulfate on the ocean floor; the range of  $\delta^{34}\text{S}$  values of the massive-laminated barites resulted from the mixing of sulfate from various sources and (or) bacteriogenic processes. We hope that future detailed petrologic, chemical, and isotopic studies of these barites will reveal the reason why their  $\delta^{34}\text{S}$  values vary so much from the presumed constant value for seawater sulfate. Such an insight should help clarify the depositional environment of the bedded barites. Such insight is also essential to evaluate the use of  $\delta^{34}\text{S}$  values as a stratigraphic tool for correlating bedded barites in Nevada.

Disseminated barite also occurs in the barite interval at East Northumberland Canyon, and all gradations between silty barite and baritic mudstones occur. Our  $\delta^{34}\text{S}$  values for one sample each of silty barite and baritic mudstone are 22.8 and 27.1 permil, respectively. These values are in the range of those for massive-laminated barites and also indicate a seawater origin for the sulfate in the disseminated barite.

In West Northumberland Canyon, probable stratigraphic equivalents of the East Northumberland bedded barites have been slightly recrystallized and depleted of carbon, and the barite has been partly replaced by silica locally near a Jurassic pluton ad-

TABLE 2.—*Stable isotope data on chert and carbonates from Slaven Chert*  
 [Map locality numbers refer to localities shown on figure 2]

Field sample number	Map locality number	Description	$\delta^{18}\text{O}$ (permil)
Chert			
68FP-66	21	Banded light- and dark-gray chert----	28.9
67FP-158	17	Laminated Black chert-----	29.1
67FP-142D	19	1-cm-thick black chert in barite (see table 1).	24.8
67FP-162A	20	Interlaminated wavy barite and chert.	26.6
67FP-162A	20	"Wormy" barite in black chert-----	28.9
		Chert matrix in barite rosettes-----	28.0
68FP-89A	14	Chert between major barite beds.	28.2
Carbonate <sup>1</sup>			
68FP-82	15	Medium- to fine-grained impure limestone 10 cm thick within lower part of exposed chert and barite sequence underlying barite interval.	26.9
DRS-4-68	10	Gray dolomite 30 cm thick overlying barite interval.	25.7

<sup>1</sup>Both carbonate samples had  $\delta^{13}\text{C}$  values of -7.5 permil.

adjacent to the Northumberland gold deposit. Such recrystallization, bleaching, and partial replacement by silica has occurred also in bedded barites in the vicinity of Tertiary dikes and sills in East Northumberland Canyon.

The  $\delta^{34}\text{S}$  values of six samples of massive-laminated barite which have undergone various degrees of recrystallization near intrusives range from 21.6 to 26.4 permil. There is no apparent correlation between  $\delta^{34}\text{S}$  values and the degree of recrystallization. The  $\delta^{34}\text{S}$  values are within the range of those obtained from unrecrystallized massive-laminated barite in East

Northumberland Canyon. This indicates that no detectable sulfur isotope fractionation occurred during recrystallization and hydrothermal alteration of the barite near the intrusives. Consequently, in most instances it should be possible to infer the origin of bedded barite and possibly make correlations even where the barite has been intensely recrystallized.

Ten samples of rosette barite have  $\delta^{34}\text{S}$  values of 29.1 to 42.4 permil. All of these values are larger than those for massive-laminated barites. The preliminary  $\delta^{34}\text{S}$  values of barite rosettes do not appear to correlate with their size, location or position in section,

or the nature of their matrix (mudstone, chert, or barite).

The rosettes presumably formed during a period of slow sedimentation on the sea floor or diagenetically below the sediment-water interface. The large  $\delta^{34}\text{S}$  values for the rosettes are typical of values that result from partial reduction of seawater sulfate by microorganisms in a closed system (Nakai and Jensen, 1964). A critical test of whether this process occurred would be a comparison of  $\delta^{34}\text{S}$  with with corresponding  $\delta^{18}\text{O}$  data. Mizutani and Rafter (1969) showed experimentally that the rate of  $^{18}\text{O}$  enrichment of  $\text{SO}_4$  remaining in solution is about one-fourth of that of  $^{34}\text{S}$  enrichment during bacteriogenic reduction of seawater sulfate. Sakai (1971) used this fact to conclude that bacteriogenic reduction of seawater sulfate was involved in the formation of Tertiary barite concretions obtained off the west coast of Japan.

Two samples of barite concretions in mudstone have  $\delta^{34}\text{S}$  values of 35.6 and 33.6 permil, and two samples of barite matrix from conglomeratic barite which is composed of clasts of barite, chert, baritic to phosphatic nodules, and barite rosettes have  $\delta^{34}\text{S}$  values of 33.6 and 40.2 permil. These values are similar to those for the rosettes and to those obtained from Tertiary barite concretions off the coasts of New Zealand (Rafter and Mizutani, 1967), California (Goldberg and others, 1969), and Japan (Sakai, 1971) and suggest that the nodules and conglomeratic matrix also formed in local closed chemical systems either on the sea floor or in the directly underlying sediments where bacterial reduction of seawater sulfate took place.

Barite occurs as crosscutting veins in two forms in the Northumberland area: as veins in chert and bedded barite and in breccia zones on both sides of East Northumberland canyon and as crystals in open fractures near the Northumberland gold deposits. The  $\delta^{34}\text{S}$  values of these occurrences range from 31.2 to 40.9 permil and are distinctly larger than those observed for the massive-laminated barite. Especially interesting is sample DRS-31-68, in which the vein barite has  $\delta^{34}\text{S}$  of 40.9 permil and the recrystallized host bedded barite has  $\delta^{34}\text{S}$  of only 21.6 permil.

The  $\delta^{34}\text{S}$  values of large clear barite crystals near the Northumberland gold mine range from 24.5 to 39.3 permil. However, the  $\delta^{34}\text{S}$  values of hydrothermal sulfates must be interpreted in terms of the  $\delta^{34}\text{S}$  values of the hydrothermal fluid before inferences can be made about the origin of sulfur in these sulfates (Ohmoto, 1972; Rye and Ohmoto, 1974). Such interpretation requires a knowledge of the physical-chemical environment of vein barite deposition. We have

not been able to collect sulfides occurring with the vein barites nor do we have enough information on our samples to evaluate the chemical environment of vein barite deposition. Furthermore, the veins are probably low-temperature, and kinetic factors often dominate low-temperature systems when aqueous sulfate is present. However, all of the vein data could be explained if the sulfate were derived from massive bedded barite in the area having an average  $\delta^{34}\text{S}$  value of 25 permil and redeposited from hydrothermal fluids at low temperatures under a range of  $f_{\text{O}_2}$  conditions. Such a variation of  $f_{\text{O}_2}$  conditions would not be unlikely in an area that has both bedded barite and organic-rich cherts and mudstones.

#### Carbon and oxygen isotope data on cherts and carbonates

The  $\delta^{18}\text{O}$  and  $\delta^{13}\text{C}$  values for various cherts and carbonates from the Devonian Slaven Chert are presented in table 2. The formation as a whole is predominantly impure chert and mudstone, whereas the barite interval is relatively free of chert but in places contains thin chert layers with chert in various proportions to barite. Carbonates are sparse in the Slaven Chert. A 10-cm-thick layer of impure limestone occurs at the base of the exposed Slaven Chert, and a 30-cm-thick layer of dolomite occurs higher in the section.

The  $\delta^{18}\text{O}$  values of cherts range from 24.8 to 28.9 permil. The values for most samples are near 28 permil, which is within the lower part of the range commonly observed for "unaltered" Devonian marine cherts (Perry, 1967; Knauth and Epstein, 1976). Samples 67FP-142D and 67FP-162A and B are intimately associated with barite, and their low  $\delta^{18}\text{O}$  values may reflect changes during diagenesis. The  $\delta^{18}\text{O}$  values of the carbonates are also typical of unaltered Devonian marine carbonates (Keith and Weber, 1964).

However,  $\delta^{13}\text{C}$  values of the carbonates (-7.5 permil) are considerably lower than those of most marine carbonates, which normally have  $\delta^{13}\text{C}$  values within the range  $\pm 4$  permil as far back as  $3 \times 10^9$  years (Becker and Clayton, 1972). Similar  $^{13}\text{C}$  depletions have been observed in marine carbonates associated with Precambrian iron formations and have been interpreted to indicate that the carbonate precipitated in organic-rich environments which were not open to the larger oceanic carbon reservoir. Such an interpretation for the East Northumberland  $\delta^{13}\text{C}$  data is consistent with the  $\delta^{34}\text{S}$  data on the barite rosettes, which suggests that, at least locally, the environment of deposition was restricted and may have involved organic matter.

## CONCLUSIONS

1. The  $\delta^{34}\text{S}$  values of bedded, massive-laminated barite in the Slaven Chert from East Northumberland Canyon range from 20.9 to 28.6 permil, with most values near 25.0 permil, a value typical of Upper Devonian marine sulfate. A Late Devonian age for the Slaven Chert at East Northumberland Canyon is indicated by new fossil evidence. Although both the sulfate and barium must have come from the Devonian ocean, the ultimate source of the barium is not clear.
2. The fact that  $\delta^{34}\text{S}$  value of the massive-laminated barite vary almost 8 permil, whereas these values in individual marine evaporites in other areas are nearly constant, suggests that either bacteria and (or) mixing of sulfur from two sources was locally involved in barite deposition or diagenesis.
3. The initial sedimentary  $\delta^{34}\text{S}$  values of massive-laminated barite were apparently retained during recrystallization, replacement by silica, and the loss of organic carbon associated with hydrothermal alteration.
4. Once the cause of  $\delta^{34}\text{S}$  variations in massive-laminated barites is determined, it may be possible to use  $\delta^{34}\text{S}$  as a stratigraphic tool in dating barites in the Nevada barite province.
5. Barite rosettes and concretions have  $\delta^{34}\text{S}$  values ranging from 29.1 to 56.3 permil, suggesting that they formed in a partially closed system either on the ocean floor or within the sediments, where bacterial reduction of seawater sulfate occurred.
6. The  $\delta^{34}\text{S}$  values on crosscutting vein barites in the area, including those from the Northumberland gold deposit, are much larger than those for bedded barites and, considering the local isotope geochemistry, are consistent with the possibility that the sulfur in the veins was derived from bedded barites.
7. The  $\delta^{18}\text{O}$  data on most cherts and carbonates in the bedded barite interval in the Slaven Chert are typical of Devonian marine cherts and carbonates, while  $\delta^{13}\text{C}$  values of the carbonates suggest they were deposited in organic-rich environments that had restricted communication with the carbon reservoir of the open ocean.
8. Evidence from conodont color alteration and chert textures indicates that the barite-bearing interval at East Northumberland Canyon did not experience prolonged high temperatures or deep

burial and that the eugeosynclinal allochthon emplaced during the Antler orogeny was a "thin-skinned" feature which apparently resulted from surficial thrusting during tectonic emplacement above transitional and miogeosynclinal rocks of the lower and middle Paleozoic outer continental shelf.

## REFERENCES CITED

- Ault, W. U., and Jensen, M. L., 1962, Summary of sulfur isotope standards, in Jensen, M. L., ed., Biogeochemistry of sulfur isotopes: Natl. Sci. Found., Symposium Proc., New Haven, Conn., Yale Univ., Apr. 12-14, 1962, p. 16-29 [1963].
- Becker, R. H., and Clayton, R. N., 1972, Carbon isotopic evidence for the origin of a banded iron formation in Western Australia: *Geochim. et Cosmochim. Acta*, v. 36, no. 5, p. 577-596.
- Claypool, G. E., Holser, W. T., Kaplan, I. R., Sakai, H., and Zak, I., 1972, Sulfur and oxygen geochemistry of evaporite sulfates: *Geol. Soc. America Abs. with Programs*, v. 4, no. 7, p. 473.
- Clayton, R. N., and Mayeda, T. K., 1963, The use of bromine pentafluoride in the extraction of oxygen from oxides and silicates for isotopic analysis: *Geochim. et Cosmochim. Acta*, v. 27, p. 43-52.
- Cloud, P. E., Jr., and Boucot, A. J., 1971, *Dzieduszyckia* in Nevada, in Dutro, J. T., Jr., ed., Paleozoic perspectives—a paleontological tribute to G. Arthur Cooper: *Smithsonian Contr. Paleobiology*, no. 3, p. 175-180.
- Craig, Harmon, 1957, Isotopic standards for carbon and oxygen and correction factors for mass-spectrometric analysis of carbon dioxide: *Geochim. et Cosmochim. Acta*, v. 12, nos. 1-2, p. 133-149.
- 1961, Standard for reporting concentrations of deuterium and oxygen-18 in natural waters: *Science*, v. 133, no. 3467, p. 1833-1834.
- Epstein, A. G., Epstein, J. B., and Harris, L. D., 1975, Conodont color alteration—an index to organic metamorphism: U.S. Geol. Survey Open-File Report 75-379, 54 p.
- Ernst, W. G., and Calvert, S. E., 1969, An experimental study of the recrystallization of porcelanite and its bearing on the origin of some bedded cherts: *Am. Jour. Sci.*, v. 267-A (Schairer Volume), p. 114-133.
- Goldberg, E. D., Somayajulu, B. L. K., Galloway, James, Kaplan, I. R., and Faure, Gunter, 1969, Differences between barites of marine continental origins: *Geochim. et Cosmochim. Acta*, v. 33, p. 287-289.
- Holser, W. T., and Kaplan, I. R., 1966, Isotope geochemistry of sedimentary sulfates: *Chem. Geology*, v. 1, no. 2, p. 93-135.
- Kay, Marshall, and Crawford, J. P., 1964, Paleozoic facies from the miogeosynclinal to the eugeosynclinal belt in thrust slices, central Nevada: *Geol. Soc. America Bull.*, v. 75, no. 5, p. 426-454.
- Keith, M. L., and Weber, J. N., 1964, Carbon and oxygen isotopic composition of selected limestones and fossils: *Geochim. et Cosmochim. Acta*, v. 28, p. 1787-1816.
- Knauth, P. L., and Epstein, Samuel, 1976, Hydrogen and oxygen isotope ratios in nodular and bedded cherts: *Geochim. et Cosmochim. Acta*, v. 40, p. 1095-1108.

- Madsen, B. M., 1974, Origin of spongy cherts: U.S. Geol. Survey Jour. Research, v. 2, no. 6, p. 685-687.
- McCrea, J. M., 1950, On the isotopic chemistry of carbonates and paleotemperature scale: Jour. Chem. Physics, v. 18, p. 849-857.
- Mizutani, Y., and Rafter, T. A., 1969, Oxygen isotopic composition of sulphates, pt. 4, Bacterial fractionation of oxygen isotopes in the reduction of sulphate and in the oxidation of sulphur: New Zealand Jour. Sci., v. 12, p. 60-68.
- Nakai, Nobuyaki, and Jensen, M. L., 1964, The kinetic isotope effect in the bacterial reduction and oxidation of sulfur: Geochim. et Cosmochim. Acta, v. 28, p. 1893-1912.
- Ohmoto, Hiroshi, 1972, Systematics of sulfur and carbon isotopes in hydrothermal ore deposits: Econ. Geol., v. 67, p. 551-578.
- Perry, E. C., Jr., 1967, The oxygen isotope chemistry of ancient cherts: Earth and Planetary Sci. Letters, v. 3, p. 62-66.
- Poole, F. G., 1974, Flysch deposits of the Antlér foreland basin, western United States, in Dickinson, W. R., ed., Tectonics and sedimentation: Soc. Econ. Paleontologists and Mineralogists Spec. Pub. 22, p. 58-82.
- Poole, F. G., Baars, D. L., Drewes, Harald, Hayes, P. T., Ketner, K. B., McKee, E. D., Teichert, Curt, and Williams, J. S., 1967, Devonian of the southwestern United States, in Oswald, D. H., ed., Internat. symposium on the Devonian System, Calgary, Alberta, Canada, Sept. 1967: Alberta Soc. Petroleum Geologists, v. 1, p. 879-912.
- Poole, F. G., and Sandberg, C. A., 1975, Allochthonous Devonian eugeosynclinal rocks in Toquima Range, central Nevada: Geol. Soc. America Abs. with Programs, v. 7, no. 3, p. 361.
- Rafter, T. A., and Mizutani, Y., 1967, Oxygen isotopic composition of sulphates, pt. 2, Preliminary results on oxygen isotopic variation in sulphates and the relationship to their environment and to their  $\delta^{34}\text{S}$  values: New Zealand Jour. Sci., v. 10, p. 816-840.
- Rye, R. O., and Ohmoto, Hiroshi, 1974, Sulfur and carbon isotopes and ore genesis—A review: Econ. Geol., v. 69, p. 826-842.
- Sakai, Hitoshi, 1971, Sulfur and oxygen isotopic study of barite concretions from banks in the Japan Sea off the Northeast Honshu, Japan: Geochemical Journal, v. 5, p. 79-93.
- Shawe, D. R., Poole, F. G., and Brobst, D. A., 1967, Bedded barite in East Northumberland Canyon, Nye County, Nevada: U.S. Geol. Survey Circ. 555, 8 p.
- , 1969, Newly discovered bedded barite deposits in East Northumberland Canyon, Nye County, Nevada: Econ. Geology, v. 64, no. 3, p. 245-254.
- Thode, H. G., and Monster, Jan, 1965, Sulfur-isotope geochemistry of petroleum, evaporites, and ancient seas, in Fluids in subsurface environments: Am. Assoc. Petroleum Geologists Mem., no. 4, p. 367-377.
- Thode, H. G., Monster, Jan, and Dunford, H. B., 1961, Sulphur isotope geochemistry: Geochim. et Cosmochim. Acta, v. 25, p. 159-174.



## FACTORS CONTRIBUTING TO THE FORMATION OF FERROMANGANESE NODULES IN ONEIDA LAKE, NEW YORK

By WALTER E. DEAN and SWAPAN K. GHOSH,<sup>1</sup>  
Denver, Colo., Shiraz, Iran

**Abstract.**—Oneida Lake is a large, shallow, eutrophic lake situated in the Ontario lowlands of central New York State. It contains the most concentrated deposit of freshwater ferromanganese nodules (in terms of amount per unit area) yet reported in the literature. The mineralogy and bulk chemistry of these saucer-shaped nodules are similar to the mineralogy and bulk chemistry of deep-sea ferromanganese nodules, but the nodules in Oneida Lake contain considerably lower concentrations of trace metals, especially cobalt, nickel, and copper. Budgets for iron and manganese in waters from Oneida Lake and its tributaries indicate that approximately 122 t (metric tons) of iron and 23 t of manganese are lost each year from the lake waters, presumably by incorporation into sediments and ferromanganese nodules. Estimates based on nodule abundance and age of the lake suggest that iron and manganese are being incorporated into ferromanganese nodules at rates of 13 and 22 t/yr, respectively. Most iron lost from the lake waters is apparently incorporated into sediments, which contain an average of 10 times more iron than manganese. Most manganese lost from the lake waters is apparently incorporated into ferromanganese nodules, which contain an average of 1.7 times more manganese than iron. In Oneida Lake, very high rates of phytoplankton productivity, combined with almost continuous wind mixing to the bottom, provide high-pH and high-Eh conditions in most of the lake. Algae also provide an effective means of concentrating and transporting iron and manganese and thereby aid in the extensive development of ferromanganese nodule deposits.

Oneida Lake is a large, shallow eutrophic lake situated in the Ontario lowlands of central New York State. Owing to the large surface area (207 km<sup>2</sup>), the elongation in the direction of dominant wind direction, and the shallow depth (mean depth, 6.8 m; maximum depth, 16.8 m), the lake waters are almost continuously wind mixed during the ice-free months and are thereby prevented from becoming thermally stratified. The lake is characterized by intense algal blooms (as high as  $2 \times 10^5$  cells/mL) during the summer months (Greeson, 1972), but because of wind mixing and lack of a hypolimnion, the high rate of oxygen production in

the surface waters of Oneida Lake is not matched by a high rate of oxygen consumption in the bottom waters, as is true for most other eutrophic lakes. Although Oneida Lake does not exhibit thermal stratification, dissolved oxygen may show some stratification, as indicated by values as low as 50 percent of saturation at depths greater than about 10 m during prolonged periods of calm weather in the summer (Greeson and Meyers, 1969). However, for water depths shallower than 10 m (encompassing about 60 percent of the lake), the bottom waters are almost always saturated or supersaturated with respect to dissolved oxygen. Well-oxygenated bottom waters provided by wind mixing and high algal productivity are probably the most important factors contributing to the development of extensive ferromanganese deposits in Oneida Lake.

**Acknowledgments.**—This research was supported by the National Science Foundation and by a Penrose Grant from the Geological Society of America. Field support by Dr. John Forney, Cornell University Biological Station, Oneida Lake, is gratefully acknowledged. Mr. Ronald Strong contributed much time and diving experience for the collection of samples.

### FERROMANGANESE NODULES

Ferromanganese nodules are concentrated mainly in the shallow, well-oxygenated central areas of Oneida Lake (fig. 1) in water depths less than 10 m. Some parts of the lake bottom in these areas are almost completely paved with nodules (fig. 2). We estimate, on the basis of visual observations, that about 25 percent of the bottom within these central areas is covered with nodules.

Oneida Lake nodules are typically saucer shaped and average about 15 cm in diameter and 5 cm in thickness. Nodules smaller than about 3 cm are roughly spherical, although larger spherical nodules as much as 10 cm in diameter have been found. More complete descriptions of the Oneida Lake nodules have been

<sup>1</sup> Department of Geology, Pahlavi University.

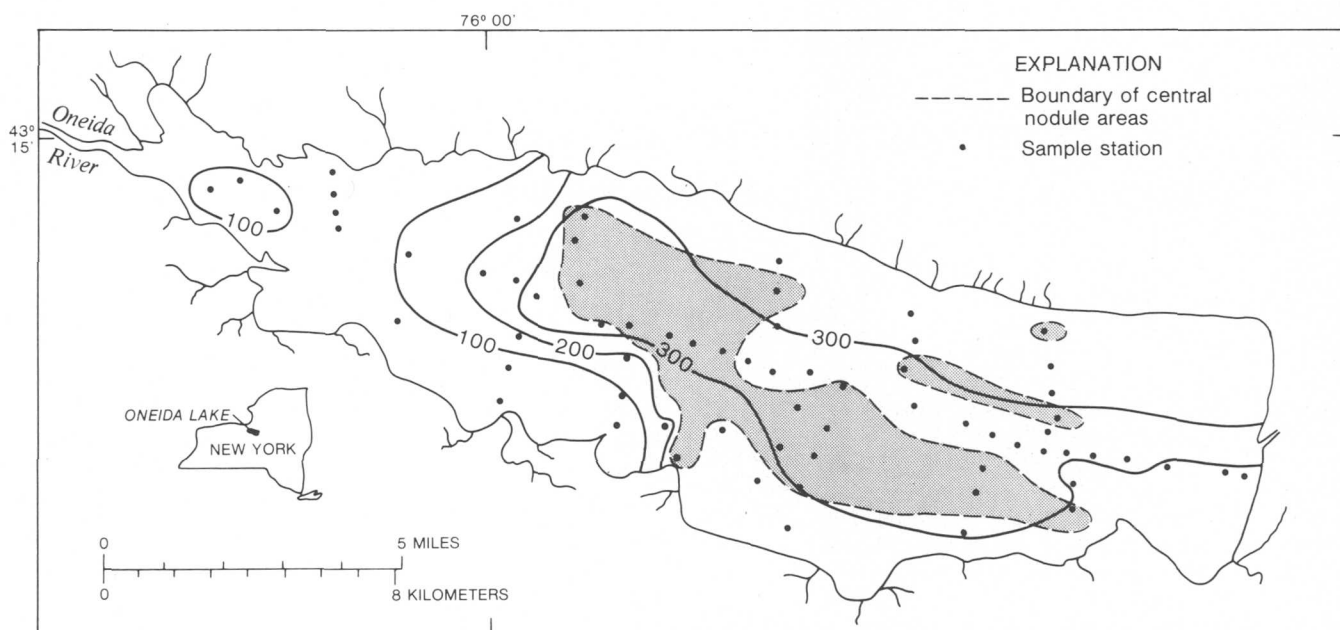


FIGURE 1.—Map of Oneida Lake, N.Y., showing sample stations, central nodule areas, and redox (Eh) potentials of bottom sediments. Eh contours are in millivolts.



FIGURE 2.—Ferromanganese nodules on bottom of Oneida Lake. Dark bands on rod are at 10-cm intervals.

presented by Dean (1970) and Dean and others (1973). Based on an average nodule of 15 cm in diameter, 5 cm in thickness, and about  $2.8 \text{ g/cm}^3$  (or  $\text{Mg/m}^3$ ) in density, 25 percent coverage within the  $50\text{-km}^2$  nodule areas amounts to a nodule density of about  $14 \text{ nodules/m}^2$ , or a total weight of about  $1.8 \times 10^6 \text{ t}$  (metric tons). We, therefore, feel that a conservative estimate of the total weight of ferromanganese nodules in Oneida Lake would be on the order of  $10^6 \text{ t}$ .

Distribution of nodules in Oneida Lake is based on visual observations by scuba divers at 68 sample stations throughout the lake (fig. 1). Divers collected a sediment sample at each of the 68 stations and, where nodules are present (20 of the 68 stations), collected representative nodules for analysis. Sediment and nodule samples were analyzed by atomic absorption for concentrations of iron, manganese, calcium, magnesium, sodium, potassium, strontium, copper, zinc, chromium, nickel, cobalt, and lead. Iron and manganese mineral phases in the nodules were identified by long exposures (up to 24 h) in a powder X-ray diffraction camera.

The dominant crystalline iron mineral phase is goethite, as evidenced by X-ray diffraction lines at 0.42 nm, 0.254 nm, and 0.244 nm. Manganese phases produced weak X-ray diffraction lines at 0.975 nm to 1.0 nm and 0.446 nm to 0.463 nm, attributed to the mineral todorokite (Burns and others, 1974), and broad lines at 0.242 nm and 0.141 nm, attributed to the mineral birnessite (also referred to as  $\delta\text{MnO}_2$ ; Gager, 1968; Cronan and Tooms, 1969; Burnes and Brown, 1972; Burns and others, 1974). Not all samples produced all lines mentioned, and some samples produced no X-ray diffraction lines, a fact suggesting that much of the material is X-ray amorphous.

Results of analyses of 132 ferromanganese nodules from Oneida Lake are presented in table 1 along with analyses of ferromanganese nodules from marine and other freshwater localities. The most striking differ-

TABLE 1.—Elemental composition of freshwater and marine ferromanganese nodules

Environment	Mn	Fe	Co	Cr	Cu	Ni	Zn	Pb
	Percent			Parts per million				
Freshwater:								
Oneida Lake, New York <sup>1</sup>								
Dry weight basis -----	27.4±12.9	14.6±5.7	23± 9	30±12	29±38	29±14	104±44	66±31
HCl-soluble basis -----	33.6±14.9	18.8±8.4	27±13	37±16	43±51	34±19	131±51	83±40
Grand Lake, Nova Scotia <sup>2</sup> ----	33	16.6	196	-----	14	296	1,665	26
Ship Harbor Lake, N. S. <sup>2</sup> ----	26.6	16.7	221	-----	7	112	475	27
Mosque Lake, Ontario <sup>2</sup> -----	15.7	40.2	135	-----	10	95	250	24
Lake George, N. Y. <sup>3</sup> -----	3.6	33.5	220	-----	1,314	702	1,177	-----
Lake Ontario <sup>4</sup> -----	17	20.6	643	-----	363	2,385	1,996	-----
Green Bay, Lake Michigan <sup>5</sup> ---	12.8±11.2	27.3±15.8	160±97	49±82	41±21	458±684	460±324	-----
Marine, shallow water:								
Baltic Sea <sup>6</sup> -----	14	22.5	160	-----	48	750	80	-----
Loch Fyne, Scotland <sup>7</sup> -----	23.3	1.6	275	56	<20	116	-----	205
Jervis Inlet, Br. Col. <sup>8</sup> -----	40.3	5	166	-----	89	393	34	-----
Marine, deep water:								
Pacific Ocean <sup>9</sup>								
Minimum -----	8.2	2.4	140	10	280	1,600	400	200
Maximum -----	41.1	26	23,000	70	16,000	20,000	800	3,600
Average -----	24.2	14	3,500	10	5,300	9,900	470	900
Atlantic Ocean <sup>1</sup>								
Minimum -----	12	9.1	600	10	500	3,100	-----	800
Maximum -----	21.5	25.9	6,800	30	4,100	5,400	-----	1,400
Average -----	16.3	17.5	3,100	20	2,000	4,200	-----	1,000

<sup>1</sup>Mean ± one standard deviation of 132 analyses (Dean and others, 1973; Ghosh, 1975).

<sup>2</sup>Harriss and Troup, 1970.

<sup>3</sup>Schoettle and Friedman, 1971.

<sup>4</sup>Cronan and Thomas, 1970; average, HCl-soluble fractions of 33 ferromanganese coatings.

<sup>5</sup>Rossmann, Callender, and Bowser, 1972; mean ± one standard deviation, HCl-soluble basis, of

Green Bay nodules.

<sup>6</sup>Manheim, 1965.

<sup>7</sup>Ku and Glasby, 1972.

<sup>8</sup>Grill, Murray, and Macdonald, 1968; average of one discoid nodule and one spherical nodule.

<sup>9</sup>Mero, 1965.

ence between deep-sea nodules and all freshwater nodules is the much higher concentrations of some trace elements, especially cobalt, nickel, and copper, in the deep-sea nodules. The Oneida nodules differ from most other freshwater nodules in that they contain more manganese than iron.

Differences in trace-element composition may be related to differences in rate of accretion. Rates of accretion of deep-sea nodules are on the order of 0.1 to 1 mm/10<sup>6</sup> yr (Ku and Glasby, 1972; Ku and Broecker, 1969; Krishnaswami and others, 1972), whereas freshwater nodules form at least three orders of magnitude faster. For example, Krishnaswami and Moore (1973) and Dean and others (1973) reported accretion rates of 2–3 m/10<sup>3</sup> yr based on <sup>226</sup>Ra gradients in nodules from Oneida Lake, N.Y., and Lake Alstern, Sweden. These rates are probably minimum average rates because re-

cent evidence has shown that growth of ferromanganese nodules in Oneida Lake is episodic, with periods of very rapid growth separated by hiatuses in which little or no growth has occurred (Moore and others, 1976). Rapid rate of accretion of freshwater nodules is further suggested by the fact that they have been observed growing on buoys in Oneida Lake, in Lake Windemere, English lake district (Gorham and Swaine, 1965), and in Lake Michigan (Rossmann and Callender, 1968).

## SEDIMENTS

The sediments associated with ferromanganese nodules in Oneida Lake are gray to brown clayey silt and sandy mud. Organic contents of sediments from all 68 stations averaged about 1.5 percent and are in general highest in the loose, flocculent clayey silts in the deeper

parts of the lake below the depth of wind mixing and summer oxygen stratification. Shoal areas in the center of the lake are probably drumlins or drumlinoid features and consist of coarse glacial till with much of the sand fraction winnowed out. The hard sand areas surrounding the shoals are strewn with cobbles and boulders from the shoals and provide the most common nuclei for ferromanganese nodules that have obvious core materials. The hard bottom areas adjacent to the shoals contain the most abundant nodules, and, in some areas, almost every cobble and boulder is enclosed in a rim of ferromanganese material at the sediment-water interface. Results of analyses of sediments from all 68 stations are summarized in table 2.

Concentrations of major elements in sediment interstitial (pore) waters are typically several times higher than in average lake water of Oneida Lake (table 3). Iron concentrations in interstitial waters are about the same as the average in the lake water, but manganese concentrations in interstitial water are typically several orders of magnitude higher than those in the lake water. Sediment Eh values range from about 40 to 400 mV and are highest in the central part of the lake (fig. 1).

TABLE 2.—Concentration of strontium, calcium, magnesium, sodium, potassium, copper, zinc, iron, and manganese in sediments from Oneida Lake

[Values are in percent dry weight of sediment, averaged for 68 sampling stations]

Element	Mean concentration
Sr -----	0.10
Ca -----	.48
Mg -----	.54
Na -----	.08
K -----	.25
Cu -----	.003
Zn -----	.01
Fe -----	2.05
Mn -----	.17

TABLE 3.—Ratios of concentrations of six elements in sediment interstitial (pore) waters from a nodule-occurring area and a nonnodule area to the average concentration of each element in Oneida Lake surface water

	Ratio of concentration of element in sediment pore water to average concentration of element in lake water	
	Nodule area	Nonnodule area
Ca -----	2.4	1.4
Mg -----	2.1	3.6
Na -----	2.1	2.1
K -----	4.1	4.6
Fe -----	.5	.7
Mn -----	40	117

## INORGANIC FACTORS

### Budgets of iron and manganese

Abundant data on the water chemistry of Oneida Lake and its tributaries have been reported by Greeson (1972). Greeson's data show that the most important sources of dissolved solids in Oneida Lake are the southern tributaries draining areas of Silurian and Devonian carbonate bedrock. A budget of total dissolved solids indicates an average input of 1120 metric tons per day, an output of 996 t/d, with a net loss to the sediments of 124 t/d. Net losses of major elements range from 0.09 t/d for potassium to 32 t/d for calcium (Greeson, 1972).

Although there are not as many data for trace elements in tributaries to Oneida Lake as there are for major elements and macronutrients, we have calculated approximate budgets for iron and manganese (table 4). Concentrations of iron and manganese given in table 4 are based on analyses of two water samples from each tributary, one collected in the spring (April 29–30, 1969) and one collected in the fall (October 1–2, 1969). Discharge values in table 4 are based on a standard 30-yr period from 1931 to 1960. Discharges for 1969, the year in which the water samples were collected for trace-element analyses, were slightly higher than the 30-yr averages, but this should have little effect on the budgets. The budgets in table 4 indicate that an average of 122 t of iron and 23 t of manganese are removed from the lake water each year, presumably by incorporation into sediments and ferromanganese nodules.

Element concentrations for Oneida Lake nodules listed in table 1 are arithmetic means based on analyses of 132 nodules. Arithmetic means and standard deviations were used in table 1 for ease of comparison with arithmetic mean concentrations reported for nodules from other localities. However, actual distributions of iron, manganese, and minor elements in Oneida Lake nodules are closer to lognormal than normal, and we feel that geometric means would be more appropriate measures of central tendency for budget calculations. Geometric mean concentrations of iron and manganese in 132 nodules are 13 and 22 t, respectively. This amounts to an average of 13 t of iron and 22 t of manganese added to nodules each year, if we assume that the estimated total of  $10^6$  t of nodules formed over the entire  $10^4$ -yr postglacial history of Oneida Lake. Comparison of these figures with annual losses of iron and manganese from lake water (table 4) suggests that almost all of manganese loss from the lake water can be explained by incorporation of manganese into ferromanganese nodules. However,

TABLE 4.—Approximate budgets for manganese and iron, Oneida Lake, N.Y.  
 [Data from Greeson (1972). Note that data in milligrams per liter are identical with data in grams per cubic meter, the SI derived unit]

Tributary	Mean annual discharge (10 <sup>9</sup> liters per year)	Mn concentration (mg/L)	Annual Mn load (kg x 10 <sup>3</sup> per year)	Fe concentration (mg/L)	Annual Fe load (kg x 10 <sup>3</sup> per year)
Scriba Creek:					
Spring-----	-----	0.045	-----	0.170	-----
Fall-----	-----	.027	-----	.075	-----
Average-----	72	.036	2.6	.123	8.9
W. Br. Fish Cr:					
Spring-----	-----	.034	-----	.110	-----
Fall-----	-----	.015	-----	.045	-----
Average-----	450	.025	11	.078	35
E. Br. Fish Cr:					
Spring-----	-----	.006	-----	.065	-----
Fall-----	-----	.002	-----	.180	-----
Average-----	500	.004	2.0	.123	62
Wood Creek:					
Spring-----	-----	.065	-----	.270	-----
Fall-----	-----	.038	-----	.065	-----
Average-----	130	.052	6.8	.168	22
Oneida Creek:					
Spring-----	-----	.060	-----	.055	-----
Fall-----	-----	.017	-----	.065	-----
Average-----	160	.039	6.2	.060	9.6
Canaseraga Creek:					
Spring-----	-----	.042	-----	.030	-----
Fall-----	-----	.022	-----	.036	-----
Average-----	24	.032	.8	.033	.8
Cowaselon Creek:					
Spring-----	-----	.047	-----	.085	-----
Fall-----	-----	.110	-----	.085	-----
Average-----	86	.079	6.8	.085	7.3
Chittenango Cr:					
Spring-----	-----	.051	-----	.100	-----
Fall-----	-----	.065	-----	.021	-----
Average-----	380	.058	22	.060	23
Ungaged streams----	360	1.041	15	1.091	33
Total Basin-----	2,162	-----	73.2	-----	201.6
Outflow - Oneida R:					
Spring-----	-----	0.038	-----	0.023	-----
Fall-----	-----	.008	-----	.017	-----
Average-----	2,162	.023	50	.037	80
kg x 10 <sup>3</sup> Mn retained per year	-----	-----	23.2	-----	-----
kg x 10 <sup>3</sup> Fe retained per year	-----	-----	-----	-----	121.6

<sup>1</sup> Average concentration in the eight gaged streams.

only about 10 percent of the iron loss can be explained by incorporation of iron into nodules. The other obvious sink for iron is the sediments. Table 2 shows that the average iron concentration in sediments from Oneida Lake is more than 10 times greater than the average manganese concentration, a fact indicating that iron is being added to the sediments at a rate that is 10 times the rate of addition of manganese. All these

figures indicate that most the manganese lost from lake water is incorporated in ferromanganese nodules and most of the iron lost from lake water is incorporated in the sediments.

#### Interstitial waters

Interstitial (pore) waters in the sediments also provide a possible sink for both iron and manganese, but,

more importantly, the distributions of iron and manganese concentrations in interstitial waters provide valuable information on the fluxes of these two elements. Iron concentrations in interstitial waters range from less than  $10 \mu\text{g/L}$  (or  $\text{mg/m}^3$ ) to  $100 \mu\text{g/L}$  and average about  $15 \mu\text{g/L}$ . Manganese concentrations in interstitial waters range between less than  $10$  and  $10\,000 \mu\text{g/L}$  and average  $150 \mu\text{g/L}$ . However, what is more important to the origin of ferromanganese nodules is the concentration of an element in interstitial water relative to the concentration of that element in the overlying lake water. Table 3 shows the ratio of concentrations of elements in interstitial waters to concentrations in average Oneida Lake surface water. For the major ions, concentrations in interstitial waters are two to four times higher than in lake water, and these concentrations are about the same in sediments from areas where nodules are present as in sediments from areas where nodules are absent. Manganese concentrations in sediment interstitial waters are generally 10 to 600 times higher than in the average lake water ( $16 \mu\text{g/L}$ ). Also, manganese concentrations in interstitial waters in sediments from nonnodule areas are generally higher than concentrations in interstitial waters in sediments from nodule areas. Iron concentrations, on the other hand, are generally lower in interstitial waters than in average lake water ( $37 \mu\text{g/L}$ ), particularly in nonnodule areas. Considering pH and Eh conditions in Oneida Lake and its tributaries, concentrations of uncomplexed iron(II) greater than about  $10 \mu\text{g/L}$  (0.01 ppm) should not occur (fig. 3). The higher concentrations (up to  $260 \mu\text{g/L}$  with a mean of  $37 \mu\text{g/L}$ ) reported by Greeson (1972) are possibly due to iron transport as ferric colloids and complexes with  $\text{HCO}_3^-$ ,  $\text{OH}^-$ , and (or)  $\text{PO}_4^{3-}$ . Uncomplexed manganese(II), on the other hand, is theoretically stable in the lake water in concentrations up to  $100 \mu\text{g/L}$ . Therefore, most of the manganese is probably transported to the lake as manganous ions and remains in that form until oxidized.

The effects of pH and Eh on the flux of iron and manganese in the sediments are illustrated in table 5, which shows the vertical distributions of Eh, pH, iron, and manganese in interstitial waters from two short cores from Oneida Lake. Interstitial waters in the core from a nodule area show a slight decrease in Eh and pH with depth, but the sediments are well oxidized to a depth of at least 50 cm. Concentrations of iron and manganese are fairly uniform below 1.0 cm with no evidence of diffusion gradients. Measurements of  $^{210}\text{Pb}$  from this core show background levels at all depths and do not exhibit a decay gradient characteristic of lake sediments that have accumulated by continuous

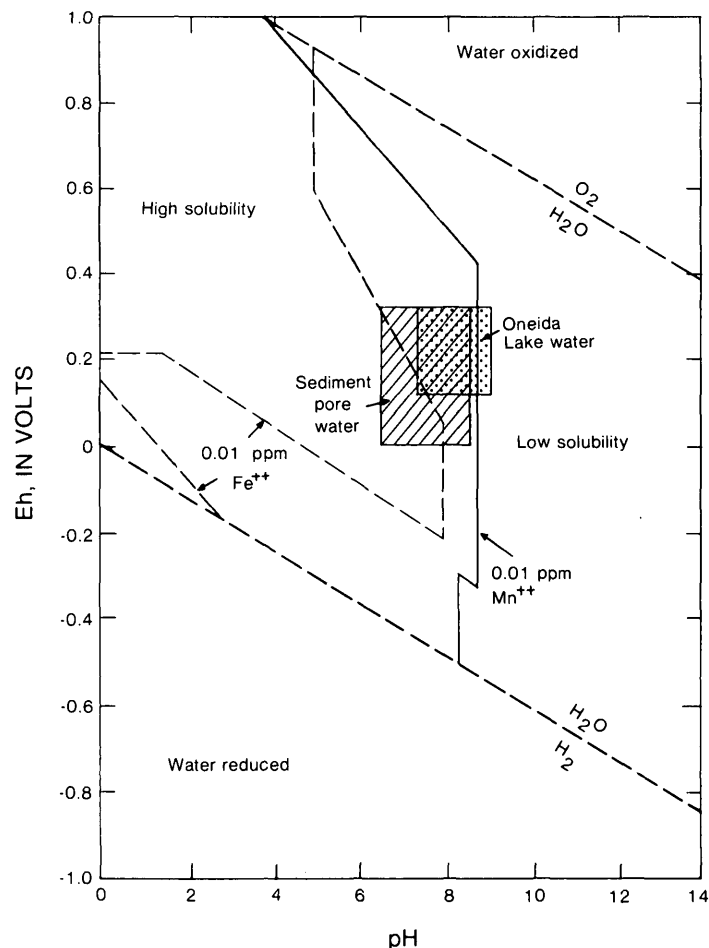


FIGURE 3.—Simplified pH-Eh diagram showing the comparative solubilities of iron and manganese in the system  $\text{H}_2\text{O-Fe-Mn-S-CO}_2$ , 1 atmosphere (101.3 kPa) total pressure, 0.01 mg/L (ppm or  $\text{g/m}^3$ ) each of iron and manganese, and 2000 mg/L each of total  $\text{CO}_2$  (as  $\text{HCO}_3^-$ ) and total S (as  $\text{SO}_4^{2-}$ ) (modified from Hem, 1972).

sedimentation (Krishnaswami and others, 1971; Robbins and Edgington, 1975). This suggests either erosion or nondeposition in the nodule areas. In either case, a hiatus would permit downward diffusion of oxygen, which would maintain high redox conditions within the sediments.

Values of Eh in interstitial waters in the core from a nonnodule area decrease from over 300 mV at the surface to 0 mV at a depth of 37–50 cm. Values of pH also decrease with depth and are in general lower than in the core from the nodule area. Iron concentrations in the upper 37 cm are about four times higher in this core than in the core from the nodule area, whereas manganese concentrations are 10 times higher in the nonnodule core. Although some oxidized iron compounds could exist at pH and Eh conditions within this core, manganese can only exist as manganous ions (fig. 3). Consequently, any manganese

TABLE 5.—Concentrations of iron and manganese and values of Eh and pH of interstitial waters from two sediment cores collected from Oneida Lake

[Data in milligrams per liter are identical with data in grams per cubic meter, the SI derived unit]

Depth (cm)	Fe (mg/L)	Mn (mg/L)	Eh (mV)	pH
Station 44 (nodules abundant)				
0	0	0	300	8.4
1 - 12	0.2	0.25	350	7.5
12 - 25	.2	.30	250	7.5
25 - 37	.2	.30	206	7.5
37 - 50	.35	.30	100	7.5
Station 21 (nodules absent)				
0	0.03	2.50	356	7.9
1 - 12	.80	2.55	300	7.5
12 - 25	.75	2.75	100	6.1
25 - 37	.80	2.70	50	6.1
37 - 50	.80	2.80	0	6.5

oxides or hydroxides present in the sediments at the time of deposition would subsequently be reduced, releasing manganous ions to the interstitial waters. Sedimentation rates in the core, determined by  $^{210}\text{Pb}$  decay gradients, are rapid at the surface (1.45 cm/yr from 1-30 cm) and decrease downward (0.13 cm/yr from 30-50 cm). Such a rapid sedimentation rate would prevent any downward diffusion of oxygen.

An additional relationship between Eh and the distribution of ferromanganese nodules is illustrated by the fact that the 300-mV Eh contour in figure 1 roughly defines the area of occurrence of nodules in the central part of the lake. Therefore, a relatively high Eh is required for nodule formation. The pH-Eh diagram for manganese (fig. 3) shows that for typical manganese concentrations in Oneida Lake on the order of 0.01 mg/L, a fairly high pH (>8) is required to precipitate manganese. Values of pH high enough to precipitate manganese occur in Oneida Lake mainly during the summer months as a result of high rates of algal photosynthesis. Manganese transported to the sediments would, therefore, be reduced throughout most of the year and would become concentrated in interstitial waters (table 3). However, iron can precipitate at lower pH values (fig. 3) and theoretically can precipitate in Oneida Lake throughout the year. As a consequence, iron would become concentrated in the sediments.

### Cyclic precipitation of iron and manganese

Why precipitated iron and manganese oxides and hydroxides should form nodules is still somewhat of a mystery, but probably it is related to electrostatic attraction, as in the model suggested by Burns and Brown (1972). Ferric hydroxide colloids accumulate on any negatively charged surface and may later "age" to goethite. This accumulation would produce a positively charged surface that would attract negatively charged hydrolyzed manganese oxides and hydroxides. The oxidation of manganese is autocatalytic and may continue until the concentration of manganese in the lake and sediment interstitial waters in the vicinity of the nodule is near zero. Precipitation of manganese is seasonal as a result of higher summertime pH values. The nature of the electrolytic attraction is also cyclic, with positively charged ferric hydroxide attracting negatively charged manganese oxides, which, in turn, attract a new surface of ferric hydroxide. Both of these cyclic processes undoubtedly contribute to the characteristic lamination as seen in cross sections of all nodules (fig. 4). Analyses by electron microprobe show that the lamination is due to alternating bands of iron-rich and manganese-rich materials.

### ORGANIC FACTORS

The previously discussed mechanisms operating in the formation of ferromanganese nodules are basically inorganic and imply that it is possible to form ferromanganese nodules without involvement of organisms. However, organic interactions could accelerate nodule formation in several direct and indirect ways. Zapffe (1931) and Krauskopf (1957) suggested that bacteria may act as catalysts in initiating the precipitation of iron and manganese. Ehrlich (1963; 1966; 1968; 1972) pointed out that his data and those of his colleagues

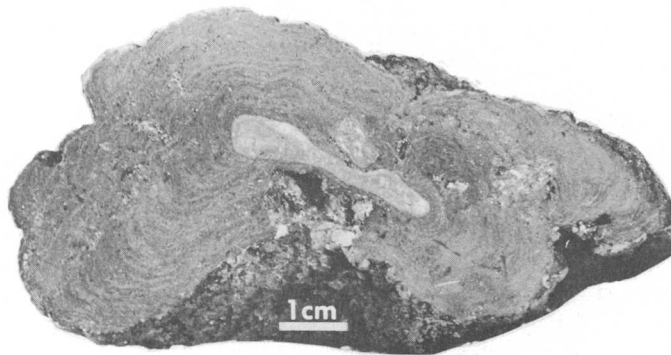


FIGURE 4.—Cross section of a ferromanganese nodule from Oneida Lake, N.Y., showing rock nucleus and characteristic concentric lamination.

strongly suggest that microbes, particularly bacteria, definitely play a role in the formation of marine ferromanganese nodules, but he does not view microbes as the only cause of nodule formation. Ehrlich concluded that the main role of bacteria in nodule formation is the enzymatic catalysis of manganese(II) oxidation.

Graham and Cooper (1959) also proposed direct organic contribution to marine nodule formation to explain the coating of Foraminifera by manganese-rich material. They suggested that the foraminifers provide a protein-rich substrate for other organisms capable of extracting trace metals from sea water. Dudley and Margolis (1974) also suggested that Foraminifera may be important in initiating ferromanganese nodule growth by concentrating trace metals. Greenslate (1974) found that cavities in planktonic skeletal debris, especially diatoms, were apparently serving as nuclei for development of incipient ferromanganese nodules. He suggested that bacteria associated with decay of the planktonic organisms, rather than the organisms themselves, may actually be responsible for the accumulation of ferromanganese.

Budgets for iron and manganese, as previously discussed, indicate average annual losses of 122 t of iron and 23 t of manganese from Oneida Lake. Figure 5 shows that the concentrations of iron and manganese exhibit seasonal variations, suggesting that rates of removal of these two elements from the lake waters are not uniform over the year. Comparisons of variations in iron and manganese concentrations (fig. 5C and 5D) during times of high phytoplankton density (fig. 5B) with those during times of low phytoplankton density further reveal that rates of removal of iron and manganese, as indicated by changes in concentration in the lake water, are negatively correlated with rates of phytoplankton productivity. In other words, manganese, and to a lesser extent iron, tend to decrease during periods of high phytoplankton density and increase during periods of low phytoplankton density. These relationships are particularly evident in the data for 1968. The apparent correlations between rates of iron and manganese removal and rates of phytoplankton productivity suggest that the phytoplankton are major controlling factors in the cycles of iron and manganese in Oneida Lake. This conclusion is supported by the fact that the most extensive freshwater ferromanganese deposit (in terms of tons per unit area) yet reported occurs in highly eutrophic Oneida Lake.

One way in which algae could participate in the cycles of iron and manganese in Oneida Lake is in the concentration of these elements from lake water, perhaps by chelation. For example, the blue-green

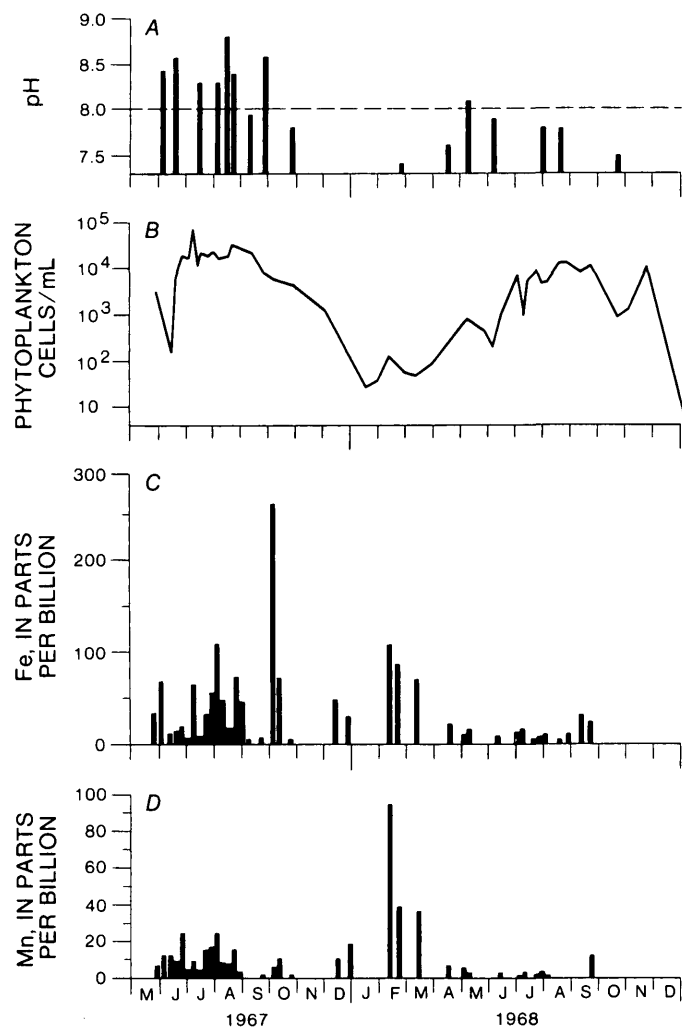


FIGURE 5.—Seasonal variations in Oneida Lake, N.Y., for the period May 1967 to January 1969. A, pH of surface water. B, Phytoplankton density. C, Concentration of iron in surface water. D, Concentration of manganese in surface water.

algae (the dominant algae in Oneida Lake, Greeson, 1972) are known to produce strong iron chelators which enable them to preferentially utilize available iron, so that their growth is enhanced and growth of competitors is restricted (Murphy and Lean, 1975; Murphy and others, 1976). Experimental field studies by Murphy and others (1976) in the Bay of Quinte, Lake Ontario, have shown that blue-green algae are capable of turning over all the iron in the bay in 1 day by chelation. Once incorporated into algal cells, the iron (and manganese) would be transported to the bottom after death of the algae and would be released on decay of the cells.

On the basis of phytoplankton density measurements in Oneida Lake by Greeson (1972), we have calculated an average standing-crop algal biomass of  $16 \times 10^{18}$  cells over the entire lake to a depth of 13 m. An average

annual standing-crop biomass of  $16 \times 10^{18}$  cells has a dry-weight equivalent of  $1.6 \times 10^7$  kg, on the assumption of an average cell density of  $1.0 \text{ g/cm}^3$ , an average cell volume of  $2 \times 10^{-8} \text{ cm}^3$  (estimate based on data compiled by Wetzel, 1975, and measured in sediment trap studies by Braidech and others, 1972), and an average cell content of 95 percent water. A semi-quantitative spectrographic analysis of a mixed assemblage of algae, collected during a blue-green algal bloom in Oneida Lake in July 1975, shows 500 ppm iron and 200 ppm manganese on a dry-weight basis. On the assumption that these are average concentrations of iron and manganese in Oneida Lake algae, an average standing-crop of  $1.6 \times 10^7$  kg contains 8000 kg iron and 3200 kg manganese. Explanation of the losses from Oneida Lake of 122 t/yr iron and 23 t/yr manganese would require about 15 standing-crop doublings to remove that much iron and about seven standing-crop doublings to remove that much manganese, if we assume that none of the iron and manganese was recycled back into the lake's hydrologic system. The assumption of no recycling is not really a practical consideration, but if the iron and manganese are released under oxidizing conditions with a relatively high pH (greater than about 8.0, fig. 3), then most of the iron and manganese would probably not be recycled.

Another important contribution by algae to the cycles of iron and manganese in Oneida Lake is in the production of a well oxygenated, high-pH environment. Figure 5A shows a seasonal variation in pH of lake surface waters which corresponds to seasonal variation in algal productivity (fig. 5B). The pH of surface waters in Oneida Lake averages about 8.0, but may reach values greater than 9.0 during the summer months owing to rapid removal of  $\text{CO}_2$  by photosynthesis (Greeson, 1972). The high pH, well-oxygenated environment created near the surface of Oneida Lake is maintained throughout most of the lake volume by almost continual wind mixing during the ice-free months. An abundance of oxygen at the bottom of Oneida Lake is also indicated by the high Eh values of interstitial waters of surface sediments over most of the lake bottom (fig. 1).

#### REFERENCES CITED

- Braidech, T., Gehring, P., and Klevend, C., 1972, Biological studies related to oxygen depletion and nutrient regeneration processes in the Lake Erie central basin, in Burns, N. M., and Ross, C., eds., Project hypo . . . an intensive study of the Lake Erie central basin hypolimnion and related water phenomena: Canada Centre for Inland Waters Paper 6 (U.S. Environmental Protection Agency Tech. Rept. TS-05-71-208-24), 182 p.
- Burns, R. B., and Brown, B. A., 1972, Nucleation and mineralogical controls on the composition of manganese nodules, in Horn, D. R., ed., Papers from a Conference on Ferromanganese Deposits on the Ocean Floor, NSF-IDOE: Washington, D.C., p. 51-62.
- Burns, R. B., Burns, V. M., and Sung, W., 1974, Ferromanganese nodule mineralogy—Suggested terminology of the principal manganese oxide phases: Geol. Soc. America Abs. with Programs, v. 6, p. 1029-1031.
- Cronan, D. S., and Tooms, T. S., 1969, The geochemistry of manganese nodules and associated pelagic deposits from the Pacific and Indian Oceans: Deep-Sea Research, v. 16, p. 335-359.
- Cronan, D. S., and Thomas, R. L., 1970, Ferromanganese concretions on Lake Ontario: Canadian Jour. Earth Sci., v. 7, p. 1346-1349.
- Dean, W. E., 1970, Fe-Mn oxidate crusts in Oneida Lake, New York: Great Lakes Research Conf., 13th, Proc., p. 1094-1100.
- Dean, W. E., Ghosh, S. K., Krishnaswami, S., and Moore, W. S., 1973, Geochemistry and accretion rates of freshwater ferromanganese nodules, in Morgenstein, M., ed., The origin and distribution of manganese nodules in the Pacific and prospects for exploration, NSF-IDOE: Washington, D.C., p. 13-20.
- Dudley, W. C., and Margolis, S. V., 1974, Iron and trace element concentration in marine manganese nodules by benthic agglutinated foraminifera: Geol. Soc. America Abs. with Programs, v. 6, p. 716.
- Ehrlich, H. L., 1963, Bacteriology of manganese nodules. I. Bacterial action on manganese in nodule enrichment: Appl. Microbiology, v. 11, p. 15-19.
- 1966, Reaction with manganese by bacteria from marine ferromanganese nodules: Devel. Indus. Microbiology, v. 7, p. 43-60.
- 1968, Bacteriology of manganese nodules. II. Manganese oxidation by cell-free extract from a manganese nodule bacterium: Appl. Microbiology, v. 16, p. 197-202.
- 1972, The role of microbes in manganese nodule genesis and degradation, in Horn, D. R., ed., Papers from a Conference on Ferromanganese Deposits on the Ocean Floor, NSF-IDOE: Washington, D.C., p. 63-70.
- Gager, H. M., 1968, Mossbauer spectra of deep-sea iron-manganese nodules: Nature, v. 220, p. 1012-1023.
- Ghosh, S. K., 1975, The origin and geochemistry of ferromanganese nodules in Oneida Lake, New York: Syracuse, N.Y., Syracuse Univ., Ph. D. dissert., 222 p.
- Gorham, E., and Swaine, D. J., 1965, The influence of oxidizing and reducing conditions upon the distribution of some elements in lake sediments: Limnology and Oceanography, v. 10, p. 268-279.
- Graham, J. W., and Cooper, S. C., 1959, Biological origin of manganese-rich deposits of the sea floor: Nature, v. 183, 1050-1051.
- Greenslate, J., 1974, Manganese and biotic debris associations in some deep-sea sediments: Science, v. 186, p. 529-531.
- Greeson, P. E., 1972, Limnology of Oneida Lake with emphasis on factors contributing to algal blooms: U.S. Geol. Survey open-file rept., 255 p.
- Greeson, P. E., and Meyers, G. S., 1969, The limnology of Oneida Lake, an interim report: New York State Water Resources Comm. Rept. Inv. RI-8, 64 p.

- Grill, E. V., Murray, J. W., and Macdonald, R. D., 1968, Todorokite in manganese nodules from a British Columbia fjord: *Nature*, v. 219, p. 358-359.
- Harriss, R. C., and Troup, A. G., 1970, Chemistry and origin of freshwater ferromanganese concretions: *Limnology and Oceanography*, v. 15, no. 5, p. 702-712.
- Hem, J. D., 1972, Chemical factors that influence the availability of iron and manganese in aqueous systems: *Geol. Soc. America Bull.* v. 83 no. 2, 443-450.
- Krauskopf, K. B., 1957, Separation of manganese from iron in sedimentary processes: *Geochim. et Cosmochim. Acta.*, v. 12, p. 61-84.
- Krishnaswami, S., Lal, D., Martin, J. M., and Meybeck, M., 1971, Geochronology of lake sediments: *Earth and Planetary Sci. Letters*, v. 11, p. 407-414.
- Krishnaswami, S., and Moore, W. S., 1973, Accretion rates of freshwater manganese deposits: *Nature*, v. 243, p. 114-116.
- Krishnaswami, S., Somayajulu, B. L. K., and Moore, W. S., 1972, Dating of manganese nodules using beryllium-10, *in* Horn, D. R., ed., *Papers from a Conference on Ferromanganese Deposits on the Ocean Floor*, NSF-IDOE: Washington, D.C., p. 117-122.
- Ku, Teh-Lung., and Broecker, W. S., 1969, Radiochemical studies on manganese nodules of deep-sea origin: *Deep-Sea Research*, v. 16, no. 6, p. 625-637.
- Ku, Teh-Lung., and Glasby, G. P., 1972, Radiometric evidence for the rapid growth rate of shallow-water continental margin manganese nodules: *Geochim. et Cosmochim. Acta.*, v. 36, no. 6, p. 699-703.
- Manheim, F. T., 1965, Manganese-iron accumulations in the shallow marine environment, *in* *Symposium on marine geochemistry*, 1964: Rhode Island Univ. Narragansett Marine Lab. Occasional Pub. 3, p. 217-276.
- Mero, J. L., 1965, *The mineral resources of the sea*: Amsterdam, Elsevier Press, 312 p.
- Moore, W. S., Dean, W. E., and Krishnaswami, S., 1976, Episodic growth of ferromanganese nodules in Oneida Lake, New York: *Geol. Soc. America Abs. with Programs*, v. 8, no. 6, p. 1016-1017.
- Murphy, T. P., and Lean, D. R. S., 1975, The distribution of iron in a closed ecosystem: *Ver. Internat. Verein. Limnologie*, v. 19, p. 258-266.
- Murphy, T. P., Lean, D. R. S., Nalewajko, C., 1976, Blue-green algae: their excretion of iron-selective chelators enables them to dominate other algae: *Science*, v. 192, p. 900-902.
- Robbins, J. A. and Edgington, D. N., 1975, Determination of recent sedimentation rates in Lake Michigan using Pb-210 and Cs-137: *Geochim. et Cosmochim. Acta.*, v. 39, no. 3, p. 285-304.
- Rossmann, Ronald, and Callender, Edward, 1968, Manganese nodules in Lake Michigan: *Science*, v. 162, p. 1123-1124.
- Rossmann, Ronald, Callender, Edward, and Bowser, C. J., 1972, Interelement geochemistry of Lake Michigan ferromanganese nodules: *Internat. Geol. Congress*, 24th, Proc., sec. 10, p. 336-341.
- Schoettle, Manfred, and Friedman, G. M., 1971, Freshwater iron-manganese nodules in Lake George, New York: *Geol. Soc. America Bull.*, v. 82, no. 1, p. 101-110.
- Wetzel, R. G., 1975, *Limnology*: Philadelphia, W. B. Saunders Co., 743 p.
- Zapffe, Carl, 1931, Deposition of manganese: *Econ. Geology*, v. 26, no. 8, p. 799-832.

## OCCURRENCE AND FORMATION OF AVICENNITE, $Tl_2O_3$ , AS A SECONDARY MINERAL AT THE CARLIN GOLD DEPOSIT, NEVADA

By ARTHUR S. RADTKE, FRANK W. DICKSON,<sup>1</sup> and JOHN F. SLACK,  
Menlo Park, Calif., Stanford, Calif., Reston, Va.

**Abstract.**—Avicennite,  $Tl_2O_3$ , occurs as grains disseminated in silicified limestones in the upper part of the East ore zone of the Carlin gold deposit, Nevada. The avicennite is formed by the oxidation of carlinite,  $Tl_2S$ , found in primary unoxidized carbonaceous ore immediately below the avicennite. The grains of avicennite closely resemble carlinite in size and shape. Some avicennite occurs as thin coatings on carlinite, but the time of its formation is unclear. Avicennite grains are polycrystalline, porous, dark gray to black, with a hackly fracture but no discernible cleavage. The Mohs hardness is  $2.0 \pm 0.5$ ; Vickers hardness ranges from 46.0 to 80.5 kg mm<sup>-2</sup>. Measured density is distinctly low, 8.9 g cm<sup>-3</sup> (or Mg m<sup>-3</sup>), relative to the calculated density, 10.34 g cm<sup>-3</sup>. The mineral is isometric, space group  $Ia\bar{3}$ .  $a=10.5468 \pm 0.0003$  angstroms or  $1.05468 \pm 0.00003$  nm,  $Z=16$ , and the volume of the unit cell is  $1173.17 \pm 0.04$  Å<sup>3</sup> or  $1.17317 \pm 0.00004$  nm<sup>3</sup>. The most intense X-ray diffraction peaks are 3.044 (100), 1.864 (38), 2.637 (37), and 1.590 (30). In reflected light, avicennite is pale to medium gray and isotropic and lacks discernible bireflectance. Reflectance in air ranges from 10.6 to 13.0 percent. Avicennite is nearly pure  $Tl_2O_3$ , containing 89.6 weight percent Tl and 10.5 weight percent O by microprobe analysis. Other elements present, detected by emission spectrographic analysis, are: Pb, 300 ppm; Ca, 100 ppm; and Si, Al, Fe, Mg, Ag, Cr, Cu, Ni, and Ti, all <50 ppm.

Avicennite was discovered in oxidized gold ores from the Carlin mine, Nevada, during investigations of epithermal gold deposits of the Western United States. Thallium minerals are rare, but thallium belongs to a suite of elements known to be present in Carlin-type epithermal gold deposits (Weissberg, 1969; Radtke and others, 1972; Radtke and Dickson, 1974; Radtke, Dickson, and Rytuba, 1974). In most deposits, the thallium is present in forms not yet identified. Small amounts of thallium also form a geochemical halo in surrounding country rocks. The Carlin deposit is one of the few places where discrete thallium or thallium-bearing minerals have been found. These include lorandite,  $TlAsS_2$  (Radtke and others, 1973); thallium-bearing orpiment,  $As_2S_3$  (Radtke, Taylor,

and Dickson, 1974); carlinite,  $Tl_2S$  (Radtke and Dickson, 1975); christite,  $TlHgAsS_3$  (Radtke and others, 1977); and weissbergite,  $TlSbS_2$  (F. W. Dickson and A. S. Radtke, unpub. data, 1977). All the thallium minerals except avicennite occur in unoxidized primary ores.

Avicennite was first found by Karpova and others (1958) at Zirabulakh, U.S.S.R., where it occurs as tiny black cubic crystals associated with hematite and calcite in veins in silicified limestone adjacent to an intrusive. The small amount available, about 20 mg, permitted only a semiquantitative analysis, from which the composition  $FeTl_7O_{12}$  was deduced. The X-ray powder diffraction pattern resembled the pattern of synthetic  $Tl_2O_3$ , but many additional lines were present, explained as being caused by unknown admixed minerals. Karpova and others (1958) did not determine whether iron was present as an essential constituent in a compound of fixed composition or whether iron and thallium oxides formed a solid solution. Fleischer (1959) listed avicennite as  $Tl_2O_3$  rather than  $FeTl_7O_{12}$  because of the similarity of the  $d$ -spacings of avicennite to those of pure  $Tl_2O_3$  reported by Zachariasen (1926) and Swanson and Fuyat (1953). The identification was clarified by Konkova and Savelev (1960), who studied avicennite from the original locality and reported that iron was present in impurities and that avicennite was essentially pure  $Tl_2O_3$ . The mode of formation of avicennite at the original locality remains unclear.

Thallium oxides have been reported as secondary minerals at other localities. Ruiz and others (1965) found thin black coatings of  $Tl_2O_3$  on uranium ores from Vizarrón, Mexico. Semenov and others (1967) detected dusty disseminations, possibly of avicennite, in chalcocite ( $Cu_5TlS_2$ ) along with inclusions of native silver, chalcocite, and vrbaita, from Greenland.

Avicennite from Carlin occurs in amounts sufficient for detailed study in a geologic setting that permits

<sup>1</sup> Department of Geology, Stanford University.

evaluation and reconstruction of the processes responsible for its formation.

*Acknowledgments.*—The authors wish to thank the staff and management of Carlin Gold Mining Co. for their support in the study. Special thanks are due Dan Higley for assisting A. S. Radtke in sampling high-thallium areas in inaccessible parts of the East ore body.

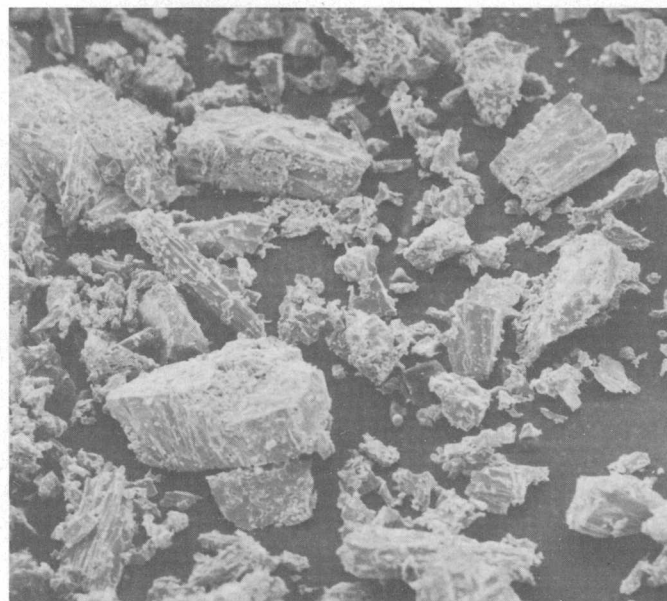
### OCCURRENCE

Avicennite grains, 0.5 mm in diameter or less, are found in silicified limestones and quartz veinlets that ramify oxidized gold ore within and adjacent to fault zones in the East pit of the Carlin deposit (mine coordinates, 22 900–23 050 N., 19 800–19 900 E., elevation 6400–6460 ft or 1950–1970 m; see geologic map, Carlin deposit, Radtke, 1973). The occurrence greatly resembles that of carlinite, which is found in unoxidized ore immediately below (Radtke and Dickson, 1975). Where avicennite occurs, postore leaching and oxidation removed large amounts of carbonate minerals and carbonaceous material and converted sulfides to oxides. During this stage, carlinite was altered to avicennite and pyrite to hematite, so that the typical assemblage of minerals avicennite + hematite + quartz was created.

Minor amounts of avicennite occur as coatings on carlinite from relatively unoxidized ore; it is visible on polished surfaces under reflected light and identifiable in microprobe analysis. Carlinite oxidizes rapidly on exposure to atmospheric oxygen (Radtke and Dickson, 1975). The coatings may have formed at any of several stages, such as during the postore oxidation stage, by action of oxygenated solutions at the lower fringe of the oxidized zone, after the open pit had exposed the rocks to air, or, possibly, subsequent to sampling.

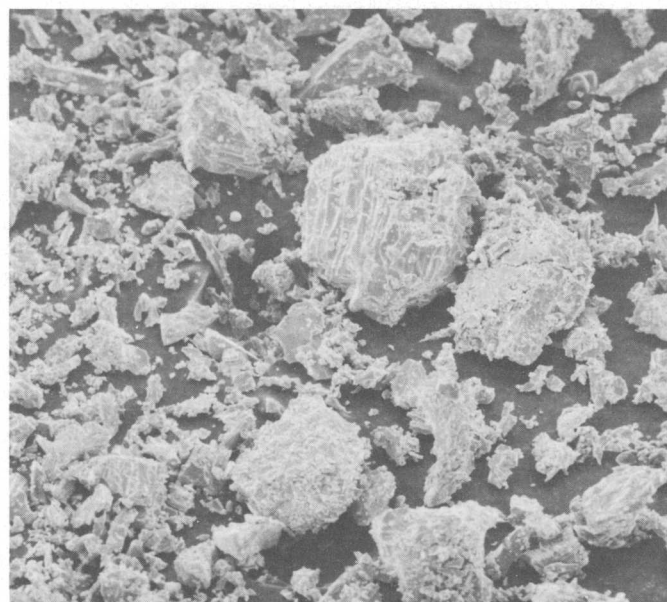
### PHYSICAL AND OPTICAL PROPERTIES

Avicennite in the oxide ores occurs as dark-gray aggregates of minute grains as well as black individual grains visible to the eye (0.5 mm in diameter). Most grains are irregular and rather angular, with shapes similar to carlinite (fig. 1A, B). The larger grains are made up of small tightly packed individual grains and consequently are somewhat porous. The density of avicennite as determined by use of the Berman balance is  $8.9 \text{ g cm}^{-3}$  (or  $\text{Mg m}^{-3}$ ), considerably less than the value of  $10.34 \text{ g cm}^{-3}$  calculated from crystal structure data. The difference between the measured and calculated densities presumably results from the porosity of the mineral. Avicennite is brittle and lacks



A

0.5 mm



B

0.5 mm

FIGURE 1.—Grains, from Carlin gold deposit, separated from host rocks by crushing and bromoform heavy-liquid sedimentation. A, Avicennite. B, Carlinite.

cleavage; individual grains break with a conchoidal fracture, but aggregates of grains display a hackly fracture. Mohs hardness is  $2.0 \pm 0.5$ ; the Vickers hardness shows some variability, ranging from 46 to  $80.5 \text{ kg mm}^{-2}$ , measured with a Leitz hardness indenter using 15- and 25-g loads. The streak is dark gray with

TABLE 1.—Reflectivities of avicennite and synthetic  $Tl_2O_3$  measured in air

[Precision on reflectivity values is  $\pm 0.1$  percent as determined by replicate analyses; reflectivities were measured relative to SiC standard]

Phase	Wavelength (nm)						
	400	470	500	546	589	650	700
Avicennite-----	11.5	12.5	13.0	12.7	12.3	10.6	11.5
Synthetic $Tl_2O_3$ ---	11.8	12.6	12.8	12.6	12.3	10.7	11.7

a brownish tint. In reflected light, avicennite is pale to medium gray, isotropic, and lacks birefractance. Reflectivity was measured in air for avicennite and synthetic  $Tl_2O_3$ , produced by reacting thallium metal in air at  $500^\circ C$  for 3 days, with the results given in table 1.

### CHEMICAL COMPOSITION

Avicennite from the Carlin gold deposit is nearly pure  $Tl_2O_3$ . Microprobe analyses presented in table 2 show that the composition is close to that of stoichiometric  $Tl_2O_3$  with no other elements present at detectable levels. Emission spectrographic analysis given in table 3 confirms the low levels of substitution in the mineral. Lead is reported at 300 ppm. Values of 100 ppm for calcium and 30 ppm or less for silicon, aluminum, iron, and magnesium possibly are produced by the presence of minor amounts of other admixed phases.

### CRYSTALLOGRAPHIC PROPERTIES

Avicennite is isometric, space group  $Ia\bar{3}$ ,  $a=10.5468 \pm 0.0003$  angstroms or  $1.05468 \pm 0.00003$  nm,  $Z=16$ ,

TABLE 2.—Microprobe analyses of avicennite from the Carlin gold deposit

[Analytical conditions: (1) thallium,  $M\beta$  characteristic line, ADP crystal, 18 kV, synthetic  $Tl_2O_3$  standard; (2) oxygen,  $K\alpha$  characteristic line, KAP crystal, 18 kV, synthetic  $Tl_2O_3$  standard]

Grain No.	Weight percent		
	Tl	O	Total
1-----	89.6	10.6	100.2
2-----	89.5	10.4	99.9
3-----	89.6	10.4	100.0
Average---	89.6	10.5	100.1
$Tl_2O_3$ -----	89.49	10.51	100.00

TABLE 3.—Semiquantitative spectrographic analysis of avicennite

[Values reported in percent of the nearest number in the series 1, 0.7, 0.5, 0.3, 0.2, 0.15, 0.1, and so forth, which represent approximate midpoints of interval data on a geometric scale. Analyst: Chris Heropoulos]

Element	Weight percent	Element	Weight percent
Si-----	0.003	Cr-----	0.0003
Al-----	.002	Cu-----	.0001
Fe-----	.003	Ni-----	.0003
Ca-----	.01	Pb-----	.03
Mg-----	.003	Ti-----	.0007
Ag-----	.0001	Tl-----	>20

and the volume of the unit cell is  $1173.17 \pm 0.04 \text{ \AA}^3$  or  $1.17317 \pm 0.00004 \text{ nm}^3$ ;  $d$ -spacings and intensity ratios of avicennite and synthetic  $Tl_2O_3$  are presented in table 4.

The  $d$ -spacings and intensity ratios for avicennite from Carlin were measured by X-ray diffractometer examination of a powder mount; silicon metal was used as an internal standard. The data were refined and unit-cell dimensions were calculated by use of the computer program of Appleman and Evans (1973). The unit-cell-edge value of  $a=10.5468(3) \text{ \AA}$  agrees well with the value for synthetic  $Tl_2O_3$  of  $10.543 \text{ \AA}$  reported by Swanson and Fuyat (1953). Both of these values are somewhat larger than the value of  $10.52 \text{ \AA}$  reported for avicennite by Konkova and Savelev (1960).

The crystal structure of synthetic avicennite was first investigated by Zachariassen (1926), who reported that it belonged to space group  $I2_13$ . Konkova and Savelev (1960), however, determined the space group to be  $Ia\bar{3}$ , the classification arrived at in later studies by Papamantellos (1968) by neutron diffraction techniques. The atoms are arranged according to a body-centered lattice of the  $Mn_2O_3$  type. The structure contains one crystallographic type of oxygen atom and two types of thallium atoms (Lee, 1971). The oxygen atoms are not packed efficiently; under high pressure the packing density increases, and a more efficiently packed structure, probably rhombohedral, is produced (Shannon, 1966; Prewitt and others, 1969).

The crystal structure of the mineral avicennite has not been determined, but the close agreement of crystallographic and powder data of both avicennite and synthetic  $Tl_2O_3$  suggests that they have the same structure.

TABLE 4.—X-ray powder diffraction data for avicennite and synthetic Tl<sub>2</sub>O<sub>3</sub>

hkl	Avicennite			Synthetic Tl <sub>2</sub> O <sub>3</sub> <sup>3</sup>	
	d <sub>calc</sub> (A) <sup>1</sup>	d <sub>obs</sub> (A) <sup>2</sup>	I/I <sub>1</sub>	d <sub>obs</sub> (A)	I/I <sub>1</sub>
200	5.273	---	---	---	---
211	4.306	4.307	17	4.304	11
220	3.729	---	---	---	---
222	3.045	3.044	100	3.042	100
321	2.819	2.819	2	2.816	3
400	2.637	2.637	37	2.635	42
411	2.486	2.486	6	2.484	6
420	2.358	2.359	1	2.357	2
332	2.249	2.249	2	2.248	4
422	2.152	2.153	1	2.149	1
431	2.068	2.068	7	2.068	8
521	1.926	1.925	2	1.924	3
440	1.864	1.864	38	1.863	33
433	1.809	1.809	2	1.808	2
442	1.758	---	---	1.758	1
532	1.711	1.710	4	1.710	5
620	1.668	1.667	1	1.668	2
541	1.627	1.626	4	1.628	4
622	1.590	1.590	30	1.589	27
631	1.555	1.555	5	1.554	6
444	1.522	1.521	6	1.522	6
543	1.492	1.491	2	1.491	3
640	1.463	1.463	<1	1.462	1
721	1.435	1.434	2	1.434	3
642	1.409	1.408	1	1.409	2
732	1.339	1.339	2	1.339	3
800	1.318	1.318	2	1.318	3
741	1.298	1.298	2	1.298	4
820	1.279	1.279	1	1.279	2
653	1.261	1.260	1	1.2597	2
822	1.243	1.242	<1	1.2428	1
743	1.226	1.225	2	1.2261	3
662	1.210	1.209	6	1.2094	6
752	1.194	---	---	---	---
840	1.179	1.179	5	1.1789	4
833	1.165	1.164	<1	1.1646	1
842	1.151	1.150	<1	---	---
921	1.137	1.137	2	1.1371	2
664	1.124	---	---	---	---
851	1.112	1.112	2	1.1110	1
932	1.088	1.087	1	1.0874	1
844	1.076	1.076	2	1.0764	2
941	1.065	1.065	1	1.0649	1
860	1.055	---	---	---	---
772	1.044	---	---	---	---
10.2.0	1.034	1.034	1	---	---
943	1.024	---	---	---	---
10.2.2	1.015	1.014	3	---	---
952	1.006	1.006	1	---	---
871	.9878	.9872	1	---	---
10.4.0	.9793	---	---	---	---
961	.9709	---	---	---	---
10.4.2	.9628	.9629	<1	---	---
873	.9549	---	---	---	---
11.2.1	.9396	---	---	---	---
10.6.2	.8914	.8913	1	---	---

<sup>1</sup>All calculated hkl's listed for d<sub>hkl</sub> ≥ 0.9628 Å. All observed hkl's with d<sub>hkl</sub> ≥ 0.8913 are listed. Indices and d(calc) from the least squares analysis of X-ray powder data using the digital computer program of Appleman and Evans (1973) and cubic cell with a = 10.5468 Å.

<sup>2</sup>X-ray diffractometer conditions are: Ni-filtered Cu radiation; CuKα = 1.54178 Å; Si used as internal standard; scanned at 1°/minute from 20°-124° 2θ. Chart X-3890.

<sup>3</sup>XPDF Card No. 5-0584, Swanson and Fuyat (1953).

## SYNTHESIS

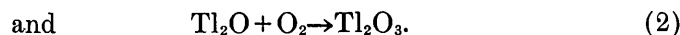
Avicennite may be prepared by reacting metallic thallium with oxygen or by precipitating Tl<sub>2</sub>O<sub>3</sub> from alkaline solutions of thallos ion by adding hydrogen peroxide (Lee, 1971). Tl<sub>2</sub>O<sub>3</sub> precipitated from solution can be dried and crystallized by heating to 500°C. Some care is necessary to avoid the formation of a series of solids of nonstoichiometric composition, with Tl to O ratios greater than 2:3 (Papamantellos, 1968), or compounds with definite compositions between Tl<sub>2</sub>O and Tl<sub>2</sub>O<sub>3</sub> (Mellor, 1924; Sabrowsky, 1969).

The synthetic Tl<sub>2</sub>O<sub>3</sub> used in our reflectivity and microprobe measurements was made by heating thallium metal in air at 500°C for several days. The d-spacings of Tl<sub>2</sub>O<sub>3</sub> prepared in this way did not differ significantly from those given by Swanson and Fuyat (1953).

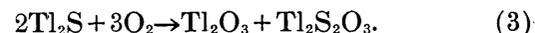
## CHEMISTRY AND GEOCHEMICAL IMPLICATIONS

The chemical behavior of Tl<sub>2</sub>O<sub>3</sub> has not been completely resolved, and conflicting statements exist in the literature. The solubility of Tl<sub>2</sub>O<sub>3</sub> is said to be low (Songina, 1964), but no reliable value has been reported. Tl<sub>2</sub>O<sub>3</sub> supposedly is readily soluble in acids. Songina (1964) stated that the decomposition of Tl<sub>2</sub>O<sub>3</sub> to Tl<sub>2</sub>O plus O<sub>2</sub> proceeds appreciably at temperatures as low as 100°C; Lee (1971), however, mentioned that elemental thallium oxidizes to Tl<sub>2</sub>O<sub>3</sub> on heating in air at dull redness. Thallic ion is a relatively powerful oxidizing agent; E° = +1.25 volts for the half reaction Tl<sup>3+</sup> → Tl<sup>+</sup> + 2e<sup>-</sup> (Lee, 1971). Part of the difficulty in characterizing thallium oxides probably results from the large number of thallium oxide compounds, some of which are nonstoichiometric in composition and poorly crystalline.

The oxidation of Tl<sub>2</sub>S has been studied by several workers (Fentress and Selwood, 1948; Reuter and Goebel, 1953). At room temperature, the reaction stepwise produces oxide and sulfoxide compounds as follows:



The overall reaction is

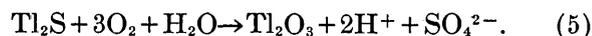


Tl<sub>2</sub>S<sub>2</sub>O<sub>3</sub> tends to disproportionate in the presence of H<sub>2</sub>O (Lee, 1971) as follows:



Tl<sub>2</sub>S<sub>2</sub>O<sub>3</sub>, Tl<sub>2</sub>SO<sub>4</sub>, and H<sub>2</sub>S (or its oxidized product, H<sub>2</sub>SO<sub>4</sub>) are highly soluble and in nature they would be transported away in moving solutions. The overall

result of reaction 3 would be to convert one formula weight of  $Tl_2S$  to one-half of a formula weight of  $Tl_2O_3$ , with a large net loss of volume. This reaction should produce a spongy residue or partially fill openings that have the size of the original carlinite grains. The rate of oxidation of carlinite is so rapid that in the presence of excess oxygen the following alternative reaction is possible:



This reaction would convert one formula weight of  $Tl_2S$  to one formula weight of  $Tl_2O_3$  with only a small change in volume. Reaction 5 seems much more probable than reaction 3 in view of the similarity of the volumes of avicennite grains to the volumes of unaltered carlinite grains (fig. 1).

Based on Lee's thermodynamic data (1971), the standard state Gibbs free energy  $\Delta G_{25^\circ C}^\circ$ , 1 atmosphere (101.3 kilopascals), for reaction 5 is  $-170$  kilocalories per mole ( $-711$  kilojoules per mole). The fugacity  $f_{O_2}$  at which carlinite and avicennite may coexist stably at standard conditions is  $10^{-56.8}$  atm, assuming  $a_{SO_4^{2-}} = 10^{-2}$  and  $a_{H^+} = 10^{-7}$ . For comparison, the  $f_{O_2}$  at which pyrite and hematite coexist at the same conditions is  $10^{-65.7}$  atm (data from Naumov and others, 1974). Therefore, pyrite would oxidize to hematite at a lower oxygen fugacity than carlinite, if equilibrium prevailed. From the thorough breakdown of both pyrite and carlinite to oxides in the zone of oxidation at Carlin, we infer that oxygen fugacities during oxidation were higher than  $10^{-56.8}$  atm within the range of oxygen fugacities expected in normal ground water originally exposed to the atmosphere.

The mode of occurrence of avicennite at Carlin and the chemical properties of carlinite are in accord with the deduction by Radtke and Dickson (1974) that late solutions of surficial origin oxidized the upper part of the primary ore bodies. The presence of avicennite therefore attests to an important part of the complex set of mineralization events at Carlin.

Avicennite forms with such facility that it is likely to be present more commonly than now realized in oxidized ore bodies in carbonate terrane, where excess acidity during oxidation was prevented by acid consumption by carbonate minerals. And because it commonly occurs as inconspicuous coatings on carlinite or possibly on other thallium-bearing minerals, or as dispersed grains, avicennite would be easily overlooked.

#### REFERENCES CITED

- Appleman, D. E., and Evans, H. T., Jr., 1973, Job 9214—Indexing least-squares refinement of powder diffraction data: U.S. Dept. Commerce, Natl. Tech. Inf. Service, PB-216188.
- Fentress, J., and Selwood, P., 1948, Thallous sulfoxylate isomerism: *Am. Chem. Soc. Jour.*, v. 70, p. 711.
- Fleischer, Michael, 1959, New mineral names, avicennite: *Am. Mineralogist*, v. 44, p. 1324-1325.
- Karpova, K. N., Konkova, E. A., Larkin, E. D., and Savelev, V. F., 1958, Avicennite—a new thallium mineral: *Akad. Nauk Uzbek, SSR Doklady*, v. 2, p. 23-25; *Abs., Am. Mineralogist*, v. 44, p. 1324.
- Konkova, E. A., and Savelev, V. F., 1960, A new thallium mineral—avicennite: *All-Union Mineralog. Soc. Mem.*, v. 89, p. 316-320.
- Lee, A. G., 1971, *The chemistry of thallium*: Amsterdam, Elsevier Publishing, Co., 336 p.
- Mellor, J. W., 1924, *A comprehensive treatise on inorganic and theoretical chemistry*, Volume 5: New York, Longmans, Green, and Co., 1004 p.
- Naumov, G. B., Ryzhenko, B. N., and Khodakovskiy, I. L., 1974, *Handbook of thermodynamic data*: U.S. Dept. Commerce, Natl. Tech. Inf. Service Rept. PB-226722, 328 p.
- Papamantellos, P., 1968, Verfeinerung der  $Tl_2O_3$ —struktur mittels neutronenbeugung: *Zeitschr. Kristallographie*, v. 126, p. 143-146.
- Prewitt, C. T., Shannon, R. D., Rogers, D. B., and Sleight, A. W., 1969, The C rare earth oxide-corundum transition and crystal chemistry of oxides having the corundum structure: *Inorganic Chemistry*, v. 8, p. 1985-1993.
- Radtke, A. S., 1973, Preliminary geologic map of the Carlin gold mine, Eureka County, Nevada: U.S. Geol. Survey Misc. Field Studies Map MF-537, scale 1:4,800.
- Radtke, A. S., and Dickson, F. W., 1974, Genesis and vertical position of fine-grained disseminated replacement-type gold deposits in Nevada and USA, in *Problems of ore deposition: Internat. Assoc. Genesis Ore Deposits (IAGOD) Symposium, 4th, Varna 1974, Proc.*, v. 1, p. 71-78.
- 1975, Carlinite,  $Tl_2S$ , a new mineral from Nevada: *Am. Mineralogist*, v. 60, p. 559-565.
- Radtke, A. S., Dickson, F. W., and Rytuba, James, 1974, Genesis of disseminated gold deposits of the Carlin type: *Geol. Soc. America Abs. with Programs*, v. 6, no. 3, p. 239-240.
- Radtke, A. S., Dickson, F. W., Slack, J. F., and Brown, K., 1977, Christite, a new thallium mineral from the Carlin gold deposit, Nevada: *Am. Mineralogist*, v. 62, p. 421-425.
- Radtke, A. S., Heropoulos, Chris, Fabbi, B. P., Scheiner, B. J., and Essington, M., 1972, Data on major and minor elements in host rocks and ores, Carlin gold deposit, Nevada: *Econ. Geology*, v. 67, p. 975-978.
- Radtke, A. S., Taylor, C. M., and Dickson, F. W., 1974, Thallium-bearing orpiment, Carlin gold deposit, Nevada: *U.S. Geol. Survey Jour. Research*, v. 2, no. 3, p. 341-342.
- Radtke, A. S., Taylor, C. M., Erd, R. C., and Dickson, F. W., 1973, Occurrence of lorandite,  $TlAsS_2$ , at the Carlin gold deposit, Nevada: *Econ. Geology*, v. 69, p. 121-124.
- Reuter, Gertold, and Goebel, Alfred, 1953, Über die oxydation des thallium (I)—sulfids, chemismus und kinetik der oxydation bei zimmertemperatur: *Zeitschr. Anorg. u. Allg. Chemie*, v. 271, p. 321-337.
- Ruiz Elizondo, Jesus, Avila Ibarra, Gloria, Cano Corona, Octavio, and Ayala Rojas, Gloria, 1965, Estudios de mineralogía—Pt. 3, Nota preliminar sobre la identificación por rayos X, de óxido tálico  $Tl_2O_3$  como mineral in minerales de Vizarrón, Municipio de Cadereyta, Querétaro: *México Univ. Nac. Autónoma Inst. Geología Bol.* 76, p. 71-80.

- Sabrowsky, H., 1969, Über einkristalle von dithalliummonoxide sowie tetrathalliumtrioxid und dessen halbleitereigenschaften: *Naturwissenschaften*, v. 56, p. 414.
- Semenov, E. I., Sorensen, H., Bessmertnaya, M. S., and Novorossova, L. E., 1967, Chalcothallite, a new sulfide of copper and thallium from the Ilimaussaq alkaline intrusive, south Greenland: *Medd. Gronland*, v. 181, no. 5, p. 13-25.
- Shannon, R. D., 1966, New high pressure phases having the corundum structure: *Solid State Commun.*, v. 4, p. 629-630.
- Songina, O. A., 1964, Redkie metally [Rare metals]: *Izdatel'stvo Metallurgiya, Moskva* (in Russian); English translation by J. Schmorak, 1970, Irsael Program for Sci. Trans., Ltd., Jerusalem.
- Swanson, H. E., and Fuyat, R. K., 1953, Standard X-ray diffraction powder patterns: *U.S. Natl. Bur. Standards Circ.* 539, v. 2, p. 28-29.
- Weissberg, B. G., 1969, Gold-silver precipitates from New Zealand thermal waters: *Econ. Geology*, v. 64, p. 95-108.
- Zachariassen, W. H., 1926, The crystal structure of the modification C of the sesquioxides of the rare earth metals and of indium and thallium: *Norsk Geol. Tidsskr.*, v. 9, p. 310-316.

## MODELS FOR CALCULATING DENSITY AND VAPOR PRESSURE OF GEOHERMAL BRINES

By ROBERT W. POTTER II and JOHN L. HAAS, Jr.,  
Menlo Park, Calif., and Reston, Va.

*Abstract.*—In a model for estimating density of a brine, the density of a natural brine at a known temperature, pressure, and composition can be calculated from the densities of the component salt solutions in the complex brine. A model for estimating vapor pressure requires two direct or indirect estimates of the vapor pressure and uses a published “reference-substance principle” to extrapolate these data 200° to 300° above the temperature of the highest observation. The methods can be used to estimate the partial molal volume and partial molal enthalpy of H<sub>2</sub>O in the natural brine and the partial molal volume change and partial molal heat change for the H<sub>2</sub>O component in the vaporization process. The equations for density and vapor pressure and the derived thermochemical properties will help in designing turbines for operation with geothermal and geopressured brines, in optimizing production conditions, and in physical and chemical modeling of a geothermal reservoir.

The effective use of saline geothermal fluids in the production of electricity requires precise pressure-volume-temperature-composition (P-V-T-X) data. These data are required to minimize scaling and corrosion, to design turbines intelligently, and to establish the optimum operating temperatures, pressures, and flow rates. Also, a set of accurate P-V-T-X data for the fluids involved is an important prerequisite to the modeling of the chemical and physical behavior of geothermal reservoirs, which contain highly saline fluids. Despite the critical importance of the P-V-T-X data in the utilization of saline geothermal resources, very limited data at the temperatures and pressures encountered in the geothermal systems are available (Potter, 1976). In this research, we present relatively simple, workable methods that can be used to accurately predict the density and vapor pressure of complex brines at elevated temperatures. Our approach was to develop a predictive equation for the density of the liquid and to adapt the reference-substance principle of Othmer and Yu (1968) for calculating the vapor pressure of the liquid. Together, these methods give a parametric equation of state for the vapor-saturated liquid.

In this report the application explicitly discussed is the prediction of the liquid properties in a geothermal reservoir. Obviously, these methods can be used to calculate the properties of any brine within the limitations discussed below.

### DENSITY OF A BRINE

#### Methods of estimation

The available published volumetric data for fluids of geothermal interest have been compiled in an annotated bibliography by Potter, Shaw, and Haas (1975). A modest amount of volumetric data for binary systems (such as NaCl-H<sub>2</sub>O) is available and has been critically evaluated and regressed to a “best” set of values for NaCl-H<sub>2</sub>O, KCl-H<sub>2</sub>O, Na<sub>2</sub>SO<sub>4</sub>-H<sub>2</sub>O, K<sub>2</sub>SO<sub>4</sub>-H<sub>2</sub>O, and CaCl<sub>2</sub>-H<sub>2</sub>O (Potter and Brown, 1975, 1976a, b, c; Potter and Clynne, 1976). Data for carbonate-water systems are available as a set of smoothed data in the International Critical Tables (National Research Council, 1928). Internally consistent data for other than binary systems in the temperature-pressure range of geothermal systems are almost nonexistent. The following table lists the temperature ranges over which internally consistent volumetric data for the binary systems are available:

Salt	Temperature range
NaCl	0-500
KCl	0-400
Na <sub>2</sub> SO <sub>4</sub>	0-325
CaCl <sub>2</sub>	0-300
K <sub>2</sub> SO <sub>4</sub>	0-200
Na <sub>2</sub> CO <sub>3</sub>	0-100
K <sub>2</sub> CO <sub>3</sub>	0-100

Because the necessary experimental data are not available, a model or method capable of predicting the P-V-T-X properties of saline geothermal fluids would prove exceedingly useful. There have been several attempts to erect theoretical models for calculating the density of mixed brines, particularly seawater

(Millero, 1973). All of these models are based on the premise that the mean ionic activity coefficient of any strong electrolyte is the same in all solutions of the same ionic strength (Lewis and Randall, 1921), from whence it follows that

$$\phi_{vs} = \sum f_i \phi_{vi} \quad (1)$$

where  $\phi_{vs}$  is the apparent molal volume of the dissolved salts,  $f_i$  is the mole fraction of component  $i$ , and  $\phi_{vi}$  is the apparent molal volume of component  $i$ . Equation 1 is generally referred to as Young's Rule (Young and Smith, 1954) and has been subsequently modified (Wood and Anderson, 1966; Reilly and Wood, 1969; Reilly and others, 1971). These modifications were tested by Millero (1973) and found to give reliable estimates for  $\phi_{vs}$  for seawater over the range of 0° to 40°C. Despite the success in calculating the properties of seawater (Millero, 1973), there are drawbacks that effectively preclude the use of the modified Young's Rule:

1. Young's Rule, as modified, defines components as ionic species and sums all the possible combinations of anions and cations. However, it is not possible to define the speculation accurately in a highly saline fluid at a high temperature.
2. In order to apply the rule, precise molal volume data are required for all the species. However, densities of the required accuracy are generally known only for temperatures less than 50°C.
3. The modified Young's Rule as used by Millero (1973) assumes the additivity of the infinite-dilution volume properties. Although this additivity holds fairly well for chlorides, it has not been generally documented for carbonates and sulfates. Furthermore, predictions based on such assumptions may not work for highly saline fluids such as the Salton Sea, Calif., geothermal fluids.

In addition to the calculations based on the modified Young's Rule, an empirical approach utilizing a similar principle has been used to calculate densities in the system  $\text{Na}_2\text{CO}_3\text{-K}_2\text{CO}_3\text{-H}_2\text{O}$  (Ginzburg, 1965). The empirical relation, which adequately describes the density of the carbonate solution, is

$$d_s = d_k + \frac{(d_n - d_k)c_n}{c_k + c_n} \quad (2)$$

where  $d_s$  is the density of the solution,  $d_k$  is the density of a  $\text{K}_2\text{CO}_3$  solution with a concentration equal to  $c_k + c_n$ ,  $d_n$  is the density of a  $\text{Na}_2\text{CO}_3$  solution with a concentration of  $c_k + c_n$ ,  $c_n$  is the weight percent

$\text{Na}_2\text{CO}_3$ , and  $c_k$  is the weight percent  $\text{K}_2\text{CO}_3$ . If a small amount of an additional component is added, such as  $\text{K}_2\text{SO}_4$ , its effect on the density can be calculated by treating it as if  $c_k$  has increased. (If a sodium-bearing salt were added,  $c_n$  would be increased.) The major difficulty of this model in calculating densities is that it is limited to ternary carbonate solutions.

Ideally, a calculation model for saline geothermal fluids should be one which (1) is not heavily dependent on ionic equilibria, (2) requires density data of moderate precision ( $\pm 0.005$  grams per cubic centimeter) for binary systems, and (3) should be flexible enough to allow calculation of the density even if data are not available for minor constituents. A model with these attributes would be useful in developing saline geothermal resources in the most economic and efficient way.

Note that density values throughout this report are given in grams per cubic centimeter, which are identical with megagrams per cubic meter, the SI derived unit.

#### Principles of the density calculation model

Millero (1973) has convincingly shown that the apparent molal volume of a solution is the same as the weighted sum of the apparent molal volumes of the components at the same ionic strength. Hence it follows that

$$d_s = d_0 + (d_1 - d_0)f_1 + (d_2 - d_0)f_2 + \dots + (d_n - d_0)f_n \quad (3)$$

where  $d_s$  is the density of the solution,  $d_0$  is the density of  $\text{H}_2\text{O}$ ,  $d_1, d_2, \dots, d_n$  are the same densities of the binary salt-water systems of the same molality as the total molality of the solution, and  $f_1, f_2, \dots, f_n$  are the concentrations (molality) of the respective salts divided by the total molality of the solution.

Equation 3 has an important drawback in that the density of pure  $\text{H}_2\text{O}$  at the temperature and pressure of interest is required. At temperatures greater than 374.136°C, the critical point of  $\text{H}_2\text{O}$ , or at pressures below the liquid-vapor coexistence, it becomes very difficult to define the density of pure water at the pressure of the saline fluid. However, because water is simply one component of each binary solution, we can redefine the reference point so that

$$d_s = d_1 + (d_2 - d_1)f_2 + (d_3 - d_1)f_3 + \dots + (d_n - d_1)f_n \quad (4)$$

where  $d_1 < d_2 < d_3 < \dots < d_n$  for computational convenience. To test this relation, the density of a ternary solution NaCl-KCl-H<sub>2</sub>O at 25°C was calculated using both equations 3 and 4, as well as defining for equation 4  $d_1 > d_2 > d_3 > \dots > d_n$  (table 1). All three methods yield the same result, 1.1272 g/cm<sup>3</sup>, which is in good agreement with the measured value of 1.1274 g/cm<sup>3</sup>. Both the calculated value and the measured value have uncertainties of  $\pm 0.0003$  g/cm<sup>3</sup>; hence, within the experimental errors, the numbers are the same.

### Density calculations on ternary and quaternary systems

We made a number of representative density calculations using equation 4 for ternary solutions (table 2). To avoid systematic errors in measurements of the densities by the various investigators, the density data for the component solutions were taken, where possible, from the same source as the density data for the ternary solutions. The limited Na<sub>2</sub>SO<sub>4</sub> data of Fabuss and Korosi (1968) were not extensive enough for the calculations; therefore, we used the data of Potter and Brown (1976c) instead. This in part, explains why deviations for NaCl-Na<sub>2</sub>SO<sub>4</sub> are greater than those for NaCl-KCl. The NaCl, KCl, HCl, and MgCl<sub>2</sub> density data used in calculating densities for the mixed solutions of Völz-Fladrich (1962) are from Potter and Brown (1975, 1976a) and the International Critical Tables (National Research Council, 1928). The

calculated densities (table 2) are in moderately good agreement with the observed densities. The error bands on the experimental and calculated densities overlap in all cases except one, NaCl (0.1601 molal) - CaCl<sub>2</sub> (0.4966 *m*) (Lee, 1966). As the concentration of CaCl<sub>2</sub> increases in Lee's solution, the error in the calculated density also increases. The error is a linear function of the square root of the molality of chloride at the 92.5-percent confidence level and can be related to the formation of associated species, and, hence, with the appropriate density data for the associated species, the calculated density can be corrected to agree with the experimental density. Despite the systematic deviation, the calculated densities are still precise enough for calculations for industrial purposes.

Few data for quaternary systems are available. Some sample calculations from two sets of data are listed in table 3. The density measurements of Nicolai, Ernst, and Wegkamp (1951) have a precision of  $\pm 0.003$  g/cm<sup>3</sup>, and Ginzburg (1965) reported that his numbers had a scatter of  $\pm 0.002$  g/cm<sup>3</sup>, although his data were reported to four decimal places. The calculated and experimental densities all overlap within their respective uncertainties.

### Density calculations on more complex systems

The only data of sufficient accuracy at elevated temperatures with which to test the density model are the density data for a synthetic seawater obtained by Fabuss and Korosi (1968) up to 150°C. Fabuss and Korosi have also measured the densities of NaCl-H<sub>2</sub>O, KCl-H<sub>2</sub>O and MgSO<sub>4</sub>-H<sub>2</sub>O up to 150°C. The CaCl<sub>2</sub>-H<sub>2</sub>O data in the calculations were taken from Potter and Clynne (1976), and the density data for KBr-H<sub>2</sub>O and MgCl<sub>2</sub>-H<sub>2</sub>O at 100°C were obtained from the International Critical Tables (National Research Council, 1928). Data for all the components were available up to 100°C. However, no data were available for KBr and MgCl<sub>2</sub> at 150°C; for the purposes of the calculations, they were calculated as KCl and CaCl<sub>2</sub>, respectively. Even using this approximation, the experimental and calculated densities agree remarkably well (table 4).

White (1965) listed analyses for a Salton Sea, Calif., brine sample whose density at 20°C was reported to be  $1.264 \pm 0.005$  g/cm<sup>3</sup> (the error is high because the density had to be determined at a higher temperature and corrected to 20°C owing to the presence of solid NaCl). The analyses show the brine to be 2.592 *m* NaCl, 0.953 *m* KCl, and 2.2155 *m* CaCl<sub>2</sub>. The other components have been lumped into the above concentrations. Using this composition and the data from Potter and Brown

TABLE 1.—Composition of calculated and observed solution densities

[Observed solution density from Fabuss and Korosi (1968).  $d_n$ , density of salt *n* in g/cm<sup>3</sup>;  $f_m$ , molal proportion of salt *n* in the solution]

No. <i>n</i>	Component	Molality	$d_n$	$f_n$
0	H <sub>2</sub> O	--	0.9970	--
1	NaCl	2.4034	1.1226	0.6800
2	KCl	1.1311	1.1369	0.3200
3	solution	3.5345	1.1274	--

$$\text{Equation 3: } d_s = d_o + (d_1 - d_o)f_1 + (d_2 - d_o)f_2 = 1.1272$$

$$\text{Equation 4, } d_1 < d_2 < d_3: d_s = d_1 + (d_2 - d_1)f_2 = 1.1272$$

$$\text{Equation 4, } d_1 > d_2 > d_3: d_s = 1.1272$$

TABLE 2.—Calculated and observed densities for ternary systems

Source of data <sup>1</sup>	Salt	Concentration	Salt	Concentration	Temp., °C	Density (g/cm <sup>3</sup> )	
						Observed	Calculated <sup>2</sup>
Fabuss and Korosi (1968)	NaCl	2.4034 m	KCl	1.1311 m	25	1.1274	1.1272
	NaCl	2.4078	KCl	1.1332	75	1.1014	1.1016
	NaCl	2.4144	KCl	1.1363	100	1.0859	1.0863
	NaCl	2.4274	KCl	1.1424	125	1.0692	1.0696
	NaCl	2.4512	KCl	1.1536	150	1.0517	1.0522
	NaCl	2.7569	Na <sub>2</sub> SO <sub>4</sub>	.2591	25	1.1239	1.1232
	NaCl	2.7621	Na <sub>2</sub> SO <sub>4</sub>	.2596	75	1.0980	1.0989
	NaCl	2.7698	Na <sub>2</sub> SO <sub>4</sub>	.2603	100	1.0822	1.0818
	NaCl	2.7849	Na <sub>2</sub> SO <sub>4</sub>	.2618	125	1.0654	1.0645
	NaCl	2.8126	Na <sub>2</sub> SO <sub>4</sub>	.2644	150	1.0476	1.0457
Lee (1966)	NaCl	.1601	CaCl <sub>2</sub>	.0375	25	1.00698	1.00696
	NaCl	.1601	CaCl <sub>2</sub>	.0871	25	1.01141	1.01135
	NaCl	.1601	CaCl <sub>2</sub>	.1459	25	1.01659	1.01651
	NaCl	.1601	CaCl <sub>2</sub>	.4966	25	1.04688	1.04655
Völz-Fladrich (1962)	NaCl	11.93%	HCl	10.11%	25	1.1356	1.1360
	NaCl	18.04	HCl	5.56	25	1.1594	1.1598
	NaCl	2.76	HCl	20.08	25	1.1160	1.1172
	MgCl <sub>2</sub>	18.5	HCl	17.99	25	1.257	1.257
	KCl	19.99	HCl	6.97	25	1.135	1.136

<sup>1</sup>Density data for Na<sub>2</sub>SO<sub>4</sub> from Potter and Brown (1976c); density data for all salts in Völz-Fladrich's solutions from Potter and Brown (1975, 1976a) and National Research Council (1928).

<sup>2</sup>Calculated using equation 4 of this report.

(1975, 1976a) and Potter and Clynne (1976), the density of the brine as a function of temperature was calculated and is tabulated as follows:

Temperature (°C)	Density (g/cm <sup>3</sup> )
25	1.264
50	1.249
75	1.237
100	1.221
200	1.142
300	1.033

The following equation describes the data as follows:

$$d_{\text{Sol}} = 1.2730 - 3.771 \times 10^{-4} T - 1.407 \times 10^{-6} T^2 \pm 0.002. \quad (5)$$

This equation yields a solution density at 20°C of  $1.265 \pm 0.002$  g/cm<sup>3</sup>, which is in excellent agreement with the measured density, particularly in view of the assumptions made for the calculation.

TABLE 3.—Calculated densities for quaternary systems

Source of data	Salt	Concentration	Salt	Concentration	Salt	Concentration	Temp., °C	Density (g/cm <sup>3</sup> )	
								Observed	Calculated
Nicolai and others (1951)	NaCl	5.766 m	KCl	0.308 m	Na <sub>2</sub> SO <sub>4</sub>	0.162 m	25	1.213	1.211
	NaCl	5.612	KCl	.617	Na <sub>2</sub> SO <sub>4</sub>	.162	25	1.218	1.216
	NaCl	5.493	KCl	.617	Na <sub>2</sub> SO <sub>4</sub>	.324	25	1.228	1.227
	NaCl	5.321	KCl	.925	Na <sub>2</sub> SO <sub>4</sub>	.324	25	1.232	1.232
	NaCl	5.321	KCl	.617	Na <sub>2</sub> SO <sub>4</sub>	.486	25	1.237	1.237
	NaCl	5.185	KCl	.925	Na <sub>2</sub> SO <sub>4</sub>	.486	25	1.242	1.243
Ginzburg (1965)	Na <sub>2</sub> CO <sub>3</sub>	23.31%	K <sub>2</sub> CO <sub>3</sub>	12.01%	K <sub>2</sub> SO <sub>3</sub>	1.80%	25	1.3911	1.3924

TABLE 4.—Calculation of the density of Fabuss and Korosi's (1968) synthetic seawater using equation 4

Salts and concentrations			
NaCl	0.4756 m	CaCl <sub>2</sub>	0.01034 m
KCl	.00923	MgCl <sub>2</sub>	.0244
KBr	.00084	MgSO <sub>4</sub>	.02973

Temp., °C	Density (g/cm <sup>3</sup> )	
	Observed	Calculated
100	0.9838	0.9838
	±.0005	±.0015
150	.9451	.9838
	±.0010	±.0015

### VAPOR PRESSURE OF A BRINE

Estimating the vapor pressure of a strong brine is almost always impractical. Most techniques are based on estimation of the osmotic coefficient of the brine. By iteration, the vapor pressure of H<sub>2</sub>O can be calculated. Such functions work well where there are sufficient data and where these data cover a large range in pressure, temperature, and composition. Under these conditions, the formulas are used, generally, to interpolate between the data points. Because the formulas always depend in part on empirical functions, extrapolation is not possible.

### Reference-substance principle

One technique to extrapolate data from lower temperatures to as much as 200° to 300°C above the temperature range of the observations, however, has proved to be fairly accurate. The technique was first suggested by Othmer in 1940 and was developed by Othmer and Yu (1968). The technique is based upon the reference-substance principle (Othmer, 1940; Othmer and Chen, 1968), where the unknown properties of a liquid are derived by comparison with those of another liquid. Othmer and his coworkers were most interested in organic liquids and solutions. However, Haas (1971a, b; 1976a, b) has used the technique, with a slight modification, to derive a function for the vapor pressure of the H<sub>2</sub>O–NaCl system from the freezing temperatures to 300°C with a precision of 0.32 percent of the observed vapor pressure. In those studies, liquid water was the reference substance.

From the Clapeyron equation for the vaporization of two liquids, Othmer and Yu (1968) have shown that the temperature  $T_x$  of a brine (or other liquid where more data are needed) and the temperature  $T_o$  of the reference substance at the same pressure can be related by the equation

$$\ln T_o + \ln T_x + c, \quad (6)$$

where  $m$  is the slope and  $c$  is the intercept. (Refer to figure 1 for a graphical description of the relation between  $T_x$  and  $T_o$  at constant pressure.) In the previous work by Haas on the H<sub>2</sub>O–NaCl system, it was found that one can improve the calculation by setting  $c=0$  and  $m=(a+bT_x)^{-1}$ . Equation 6 can be rewritten as

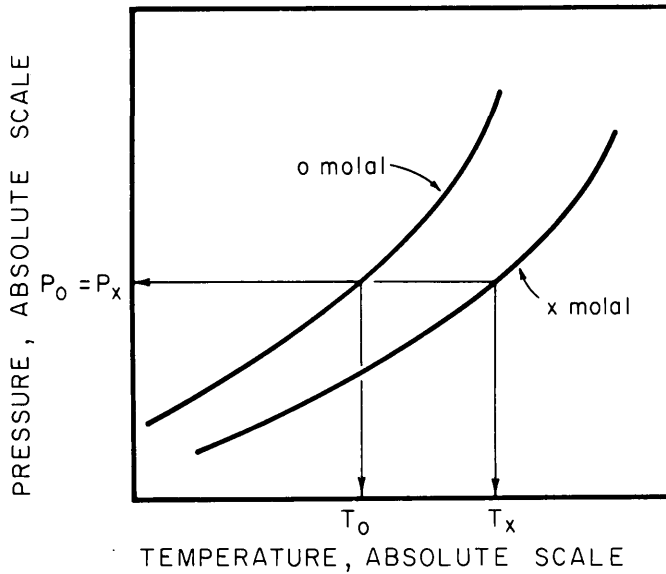


FIGURE 1.—Schematic representation of the relation between  $T_x$  and  $T_o$ .  $T_x$  is the temperature of the brine,  $x$  molal, and  $T_o$  is the temperature of liquid water, 0 molal, at the same pressure. The relation between  $T_x$  and  $T_o$  is given in the text.

$$\ln T_o = (a + bT_x)^{-1} \ln T_x \quad (7)$$

Knowing the vapor pressure for liquid water at  $T_o$  gives us the same pressure for the brine at  $T_x$ . In the applications described in this report, both the solvent and the reference substance is liquid water. Therefore, the assumption that  $c$  is small is valid because the differences between  $\ln T_o$  and  $\ln T_x$  at constant pressure will be nil at  $\ln T_o = 0$  (or at  $T_o = 1$  K).

Equation 6 was derived from the differential equation  $(\partial \ln T_o)_{p,x}$

$$= \left( \frac{\Delta \bar{H}}{\Delta \bar{V}} \right)_x / \left( \frac{\Delta \bar{H}}{\Delta \bar{V}} \right)_o \cdot (\partial \ln T_x)_{p,x} \quad (6a)$$

where  $(\Delta \bar{H}/\Delta \bar{V})_o$  and  $(\Delta \bar{H}/\Delta \bar{V})_x$  are the ratios of partial molal heat to partial molal volume for the vaporization of  $H_2O$  from the reference liquid and brine, respectively. In the derivation of equation 6 from equation 6a, as a first approximation, Othmer and Yu (1968) assumed that the ratio of the two ratios was independent of temperature. This assumption must be invalid; therefore, a linear function,  $a' + b'T_x$ , was used. (Haas (1971a, b; 1976a, b) used the reciprocal,  $(a + bT_x)^{-1}$ ; however, either expression is valid, and, hence, the form of equation 7.)

## $H_2O$ -NaCl system

Figures 2, 3, and 4 demonstrate the application of the principle by using the data for a 1-*m* NaCl solution. In figure 2, the function  $(\ln T_x/\ln T_o) - 1$  is plotted as a function of  $T_x$ , the temperature of the brine. Using least-squares regression, the constants  $a$  and  $b$

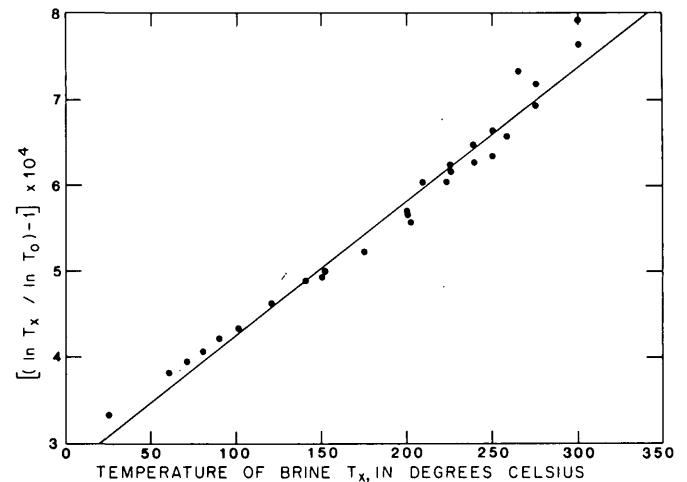


FIGURE 2.—Plot of the function  $((\ln T_x/\ln T_o) - 1)$  against  $T_x$ , the temperature of the brine.  $T_o$  is the temperature of liquid water that has the same vapor pressure as the brine at  $T_x$ .

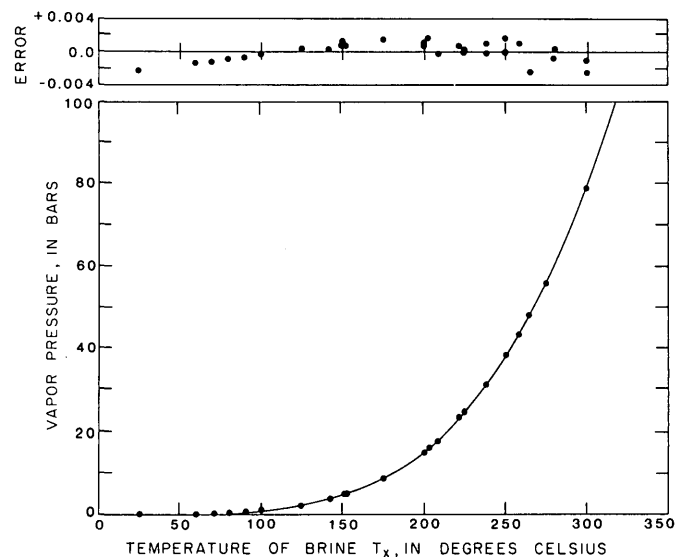


FIGURE 3.—Plot of the vapor pressure of a 1-*m* NaCl solution as a function of temperature. Solid circles are the published experimental data; solid line was derived by using the function  $\ln T_o = (a + bT_x)^{-1} \ln T_x$  and the vapor pressure data for liquid water at  $T_o$ . The error plot at the top shows the relative error (observed-calculated)/observed for each observation. The data were taken from Smith (1939), Smith and Hirtle (1939), Gardner, Jones, and deNordwall. (1963). Lindsay and Liu (1968), Liu and Lindsay (1971), Gardner (1969), Robinson and Stokes (1959), and Bain (1964).

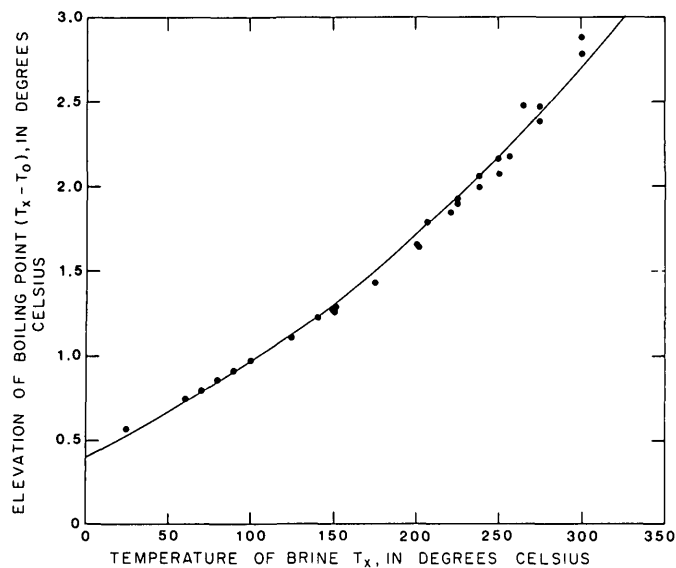


FIGURE 4.—Plot of the boiling point elevation of a 1-*m* NaCl solution as a function of temperature. Solid circles are derived from published experimental data (see fig. 3); solid line was calculated using the function  $\ln T_0 = (a + bT_x)^{-1} \ln T_x$ .

(eq 7) were found to be 0.99984279 and  $1.5668108 \times 10^{-6}$ , respectively. Because the properties of H<sub>2</sub>O in the reference substance and in the brine are being compared, a minimum of six digits to the right of the decimal is needed. To avoid introducing error due to rounding off of *a* and *b*, we carry eight digits.

These constants were used to calculate the vapor pressure of the 1-*m* NaCl solution (fig. 3). At the top of figure 3 is an error plot where the relative error is plotted as a function of the brine temperature  $T_x$ . Figure 4 shows the elevation of the boiling point  $T_x - T_0$  plotted as a function of the brine temperature  $T_x$ .

### Complex brines

The previous section demonstrates the success of the method in modeling a simple brine. In that case, all available data were used to obtain the constants *a* and *b*. However, equation 7 is a single-valued function and, in principle, requires as few as two well-defined data points to determine *a* and *b*. Figure 5 shows the vapor pressure of selected brines in the system H<sub>2</sub>O–Na<sub>2</sub>O–Al<sub>2</sub>O<sub>3</sub> (Dibrov and others, 1964). The vapor pressure of liquid water is also plotted (curve 1) for reference. The data at 75° and 300°C were used to calculate the constants *a* and *b*. The reported experimental precision for the measurement of vapor pressure of H<sub>2</sub>O in the apparatus is 1 percent. Judging from the error plots given at the top of Dibrov, Mal'tsev, and Mashovets' (1964) figure 1, the experimental precision for the

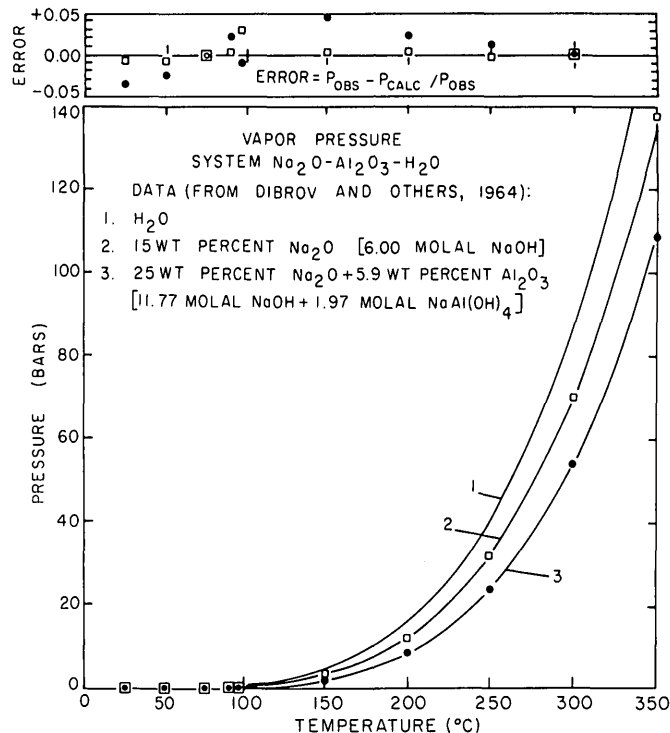


FIGURE 5.—Observed and calculated vapor pressure of some complex brines in the system Na<sub>2</sub>O–Al<sub>2</sub>O<sub>3</sub>–H<sub>2</sub>O. For reference, curve 1 is the vapor pressure of liquid water. Observed data were taken from Dibrov, Mal'tsev, and Mashovets (1964).

NaOH–H<sub>2</sub>O and NaOH–NaAl(OH)<sub>4</sub>–H<sub>2</sub>O systems must be somewhat greater.

Another complex brine for which more accurate data are available is simulated seawater. Liu and Lindsay (1971) reported smoothed boiling-point elevations for concentrations of a simulated seawater consisting of 0.42663 *m* NaCl, 0.02976 *m* NaSO<sub>4</sub>, and 0.06726 *m* MgCl<sub>2</sub>. The constants *a* and *b* were calculated using the values for a fourfold concentrate of the above solution at 75° and 100°C. Figure 6 graphically compares the predicted values (solid line) with the tabulated data. The error at 300°C is 0.47° or 0.05 megapascal if vapor pressure were calculated. These errors are small when the magnitude of the extrapolation is considered. If *a* and *b* were determined from data points farther apart than 25°, these errors would be smaller.

### Procedures for calculations

In the last example above, data at two temperatures 25°C apart were used to estimate the boiling-point elevation. It is obvious that the greater the spread in the known data, the better the estimation, because errors in the known data have correspondingly less

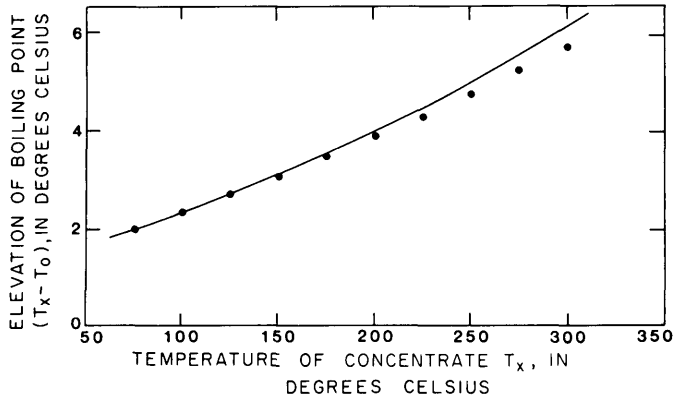


FIGURE 6.—Plot of boiling-point elevation ( $T_x - T_o$ ) for a concentrate of a simulated seawater against temperature. Data from Liu and Lindsay (1971). Solid line was calculated using equation 7 and observations at 75° and 100° C only.

effect. Commonly available data for solutions are (1) depression of the freezing point (for dilute solutions), (2) the normal boiling-point elevation where the vapor pressure of the brine is 101.3 kilopascals (1 atmosphere), and (3) osmotic coefficients near room temperature. From any two of these or from directly observed vapor pressures of the brine of interest, the constants  $a$  and  $b$  of equation 7 may be estimated.

From the freezing-point depression  $\tau$ , the temperature of the freezing point  $T_f$  is calculated.

$$T_f = 0.01 - \tau \quad (8)$$

Then, reference tables are used to determine the vapor pressure of ice at  $T_f$  ( $= T_x$ ) and  $T_o$ , the temperature at which metastable liquid water has the same vapor pressure.

Data for the boiling-point elevation  $\theta$  are less complicated to use because  $T_o$  is given. The temperature of the brine  $T_x$  at the same pressure as liquid water at  $T_o$  is

$$T_x = T_o + \theta \quad (9)$$

The osmotic coefficient  $\phi$  for a brine is used to obtain  $T_x$  and  $T_o$  at the same pressure, given  $T_x$ , by relating the osmotic coefficient and the activity of  $H_2O$ ,  $\alpha$ , in the equation

$$\ln \alpha = - \frac{(\sum m_i) W_1}{10^3} \phi \quad (10)$$

where  $\sum m_i$  is the sum of all the ionic molalities, and  $W_1$  is the molecular weight of  $H_2O$ . At temperatures of and below 100°C, the fugacity coefficient for vapor-

saturated liquid is near unity (Haas, 1970). Therefore we can make the approximation

$$P = \alpha \cdot P(\text{saturated}) \quad (11)$$

where  $P$  is the vapor pressure of the brine at  $T_x$  and  $P$  (saturated) is the vapor pressure of liquid water at the same temperature  $T_x$ . Reference tables are used to determine the temperature  $T_o$  of liquid water at the pressure  $P$ .

The constants  $a$  and  $b$  of the 1- $m$  NaCl solution were found to be 0.99992323 and  $1.3667426 \times 10^{-6}$ , respectively, when the freezing-point depression (Momicchiolo and others, 1970) and boiling-point elevation (Smith, 1939) were used. The vapor pressures for liquid water and ice came from Bain (1964) and Goff (1963), respectively. Figure 7 shows the new equation (solid line) compared to the available data and the equation derived from the least-squares analysis (dashed line). Figure 8 gives the observed vapor pressures of the 1- $m$  solution and the calculated fit using these two observations (solid line). The error plot is at the top of the figure. When compared with figure 3, divergence occurs near 300°C, an extrapolation of 200° above the normal boiling point.

## APPLICATIONS

The two models described in this report have been shown to describe adequately the density (or specific

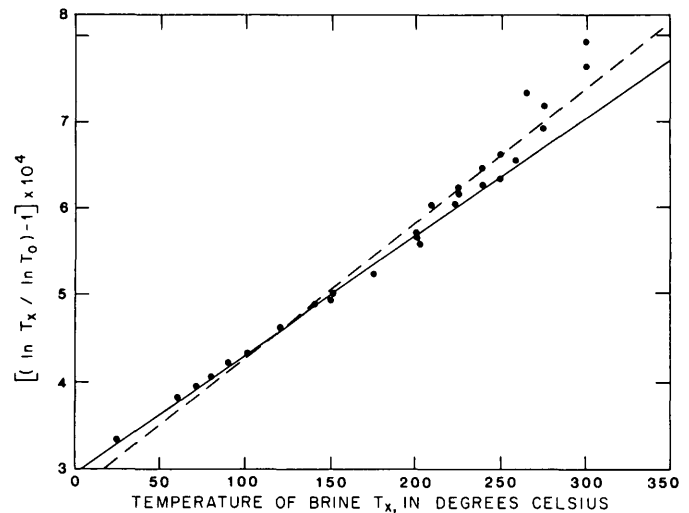


FIGURE 7.—Comparison of the function  $((\ln T_x / \ln T_o) - 1)$  as estimated from freezing-point depression and boiling-point elevation (solid line) of 1- $m$  NaCl solution with observations (solid circles) and least-squares regression of the data (dashed line). References for observations are given in legend for figure 3. Freezing-point depression was interpolated from data in Momicchioli and others, (1970) and boiling-point elevation from Smith (1939).

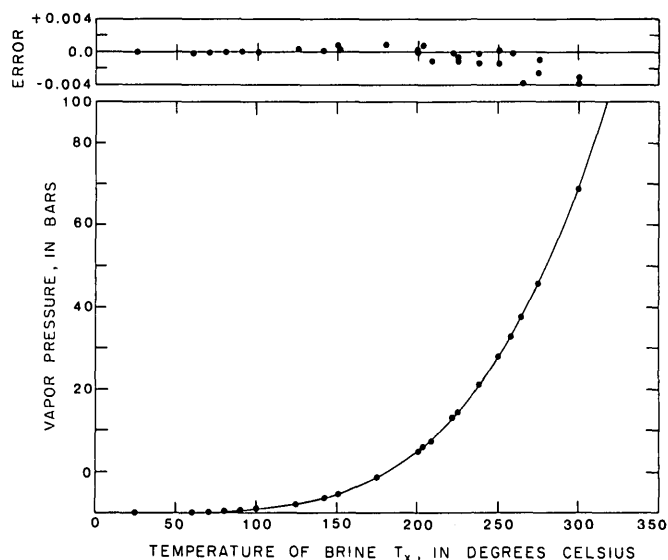


FIGURE 8.—Comparison of predicted (line) and observed (circles) vapor pressures of 1-*m* NaCl solution. Predicted curve was derived from freezing-point depression and normal boiling-point elevation. Relative error plot of the fit is shown at top of figure.

volume) and the vapor pressure of complex brines at elevated temperatures along the liquid-vapor coexistence surface. The calculated density is of sufficient accuracy that one can get a first estimate of the partial molal volume of the water in the liquid. To obtain  $V(\text{H}_2\text{O})$ , one keeps the proportion of each salt to the total concentration constant.

The molal volume of the solution  $V_s$  is plotted as a linear function of the mole fraction of the water  $N_{\text{H}_2\text{O}}$ . The terms  $N_{\text{H}_2\text{O}}$  and  $V_s$  are calculated from equations 12 and 13, respectively:

$$N_{\text{H}_2\text{O}} = \frac{55.51}{55.51 + \sum_{i=1}^n m_i} \quad (12)$$

and

$$V_s = \frac{1}{d} \left( \frac{1,000 + \sum_{i=1}^n m_i W_i}{n} \right) \frac{\text{cm}^3}{\text{mole}}, \quad (13)$$

where  $n$  is the number of salts,  $m_i$  is the molality of the  $i$ th salt,  $d$  is the estimated density, and  $W_i$  is the molecular weight of the  $i$ th salt. The constant 55.51 is the number of moles of water in a kilogram of water. The partial molal volume of water,  $V(\text{H}_2\text{O})$ , is obtained graphically by drawing the tangent at the mole fraction corresponding to the composition of

interest and determining the intercept of that tangent with the ordinate at  $N_{\text{H}_2\text{O}} = 1$ .

Haas (1976a) described in detail how the estimation of vapor pressure in the  $\text{H}_2\text{O}$ -NaCl system was used to estimate the heat of vaporization of the  $\text{H}_2\text{O}$  component and, when combined with  $V(\text{H}_2\text{O})$ , the partial molal enthalpy of the  $\text{H}_2\text{O}$  component in the liquid. The same procedure can be used for complex brines containing no volatile components other than the solvent water.

The predictive techniques for physical properties of the brine and of the thermochemical properties of the water component have many applications. For the utilization of geothermal brines, techniques such as those developed here are needed to describe the behavior of the complex natural solutions as a function of changes in temperature, vapor pressure, and water content. These techniques can be used to calculate boiling curves for mineralizing ore fluids, following the approach given by White (1968) or Haas (1971b). Because density estimates are equally valid whether or not vapor is present, the density of aqueous solutions in a geopressed reservoir or of pore fluid in the shallow parts of the Earth's crust can also be estimated. Among others, theories on spontaneous convection in a sulfide-mineralizing environment can be tested.

The density-estimation method will give reliable results, provided there are no concentration-dependent changes in the components, such as those in aqueous sulfuric acid ( $\text{H}_2\text{SO}_4$ ). In dilute solutions (activity of  $\text{H}^+ \leq 10^{-2}$   $m$ ), the species present are two  $\text{H}^+$  and one  $\text{SO}_4^{2-}$  for every molecule of dissolved  $\text{H}_2\text{SO}_4$ . In an intermediate range of concentration (activity of  $\text{H}^+$  between  $10^{-2}$  and about  $10^1$   $m$ ), the dominant species are  $\text{H}^+$  and  $\text{HSO}_4^-$ . In the concentrated region (greater than  $10^1$   $m$ ), the dominant dissolved species is unionized  $\text{H}_2\text{SO}_4$ . Because the nature of dissolved species changes with concentration, few predictive techniques work for sulfuric acid. Sulfuric acid is not common in natural brines, and most components of natural brines do not change with concentration. Therefore, few problems are to be expected in the application of the method to natural brines.

The estimation of vapor pressure is not subject to such failures. Here, failure will stem from too great an extrapolation of the data or from using data too closely spaced in temperature to get reliable estimates of the constants in the term  $(a + bT_x)$ . Greater extrapolations could be made by adding a term  $cT_x^2$  to the above, but the data are seldom of sufficient accuracy to justify the additional term.

In summary, the procedures given here can be used to estimate P-T-V-X properties of naturally occur-

ring aqueous liquids. They will also permit the estimation of the partial molal volume and partial molal enthalpy of the H<sub>2</sub>O component in the liquids. The easy calculation of these parameters should contribute significantly to the study of geochemical and geophysical processes where water is a significant component.

### REFERENCES CITED

- Bain, R. W., 1964, Steam tables 1964: Edinburgh, Her Majesty's Stationery Office, 147 p.
- Dibrov, I. A., Mal'tsev, G. Z., and Mashovets, V. P., 1964, Saturated vapor pressure of caustic soda and sodium aluminate solutions in the 25–350° temperature range over a wide range in concentrations: *Jour. Applied Chem. USSR*, v. 37, p. 1907–1915.
- Fabuss, B. M., and Korosi, Alexander, 1968, Properties of sea water and solutions containing sodium chloride, potassium chloride, sodium sulfate, and magnesium sulfate: U.S. Office Saline Water Research Development Progress Rept. No. 384, 133 p.
- Gardner, E. R., 1969, Osmotic coefficients of some aqueous sodium chloride solutions at high temperature: *Faraday Soc. Trans.*, v. 65, p. 91–97.
- Gardner, E. R., Jones, P. J., and deNordwall, H. J., 1963, Osmotic coefficients of some aqueous sodium chloride solutions at high temperature: *Faraday Soc. Trans.*, v. 59, p. 1994–2000.
- Ginzburg, D. M., 1965, [The density and vapor pressure of sodium and potassium carbonate solutions]: *zhur. Prikladnaya Khim.*, v. 38, p. 55–58 (in Russian).
- Goff, J. A., 1963, Saturation pressure of water on the new Kelvin scale: Humidity moisture, Papers, Intern. Symp., Washington, D. C., 1963, Proc., v. 3, p. 289–292.
- Haas, J. L., Jr., 1970 Fugacity of H<sub>2</sub>O from 0° to 350°C at the liquid-vapor equilibrium and at 1 atmosphere: *Geochim. Cosmochim. Acta*, v. 34, p. 929–932.
- 1971a, Thermodynamic correlations for brines: NaCl–H<sub>2</sub>O liquid-vapor equilibria [abs.]: *Am. Geophys. Union Trans.*, V. 52, p. 379.
- 1971b, The effect of salinity on the maximum thermal gradient of a hydrothermal system at hydrostatic pressure: *Econ. Geology*, v. 66, p. 940–946.
- 1976a, Physical properties of the coexisting phases and thermochemical properties of the H<sub>2</sub>O component in boiling NaCl solutions: *U.S. Geol. Survey Bull.* 1421–A, 73 p.
- 1976b, Thermodynamic properties of the coexisting phases and thermochemical properties of the NaCl component in boiling NaCl solutions: *U.S. Geol. Survey Bull.* 1421–B, 71 p.
- Lee, Shiu, 1966, The apparent and partial molal volumes of electrolytes in water and in aqueous sodium chloride solutions: Yale Univ., Ph. D. thesis, 141 p.; *Univ. Microfilms*, Order No. 66–4906; *Dissertation Abs.*, v. B27, p. 131.
- Lewis, G. N., and Randall, M., 1921, The activity coefficient of strong electrolytes: *Jour. Am. Chem. Soc.*, v. 43, p. 1112–1154.
- Lindsay, W. T., Jr., and Liu, C.-T., 1968, Vapor pressure lowering of aqueous solutions at elevated temperatures: U.S. Office Saline Water Research Development Rept. 347, 235 p.
- Liu-C.-T., and Lindsay, W. T., Jr., 1971, Thermodynamic properties of aqueous solutions at high temperatures: U.S. Office Saline Water Research Development Rept. 722, 124 p.
- Millero, F. J., 1973, Seawater—A test of multicomponent electrolyte solution theories, pt. 1, Apparent equivalent volume, expansibility, and compressibility of artificial seawater: *Jour. Solution Chemistry*, v. 2, p. 1–22.
- Momicchioli, F., Devoto, O., Grandi, G., and Cocco, G., 1970, Thermodynamic properties of concentrated solutions of strong electrolytes, pt. 1, Activity coefficients of water from freezing-point depressions for alkali chlorides: *Ber. Bunsen-Gesell. phys. Chemie*, v. 74, p. 59–66.
- National Research Council, 1928, International critical tables of numerical data, physics, chemistry and technology: New York, McGraw-Hill Book Co., v. 3, 444 p.
- Nicolai, H. W., Ernst, W., and Wegkamp, H., 1951, [Viscosity as an analytical method for electrolyte solutions]: *Chem. Weeblad*, v. 47, p. 88–90 (in Dutch).
- Othmer, D. R., 1940, Correlating vapor-pressure and latent-heat data, a new plot: *Industrial Eng. Chemistry*, v. 32, p. 841–856.
- Othmer, D. R., and Chen, H.-T., 1968, Correlating and predicting thermodynamic data: *Industrial Eng. Chemistry*, v. 60, no. 4, p. 39–61; reprinted in *Am. Chem. Soc.*, 1968, *Applied thermodynamics*: Washington, D.C., *Am. Chem. Soc. Pubs.*, p. 115–139.
- Othmer, D. F., and Yu, E. S., 1968, Correlating vapor pressures and vapor volumes—Use of reference substance equations: *Industrial Eng. Chemistry*, v. 60, no. 1, p. 22–35.
- Potter, R. W., II, 1976, An assessment of the status of the available data on the P–V–T properties for the major components in geothermal brines: United Nations symposium on the development and use of geothermal resources, San Francisco 1975, Proc., 1975, v. 1, p. 827–829.
- Potter, R. W., II, and Brown, D. L., 1975, The volumetric properties of aqueous sodium chloride solutions for 0° to 500°C at pressures up to 2000 bars based on a regression of the available literature data: *U.S. Geol. Survey Open-File Rept.* 75–636, 31 p.
- 1976a, The volumetric properties of vapor saturated aqueous saturated aqueous potassium chloride solutions from 0° to 400°C based on a regression of the available literature data: *U.S. Geol. Survey Open-File Rept.* 76–243, 6 p.
- 1976b, The volumetric properties of vapor saturated aqueous sodium sulfate solutions from 0° to 325°C based on a regression of the available literature data: *U.S. Geol. Survey Open-File Rept.* 76–255, 6 p.
- 1976c, The volumetric properties of vapor saturated aqueous potassium sulfate solutions from 0° to 200°C based on a regression of the available literature data: *U.S. Geol. Survey Open-File Rept.* 76–501, 7 p.
- Potter, R. W., II, and Clynne, M. A., 1976, The volumetric properties of vapor saturated aqueous calcium chloride solutions from 0° to 300°C based on a regression of the available literature data: *U.S. Geol. Survey Open-File Rept.* 76–365, 7 p.
- Potter, R. W., II, Shaw, D. R., and Haas, J. L., Jr., 1975, Annotated bibliography of studies on the density and other volumetric properties for major components in geothermal waters 1928–74: *U.S. Geol. Survey Bull.* 1417, 78 p.

- Reilly, P. J., and Wood, R. H., 1969, The prediction of the properties of mixed electrolytes from measurements on common ion mixtures: *Jour. Phys. Chemistry*, v. 73, p. 4292-4302.
- Reilly, P. J., Wood, R. H., and Robinson, R. A., 1971, The prediction of osmotic and activity coefficients in mixed-electrolyte solutions: *Jour. Phys. Chemistry*, v. 75, p. 1305-1315.
- Robinson, R. A., and Stokes, R. H., 1959, *Electrolyte solutions*: London, Butterworths, 2d ed., 571 p.
- Smith, R. P., 1939, The boiling point elevation, pt. 2, Sodium chloride 0.05 to 1.0 M and 60 to 100°: *Am. Chem. Soc. Jour.*, v. 61, p. 500-503.
- Smith, R. P., and Hirtle, D. S., 1939, The boiling point elevation, pt. 3, Sodium chloride 1.0 to 4.0 M and 60 to 100°: *Am. Chem. Soc. Jour.*, v. 61, p. 1123-1126.
- Volz-Fladrich, H., 1962, [Physical-chemical examinations on the systems  $MgCl_2-HCl-H_2O$ ,  $NaCl-HCl-H_2O$ , and  $KCl-HCl-H_2O$ ]: *Freiberger Forschungshefte*, v. 134, p. 1-85 (in German).
- White, D. E., 1965, Saline waters of sedimentary rocks, *in* *Fluids in subsurface environments—A symposium*: *Am. Assoc. Petroleum Geologists Mem. No. 4*, p. 342-366.
- 1968, Hydrology, activity, and heat flow of the Steamboat Springs thermal system, Washoe County, Nevada: *U.S. Geol. Survey Prof. Paper 458-C*, 109 p.
- Wood, R. H., and Anderson, H. L., 1966, Heats of mixing of aqueous electrolytes, pt. 3, A test of the general equations with quaternary mixtures: *Jour. Phys. Chemistry*, v. 70, p. 1877-1879.
- Young, T. F., and Smith, M. B., 1954, Thermodynamic properties of mixtures of electrolytes in aqueous solutions: *Jour. Phys. Chemistry*, v. 58, p. 716-724.



## SPECTROCHEMICAL DETERMINATION OF SUBMICROGRAM AMOUNTS OF TUNGSTEN IN GEOLOGIC MATERIALS

By REINHARD W. LEINZ and DAVID J. GRIMES, Denver, Colo.

**Abstract.**—A rapid, sensitive, emission spectrographic method for the determination of tungsten in geologic materials has been developed. Sample fusion with potassium hydroxide followed by a hot-water leach renders the tungsten soluble. Acidification of the solution, reduction with titanium trichloride, complexing with thiocyanate, and ether extraction separate and concentrate the tungsten. An aliquot of the ether solution is pipetted into the cavity of a preformed graphite electrode containing 6 milligrams of sodium carbonate and is evaporated. The carbonate flux prevents formation of refractory tungsten carbide during arcing, resulting in nearly complete volatilization of tungsten during a short exposure period. Spectra from direct-current arc excitation of the tungsten are recorded on film and visually compared to standard spectra. A determination limit of 0.2-part-per-million tungsten is obtained from a 0.5-gram sample with a sample completion average of 30-50 samples per man-day.

Analytical methods for the determination of tungsten in geologic samples, if not lengthy and tedious, often suffer the lack of sensitivity required in geochemical investigations. Gair, Windolph, and Wright (1975) noted in a survey of the Hamme tungsten district, North Carolina, that the tungsten values reported in soils over mineralized quartz veins were not much higher than the detection limit of the analytical method. Hobbs and Elliott (1973, p. 677) pointed out that in tungsten geochemical research, "One of the key restraints . . . has been the inability to analyze with accuracy for small amounts of tungsten."

To date, analysts have relied heavily on spectrophotometric determinations of tungsten after complexing it with one of several reagents. Ward's method (1951) utilizes visual estimation of the yellow-green tungsten thiocyanate complex. Lillie and Greenland (1973) made use of this complex in their isotope-dilution procedure. The tungsten dithiol complex is the measured species in methods developed by Jeffery (1956), Chan and Riley (1967a), Stanton (1970), and Quin and Brooks (1972).

Tungsten is routinely determined down to 50 parts per million in the 30-element spectrographic analysis

described by Grimes and Marranzino (1968) and to submicrogram levels by the neutron-activation technique of Simon and Rollinson (1975).

This report describes a chemical preparation consisting of a rigorous alkali fusion, a hot-water leach, tungsten reduction, complexing with thiocyanate and ether extraction followed by a direct-current arc emission spectrographic determination that employs a sodium carbonate flux. The determination limit of this method (0.2 ppm) is below the average crustal abundance for tungsten (1-1.3 ppm) as given by Hobbs and Elliott (1973). No interelement interferences have been found, and the precision is more than adequate for most geochemical exploration investigations. Thirty to fifty samples can be analyzed per man-day and simplicity of the method allows for determinations to be made in existing U.S. Geological Survey mobile field laboratories.

### REAGENTS AND APPARATUS FOR CHEMICAL PREPARATION

All reagents are reagent grade, except for the titanium trichloride (20 percent solution) which is technical grade, and are listed as follows:

- Potassium hydroxide, pellet form.
- Hydrochloric acid, concentrated.
- Titanium trichloride, 20 percent solution.
- Potassium thiocyanate solution, 25 percent (weight per volume) in water, prepared daily.
- Isopropyl ether.
- The apparatus is listed as follows:
- Nickel crucibles, 50 milliliter capacity.
- Muffle furnace.
- Vortex mixer.
- Centrifuge, with heads for 16-millimeter and 25-mm-diameter tubes.
- Micropipette, 60 microliter capacity.
- Test tubes, 16 by 150 mm disposable and 25- by 150-mm screwcap.

### PROCEDURE

Weigh 0.5 gram of the powdered sample (ground or sieved to at least -80 mesh) into a 75-mL nickel crucible. Add 2.5 g pelletized potassium hydroxide and distribute evenly with the sample on the bottom of the crucible. Fuse in a muffle furnace by increasing the temperature slowly from room temperature to 450°C. Alternatively, heat gently over an open flame until the sample is thoroughly wetted with molten potassium hydroxide and then heat an additional 2 minutes.

Cool the crucible and carefully add 7 mL hot water to dissolve the soluble fusion products. Use a glass stirring rod to break up the melt and with the aid of a funnel transfer the solution and residue to a 16- by 150-mm test tube. Rinse the crucible with 1 mL water and transfer as above. Centrifuge and decant the liquid into a 25- by 150-mm screwcap test tube. Rinse the residue with 3 mL water, centrifuge, and add the liquid to the same tube. The residue may now be discarded.

With caution, add 12mL concentrated hydrochloric acid to the highly basic solution in the screwcap tube. Cool the tube in a water bath, add 4 mL of the 20 percent titanium trichloride solution and vortex. Add 1 mL of the 25 percent potassium thiocyanate solution and 1 mL of isopropyl ether, capping and shaking the tube for 2 min after each addition. Centrifuge the tube so that a sufficient amount of ether layer is obtained for pipetting with the 60- $\mu$ L micropipette. The final two-phase solution is stable under refrigeration in the capped tube for at least 2 weeks.

### SPECTROGRAPHIC INSTRUMENTATION AND MATERIALS

Spectrograph, 1.5-meters Wadsworth-mounted, with a dispersion of 5.4 angstroms per millimeter over the spectral range of 2100-4800 Å in the second order. Source, spark-ignited direct-current arc—220 volts with arc current variable in steps from 2 to 15 amperes.

Comparator, 20 $\times$  magnification.

Electrodes, anode—6.15-mm-diameter undercut graphite electrode [Ultra carbon No. 100-L (U-7)]; cathode—4.57-mm-diameter graphite rod [Ultra carbon No. 105 (U-7)].

Film, 35-mm spectrum analysis No. 1 emulsion.  
Sodium carbonate, Johnson Matthey Spec-Pure.

### SPECTROGRAPHIC PARAMETERS

Analytical gap, 4 mm.  
Slit, 20 microns.

Hartmann diaphragm, 1.0 mm.

Current, 15 A.

Exposure, 30 seconds.

Processing, Kodak D-19—20°C—2 min; Kodak fixer—20°C—5 min.

### SPECTROGRAPHIC DETERMINATION

Weight 6 milligrams of spectrographically pure sodium carbonate powder and transfer it to the cavity of the graphite electrode with the aid of an aluminum funnel. Carefully pipet 60  $\mu$ L of the ether layer into the electrode crater that contains the sodium carbonate and oven dry at 110°C for 10 min. (Avoid pipetting any of the acid layer into the electrode because the ensuing reaction with the sodium carbonate will produce low tungsten results).

After cooling, clamp the sample and counter electrodes into the arc stand of the spectrograph, set the electrode gap at 4 mm, and arc the sample for 30 sec at 15 A. When Hartmann diaphragm is set at 1.0 mm, 24 samples can be recorded on each length of film. Process the exposed film in developer at 20°C for 2 min, in fixer at 20°C for 5 min, wash in cold water, and air dry. Visually compare the resultant spectra with standard spectra by means of a 20 $\times$  comparator. A concentration range from 0.2 to 500 ppm is obtained by use of the tungsten line at the wavelength of 2946.9 Å.

### STANDARDS

Tungsten stock solutions are as follows:

1000 micrograms per milliliter: Dissolve 0.8973 g sodium tungstate dihydrate ( $\text{Na}_2\text{WO}_4 \cdot 2\text{H}_2\text{O}$ ) in 500 mL of 0.1 molar KOH.

100  $\mu\text{g}/\text{mL}$ : Dilute 10 mL of the 1000  $\mu\text{g}/\text{mL}$  to 100 mL with 0.1 molar KOH.

Prepare solutions of 10  $\mu\text{g}/\text{mL}$  and 1.0  $\mu\text{g}/\text{mL}$  in a similar manner.

To twelve 25- by 150-mm screwcap test tubes, add 2.5 g potassium hydroxide and dissolve with 10 mL water. Using the above stock solutions, and 0, 0.2, 0.5, 1.0, 2.0, 5.0, 10, 20, 50, 100, 200, and 500 micrograms of tungsten to the tubes. Cautiously add 12 mL concentrated hydrochloric acid and cool in a water bath. Add 4 mL titanium trichloride and vortex. Add 1 mL of 25-percent potassium thiocyanate and 2 mL isopropyl ether (extractions of the standards into 2 mL ether and samples (0.5 g) into 1 mL ether allow direct tungsten measurements in micrograms per milliliter or parts per million to be made), capping and shaking the tubes for 2 min after each addition. Allow the phases to separate.

Weight 6 mg sodium carbonate into the cavities of

12 graphite electrodes, then carefully add 60  $\mu\text{L}$  from the ether layer of successive standards. Continue as in a procedure for spectrographic determination.

The range of the prepared standards on film is from 0.2 to 500 ppm (excluding the blank) with three standards or steps between each order of magnitude. For semiquantitative analysis, the density and width of an appropriate tungsten line in the spectrum of the sample is visually compared with the tungsten line at the same wavelength in the standard spectrum. An estimate of the tungsten concentration in the sample is based on directly matching densities or the sample line density falling between the densities of two adjacent standard lines. Thus, values for tungsten are reported in six concentration steps between each order of magnitude in the following series: 0.2, 0.3, 0.5, 0.7, 1.0, 1.5, 2.0, 3.0, 5.0, 7.0, 10.0, 15, 20, 30, 50, 70, 100, 150, 200, 300, and 500 ppm.

### DISCUSSION OF PROCEDURE

Fusing the sample with potassium hydroxide and leaching the melt with water solubilize any tungstate minerals present as potassium tungstate. Potentially troublesome iron is simultaneously precipitated as hydroxide and discarded. Acidification of the supernatant solution with hydrochloric acid and addition of the reducing agent, titanium trichloride, produce a "genotypic" compound ("one having the same basic structure, but differing in the charges on cations and anions") known as tungsten blue (Cotton and Wilkinson, 1972). In greater than 4 *N* hydrochloric acid and in the presence of excess titanium trichloride, tungsten blue appears to react with thiocyanate ions to yield a yellow-green to green complex whose structure is uncertain (perhaps an oxoanion) and whose stability is certain only in solution. This complex is quantitatively extractable from the acidic aqueous layer into the nonpolar isopropyl ether. More than 95-percent extraction is attained into 1 mL of ether at the 250- $\mu\text{g}$  level.

Formation and extraction of metallic thiocyanates other than tungsten is minimal and does not affect extraction or spectral determination of the tungsten. Molybdenum, for example, complexes only to a slight extent under the highly acidic and reducing-reaction conditions.

Aside from solubilizing tungsten minerals present in the sample, the fusion and leaching also put silica into solution. Upon acidification, the silica forms silicic acid which may form a gel in the ether phase. Centrifuging is often necessary to clear a sufficient amount of ether for pipetting.

During high-temperature arcing in emission spectrographic analysis, tungsten species are usually reduced to refractory tungsten carbide (boiling point, 6000°C) when singularly present in the graphite electrode crater. This often necessitates a long burn time, filtered emitted light, and a narrow entrance slit, all of which decrease sensitivity.

The authors found that sodium carbonate present in the crater during arcing inhibits formation of the carbide and allows tungsten to volatilize in a more oxidized and lower boiling form, probably as the trioxide  $\text{WO}_3$  (bp. about 1400°C). The presence of sodium vapor in the arc also lowers the arc temperature which minimizes the ionization of tungsten atoms. In contrast, the much higher temperature of a carbon vapor arc increases the percentage of tungsten atoms ionized. Neutral and ionized atoms of the same element emit different spectra, the intensities of which are proportional to the population of each species present in the arc. The 2946.9-Å tungsten line is produced by excitation of neutral atoms; therefore, its intensity is increased by the presence of sodium vapor in the arc. A comparison of tungsten emission with and without the presence of sodium carbonate is shown in figure 1. The graphical data presented in figure 1 was obtained from a 15-sec interval moving-plate study of 60  $\mu\text{L}$  of a 200- $\mu\text{g}/\text{mL}$  tungsten standard pipetted into two electrodes, one of which contained 6 mg of the sodium carbonate flux.

Lower detection limits may be obtained by pipetting additional aliquots of the ether phase into the electrode crater. However, because the ether does contain some dissolved acidic aqueous phase that reacts with the carbonate flux, a new set of spectrographic standards must be prepared. For reliable analysis an equal quantity of ether must be pipetted for both sample and standard.

### PRECISION AND ACCURACY

The precision of this method was established from data of 12 repeat analyses of 12 different samples (table 1). The samples were various geologic materials and contained several different tungsten minerals such as scheelite ( $\text{CaWO}_4$ ) in skarns I and II and huebnerite ( $\text{MnWO}_4$ ) in soils I and II. The coefficient of variation ranged from 10 to 27 percent, with all or most values from any one sample falling within one spectrographic reporting step of the mean.

Accuracy was approximated by comparison of the mean of the 12 replicate analysis of the granite G-2 standard and the glass standards GSB, GSC, GSD, and GSE with values found in the literature (table 1).

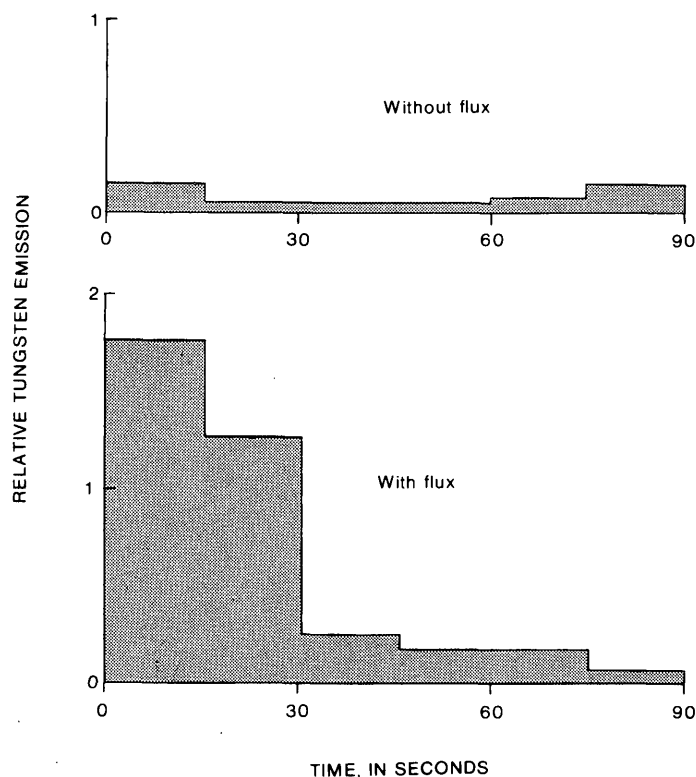


FIGURE 1.—A comparison of tungsten emission with and without sodium carbonate flux (6 mg  $\text{Na}_2\text{CO}_3$ ).

Both precision and accuracy are well within an acceptable range for most geochemical exploration investigations involving tungsten. If a more quantitative analysis was required, incorporation of an internal standard with the flux as well as plots of emulsion calibration and working curves obtained from densitometric measurements of spectral lines would be necessary.

TABLE 1.—Summary of tungsten precision and accuracy studies on 12 repeat analyses for various sample types

Sample type	Range (ppm)	Mean (ppm)	Standard deviation	Coefficient of variation (percent)	Literature values (ppm)
High Fe-Mn marble--	15 - 30	20	5.2	26	---
Skarn I-----	100 - 150	146	14.4	10	---
Skarn II-----	7 - 15	9.4	2.3	24	---
Granite (G-2)-----	0.15- 0.2	.18	.03	17	<sup>1</sup> 0.1±0.3; <sup>2</sup> 0.4
Soil I-----	2 - 5	2.9	.79	27	---
Soil II-----	150 - 200	192	19.5	10	---
Porphyry copper					
Ore (sulfide)-	30 - 70	48	10.3	21	---
Jasperoid-----	100 - 150	133	24.6	19	---
Glass standards:					
GSB-----	0.5 - 1	.68	.17	25	<sup>3</sup> 0.5 est.
GSC-----	5 - 7	5.3	.78	15	.5 est.
GSD-----	30 - 50	47	7.8	17	350
GSE-----	300 - 500	400	104	26	420

<sup>1</sup> Simon and Rollinson (1975).

<sup>2</sup> Chan and Riley (1967b).

<sup>3</sup> Myers and others (1976).

## SUMMARY

The proposed method combines a chemical separation and preconcentration with an emission spectrographic determination and enables tungsten measurements to be made in geologic materials in amounts below crustal abundance. Interelement interferences, which pose problems in many of the colorimetric procedures, such as the interference from molybdenum, are virtually eliminated. The method's precision and accuracy are more than adequate for most geochemical exploration studies, its simplicity allows for adaptation to the mobile laboratories of the U.S. Geological Survey, and its rapidity permits an average of 30-50 sample analyses per man-day.

## REFERENCES CITED

- Chan, K. M., and Riley, J. P., 1967a, Determination of tungsten in silicates and natural waters: *Anal. Chim. Acta*, v. 39, p. 103-113.
- 1967b, Determinations of vanadium, molybdenum, and tungsten in the new series of U.S. Geological Survey analyzed samples: *Chem. Geology*, v. 2, p. 171-172.
- Cotton, F. A., and Wilkinson, Geoffrey, 1972, *Advanced inorganic chemistry*: New York, John Wiley & Sons, 947 p.
- Gair, J. E., Windolph, J. F., Jr., and Wright, N. A., 1975, Preliminary results of geochemical soil survey, Hammett tungsten district, North Carolina: U.S. Geol. Survey Circ. 711, 19 p.
- Grimes, D. J., and Marranzino, A. P., 1968, Direct-current arc and alternating-current spark emission spectrographic field methods for the semiquantitative analysis of geologic materials: U.S. Geol. Survey Circ. 591, 6 p.
- Hobbs, S. W., Elliott, J. E., 1973, Tungsten, in Brobst, D. A., and Pratt, W. P., eds., *United States mineral resources*: U.S. Geol. Survey Prof. Paper 820, p. 667-678.
- Jeffrey, P. G., 1956, The simultaneous photometric determination of molybdenum and tungsten in silicate rocks: *Analyst*, v. 81, no. 959, p. 104-109.
- Lillie, E. G., and Greenland, L. P., 1973, Spectrophotometric determination of tungsten in rocks by an isotope dilution procedure: U.S. Geol. Survey Jour. Research, v. 1, no. 5, p. 555-558.
- Myers, A. T., Havens, R. G., Connor, J. J., Conklin, N. M., and Rose, H. J., 1976, Glass reference standards for the trace-element analysis of geological materials—Compilation of interlaboratory data: U.S. Geol. Survey Prof. Paper 1013, 29 p.
- Quin, B. F., and Brooks, R. R., 1972, The rapid determination of tungsten in soils, stream sediments, rocks and vegetation: *Anal. Chim. Acta*, v. 58, p. 301-309.
- Simon, F. O., and Rollinson, C. L., 1975, Determination of tungsten in geologic materials by neutron activation analysis: U.S. Geol. Survey Jour. Research, v. 3, no. 4, p. 475-478.
- Stanton, R. E., 1970, The colorimetric determination of tungsten in soils, sediments, and rocks by zinc dithiol: *Australasian Inst. Mining and Metallurgy Proc.*, no. 236, p. 59-60.
- Ward, F. N., 1951, A field method for the determination of tungsten in soils: U.S. Geol. Survey Circ. 119, 4 p.

## IMPACT OF SEWERAGE SYSTEMS ON STREAM BASE FLOW AND GROUND-WATER RECHARGE ON LONG ISLAND, NEW YORK

By E. J. PLUHOWSKI and A. G. SPINELLO, Reston, Va., Syosset, N. Y.

*Abstract.*—Statistically significant decreases in the ratio of base flow to total flow of streams along the south shore of Long Island, N.Y., are due to the use of expanding storm-sewer and sanitary-sewer networks. Base-flow losses due to sewerage ranging from virtually none at Connetquot River (largely unaffected by urban development) to 211 liters per second, or a 60-percent decrease below natural levels, during 1965-74 at East Meadow Brook (which drains part of highly urbanized Nassau County). Nearly 75 percent of the base-flow loss at East Meadow Brook during 1965-74 was caused by a network of sanitary sewers west of the stream; the remainder resulted from loss of recharge in areas serviced by stream-directed storm sewers. In areas of the Carlls River basin serviced by stream-directed storm sewers, recharge depletion averaged only about 4 liter per second per square kilometer whereas in the more intensely urbanized East Meadow Brook basin, recharge depletion in such areas averaged 18 (L/s)/km<sup>2</sup>.

The eastward spread of urbanization across Long Island has been accompanied by increasingly complex sewerage systems. The large-scale conversion of open land areas to paved, impervious surfaces, concurrent with the redirection of surface runoff to streams and the disposal of waste water to the oceans through sewer systems, has resulted in a loss of recharge to the ground-water reservoir. The purpose of this investigation is to define and evaluate the impact of the sewerage systems on stream base flow and ground-water recharge.

### PREVIOUS RESEARCH

The effects of the installation of a sanitary-sewer system in western Nassau County on ground-water levels, which were lowered by 2.1 meters during 1953-72, were described by Garber and Sulam (1976). Contamination of the upper glacial aquifer by cesspools, septic tanks, and sewage lagoons in developed areas of Nassau and Suffolk Counties was described by Pluhowski and Kantrowitz (1964) and Cohen, Franke, and Foxworthy (1968). The alteration of flood-peak characteristics of East Meadow Brook in south-central Nassau County as a result of the diversion of urban runoff to storm sewers has been described by Seaburn (1969).

### DEVELOPMENT OF WASTE-WATER DISPOSAL SYSTEMS

Before World War I, when extensive parts of Nassau and Suffolk Counties were devoted to agriculture, wells were dug or driven into the upper glacial aquifer to provide much of the water supply for domestic use, and waste water was returned to the aquifer through cesspools and septic tanks (Heath and others, 1966). Storm runoff was channeled to low-lying areas, watercourses, or ponds. Thus, except for small consumptive losses, virtually all ground water pumped for water supply was returned to the upper glacial aquifer. After World War I, a slow but steady urban expansion began in western Nassau County and along railroad trunklines in central and southern Nassau County and southwestern Suffolk County. In 1927, the village of Freeport built a sanitary sewerage system servicing 11 square kilometers. The system processed domestic and industrial waste water and discharged its effluent to tidewater south of the village.

To cope with ever-increasing amounts of storm runoff, as urban development reduced infiltration area, and to conserve ground-water reserves, Nassau County officials approved construction of several experimental storm-water collection basins in 1935 (Welsch, 1935). These excavations, known as recharge basins, were designed to allow rapid infiltration of runoff conveyed to them by storm sewers. More than 2100 recharge basins had been constructed on Long Island by 1969 (Seaburn and Aronson, 1974), principally in the central part of Nassau and Suffolk Counties. However, the construction of storm sewers has continued at a steady rate, especially in southern Nassau County and southwestern Suffolk County, where they convey the bulk of storm runoff directly to streams rather than to ponds or recharge basins.

Although the system of recharge basins combined with cesspools, septic tanks, and diffusion wells serves to conserve ground water, increasing contamination of the upper glacial aquifer prompted officials of both counties to adopt plans for treating sanitary sewage at

large-volume processing plants. In addition, regional sewer districts were established to provide secondary waste-water treatment in order to reduce the chance of water-supply contamination. Work on Sewer District 2 (fig. 1) in western Nassau County began in 1953, and sewer hookups were completed in 1964. Effluent from the Bay Park sewage-treatment plant, which serves the 181-km<sup>2</sup> area of Sewer District 2, increased steadily from  $2.2 \times 10^4$  cubic meters per day in 1953 to  $26 \times 10^4$  m<sup>3</sup>/d in 1972 (Garber and Sulam, 1976). Effluent from the Bay Park facility is discharged to tidewater at Reynolds Channel (Pluhowski, 1972, fig. 11).

Sewer construction is presently underway in Sewer District 3 in Nassau County and in southwestern Suffolk County (fig. 1). Since January 1974, a small quantity of waste water has been processed at Nassau County's Sewer District 3 treatment plant. Effluent from this facility, as in Sewer District 2, is discharged to tidewater. The 272-km<sup>2</sup> Sewer District 3 in Nassau County is scheduled for completion in 1990.

Depending on whether the sewer pipes are above or below the water table, either ground water will infiltrate into the sewer pipes or sewage will exfiltrate from the system into the unsaturated zone. The fluids move into or out of sewers principally through poorly sealed joints and manholes and through cracks in the pipes. In

a properly designed and constructed sewer system, leakage is small relative to the design conveyance capacity of the pipes (Fair and Geyer, 1954).

In Sewer District 2, depth to the water table ranges from 0 to about 45 m. Sewers were generally placed in trenches at an average depth of 3 m below land surface. Except in the southern part of the district, practically all sewers lie above the water table. Thus, it is likely that more sewage is exfiltrating from the Sewer District 2 system than ground water is infiltrating into the system. However, owing to the difficulty of locating and measuring pipe seepage, it is not practical to assess the net gain or loss of fluid volume received by the Bay Park treatment plant. In any case, the discharge of effluent from the plant to tidewater represents a permanent loss of recharge to the ground-water reservoir since the cesspool- and septic-tank system was abandoned.

### STREAM CHARACTERISTICS

Long Island streams are widely spaced and are characterized by straight channels, with few, if any, tributaries. Streamflow, composed of direct runoff and base flow, exhibits well-sustained low flows and attenuated flood discharges. Direct runoff, or storm flow, under natural conditions, consists of precipitation both falling directly on the streams and contiguous lakes, and flowing overland in the immediate vicinity of the stream channels. Owing to the high permeability of soils and the flat terrain in most parts of Long Island, a raindrop falling more than a few meters from the stream channel probably does not enter the stream as runoff, but infiltrates the soil and eventually reaches the streams as ground-water discharge. Base flow, or dry-weather flow, consists entirely of ground water discharging from the upper glacial aquifer. Ground-water levels adjacent to Long Island streams are directly related to base flow (Pluhowski and Kantrowitz, 1964).

### APPROACH

Six streams along the south shore of Long Island were selected for analysis to evaluate the impact of sewers on base flow (fig. 2). Pertinent basin characteristics of the six drainage basins are given in table 1. The topographic divide between north- and south-flowing streams on Long Island bears little or no relation to the main ground-water divide. Accordingly, large dissimilarities are apparent between the ground-water drainage areas and the surface-drainage areas above many of the gaging stations (table 1). Topography, geology, precipitation, and evapotranspiration

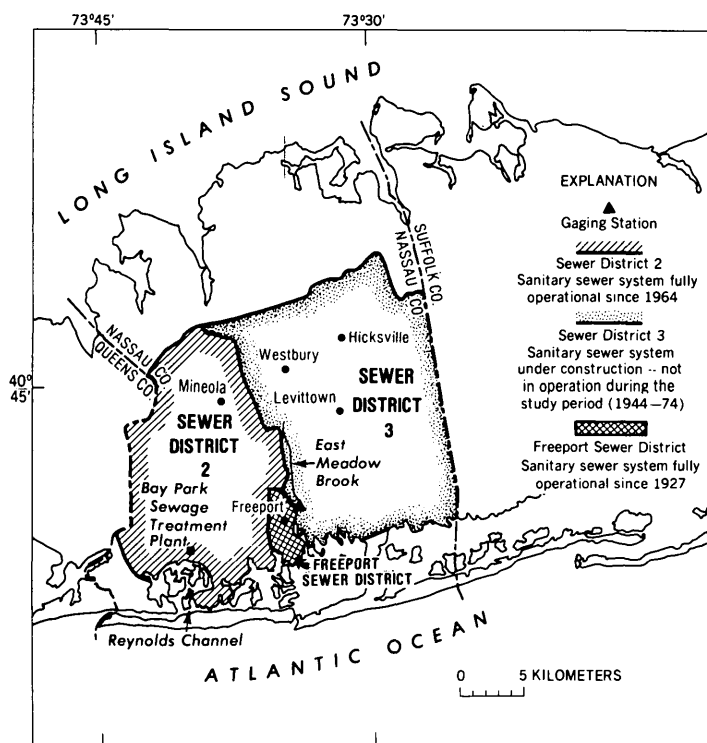


FIGURE 1.—Location of the Freeport Sewer District and Nassau County Sewer Districts 2 and 3.

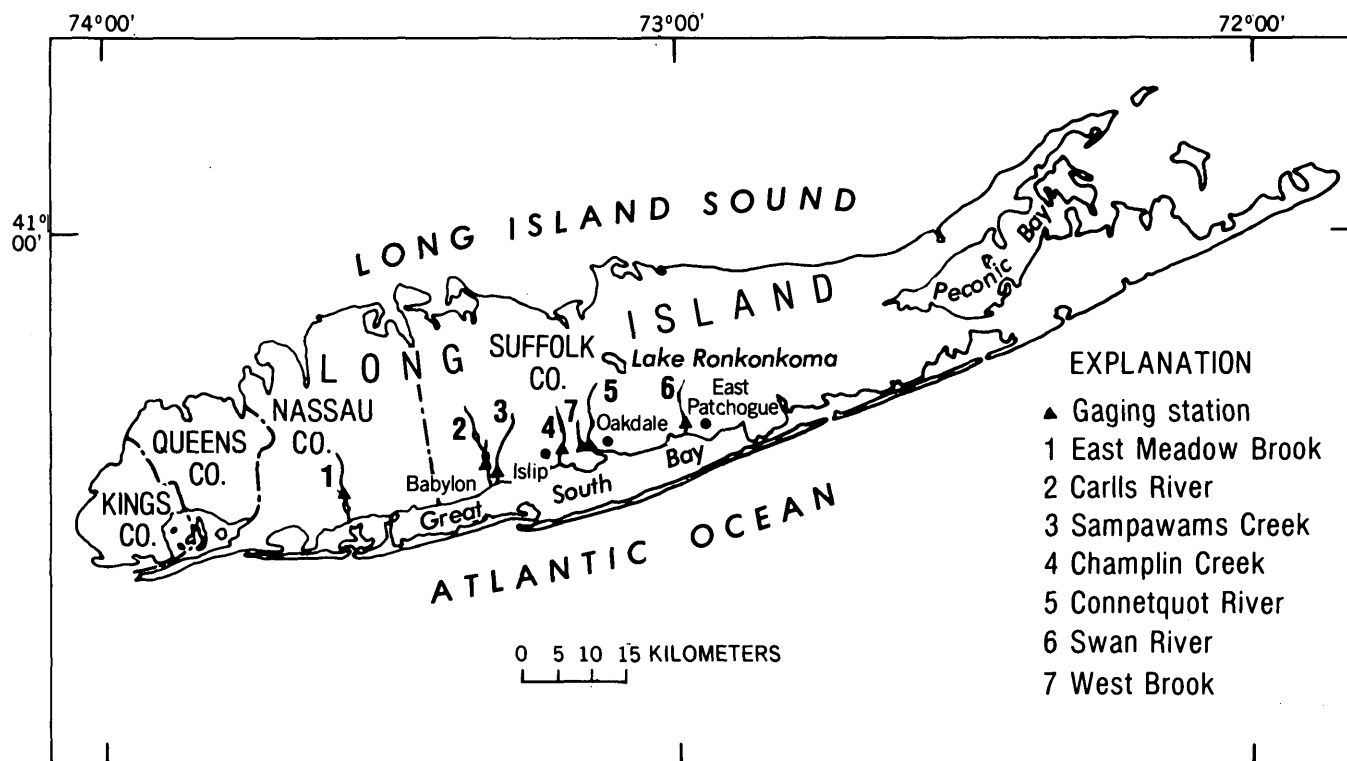


FIGURE 2.—Location of streams studied.

TABLE 1.—Summary of streamflow data for six study streams, adjusted to base period 1944-74

Station name and number	Drainage area		Mean discharge (L/s)	Mean base flow (L/s)	Ratio of base flow to total flow (percent)
	Surface (km <sup>2</sup> )	Ground water (km <sup>2</sup> )			
East Meadow Brook at Freeport-01310500---	80	31	416	340	81.7
Carlls River at Babylon-01308500----	90.5	45.5	733	677	92.4
Sampawams Creek at Babylon-01308000----	59.5	19.5	263	241	91.6
Champlin Creek at Islip-01307000-----	17	14	195	187	95.9
Connetquot River near Oakdale-01306500----	62	70	1068	1028	96.3
Swan River near East Patchogue-01305500--	23	28.5	351	337	96.0

rates are similar at all study basins, so that they are hydrologically equivalent. Each stream in the study area drains southward and is underlain by unconsolidated deposits ranging in depth from about 270 m at East Meadow Brook on the west to about 520 m at Swan River to the east. Because the upper glacial aquifer is the sole source of ground-water outflow to each stream, ground-water contributing areas were the only drainage areas used in the computations. Ground-water contributing areas for each stream-gaging station were delineated from water-table maps prepared by Koszalka (1975).

Through hydrograph separation procedures outlined by Chow (1964, p. 10-14), base flow, expressed in per-

centage of total streamflow, was determined for each study station. All data were analyzed for a common base period, October 1, 1943, to September 30, 1974 (1944-74 water years), which is equivalent to the Connetquot River period of record, the longest streamflow record available in southwestern Suffolk County.

**Land use**

The extent and type of urban development varies widely among the stream basins, as shown in table 2. The most intensely urbanized basin is East Meadow Brook, where 72 percent of the area is built up, of which 14 percent is commercial and industrial development. Although the percentage of urban areas classified as "Residential" and "Other" at Champlin Creek

TABLE 2.—Land use in six study basins, in percent [Based on report issued by Nassau-Suffolk Regional Planning Board (1968)]

Gaging station	Rural			Urban		
	Forest	Agri-culture	Open land	Water	Resi-dential	Other <sup>1</sup>
East Meadow Brook at Freeport-----	5	1	22	--	58	14
Carlls River at Babylon-----	7	10	25	1	54	3
Sampawams Creek at Babylon-----	1	6	25	--	64	4
Champlin Creek at Islip-----	5	2	19	1	51	22
Connetquot River near Oakdale----	27	--	30	2	40	1
Swan River at East Patchogue--	39	2	27	--	28	4

<sup>1</sup> Principally industrial, commercial, and institutional land uses.

slightly exceeds the percentage for East Meadow Brook, 22 percent of the land classified as "Other" in the Champlin Creek basin is institutional. The bulk of this category consists mainly of a large State hospital surrounded by extensive grassy areas and parks. Thus, the total pervious area in the Champlin Creek basin is greater than that in the East Meadow Brook basin.

Both the Connetquot River and Swan River basins are primarily rural, and large parts of both basins are forested, unlike the four study basins to the west. The Connetquot River flows through a State forest preserve that extends to the drainage-area boundaries along much of the perennial part of the river. This large undeveloped area forms a buffer zone between the river and eastward-spreading urban development. The Connetquot River basin is one of the few areas on Long Island in which undisturbed streamflow conditions are preserved.

### Statistical analysis of base flow

The homogeneity of base flow among the six streams was analyzed statistically. A sampling scheme using the ratio of base flow to total streamflow for each stream at 5-year intervals, beginning with the 1949 water year, was prepared (table 3). This approach minimizes the number of estimates required to fill in missing data resulting from varying periods of record, yet includes an adequate number of sample events. A one-way analysis of variance (Duncan, 1959) was used to test the hypothesis that no difference in the base-flow characteristics exists among the study streams and that variations among the sampled data were due solely to chance.

### Results

The results of the test are given in table 4. The variance ratio of 13.6 among the streams exceeds the  $F$ -distribution value of 3.70 at the 1-percent level. There is less than 1 chance in 100 that the computed variance ratio could have been attained if the homogeneity hypothesis was correct. Therefore, the hypothesis that the

TABLE 3.—Ratio of base flow to total streamflow for six study streams, in percent

Water year	Swan River	Connetquot River	Champlin Creek	Sampawams Creek	Carlls River	East Meadow Brook
1949	98.2	96.6	96.3	95.2	95.7	91.2
1954	96.6	95.3	94.1	89.3	93.4	81.1
1959	97.6	97.3	95.7	92.6	92.9	83.2
1964	95.4	95.0	94.9	90.2	92.4	77.9
1969	95.9	96.0	93.2	88.5	84.2	66.1
1974	93.1	96.4	194.5	92.7	88.4	64.8

<sup>1</sup> Estimated, based on correlation analyses with nearby streams.

TABLE 4.—One-way analysis of variance of data in table 3

Source of variation	Sum of squares	Degrees of freedom	Mean square	Variance ratio
Among periods-----	1,512.8	5	302.6	<sup>1</sup> 13.6
Error-----	668.8	30	22.3	----
Total-----	2,181.6	35	-----	----

<sup>1</sup> Significant at the 99-percent level.

base-flow characteristics of the streams are similar was rejected. Moreover, it is concluded that some factor has significantly altered the base-flow characteristics of some of the study basins.

In order to identify the principal source of variation in the data, the five degrees of freedom assigned to the streams (table 4) were tested by an individual degree-of-freedom analysis. Comparisons were made by first testing the two easternmost, rural streams (Swan River and Connetquot River) and then introducing into the analyses, in succession, each of the four urbanized streams to the west. Five analyses were made, in which the final analysis consisted of a comparison of East Meadow Brook (stream farthest west) contrasted with the combined effect of all five streams to the east. Results showed that about 90 percent of the variance in table 4 was due to the inclusion of East Meadow Brook in the analysis.

### Discussion

The most obvious factor affecting the hydrology of the study basins is the extent to which the surface infiltration capacity of the well-drained soils common to all the basins has been reduced. Storm water from impervious roads, roof tops, sidewalks, and parking lots is now channeled through storm sewers to recharge basins or watercourses. Seaburn and Aronson (1974) found that where recharge basins are used to dispose of storm water, ground-water recharge from precipitation is about equal to recharge under natural conditions. Thus, storm sewers that discharge into recharge basins have little, if any, effect on ground-water levels or on base flow. However, storm sewers that empty into channels, in effect, speed the delivery of runoff to streams. Precipitation that would have infiltrated the ground and recharged the water-table aquifer under natural conditions is instead conveyed rapidly to a stream as direct runoff. Although the overall impact of this process on total volume of streamflow is probably small, its effect on the ratio of base flow to storm flow in the affected watercourses may be considerable.

Storm sewers, ranging from 380 to 1400 millimeters in diameter, carry storm water to all six study streams (Pluhowski, 1970). Extensive storm-sewer networks

discharge directly into Champlin Creek, Sampawams Creek, Carlls River, and East Meadow Brook. In contrast, relatively small amounts of storm water are conveyed to Swan River, and Connetquot River receives street runoff from just three highway crossings. In addition to having extensive stream-directed storm sewers discharging from both banks, the East Meadow Brook channel closely follows the southeast border of Sewer District 2 (fig. 1). Thus, base flow at East Meadow Brook is reduced not only by stream-directed storm sewers, but also by the decline in ground-water levels resulting from the regional sanitary-sewer network to the west and pumping in Queens County.

**BASE FLOW**

The percentage of total annual streamflow that occurs as base flow is largely a function of storm intensity and frequency. For example, the highest percentage base flow (98.2) at Connetquot River was during the 1957 water year, a dry year with few major storms. The lowest percentage (94.3) was in 1958, a wet and stormy year on Long Island. An inverse correlation is also found in the relation between percentage base flow and the volume of base flow. For example, during the water year with the highest percent base flow at

Connetquot River (1957), actual base flow averaged 1020 L/s, whereas during the year with the lowest percent (1958), base flow averaged 1190 L/s.

**Temporal variations**

To evaluate the impact of sewerage systems on base flow and to detect long-term trends, records were plotted of percentage base flow for East Meadow Brook, Carlls River, and Connetquot River (fig. 3). The percentage base flow at Connetquot River was consistently high (96.3 average) throughout the period of record. At Carlls River, a slow but steady decline in percentage base flow began about 1957, indicating that an increasing volume of storm water was probably being diverted to its channel. At East Meadow Brook, where the percentage base flow had been fairly steady during 1938-52, a downward trend began in the early 1960's and turned sharply lower in the mid-1960's. After a recovery in the late 1960's, the base flow stabilized at 65 percent. The radical changes in streamflow patterns at East Meadow Brook seem to correlate with sewer construction in the basin during three periods: 1944-52 (period 1), 1953-64 (period 2), and 1965-74 (period 3).

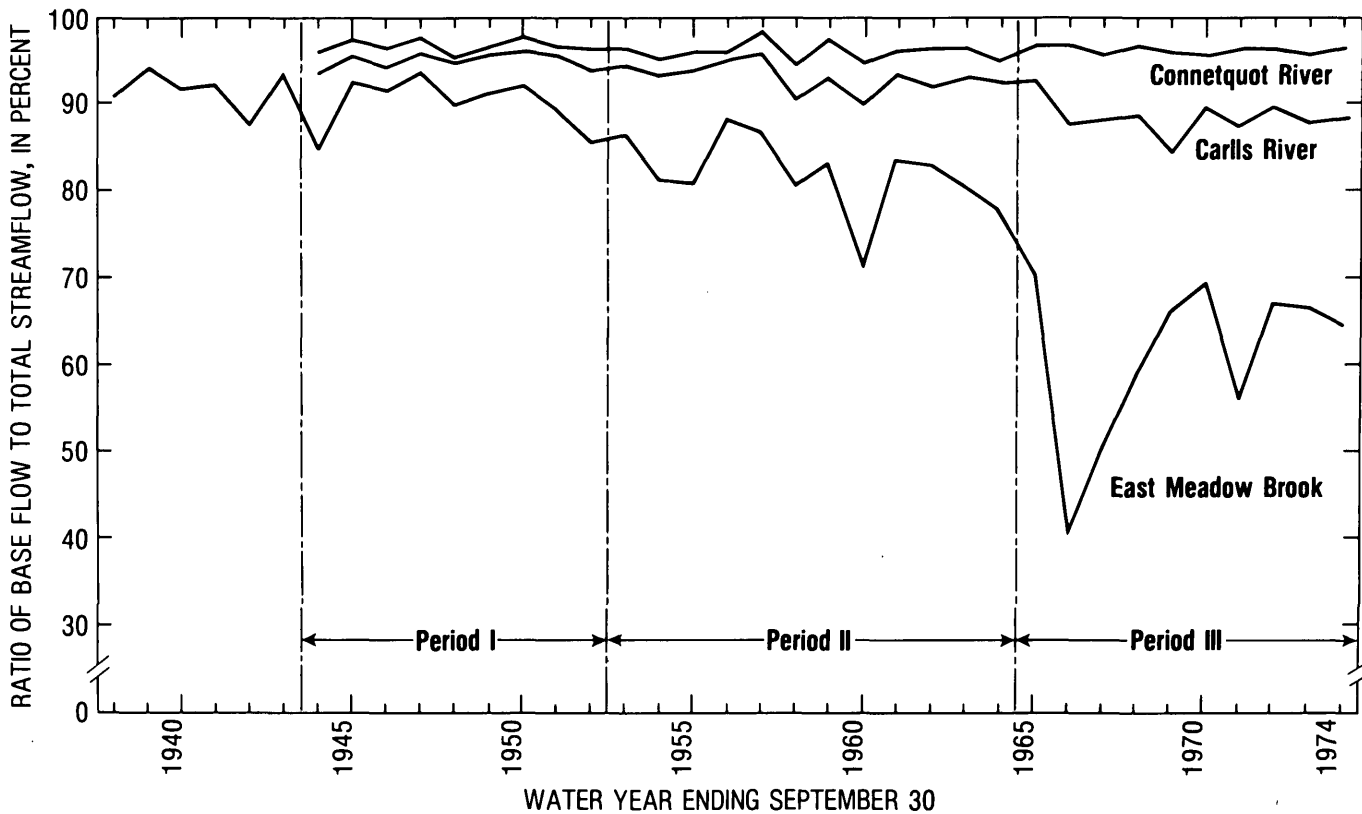


FIGURE 3.—Ratio of base flow to total streamflow for three study streams, 1938-74.

Period 1 was a time of rapid expansion of storm-sewer systems, when cesspools and septic tanks constituted the predominant waste-water disposal system. Period 2 represents the construction phase of the sanitary-sewer network of Sewer District 2, which was completed in 1964. Construction of stream-directed storm sewers in the East Meadow Brook basin was rapid before the middle of period 2, but this activity declined shortly after 1960 (Seaburn, 1969). Throughout period 3, Sewer District 2 was fully operational, and storm-sewer construction continued, but at a declining rate, as land zoned for development became increasingly scarce.

A one-way analysis of variance was applied to test the hydrologic similarity of the three periods for each stream. The results of the analysis, shown in table 5, indicate that there is no difference among the periods at Connetquot River, but that they are significantly different at the 1-percent level at both Carlls River and East Meadow Brook. The probability of obtaining a variation in percentage base flow among three such periods from a population of hydrologically homogeneous data is much less than 1 in 100 at both streams. Thus, it can be concluded that significant changes in ratio of base flow to total flow have evolved at Carlls River and East Meadow Brook over the 31-yr study period (1944-74). These changes are probably due in large measure to sewerage in both basins.

### Loss of base flow

Estimates of base-flow loss at Carlls River and East Meadow Brook for each of the three time periods are shown in table 6 (col. 5). The theoretical base flow

TABLE 5.—One-way analysis of variance to detect changes in the base-flow patterns of three study streams

Source of variation	Sum of squares	Degrees of freedom	Mean square	Variance ratio
<b>Connetquot River:</b>				
Among periods----	2.57	2	1.28	1.91
Error-----	18.82	28	.67	----
Total -----	21.39	30	----	----
<b>Carlls River:</b>				
Among periods----	225.95	2	112.98	<sup>1</sup> 39.6
Error-----	79.79	28	2.85	----
Total -----	305.74	30	-----	----
<b>East Meadow Brook:</b>				
Among periods----	4,416.1	2	2,208	<sup>1</sup> 52.0
Error-----	1,190.1	28	42.5	----
Total -----	5,606.2	30	-----	----

<sup>1</sup> Significant at the 99-percent level.

(col. 4) is estimated natural base flow at each gaging station and is the base flow that would occur if there were no sewers. It is based on the ratio of base flow to total streamflow at Connetquot River and at the special-purpose West River gage (Pluhowski and Kantrowitz, 1964, p. 115-116). Connetquot River flows through an extensive forested State park for much of its length and is largely protected from urban storm runoff. The relatively small West Brook basin (fig. 2) lies almost entirely in undeveloped State property, so that it also is unaffected by urbanization. The average percentage of base flow to total flow is 96.3 and 96.7 percent at Connetquot River and West Brook, respectively. The mean value of 96.5 percent for both streams was used to estimate the base flow before man influenced it at Carlls River and for the 1944-52 period

TABLE 6.—Base-flow loss and recharge attrition due to sewerage at the Carlls River and East Meadow Brook basins

[In liters per second unless otherwise indicated]

(1)	(2)	(3)	(4)	(5)	(6)	(7)	(8)
Water years	Mean discharge	Mean base flow	Theoretical base flow	Base-flow loss due to sewerage (col.4 - col.3)	Total area (km <sup>2</sup> )	Recharge loss (col.5 x 1.5)	Recharge loss (col.7 ÷ col.6) [(L/s)/km <sup>2</sup> ]
<b>Carlls River:</b>							
1944-52-----	767	728	740	12	<sup>1</sup> 7.5	18	2
1953-64-----	816	759	787	28	<sup>1</sup> 10.5	42	4
1965-74-----	603	532	582	50	<sup>1</sup> 10.5	75	7
<b>East Meadow Brook:</b>							
1944-52-----	498	447	481	34	<sup>1</sup> 2.8	51	18
1953-64-----	513	422	<sup>3</sup> 549	127	<sup>2</sup> 12.2	190	16
1965-74-----	229	144	<sup>3</sup> 355	211	<sup>2</sup> 15.5	316	20

<sup>1</sup> Consists only of storm sewers discharging directly into streams.

<sup>2</sup> In addition to storm sewers, includes 1.3 km<sup>2</sup> of sanitary sewers constructed during 1953-64 and 2.8 km<sup>2</sup> of Sewer District 2 sanitary sewers completed during 1965-74.

<sup>3</sup> From correlation analysis of total streamflow during 1944-52 at Connetquot River and East Meadow Brook.

at East Meadow Brook. For example, during 1965-74 at Carlls River, the theoretical base flow of 582 L/s (table 6, col. 4) was computed as the product of mean discharge (col. 2) for the period (603 L/s) and 0.965. By subtracting "measured" mean base flow (col. 3), obtained by hydrograph separation procedures, from the theoretical base flow (col. 4), values of base-flow depletion (col. 5) were computed.

During 1944-52 at the East Meadow Brook basin and throughout the study period (1944-74) at Carlls River, storm sewers were used to dispose of surface runoff, whereas cesspools and septic tanks were used to process sanitary sewage. Because cesspools and septic tanks have little, if any, net effect on regional water balances, the loss of base flow during the three study periods at Carlls River and during 1944-52 at East Meadow Brook was probably due in large measure to the present network of stream-directed storm sewers. For a stream basin having storm-water sewers but no sanitary sewers, the total volume of streamflow is not changed; only the ratio of base flow to storm flow is altered. The theoretical base flow for unsewered conditions can be estimated by multiplying total streamflow by 0.965, the previously determined ratio of base flow to total streamflow in undisturbed streams. The loss of base flow in the study area during 1944-52 ranged from 12 L/s at Carlls River to 34 L/s in the more highly urbanized East Meadow Brook basin. Owing to an expanding network of storm sewers discharging into Carlls River, base-flow losses increased to 28 L/s during 1953-64 and to 50 L/s during 1965-74.

Installation of a sanitary-sewer system effectively diverts potential recharge away from the upper glacial aquifer, where the sewers are above the water table. As a result, both ground-water levels and the base flow of streams decline, and, because no additional stormflow is added, the total volume of streamflow dwindles. Of the six streams analyzed, only East Meadow Brook was affected by a regional sanitary sewer system during the study period (1944-74). Thus, to estimate the theoretical base flow of that stream during sewer construction, which began in 1953, it was necessary to correlate mean annual discharge of East Meadow Brook with concurrent values for Connetquot River during the preconstruction years (1944-52). Estimates of mean annual discharge at East Meadow Brook were then obtained for the 1953-64 sewer construction period and the 1965-74 postconstruction period, based on the largely undisturbed Connetquot River basin. These estimated mean annual discharges were multiplied by 0.965 to obtain theoretical base-flow discharges of 549 L/s and 355 L/s at East Meadow Brook during 1953-64 and 1965-74, respectively (table

6, col. 4). Base flow decreased dramatically at East Meadow Brook during and after construction of the sanitary sewage system, as potential recharge was diverted from the basin. A base-flow loss of 34 L/s during 1944-52 was followed by losses of 127 L/s in the 1953-64 construction period and 211 L/s in the 1965-74 postconstruction period (table 6, col. 5). During 1965-74 estimated theoretical base flow exceeded the actual measured mean total discharge by 126 L/s. Clearly, the significant reduction in the sustained flow of the stream has been caused principally by the sanitary sewer system associated with Sewer District 2.

### Impact of Sewer District 2

Within 5 yr after completion of Sewer District 2 in 1964, the base flow of East Meadow Brook stabilized at 65 percent of total streamflow (fig. 3). Mean estimated base-flow loss due to separate storm and sanitary sewer systems during the postconstruction period (1964-74) was 211 L/s. To estimate the base-flow losses due to each type of sewage system, it was necessary to examine the preconstruction period (1944-52) and the early years of the construction phase when the impact of Sewer District 2 on streamflow was minimal.

Base flow at East Meadow Brook averaged 89 percent of total streamflow during 1944-52, but this dropped to 85 percent during 1953-58 as the storm-sewer network discharging direct runoff to the stream expanded rapidly (Seaburn, 1969, table 3). Construction of Sewer District 2 during 1953-58 had little if any effect on base flow in East Meadow Brook because ground-water levels adjacent to the stream declined only slightly through 1958 (Franke, 1968, table 1). Thus, the decline of percentage base flow from 1953-58 was due to storm sewers rather than the combined effect of storm and sanitary sewers. Ground-water levels declined steadily after 1959, as an increasing number of sanitary sewer hookups were completed. As a direct result, ground-water discharge declined, and the ratio of base flow to total streamflow dwindled.

The theoretical base flow of East Meadow Brook for the postconstruction period was computed to be 355 L/s. This is the base flow that would have occurred if the basin was left undisturbed. It is estimated that during 1965-74, base flow at East Meadow Brook would have declined to 84 percent of total streamflow had Sewer District 2 not been constructed. Thus, the base flow of the stream would have been about 300 L/s, or 55 L/s below theoretical level. Actual base flow for the postconstruction period was 144 L/s, or 211 L/s below theoretical level. The base-flow loss at East Meadow Brook due to the sanitary sewer network of Sewer Dis-

trict 2 is estimated to be 211 L/s minus 55 L/s, or 156 L/s. Thus, nearly 75 percent of the loss of base flow of East Meadow Brook during the postconstruction period was due to the District 2 sanitary sewer system west of the basin.

Only a small part of the area contributing ground-water discharge to East Meadow Brook underlies Sewer District 2. Throughout the study period, much of the base flow entering East Meadow Brook originated in unsewered areas east and northeast of the stream. Thus, it seems that the loss of base flow resulted from a gradual lowering of ground-water levels that spread from Sewer District 2 to unsewered areas to the east.

### RECHARGE DEPLETION

The recharge area of a gaging station, as used in this study, is the area upstream from the gage, bordered on the north by the main east-west ground-water divide across Long Island and on the east and west by interstream ground-water divides that separate the gaged stream from adjoining basins. Thus, "recharge area" as used herein is coincident with the ground-water contributing area above the gaging station.

Recharge to the ground-water systems above the gaging stations may be separated into three components, in terms of its path of discharge: (1) ground water seeping into the streams and measured as base flow, (2) ground water moving under and past the lower basin boundary as underflow, and (3) ground water evaporated and transpired. The bulk of the ground-water evapotranspiration on Long Island occurs along the marshes and wetlands at or near the shore. Owing to the small amount of wetland areas flanking streams above the gages and because ground-water evapotranspiration is estimated to be only about 10 mm annually on Long Island (Cohen and others, 1968, p. 46), ground-water evapotranspiration was assumed to be negligible in this analysis. Accordingly, recharge depletion is assumed to be equivalent to the sum of base-flow losses and underflow losses.

At the gaging stations, about two-thirds of the total outflow from the ground-water contributing area is base flow, and one-third is underflow (Pluhowski and Kantrowitz, 1964, p. 54). By proportionally adjusting base-flow losses (table 6, col. 5), it is possible to estimate the loss of recharge resulting from sewerage. The assumption of concurrently proportional base flow and underflow losses is reasonable with reference to the upper glacial aquifer in view of the multiyear time frame (table 6, col. 1) used for each of the study periods. This assumption may be less acceptable with regard to underflow deep within the ground-water re-

servoir; however, the adjustment was made as the best available method of estimating the overall effect of the regional sanitary-sewer system on ground-water outflow.

Recharge losses (table 6, col. 7) were estimated by multiplying column 5 (base-flow loss) by 1.5 to account for reduced underflow from the recharge area. Recharge losses, in liters per second per square kilometer (col. 8), were estimated by dividing column 7 by the area serviced by stream-directed storm sewers in each basin. Averaged over the entire study period (1944-74), the loss of recharge in the Carlls River basin in areas serviced by stream-directed storm sewers was only about 4 (L/s)/km<sup>2</sup>. By way of contrast, recharge depletion in the more highly urbanized East Meadow Brook basin was about 18 (L/s)/km<sup>2</sup>. These losses were sustained principally in the interstream zone near the south shore, where storm waters are frequently conveyed directly to streams. The heavy recharge depletion in parts of the East Meadow Brook basin serviced by stream-directed storm sewers is due to the interception of runoff by an extensive network of storm drains and to the sanitary sewers of Sewer District 2, which effectively convey potential recharge into tidal Reynolds Channel (fig. 1).

### CONCLUSIONS

Significant decreases in the ratio of base flow to total discharge of streams along the south shore of Long Island have been caused by storm-sewer systems discharging runoff directly to watercourses and to the completed sanitary sewer network of Sewer District 2 in Nassau County. The general lowering of ground-water levels in Sewer District 2 has diminished the base flow of East Meadow Brook by 60 percent since 1953. Nearly 75 percent of the base-flow loss is attributed to the sanitary sewer network of Sewer District 2, and the remainder is attributed to stream-directed sewers. The Carlls River basin in southwestern Suffolk County sustained base-flow losses that are estimated to have ranged from 12 L/s during 1944-52 to 50 L/s during 1965-74. There were no sanitary sewers in the Carlls River basin during the study period (1944-74); therefore, the loss of base flow was due principally to storm sewers conveying runoff to the stream. Base-flow losses at Carlls River were less than 10 percent of the estimated base flow under undisturbed conditions, whereas similar losses at East Meadow Brook after completion of Sewer District 2 averaged 35-40 percent of the estimated undisturbed base flow under a no-sewer regime. Little or no loss of base flow was detected at Connetquot River or Swan River, where urban development is much less intense than in the four other study basins.

It is predicted that completion of Nassau County Sewer District 3, east of East Meadow Brook, in 1990 will result in further losses of sustained streamflow. Within 5 years of the completion of Sewer District 2, the ratio of base flow to total flow at East Meadow Brook stabilized in the range of 60–65 percent, down from 85–89 percent before the full sanitary-sewer development. Base flow is expected to diminish further in Carlls River and in other streams draining southwestern Suffolk County after completion of a sanitary-sewer system currently being constructed in that area.

Recharge depletion in Carlls River basin areas serviced by stream-directed storm sewers averaged only about 4 (L/s)/km<sup>2</sup>, whereas in the more urbanized East Meadow Brook basin recharge-depletion rates in similar areas averaged about 18 (L/s)/km<sup>2</sup>.

#### REFERENCES CITED

- Chow, V. T., 1964, *Handbook of applied hydrology*: New York, McGraw-Hill Book Co., p. 14-2-14-12.
- Cohen, Philip, Franke, O. L., and Foxworthy, B. L., 1968, *An atlas of Long Island's water resources*: New York Water Resources Bull. 67, 117 p.
- Duncan, A. J., 1959, *Quality control and industrial statistics*: Homewood, Ill., Richard D. Irwin, Inc., p. 519-535.
- Fair, G. M., and Geyer, J. C., 1954, *Water supply and waste-water disposal*: New York, John Wiley & Sons, Inc., p. 325.
- Franke, O. L., 1968, *Double-mass-curve analysis of the effects of sewerage on ground-water levels on Long Island, New York*: U.S. Geol. Survey Prof. Paper 600-B, p. B205-B-209.
- Garber, M. S., and Sulam, D. J., 1976, *Factors affecting declining water levels in a sewerage area of Nassau County, New York*: U.S. Geol. Survey Jour. Research, v. 4, no. 3, p. 255-265.
- Heath, R. C., Foxworthy, B. L., and Cohen, Philip, 1966, *The changing pattern of ground-water development on Long Island, New York*: U.S. Geol. Survey Circ. 524, 10 p.
- Koszalka, E. J., 1975, *The water table on Long Island, New York, in March 1974*: Long Island Water Resources Bull. LIWR-5, 7 p., 3 pls.
- Nassau-Suffolk Regional Planning Board, 1968, *Existing land use*: Nassau-Suffolk Regional Comprehensive Plan Series, 30 p.
- Pluhowski, E. J., 1970, *Urbanization and its effect on the temperature of streams on Long Island, New York*: U.S. Geol. Survey Prof. Paper 627-D, 110 p.
- , 1972, *Hydrologic interpretation based on infrared imagery of Long Island, New York*: U.S. Geol. Survey Water-Supply Paper 2009-B, 20 p.
- Pluhowski, E. J., and Kantrowitz, I. H., 1964, *Hydrology of the Babylon-Islip area, Suffolk County, Long Island, New York*: U.S. Geol. Survey Water-Supply Paper 1768, 119 p.
- Seaburn, G. E., 1969, *Effects of urban development on direct runoff to East Meadow Brook, Nassau County, Long Island, New York*: U.S. Geol. Survey Prof. Paper 627-B, table 3, p. B6.
- Seaburn, G. E., and Aaronson, D. A., 1974, *Influence of recharge basins on the hydrology of Nassau and Suffolk Counties, Long Island, New York*: U.S. Geol. Survey Water-Supply Paper 2031, 66 p.
- Welsch, W. F., 1935, *Comprehensive drainage plan for Nassau County, New York—Summary report*: Nassau County Sanitation Comm., 23 p.



## HYDRAULIC CHARACTERISTICS OF THE WHITE RIVER STREAMBED AND GLACIAL-OUTWASH DEPOSITS AT A SITE NEAR INDIANAPOLIS, INDIANA

By WILLIAM MEYER, Indianapolis, Indiana

*Prepared in cooperation with the State of Indiana, Department of Natural Resources*

**Abstract.**—An aquifer test was made in the glacial-outwash aquifer along the course of the White River in Marion County, Ind., to establish the hydraulic characteristics of this unit and the hydraulic conductivity of the White River streambed at a site 11 kilometers south of the center of downtown Indianapolis. In the immediate vicinity of the site, at a depth of about 15 meters below land surface, a clay lens separates the outwash aquifer into an upper sand and gravel unit 12 m thick and a lower unit 8.5 m thick. At the site of the test well, the clay lens is 3.0 m thick. The test was made in the upper sand and gravel unit, and data were analyzed for an assumed condition of no, or at least negligible, transient leakage from the clay lens underlying this unit. As no observation wells were installed in the clay lens, this assumption cannot be directly substantiated. However, observation wells beneath the clay lens indicated that a head loss was not induced below the clay lens by the test well, and the closeness of the values obtained for transmissivity of the upper unit by three different methods strongly supports the assumption. Results of the test include for the upper unit: lateral hydraulic conductivity, 108 meters per day; range of transmissivity (determined by three techniques), from 1400 to 1670 meters squared per day; specific yield, 0.08; and vertical hydraulic conductivity of the streambed, 2.2 m/d. These results should be of use in assessing the potential supply and in developing one of Indiana's major aquifer systems because a knowledge of aquifer characteristics is essential for proper design and spacing of wells.

A cooperative study between the State of Indiana, Department of Natural Resources, and the U.S. Geological Survey to determine the availability of ground water in Marion County (Meyer and others, 1975) included determination of the hydraulic characteristics of the sand and gravel aquifer underlying the White River and Fall Creek and definition of the hydraulic connection between these streams and the aquifer. The aquifer is of glacial-outwash origin and consists of a mixture of sand, sand and gravel, and gravel deposits interspersed with clay lenses. Water in the deposits is generally unconfined, although water in deposits beneath the clay lenses in some local areas is confined.

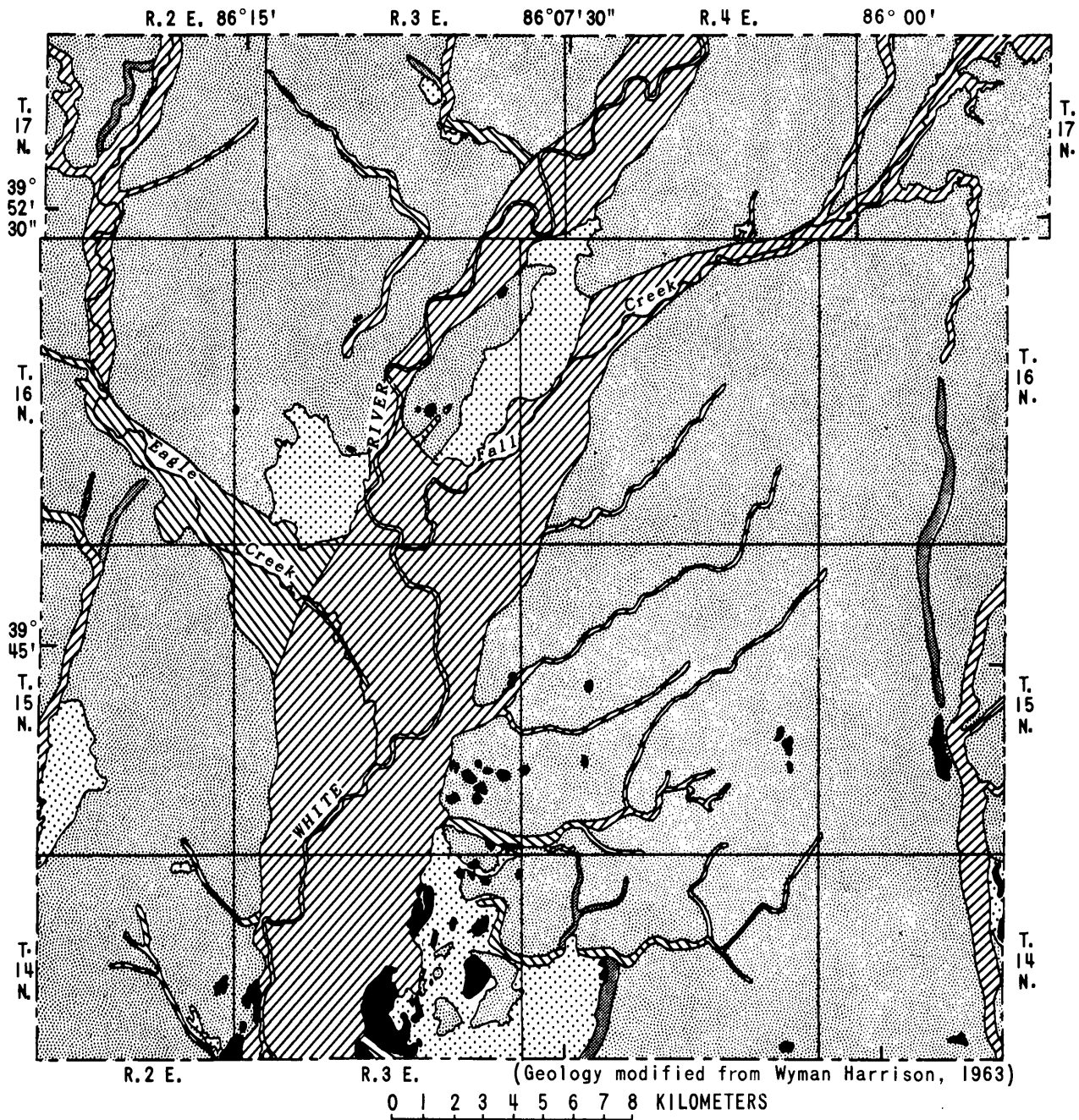
The major part of ground water presently (1976) pumped in the county is withdrawn from the outwash aquifer, and the potential for additional development in it is greater than for any other aquifer in the county (Meyer and others, 1975). Areal extent of the outwash deposits within the county is shown in figure 1.

White River and Fall Creek are gaining streams throughout their respective reaches in Marion County, and the response of observation wells in the outwash aquifer to changes in stream stage indicate a hydraulic connection between these streams and the aquifer. To help define this connection and determine the hydraulic characteristics of the aquifer, the aquifer was tested at a point 11 kilometers south of the center of downtown Indianapolis and along the White River where the characteristics of the streambed are fairly representative of the lower 9.6-km reach of the river in Marion County. This report summarizes the test procedure and the results of the aquifer test, which were assimilated into the larger overall ground-water study of the county.

The data are significant in their own right, however, as they provide detailed information on the hydrologic conditions in the immediate vicinity of the test site and thus are of potential use to engineers and planners concerned with developing ground water in this area. A knowledge of aquifer characteristics and streambed permeability is essential for proper design and spacing of wells.

### GENERAL GEOHYDROLOGIC CONDITIONS OF THE TEST-SITE AREA

The location of the test-site area is shown in figure 2. The outwash aquifer is divided into upper and lower units of sand and gravel by a clay lens, which is about 15 meters below the land surface throughout the immediate area. An east-west section of the outwash in the test area is shown in figure 3. As can be seen from



EXPLANATION

- |  |   |
|--|---|
| <ul style="list-style-type: none"> <li> Disintegration or end moraine</li> <li> Outwash plain</li> <li> Kames and linear disintegration ridges of stratified drift</li> </ul> | <ul style="list-style-type: none"> <li> Valley or valley segment developed by melt-water flow in ice-walled channel</li> <li> Valley or valley segment developed by melt-water flow along former ice margin (may have been initiated by melt-water flow in ice-walled channel)</li> <li> High-level valley developed by melt-water flow in ice-walled channel</li> </ul> |
|--|---|

FIGURE 1.—Surficial geology of Marion County, Ind.

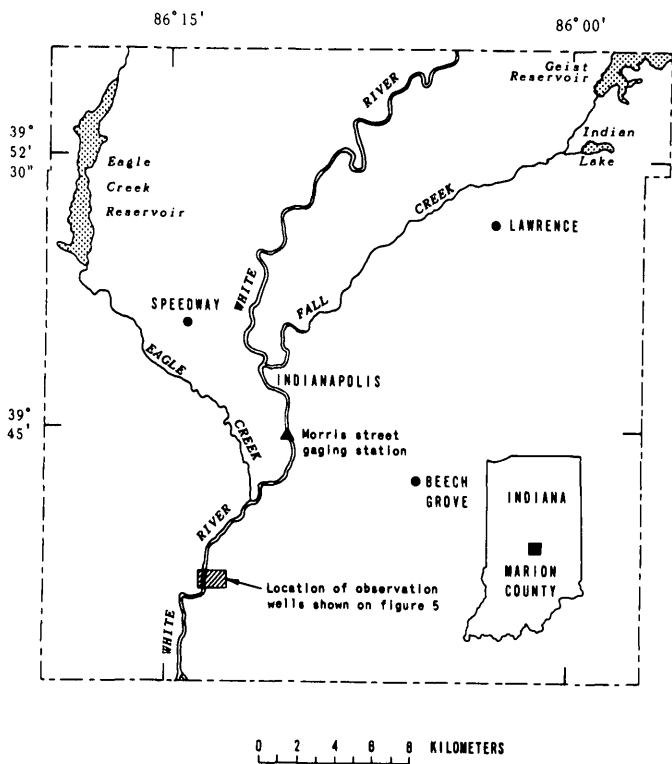


FIGURE 2.—Site of aquifer test in Marion County, Ind.

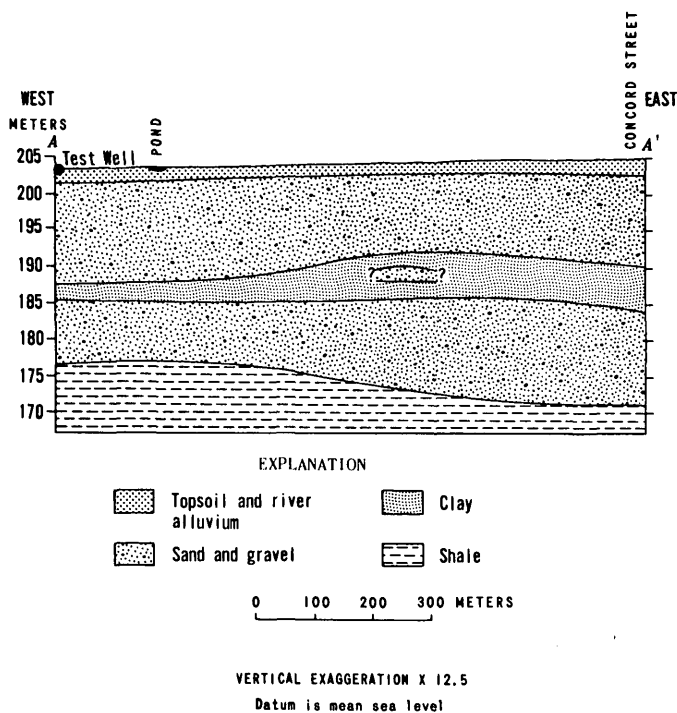


FIGURE 3.—East-west (A-A') section of test site, Marion County, Ind. Location of section is shown in figure 5.

the figure, thicknesses of the sand and gravel units and the clay lens vary. At the immediate site of the test well, saturated thickness of the upper sand and gravel unit was 12 m; of the clay lens, 3 m; and of the lower sand and gravel unit, 8.5 m. Shale is immediately below the lower sand and gravel unit.

Figure 4 is a water-table-contour map of the outwash aquifer in February 1975. The contours indicate a general movement of water from the outwash into the White River. This discharge was estimated to be 3.9 meters cubed per day per meter of channel length for water levels measured in the outwash in April 1974 (Meyers and others, 1975, p. 29) As indicated by water levels measured on December 5, 1974, in observation wells along the east bank of the river, the gradient toward the river ranged from 0.01 to 0.04 meter per meter and averaged 0.03 m/m. On the same day, flow

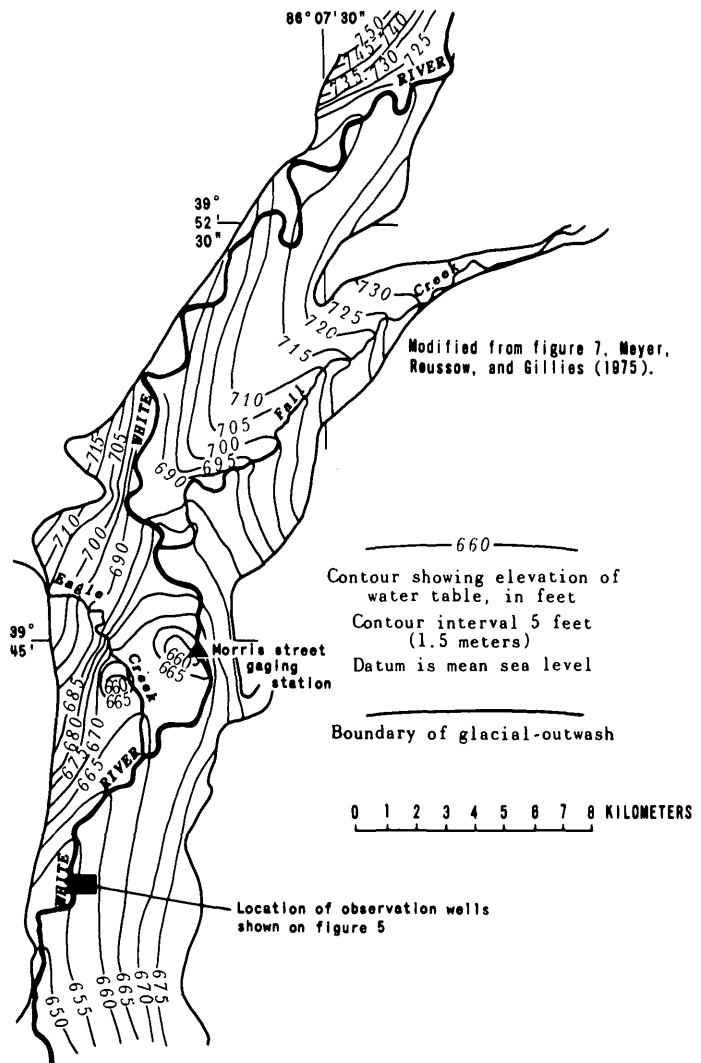


FIGURE 4.—Water levels in outwash aquifer, Marion County, Ind., February 1975. (Feet multiplied by 0.3048 equals meters.)

in the White River at the Morris Street gaging station, 8 km upstream from the test site (fig. 2) was 11 meters cubed per second. This flow is equaled or exceeded 61 percent of the time.

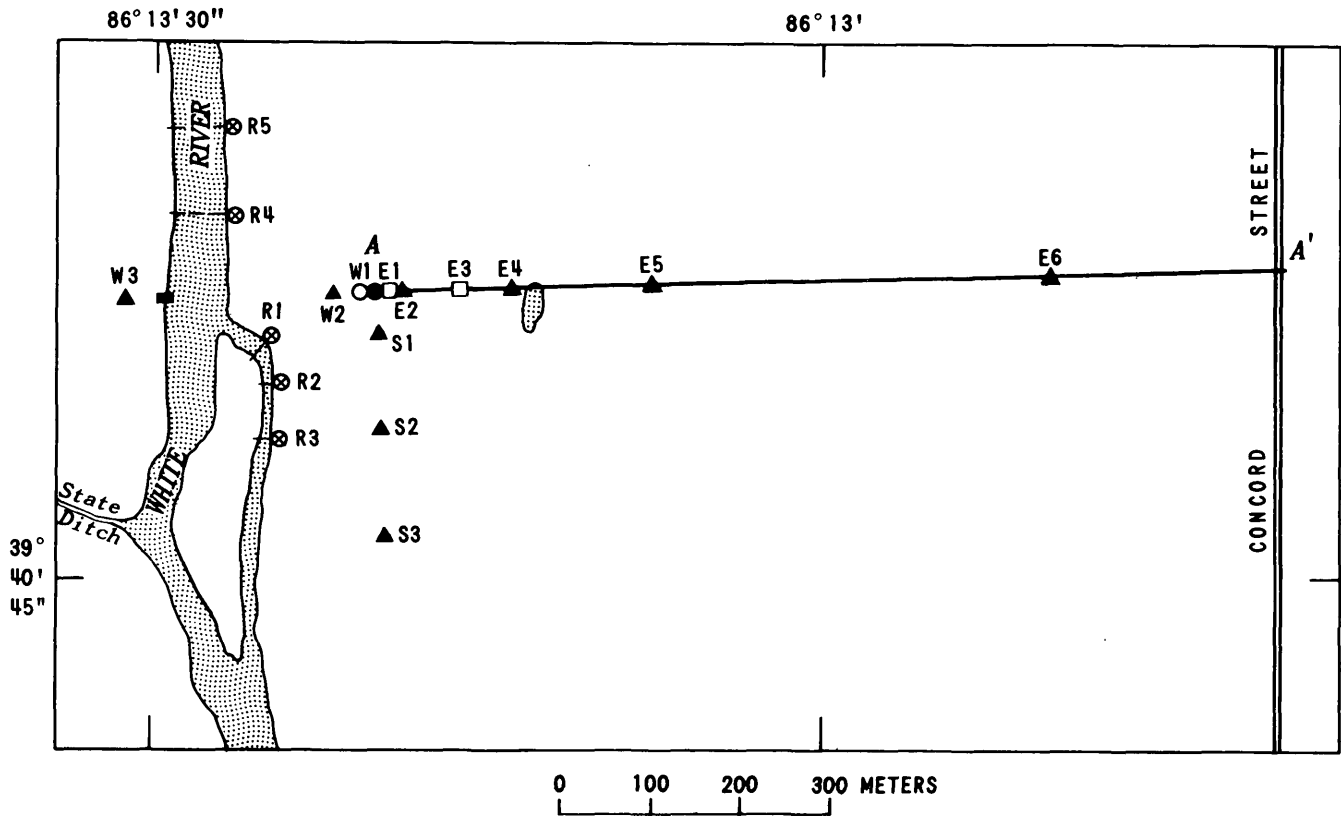
**Characteristics of the stream channel**

Several cross sections of the White River, spaced 60-90 m apart, were made at the locations shown in figure 5 to determine the width and the depth of the stream and the nature of the streambed. Stream widths ranged from 53 to 72 m for sections upstream from the island shown in figure 5. The average depth of the stream ranged from 0.86 to 1.4 m. Width of the minor branch of the river on the east side of the island

ranged from 16 to 27 m, and the average depth at the cross sections ranged from 0.5 to 0.7 m.

At the time the cross sections were made, flow in the White River at the Morris Street gage was 11 m<sup>3</sup>/s. Before the aquifer test, flooding increased the width of the stream to approximately 90 m. At the start of and during the aquifer test, the stream had returned to the widths mentioned in the preceding paragraph.

The streambed at each of the seven sections consisted of a firm sand and gravel bottom. Near the banks at some locations were areas of fine silty material 3 m wide or less. The water was murky and obscured the streambed except in shallow areas.



**EXPLANATION**

- |      |                                    |      |                             |
|------|------------------------------------|------|-----------------------------|
| ▲ E5 | Shallow-deep observation well pair | ⊗ R5 | River-line observation well |
| ○ W1 | Deep observation well              | ■    | River-stage recorder        |
| □ E3 | Observation well below clay lens   | ---  | Site of cross section       |
| ●    | Test well                          | ▭    | Pond                        |

FIGURE 5.—Location of observation wells for aquifer test, Marion County, Ind.

## INSTALLATION OF WELLS

### Well for pumping

A well for pumping (test well) was installed 179 m from the main stem of the White River (fig. 5). The shortest distance from the well to the minor branch of the White River (the channel on the east side of the island) was 131 m. Before installation of the well, the site was test drilled, and aquifer samples were obtained at 1.5-m intervals beginning 3 m below the land surface. Here, the aquifer is primarily a mixture of coarse sand to medium gravel—93 percent or more coarse sand by weight, or 80 percent or more of fine to medium gravel—in each of the 1.5-m zones.

The test well consisted of a 300-millimeter-diameter, unperforated, standard (black-line) casing extending 9 m below land surface and a 6.1-m length of wire-wound, stainless steel screen attached to the bottom of the casing. The bottom of the screen was on the clay lens. Water levels just outside the test well were observed during pumping by a special observation well consisting of a 38-mm-diameter (black) pipe with a 760-mm length of drive-point screen welded to the outside of the well screen. The middle of the screen of the drive point was placed at the middle of the screen of the test well.

The test well was developed by surging and intermittent pumping for several days until most of the fine-grained material in the vicinity of the screen had been removed. Temporary pumping rates exceeded 63 liters per second during the process. A step-drawdown test made 1 week after the well was developed indicated that the well had been adequately developed.

### Observation wells in the outwash aquifer

Locations of observation wells installed for the aquifer test are shown in figure 5. Each well consisted of a 38-mm-diameter black pipe with a 760-mm length of drive-point screen at the bottom. Except as indicated otherwise in figure 5, each observation well site consisted of a pair of observation wells, one shallow and one deep. The shallow wells were screened at a depth 3 m below the water table, which was equivalent to 25 percent penetration of the aquifer. The deep wells were screened at a depth equal to the middle of the screened interval of the pumped well, which was equivalent to 75 percent penetration of the aquifer.

The observation wells on the east-west line perpendicular to the river (W1-W3 and E1-E6, fig. 5) and passing through the test-well site were positioned so that horizontal and vertical hydraulic conductivity and specific yield of the aquifer could be determined using the methods described by Bennett and others (1967).

The observation wells on the line parallel to the river (S1-S3, fig. 5) and extending through the test-well site were installed so that the aquifer test could be analyzed by techniques described by Rorabaugh (1956). Norris and Fidler (1969) described these techniques in detail as part of a report on the hydrogeology of the Scioto River valley in Ohio.

Two observation wells were screened in the sand and gravel unit below the clay lens (E1 and E3, fig. 5) to determine if there was leakage from the lower sand and gravel unit through the clay lens during the aquifer test. These wells were placed at distances 15 and 91 m from the test well on the east-west line.

### Observation wells on east bank of river

To determine changes in ground-water levels beneath the river relative to stream stage, five observation wells (R1-R5) were installed along the east bank of the White River (see fig. 5). Each well was about 1 m from the edge of the river and consisted of a 38-mm-diameter black pipe attached to a 760-mm length of drive-point screen. The middle of the screen was 1.1 m below the streambed elevation established at the bank during the cross sectioning. Each well was screened in sand and gravel and was surged, slugged, and pumped to insure that it was open to the aquifer. An attempt to install the first of these wells directly into the streambed resulted in clogging the well screen. Subsequent efforts to clear the screen simply opened the well directly to the river, probably because of the gravelly nature of the streambed.

Because of their proximity to the river, the five observation wells should have been in the zone where vertical flow predominated. Drawdowns measured during the aquifer test reflected the effects of the vertical conductivity of the streambed rather than the horizontal hydraulic conductivity of the aquifer.

## MEASUREMENT OF STREAM STAGE

A recorder on the west side of the river at the location shown in figure 5 furnished continuous-stage data for the White River. Two staff gages were installed near the edge of the river: one on the west bank several feet upstream from the recorder and the other on the east bank directly across from the recorder. The continuous-stage recorder was mounted on a 38-mm-diameter pipe attached to a 760-mm length of drive-point screen extending into the river. Pipe and screen were permanently fixed so that the screen was fully submerged at all times with its bottom slightly above the streambed. The water-level recording unit was mounted at the top of the pipe. Measurements of stream

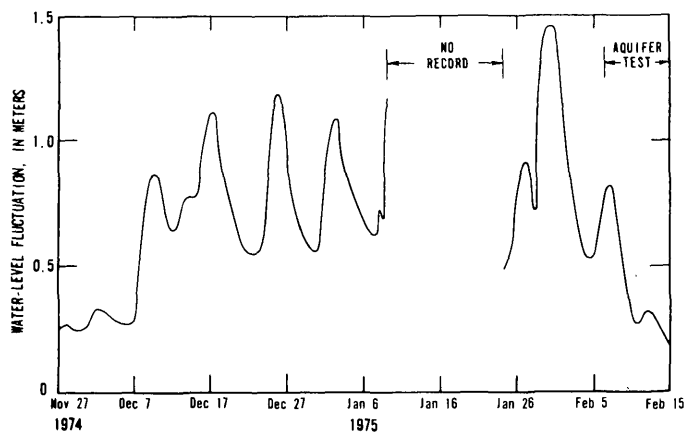


FIGURE 6.—Hydrograph of White River at Concord Street, Indianapolis, Ind.

stage were begun on November 27, 1974, and were continued until the aquifer test ended. Flooding during mid-January interrupted the record for 13 days. Fluctuation of stream stage with time, both before and during the aquifer test, is shown in figure 6.

#### PRETEST CONDITIONS

The aquifer test was originally scheduled for October or early November. Long periods of little or no precipitation accompanied by extended periods of base-flow recession and relatively stable ground-water levels are common during this time of the year, conditions most preferred for the analysis of aquifer-test data. Unfortunately, various difficulties in contractual arrangements for the test well delayed its installation until the middle of December. As shown by figure 6, this was a time when fluctuations in river stage resulting from cyclonic winter storms caused significant fluctuations in ground-water levels.

#### River stage and ground-water levels

Background data on river stage and ground-water levels were collected for several months before pumping was started. The effect of stream stage on ground-water levels from about November 26, 1974, through about January 11, 1975, in the line of observation wells perpendicular to the river (fig. 5) is shown in figure 7. As would be expected, each significant change in stream stage was transmitted back into the aquifer with diminishing amplitude and with a time lag. Other observations based on the background data and useful in the analysis of the aquifer test are as follows: (1) Water levels in the river line of observation wells (R1-R5) accurately reproduced all except major fluctuations in stream stage without a time lag or loss in amplitude, (2) water levels in the line of observa-

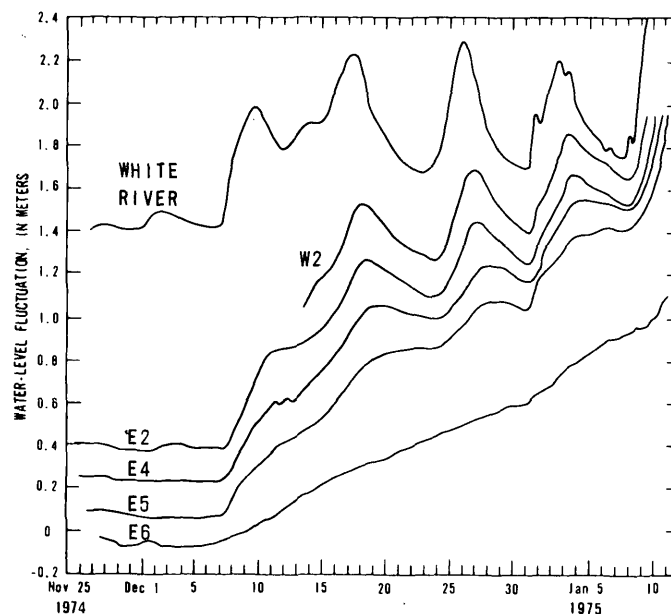


FIGURE 7.—Fluctuation of water levels in observation wells in a line perpendicular to the White River near Indianapolis, Ind.

tion wells parallel to the river (S1-S3) responded virtually in unison and with about the same time lag to change in the stream stage, and (3) water levels in the aquifer-test area declined at a constant rate whenever the river stage declined significantly for several days. These observations were particularly important because they allowed a means for analyzing the aquifer-test data during a period of fluctuating stream stage.

#### THE AQUIFER TEST

As indicated by the background information, the preferred time for the aquifer test was a time of declining stream stages and ground-water levels. These conditions were met in early February, and testing was begun on the morning of February 6, 1975. Unfortunately, a light rainfall, which began in the evening of February 5, caused the river to rise slowly. The river peaked between 2:30 and 3:00 p.m. (eastern standard time) on February 7 after a rise of 0.3 m.

This minor flood pulse was transmitted back into the ground-water system away from the stream at diminishing rate and amplitude. Water levels in the river line of observation wells (R1-R5) were reproducing the stream-stage fluctuation at the start of pumping. Water levels in observation wells W1, W2, and E2, within 49 m east or west of the test well, and S1-S3 in the line parallel to the river, had ceased declining by midnight on February 5 and were stationary on the morning of February 6 when the aquifer test was

begun. Water levels in observation wells E4–E6, farther east of the test well, were still declining at the beginning of pumping but at a diminished rate from that established before February 5. The water levels in observation wells E1 and E3 in the lower sand and gravel unit were declining at an identical rate before and at the beginning of the aquifer test.

#### Determination of aquifer transmissivity and hydraulic conductivity

Location of the observation wells had been selected so that the techniques described by Bennett and others (1967) and Norris and Fidler (1969) could be used to analyze the aquifer test data. However, the water-level fluctuations induced by the rising and falling river stage in observation wells in the line of wells perpendicular to the river could not be accurately measured, so the techniques of Bennett and others (1967) for determining vertical hydraulic conductivity and the specific yield of the aquifer could not be used. Because water levels in the observation wells in the line parallel to the river responded in unison to changes in stream stage, Rorabaugh's (1956) technique to determine transmissivity could still be used on data obtained from these wells.

#### Lateral hydraulic conductivity

The lateral hydraulic conductivity of the aquifer was calculated by the distance-drawdown technique, incorporating the assumptions used by Bennett and others (1967). The drawdown data measured in the deep observation well W1 (fig. 5), 5.5 m west of the test well, and the observation well placed at the middle, but just outside the screen of the test well, were plotted on semilog paper as drawdowns against the log of distance. These plots were made at various times beginning 100 minutes after pumping began. The slope of the lines remained constant with time, and this slope,  $\partial s/\partial(\log r)$ , was inserted into the equation

$$P_L = \frac{2.3 Q_w}{2\pi L \frac{\partial s}{\partial(\log r)}} \quad (1)$$

for the flow,  $Q_w$ , equal to the pumped rate of the test well;  $L$ , equal to the screen length; and  $P_L$ , the lateral permeability. As stated by Bennett and others (1967), use of this method requires the assumptions that the flow,  $Q_w$  (41 L/s), occurs within the interval,  $L$  (6.1 m), at radii between the discharging well and the observation well, and that this flow is horizontal, radial, and uniformly distributed throughout the interval,  $L$ . Considering the short distance from the observation

well to the test well for which the distance-drawdown data were obtained, the known geohydrologic conditions, and, finally, the consistency of the distance-drawdown slope on semilog paper with time, these assumptions should not be too restrictive. Water levels in each of the two observation wells were assumed to have responded identically to changes in stream stage. Considering the short distance between the two wells, this assumption is probably valid. The lateral hydraulic conductivity based on this slope is 108 meters per day. If this value is assumed to be constant for the full saturated thickness of the aquifer, the aquifer transmissivity is equal to 1400 meters squared per day.

#### Transmissivity

Drawdowns in observation wells S1 and S2, in the line of observation wells parallel to the river, after 24, 48, 72, and 96 hours of continuous pumping were plotted against distance on semilog paper (fig. 8) to determine transmissivity of the aquifer in the manner outlined by Norris and Fidler (1969). This technique of analysis was considered valid because the effect of

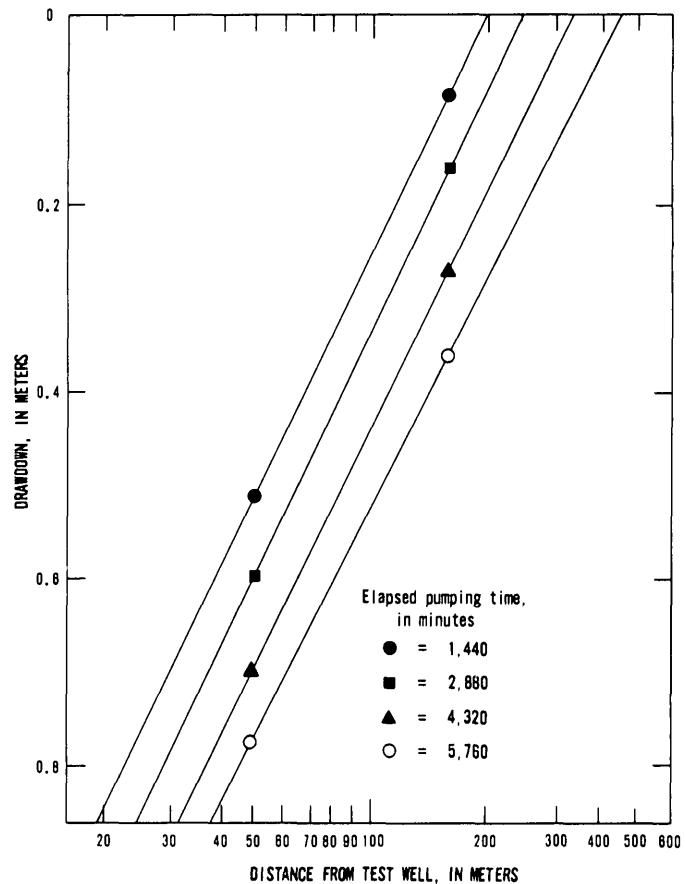


FIGURE 8.—Average drawdowns (corrected for dewatering) for observation-well pairs S1 and S2, deep and shallow.

the minor flood pulse on February 5 through 7 on ground-water levels can be assumed to have arrived simultaneously at each well in the parallel line and to have affected these wells equally. Water-level measurements in observation well S3 indicated that the effect of the flood pulse on ground-water levels along the parallel line was minimal during the entire test period and that the slope of the line describing the relation of drawdown and distance was virtually unaffected.

In the preceding analysis, the volume of water contributed by the transient movement out of the clay lens or movement from the lower sand and gravel unit through the clay lens was assumed to be negligible. Data collected in the two observation wells in the lower sand and gravel unit (E1 and E3) indicated that water levels in these two wells were declining at identical rates before the beginning of pumping and that their rates of decline remained identical during and after the pumping period. This would indicate that pumping caused no decline in head in the lower sand and gravel unit and, therefore, induced no flow of water from the lower sand and gravel unit.

Drawdowns plotted in figure 8 were obtained by correcting the original drawdown data at each shallow-deep pair of observation wells for the effect of partial penetration by averaging the drawdowns recorded in the two wells and then correcting this average value,  $s_a$ , for dewatering effects by subtracting the value,  $s_a/2m$ , from it (Jacob, 1944).

Values of drawdown,  $s_1$  and  $s_2$ , at selected radii,  $r_1$  and  $r_2$ , respectively, were obtained from each of the curves in figure 8 and were inserted into the equation

$$\frac{s_1}{s_2} = \frac{\log \frac{\sqrt{4a^2 + r_1^2}}{r_1}}{\log \frac{\sqrt{4a^2 + r_2^2}}{r_2}} \quad (2)$$

to determine  $a$ , which is defined as the effective or weighted-average distance (also called the line-source distance) from the pumped well to the stream. The appropriate value for  $a$  can be determined by a trial and error method of substituting various values for  $a$  into equation 2 until the appropriate value of  $s_1/s_2$  is obtained or by graphical methods described in detail in Norris and Fidler (1969). After  $a$  is determined, transmissivity,  $T$ , is calculated from the equation

$$T = \frac{527.7 Q \log \frac{\sqrt{4a^2 + r^2}}{r}}{s} \quad (3)$$

where  $Q$  is equal to the pumping rate of the well. Equations 2 and 3 are from Rorabaugh (1956). Values of transmissivity and line-source distance  $a$ , determined after 24, 48, 72, and 96h of pumping, are given in table 1.

The minor flood pulse, which began on February 5, 1975, caused the effective distance from the test well to the line source to decrease initially as ground-water levels between the test well and the river began to rise and then recede after these water levels began to decline. This effect is seen in table 1.

### Specific yield

Transmission of the minor flood pulse of the White River back into the aquifer with both diminishing amplitude and a time lag precluded the use of distance-drawdown data obtained from observation wells in the line perpendicular to the White River (fig. 5) for determining the specific yield of the aquifer. Therefore, the specific yield was determined from time-drawdown data obtained from the deep and shallow pair of observation wells at S2. Values of drawdown at a given time in the two wells were first averaged and were then corrected for dewatering in the manner described previously. These corrected values were plotted against the appropriate time on log-log paper, and the resulting curve (fig. 9) was overlaid on the type curves prepared by Stallman (1963, pl. 3). As shown in figure 9, the first 1800 min of data are on the curve  $K = 1.4$ , indicating a recharge boundary. After this time, the rate of drawdown increased significantly, and the time-drawdown data deviated significantly from the type curve. The increase in the rate of drawdown was observed at virtually the same time in the entire parallel line of observation wells, including the

TABLE 1.—Calculated values of line-source distance  $a$  and transmissivity for observation wells S1, S2, and S3

Time (days)	Transmissivity (m <sup>2</sup> /d)	Distance to line source $a$ (m)
1	1,670	98
2	1,500	113
3	1,580	162
4	1,610	210

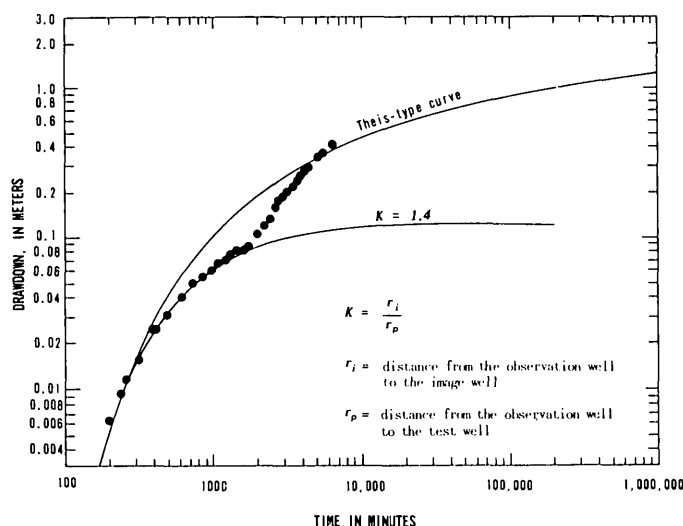


FIGURE 9.—Average drawdown (corrected for dewatering) in deep and shallow well pairs S1 and S2 versus time.

test well. The White River had peaked approximately  $3\frac{1}{2}$  h previously and had begun falling rapidly (see fig. 6). Because of these changing conditions and the virtually simultaneous increase in drawdown in all the observation wells in the line parallel to the White River, the increased rate of drawdown after about 1800 min (fig. 9) was interpreted to be the result of the decreasing ground-water level induced by the falling river stage. A transmissivity equal to  $1540 \text{ m}^2/\text{d}$  was obtained by using the first 1800 min of drawdown to obtain a match point on the Stallman-type curve. This value is consistent with the values obtained from the other two methods previously discussed. The value of specific yield obtained was 0.08. Finally, the distance to the image well as determined from the type-curve match was consistent with the field geometry and the calculated value of  $a$  for 1 day of pumping given in table 1.

#### Vertical hydraulic conductivity of streambed

The vertical hydraulic conductivity  $P_s$  of the White River streambed was determined by use of the Darcy equation

$$P_s = \frac{Q}{\left(\frac{\Delta h}{\Delta m}\right) A} \quad (4)$$

where  $Q$  is the quantity of water diverted from the area of the streambed;  $(\Delta h/m)_{av}$  is the average gradient between the ground-water system under the river and stream stage at the end of pumping, determined from stream-stage data and water-level in ob-

servation wells R1–R5; and  $A$  is the area of the streambed affected by the test well at the end of the aquifer test, obtained from drawdown data for observation wells R1–R5.

The drawdown that the test well induced in the river line of observation wells (R1–R5) was determined by superimposing the hydrograph of the river on the hydrograph of each observation well measured during the aquifer test and determining the difference between these two curves at various times. With this technique, each of the river-line observation wells is assumed to reproduce the river hydrograph in the absence of pumping. This assumption is supported by data collected in the river observation wells before the aquifer test. The river hydrograph and water levels in river observation wells R1, R2, and R5 are shown in figure 10. A semilog plot of drawdowns measured in these wells and in wells R3 and R4 at the end of the test against distance is shown in figure 11.

The area of the streambed affected by the test well at the end of the pumping period was determined by striking an arc from the test well through the river with the radius of the arc equal to the zero intercept (213 m) of figure 11. The area of the streambed thus determined was equal to 6450 meters squared.

An average value for the induced gradient,  $(\Delta h/\Delta m)_{av}$ , under the streambed was calculated in a method analogous to that described by Norris and Fidler (1969). In this method, the drawdown at selected points along the near and far edges of the stream in the affected area of the streambed are determined by measuring the distance of each of these points from the pumped well, determining the drawdown at these distances in figure 11, and then averaging the entire

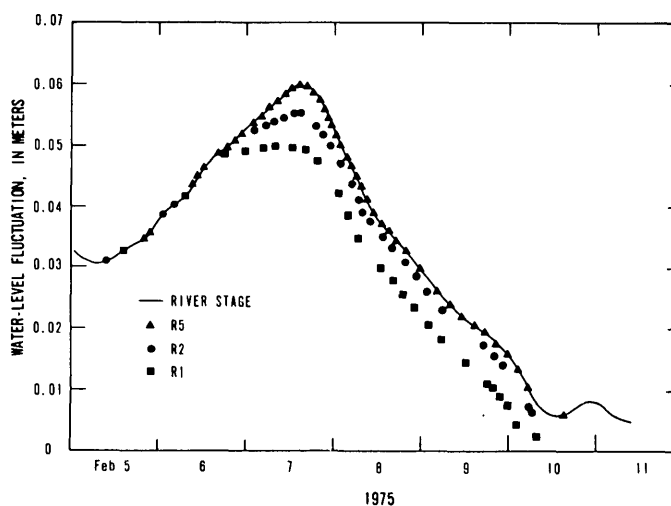


FIGURE 10.—Hydrographs of White River and selected observation wells, Marion County, Ind.

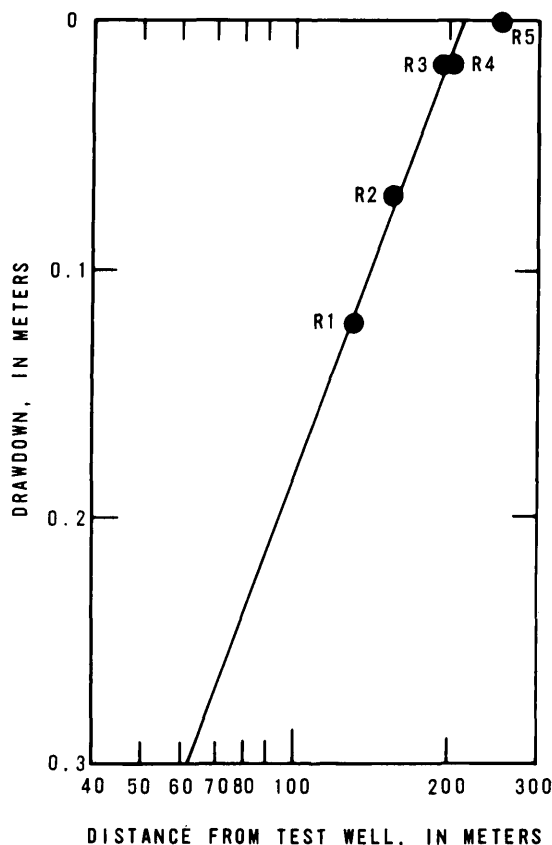


FIGURE 11.—Relation of drawdown in observation wells R1-R5 and distance from test well, Marion County, Ind.

set of values obtained. The average value for drawdown under the river (0.05 m) thus determined was converted to an average gradient under the affected streambed area  $(\Delta h/\Delta m)_{av}$  by dividing the average drawdown by 1.1 m (the distance between the screens in the river line of observation wells and the streambed).

The quantity of water being diverted from the river at the end of the pumping period was obtained by the technique presented by Theis (1941) for determining the percentage of water diverted from a source of recharge at a given time as a result of pumping. This percentage is determined by calculating a variable,  $f$ , which is equal to  $Tt/a^2S$ , and entering a curve presented by Theis (1941), where  $f$  is the abscissa and the percentage of water diverted from the recharge source is the ordinate. The value of  $f$  was calculated for  $t$  equal to the total time of pumping and for values of  $T$ ,  $a$ , and  $S$  that were previously determined for the aquifer. The quantity of water being diverted from the river was 65 percent (using  $f = 0.14$ ) of the 41 L/s pumping rate.

From the values of  $Q$ ,  $(\Delta h/\Delta m)_{av}$ , and  $A$  thus determined, the value for vertical hydraulic conductivity of the streambed calculated from equation 4 was 2.2 m/d.

### SUMMARY AND CONCLUSIONS

Lateral hydraulic conductivity of the upper sand and gravel unit at the aquifer test site was determined to be 108 m/d. Transmissivity of the unit (determined by three different techniques) ranged from 1500 to 1670  $m^2/d$ . The specific yield of this upper unit was determined to be 0.08. Finally, the vertical hydraulic conductivity of the streambed was calculated to be 2.2 m/d.

The test was made in the upper sand and gravel unit, and data were analyzed for an assumed condition of no, or at least negligible, transient leakage from the clay lens underlying this unit. Because no observation wells were installed in the clay lens, this assumption cannot be directly substantiated. However, observation wells beneath the clay lens indicated that a head loss was not induced below the clay lens by the test well, and the closeness of the values obtained for transmissivity by three different methods strongly supports this assumption.

The analysis of the test data was complicated by the minor flood pulse on the White River, which began the night before pumping began. Background data collected on the stream stage and ground-water levels had indicated that changes in stream stage could induce ground-water-level changes far greater than those that would be induced during the aquifer test. These background data also proved useful in the subsequent analysis of the aquifer-test data.

Results of the study should be of use in assessing the potential supply and in developing one of Indiana's major aquifer systems.

### REFERENCES CITED

- Bennett, G. D., Ata-Ur-Rehman, Ijaz Ahmed Sheikh, and Sabir Ali, 1967. Analysis of aquifer tests in the Punjab region of West Pakistan: U.S. Geol. Survey Water-Supply Paper 1608-G, p. G1-G56.
- Harrison, Wyman, 1963. Geology of Marion County, Indiana: Indiana Dept. Conserv., Geol. Survey Bull. 28, 78 p.
- Jacob, C. E., 1944. Notes on determining permeability by pumping tests under water-table conditions: U.S. Geol. Survey open-file rept., 25 p.
- Meyer, William, Reussow, J. P., and Gillies, D. C., 1975. Availability of ground water in Marion County, Indiana: U.S. Geol. Survey Open-File Rept. 75-312, 87 p.
- Norris, S. E., and Fidler, R. E., 1969. Hydrogeology of the Scioto River Valley Near Picketon, south-central Ohio: U.S. Geol. Survey Water-Supply Paper 1872, 70 p.

Rorabaugh, M. I., 1956, Ground water in northeastern Louisville, Kentucky, with reference to induced infiltration: U.S. Geol. Survey Water-Supply Paper 1360-B, p. B101-B169.

Stallman, R. W., 1963, Type curves for the solution of single boundary problems, *in* Bentall, Ray, compiler. Shortcuts

and special problems in aquifer tests: U.S. Geol. Survey Water-Supply Paper 1545-C, p. C45-C47.

Theis, C. V., 1941, The effect of a well on the flow of a nearby stream: Am. Geophys. Union Trans., 22d Ann. Mtg., pt. 2, p. 734-738.



**CHANGE OF ADDRESS FORM**

NAME—FIRST, LAST		
COMPANY NAME OR ADDITIONAL ADDRESS LINE		
STREET ADDRESS		
CITY	STATE	ZIP CODE
PLEASE PRINT OR TYPE		
(or) COUNTRY		

Mail this form to: NEW ADDRESS

Superintendent of Documents  
 Government Printing Office SSOM  
 Washington, D.C. 20402

Attach last subscription  
label here.

**SUBSCRIPTION ORDER FORM**

**SUBSCRIPTION ORDER FORM**

**ENTER MY SUBSCRIPTION TO:**

@ \$18.90 Domestic; @ \$23.65 Foreign.

NAME—FIRST, LAST		
COMPANY NAME OR ADDITIONAL ADDRESS LINE		
STREET ADDRESS		
CITY	STATE	ZIP CODE
PLEASE PRINT OR TYPE		
(or) COUNTRY		

Remittance Enclosed (Make checks payable to Superintendent of Documents)

Charge to my Deposit Account No. ....

**MAIL ORDER FORM TO:**  
 Superintendent of Documents  
 Government Printing Office  
 Washington, D.C. 20402



## RECENT PUBLICATIONS OF THE U.S. GEOLOGICAL SURVEY

The following books may be ordered from the Branch of Distribution, U.S. Geological Survey, 1200 South Eads Street, Arlington, VA 22202 (an authorized agent of the Superintendent of Documents, Government Printing Office). Prepayment is required. Remittances should be sent by check or money order payable to U.S. Geological Survey. Give series designation and number, such as Bulletin 1368-A, and the full title. Prices of Government publications are subject to change. Increases in costs make it necessary for the Superintendent of Documents to increase the selling prices of many publications offered. As it is not feasible for the Superintendent of Documents to correct the prices manually in all the previous announcements and publications stocked,

the prices charged on your order may differ from the prices printed in the announcements and publications.

In addition to the publications mentioned below, other professional papers, water-supply papers, bulletins, circulars, single copies of the periodical "Earthquake Information Bulletin," maps, and items of general interest, such as leaflets, pamphlets, and booklets, are available at the above address. All new Survey publications are listed in a free monthly catalog, "New Publications of the Geological Survey"; to subscribe, send name and address to U.S. Geological Survey, 329 National Center, Reston, VA 22092. (Some reports that are now out of print at the Superintendent of Documents can also be obtained at the Branch of Distribution address.)

### Professional Papers

- P 533. Cenozoic fossil mollusks from western Pacific islands; Gastropods (Eratoidae through Harpidae), by H. S. Ladd. 1977. 84 p., 23 plates. \$3.25.
- P 751-D. Geochemical effects of recharging the Magothy aquifer, Bay Park, New York, with tertiary-treated sewage, by S. E. Ragone. 1977. p. D1-D22. \$1.40.
- P 759-C. Distribution of bottom sediments on the continental shelf, northern Bering Sea, by D. A. McManus, D. M. Hopkins, and C. H. Nelson. 1977. p. C1-C31. \$1.60.
- P 813-G. Summary appraisals of the Nation's ground-water resources—Great Basin region, by T. E. Eakin, Don Price, and J. R. Harrill. 1976. p. G1-G37; plate in pocket. \$2.40.
- P 881. Geologic evaluation of waste-storage potential in selected segments of the Mesozoic aquifer system below the zone of fresh water, Atlantic Coastal Plain, North Carolina through New Jersey, by P. M. Brown and M. S. Reid. 1976 (1977). 47 p.; plates in pocket. \$11.
- P 999. Stillwater Complex, Montana: Rock succession, metamorphism and structure of the complex and adjacent rocks, by N. J. Page, 1977. 79 p., plates in pocket. \$4.50.
- P 1002. The Guatemalan earthquake of February 4, 1976, a preliminary report, by A. F. Espinosa, editor. 1976. 90 p. \$2.50.
- P 1007. Stratigraphy, petrology, and depositional environment of the Kenwood Siltstone Member, Borden Formation (Mississippian), Kentucky and Indiana, by R. C. Kepferle. 1977. 49 p. \$2.30.
- P 1026. Revisions of *Ulmus* and *Zelkova* in the middle and late Tertiary of western North America, by Toshimasa Tanai and J. A. Wolfe. 1977. 14 p., 4 plates. \$2.

- P 1027. Paleozoic-Mesozoic boundary in the Berry Creek quadrangle, northwestern Sierra Nevada, California, by Anna Hietanen. 1977. 22 p., plate in pocket. \$1.90.
- P 1059. GIRAS: A geographic information retrieval and analysis system for handling land use and land cover data, by W. B. Mitchell, S. C. Guptill, K. E. Anderson, R. G. Fegeas, and C. A. Hallam. 1977. 16 p. \$1.80

### Bulletins

- B 1416. Mineral resources of the Joyce Kilmer-Slickrock Wilderness, North Carolina-Tennessee, by F. G. Lesure, E. R. Force, J. F. Windolph, and J. J. Hill. 1977. 89 p.; plates in pocket. \$3.15.
- B 1422-C Triassic stratigraphy in the northern part of the Culpeper Basin, Virginia and Maryland, by K. Y. Lee. 1977. p. C1-C17; plate in pocket. \$1.20.
- B 1431. Mineral resources of the Bradwell Bay Wilderness and the Sopchoppy River Study Area, Wakulla County, Florida, by C. C. Cameron and P. C. Mory, *with sections on Phosphate*, by J. B. Cathcart, *and Sand*, by P. J. Geraci. 1977. 37 p.; plate in pocket. \$1.60.
- B 1435-B. The Rio Abajo, Pitahaya, and Daguaio Formations in eastern Puerto Rico, by J. W. M'Gonigle. 1977. p. B1-B10. \$1.
- B 1436. Geology of the Yreka quadrangle, Siskiyou County, California, by P. E. Hotz. 1977. 72 p.; plate in pocket. \$2.75.

### Water-Supply Papers

- W 1757-N. Geohydrology of North Eastern Province, Kenya, by W. V. Swarzenski and M. J. Mundorff. 1977. p. N1-N68, plates in pocket. \$3.30.

## ANNOUNCEMENT

### DIRECT-MAIL SALES OF USGS OPEN-FILE REPORTS

By the  
U.S. Geological Survey

#### Purpose of Program

- To furnish microfiche or paper-duplicate copies of open-file reports from a single, centrally located facility.
- To provide faster order-filling service to the public for copies of open-file reports.
- To increase the availability of earth-science information to the scientific community.

#### Order USGS Open-File Reports From:

Open-File Services Section, Branch of Distribution, U.S. Geological Survey, Box 25425, Federal Center, Denver, CO 80225. (Telephone: 303-234-5888.)

Price information will be published in the monthly listing "New Publications of the Geological Survey."

This facility will stock open-file reports only. Please do not mix orders for open-file reports with orders for any other USGS products. Checks or money orders, in exact amount for open-file reports ordered, should be made payable to U.S. Geological Survey. Prepayment is required.

Order by series and number (such as Open-File Report 77-123) and complete title.

Inquiries concerning this new program should be sent to the address given above.

**U.S. GOVERNMENT**  
**PRINTING OFFICE**  
PUBLIC DOCUMENTS DEPARTMENT  
**WASHINGTON, D C 20402**  
OFFICIAL BUSINESS  
PENALTY FOR PRIVATE USE \$300

FOURTH-CLASS MAIL  
POSTAGE & FEES PAID  
USGS  
PERMIT No. G23